CALIBRATION SYSTEM DESIGN AND DETERMINATION OF FILTER CALIBRATION REQUIREMENTS FOR SNAP

Nick Mostek

Submitted to the faculty of the University Graduate School
in partial fulfillment of the requirements
for the degree
Doctor of Philosophy
in the Department of Astronomy,
Indiana University
September, 2007

Accepted by the Graduate Faculty, Indiana University, in partial fulfillment of the requirements for the degree of Doctor of Philosophy.

Doctoral Committee

Stuart Mufson, Ph.D.

Constantine Deliyannis, Ph.D.

Kent Honeycutt, Ph.D.

Jim Musser, Ph.D.

August 24, 2007

For my wife, April,

and my parents, Dan and Betty

ACKNOWLEDGEMENTS

To begin, I would like to thank my parents, Dan and Betty Mostek. My parents have always encouraged me to choose a career path that I would enjoy every day. They have supported me without complaint for almost 30 years, and I truly admire their unending selflessness. I also would like to thank my brothers, Ken and John, who will never let a little competition come between family, and my sister Krista, who gives more to others on a daily basis than I probably will during my entire life. I can say without reservation that the members of my family are all wonderful people, and I wish I could spend more time with them everyday.

I would like to thank all my teachers and professors that I have had over the last 25 years, with particular mention of my high-school math teacher Gary Stensaas. Gary has taught generations of students, and I cannot fathom the amount of patience he had to teach algebra to 16 year olds for years on end. I would like to thank my graduate advisor, Stuart Mufson. While Stu and I have been known to have a disagreement from time to time, there is no doubt in my mind that I am a better scientist because of his rigorous skepticism. Stu has not only taught me how to practice science, but how to survive in science. I would like to thank Senior Scientist Chuck Bower, Technicians Brice Adams and Mark Gebhard, and Computer Guru Eric Ost, who provided essential support for this dissertation. I must also thank the SNAP collaboration for support of this research, particularly Susana Deustua, Ralph Bohlin, Michael Richmond, Mike Lampton, Mike Sholl, Chris Bebek, Alex Kim, Gary Kushner, Greg Tarle, Matt Brown, Natalie Roe, and Michael Levi.

I would like to thank the graduate friends that I have made during my time

in graduate school, including Brian Rebel, Steve Margheim, Adam Rengstorf (and family), Stella Kafka, and Heidi Tebbe. All of them left graduate school before me, and they were sorely missed. I also have a large group of friends with whom I play softball, and they have kept me sane and grounded while I worked my way through graduate school. I thank them for their friendship and nearly constant laughter.

Finally, I would like to thank my wife, April. Words cannot describe how much I love her. She has supported me in every way possible during my time in graduate school. Her patience and understanding has been superhuman, particularly since I began writing this dissertation. She is also an incredibly talented graphic designer, and I "employed" her talents to help design the MICCS figures in Chapter 5. April truly is my better half, and I can only hope that I am worthy of her.

Thank you all. Now on with the show....

Nick Mostek

CALIBRATION SYSTEM DESIGN AND DETERMINATION OF FILTER CALIBRATION REQUIREMENTS FOR SNAP

The SuperNova/Acceleration Probe (SNAP) is a proposed space-based, wide-field telescope designed to measure the properties of dark energy in our universe. SNAP will measure ∼2000 type Ia supernovae, and the reduction of systematic errors in the relative spectrophotometric measurements will be critical to the mission science. A stringent systematic error requirement of 2% in color photometry is driving the SNAP calibration methodology and system design into new areas of space-based, radiometric calibration for astronomical missions.

At the forefront of these new calibration techniques is the use of narrowband light and photodiodes to measure the precise irradiance incident on SNAP filters and detectors. Using these techniques, I have built the Monochromatic Illumination and Cryogenic Calibration System (MICCS) to address the SNAP calibration hardware requirements. With this system, I can transfer the NIST irradiance calibration of an InGaAs photodiode to transfer photodiodes operated at 140K as well as measure the transmission of interference filters at incident angles and temperature similar to that used on the SNAP focal plane.

Due to size and light efficiency constraints, I also investigated the use of light emitting diodes (LEDs) as calibrating light sources onboard SNAP. When coupled with calibrated photodiodes, a selection of LEDs could fly onboard SNAP and be

used to track changes in the SNAP interference filters during the lifetime of the experiment. The error from this LED calibration technique will be propagated to the dark energy parameters to determine what design constraints are required of the onboard illumination system.

CONTENTS

LIST OF FIGURES

Figure

LIST OF TABLES

Table

LIST OF APPENDICES

Appendix

CHAPTER 1

Introduction

1.1 Overview

The discovery that the universe is accelerating in expansion has radically altered the modern day view of cosmology. This unexpected result has led to a deluge of theories that propose a wide range of physical models to explain the acceleration. Two of the leading theories include a modification of gravity at the largest distance scales or an unseen "dark energy" powering the acceleration. These theories are consistent with the level of precision in current datasets, and cosmologists are left seeking more accurate measurements of the expansion to distinguish between physical models.

One method to measure the expansion of the universe is through astrophysical objects with a known luminosity, called "standard candles". When measured on cosmological scales, a comparison of the luminosities for these objects can reveal how the universe has expanded over time. Over the past two decades, type Ia supernovae (SNIa) luminosities have been studied and standardized for use as a standard candle sources (see Höflich et al. (2003) for a review). With only a 10-15% intrinsic dispersion in brightness, measurements of SNIa have successfully shown that the universe is undergoing accelerating expansion.

Further study of the cosmological expansion with SNIa requires a larger sample size that spans cosmic distance scales. These requirements have been used to argue in favor of a dedicated space-based mission that can observer SNIa in the near infrared wavelength regime (Linder and Huterer, 2003). In the next generation of proposed

cosmology missions (SNAP Collaboration: G. Aldering et al., 2004; Benford and Lauer, 2006; Phillips et al., 2006), large datasets of SNIa will become available and will improve our knowledge of the dark energy that may be driving the accelerated expansion of the universe. One such mission, the Supernova/Acceleration Probe (SNAP), will conduct a survey for SNIa with tight control of the systematic error in the SNIa photometry. This emphasis on controlling systematic error will allow SNAP to measure each SNIa magnitude to a high degree of accuracy and therefore precisely map the expansion history of the universe that will yield a better understanding the dark energy.

Since the SNAP mission is vitally interested in minimizing systematic errors in SNIa measurements, the photometric calibration of the SNAP instrumentation will contribute significantly to the final accuracy of the cosmological measurements. In this dissertation, I will discuss methods that I developed to calibrate the SNAP focal plane for photometry. I will outline the photometric calibration plan and present a set of candidate standard stars that have been monitored for stability in the SNAP survey field. I will also detail the current designs of the onboard calibration system and study the effects of filter transmission calibration errors on the determination of the cosmological parameters. The latter study will require the use of a monochromator-based calibration light source and lead to science-driven recommendations for the calibration of SNAP.

1.2 Dark Energy Theory

The expansion of the universe can be described using a set of dynamical equations derived from General Relativity and the Robertson-Walker metric known as the Friedmann-Lemaître equations (Yao et al., 2006). The first equation describes the expansion/contraction of the universe as a function of the energy density ρ, geometry

k, and cosmological constant term Λ, and is written as

$$H^2(a) \equiv \left(\frac{\dot{a}(t)}{a(t)}\right)^2 = \frac{8\pi\ G}{3}\rho - \frac{k}{a^2} + \frac{\Lambda}{3}, \tag{1.1}$$

where $a(t)$ is the time-dependent dimensionless scale factor for a co-moving volume (or "expansion history") of the universe[1]. This equation is referred to as the Friedmann equation, and for notation purposes, it is expressed in "natural" units where $c \equiv 1$. In this framework, k has the values of -1, 0, or 1 depending on whether the geometry of the universe is open, Euclidean, or closed, respectfully. In the local universe at time t_0 ($\equiv$ now), H_0 is defined as a current value of the $H(a)$ and is known as the Hubble constant. Therefore, $H(a)$ is referred to as the "Hubble parameter". In a flat Euclidian universe with no cosmological constant (where $k = 0$ and $\Lambda = 0$), a critical density can be defined from Equation 1.1 such that

$$\rho_c \equiv \frac{3H^2}{8\pi\ G}. \tag{1.2}$$

The second Friedmann-Lemaître equation describes the scale factor acceleration behavior with respect to the dynamical pressure p,

$$\frac{\ddot{a}(t)}{a(t)} = \frac{\Lambda}{3} - \frac{4\pi\ G}{3}(\rho + 3p). \tag{1.3}$$

To obtain the behavior of the energy density with time, Equation 1.1 is differentiated with respect to time and $\ddot{a}$ is eliminated with Equation 1.3. With the equation of state for the universe defined as $w \equiv p/\rho$ and assumed to be constant, the change in energy density can be written as

$$\dot{\rho} = -3\rho(1 + w)\frac{\dot{a}}{a} \tag{1.4}$$

[1]Alternatively, the dimensionless scale factor $a(t)$ can be written as $a(t) = R(t)/R_0$ where R contains the units of the comoving distance and $R_0 = R(t_0)$. Therefore, $a(t) = R(t)$ if $R_0 \equiv 1$.

(Yao et al., 2006). This equation can also be obtained through the First Law of Thermodynamics, where $dE + pdV = d(\rho a^3) + pd(a^3) = 0$. Further, Equation 1.4 can be integrated to yield

$$\rho \propto a^{-3(1+w)}. \tag{1.5}$$

With the equation of state, Equation 1.5 allows one to study how different forms of energy in the universe affect the expansion behavior. Common examples of the equation of state (EOS) include:

$$\begin{aligned} \text{pressureless matter}: \quad & w = 0 \Rightarrow \rho \propto a^{-3}, \\ \text{radiation}: \quad & w = \frac{1}{3} \Rightarrow \rho \propto a^{-4}, \\ \text{vacuum energy}: \quad & w = -1 \Rightarrow \rho \propto \text{constant}. \end{aligned} \tag{1.6}$$

To examine which values of w can contribute to an accelerated expansion in the scale factor, the deceleration parameter q_0 is defined by dividing Equation 1.3 by 1.1 so that

$$q_0 = -\left(\frac{a\ddot{a}}{\dot{a}^2}\right)_0 = \frac{1}{2}\Omega_M + \frac{(1+3w)}{2}\Omega_\Lambda \tag{1.7}$$

where $\Omega \equiv \rho/\rho_c$, Ω_M is the present day matter component of Ω, and Ω_Λ is the vacuum energy component defined as $\Omega_\Lambda \equiv \Lambda/3H^2$. This formulation shows that values of $w < -1/3$ may lead to negative values of deceleration in the scale factor and therefore an acceleration in the expansion rate. Such an equation of state with negative w may have an unknown energy component that is often referred to as "dark energy".

Using the same definitions for the dimensionless mass density Ω_M and vacuum energy density Ω_Λ, the Friedmann equation for a flat universe and a cosmological constant can be written as

$$\left(\frac{H(a)}{H_0}\right)^2 = \frac{\Omega_M}{a^3} + \Omega_\Lambda, \tag{1.8}$$

where H_0 is the Hubble constant.

Direct measurements of the Hubble parameter require a measure of the timescale of the expansion. Photons provide just such a measure of the universal timescale. As the universe expands, the wavelengths of photons traveling across space are stretched along with space itself. This stretching can be measured by comparing the photon wavelength, λ_0 in the observer's rest frame $a(t_0)$ to the photon wavelength λ from a cosmic origin frame $a(t)$ at an earlier time. The stretch of the photon wavelength from its original wavelength is called its "redshift" z, and it is defined as

$$z \equiv \frac{\lambda - \lambda_0}{\lambda_0} = \frac{\Delta\lambda}{\lambda}. \tag{1.9}$$

Using the Friedmann-Robertson-Walker metric, a relation between the redshift and the scale factor can be written as

$$(1 + z) = \frac{\lambda}{\lambda_0} = \frac{1}{a}. \tag{1.10}$$

Because the nature of dark energy is not known, we cannot assume that the dark energy equation of state, and therefore the dark energy density, is constant over cosmic time. Using the relation of redshift to the scale factor from Equation 1.10, the dark energy density can be generalized to a form that is allowed to evolve with time. Models of dark energy that have energy densities that can change with time are called "Quintessence" models. For an evolving w, the dark energy density can be found by integrating Equation 1.4 so that

$$\rho_{DE} = \rho_{DE,0} \exp\left\{-3 \int_0^z \frac{dz'}{(1 + z')}[1 + w(z')]\right\} \tag{1.11}$$

where $\rho_{DE,0}$ is the current value of the dark energy density (Dodelson, 2003; Brown, 2007). Since the true functional form of $w(z)$ is unknown, a parameterization that is

commonly used in today's literature (Linder, 2003) is

$$w(z) = w_0 + w_a \frac{z}{(1+z)}. \tag{1.12}$$

This $w(z)$ parameterization with w_0 and w_a allows for the EOS to behave as a cosmological constant for $w_0 = -1$ and $w_a = 0$. If $w_a \neq 0$, then the contribution from dark energy can vary with time. The parameterization for dark energy EOS in Equation 1.12 can therefore be used in a wide variety of models.

The Hubble parameter can now be rewritten and generalized for the time-varying dark energy EOS $w(z)$ in the form

$$\left(\frac{H(a)}{H_0}\right)^2 = \Omega_M(1+z)^3 + (1-\Omega_M)\exp\left[3\int_0^z \frac{dz'}{(1+z')}(1+w_0+w_a\frac{z'}{(1+z')})\right]. \tag{1.13}$$

I adopt this model using Ω_M, w_0, and w_a for this dissertation.

1.3 Luminosity Distance through Type Ia Supernovae

The expansion history of the universe can be determined by measuring distance across a range of redshifts. This data effectively measures the change in the scale factor over a range of cosmic time. Formally, the physical distance from the present time to an earlier time can be calculated by integrating the Hubble parameter over a redshift range of interest. To measure the expansion of the universe over measured distances in space, a comoving distance is defined. Conceptually, the comoving distance is a constant distance between two points in space. The physical distance between the two points is the scale factor times the comoving distance. Mathematically, the comoving distance is expressed as

$$r(z) = \int_0^z \frac{dz'}{H(z')} \tag{1.14}$$

where $H(z)$ is given by Equation 1.13. An approach to determining r is to measure the luminosity distance to an astrophysical object with a known brightness. The luminosity distance is related to the comoving distance by

$$d_L(z) = (1+z)r(z) = \sqrt{\frac{\mathcal{L}}{4\pi\mathcal{F}}}, \tag{1.15}$$

where $\mathcal{L}$ is the standard luminosity of the astrophysical object and $\mathcal{F}$ is its measured flux. A typical unit used by astronomers to method to measure luminosity distance is the distance modulus $\mu(z)$, which is calculated as

$$\begin{aligned} \mu(z) &= m(z) - \mathcal{M} \\ &= -2.5\log_{10}(\mathcal{F}/\mathcal{F}_0) - \mathcal{M} \\ &= 5\log_{10}(d_L(z)) + 25, \end{aligned} \tag{1.16}$$

where $m(z)$ is the observed magnitude of the object at a given redshift and $\mathcal{M} \equiv M - 5\log_{10}[H_0/100 kms^{-1}Mpc^{-1}]$ with M being the absolute magnitude of the object. The $\mathcal{M}$ parameter is dubbed a "nuisance" parameter since the absolute magnitude of the object only affects H_0 and not the expansion history $H(z)$. Therefore, the ideal "standard candle" will have a measured redshift, observed magnitude (corrected for intervening astrophysical effects), and a known M. These quantities lead to the object's distance modulus and consequently luminosity distance.

Historically, measuring luminosity distance has been hampered by two major difficulties. First, there are few astrophysical sources with a standardized luminosity in the rest frame *and* the observed cosmic frame. Often, astrophysical objects have undergone evolution, such as metallicity enrichment or modified morphology, as the universe expands. These evolutionary effects can be difficult to separate from the effect of cosmological expansion on the object's brightness. Another difficulty with

measuring luminosity distance is finding a standardized object of sufficient brightness so that it can be measured at large distances. Both of these problems can be overcome with observations of type Ia supernovae.

Supernovae are bright stellar explosions that are observable at large cosmic distances. There are two types of supernova explosions. Type Ia supernovae are generated from a close binary star system with a white dwarf and a companion main sequence or red giant star. If the separation between the stars is small enough, the white dwarf will accrete gas from the atmosphere of the companion star. As the gaseous material falls onto the white dwarf, it adds to the hydrogen envelope and the total mass of the white dwarf. Eventually, the white dwarf mass will approach the Chandresekhar limit of 1.4 solar masses and the electron degeneracy pressure supporting the star will not be able to counterbalance the inward gravitational pull of the star. The resulting gravitational collapse causes compressional heating in the star which takes the form a burning deflagration wave. This wave forces a thermonuclear runaway explosion that destroys the binary system. Type II supernovae occur from a single massive star in an advanced stage of its evolution. As the nucleosynthesis within the core of the massive star builds up to heavy elements up to iron, the high densities force the core to collapse under the immense gravitational pull. The resulting runaway gravitational collapse can be stopped by the onset of neutron degeneracy pressure, but the sudden halt causes a luminous outward expanding shock wave. While both type Ia and II supernovae are similar in name, they have very different physical mechanisms behind their violent explosions.

Since Type Ia supernovae occur consistently at the Chandresekhar limit, mass differences (and hence luminosity differences) between events are minimized. Type II supernovae are more likely to be affected by evolution effects such as metallicity enrichment, and therefore have a larger range of intrinsic dispersion in their inherent luminosities. The homogeneity of mass and physics behind SNIa explosions provide

consistent luminosities to use as standard candles. In terms of measuring luminosity distance, measurements of SNIa brightness over a range of redshifts are highly useful in measuring luminosity distance.

The brightness of SNIa explosions have a characteristic light curve in which the brightness of the event rises quickly over several days, peaks, and then decreases over a few weeks. The peak brightness (or magnitude) of these light curves is used as a standard candle which is independent of redshift. To calibrate these light curves as standard candles, corrections must be made to the observed magnitudes to remove intervening effects of time-dilation, instrumental bandpasses, and host galaxy extinction.

Because the universal expansion affects both space and time, time dilation must be removed from the SNIa light curve timescale. For a measured SNIa redshift z, the effect of time dilation on the light curve timescale causes it to be stretched by $(1 + z)$. The time-dilation effect was first measured by Hamuy et al. (1995) for SNIa through an empirical relationship between the light curve width and peak B-band magnitude (termed the "width-luminosity" relationship). Parameterizing the magnitude correction through the change in the B magnitude from peak to 15 days after peak (termed $\Delta\ m_{15}$), Hamuy et al. corrected the SNIa peak magnitudes to $\sigma < 0.2$ mag. Another technique to calibrate the SNIa width-luminosity relationship is termed the "stretch" correction and was introduced by Perlmutter et al. (1998). The stretch correction to the peak B magnitude was parameterized as

$$\Delta\ m_b(s) = \alpha(s - 1), \tag{1.17}$$

where α is fit parameter for all SNIa light curves being standardized in the sample and s is the stretch factor for each individual supernova. Figure 1.1 shows 18 local SNIa light curves from the Calán/Tololo Survey (Hamuy et al., 1996) before and after the

stretch correction. The figure demonstrates the excellent consistency between SNIa light curves after the effect of time-dilation has been removed from the SNIa light curves. The stretch correction for the width-luminosity relation from Perlmutter et al. reduced the error in SNIa peak magnitudes to σ_m=0.17.

To measure SNIa light curves over large distances, it is necessary to measure SNIa photons that have been redshifted from their original emission wavelength. Therefore, it is common to use bandpass filters optimized for different wavelength ranges to cover a wide range of redshifts to and increase the signal-to-noise in the SNIa photometry. Another correction required standardize SNIa measurements is to transform each redshifted SNIa peak magnitude from its measured filter band into a single filter band where $z = 0$ (called the rest-frame filter band). The corrections of redshifted magnitudes from one filter band to a rest-frame filter band are called K-corrections (Oke and Sandage, 1968; Kim et al., 1996). The definition of the multiband K-correction for SNIa peak magnitudes from filter x to filter y is written as

$$\begin{aligned} K_{xy} = & - 2.5\log_{10}\left[\frac{\int \mathcal{Z}(\lambda)\tau_x(\lambda)d\lambda}{\int \mathcal{Z}(\lambda)\tau_y(\lambda)d\lambda}\right] \\ & + 2.5\log_{10}(1+z) + 2.5\log_{10}\left[\frac{\int F(\lambda)\tau_x(\lambda)d\lambda}{\int F(\lambda/(1+z))\tau_y(\lambda)d\lambda}\right], \end{aligned} \quad (1.18)$$

where $\mathcal{Z}(\lambda)$ is an idealized spectrum of an SNIa source at z=0, $\tau_x(\lambda)$ is the filter transmission function for filter x, and $F(\lambda)$ is the measured SNIa spectrum at peak magnitude. Note that if the K-correction is applied to a redshifted magnitude within a single filter band, $x = y$, and the first term is eliminated to recover the original K-correction from Oke and Sandage (1968). The idealized spectrum can either be a pre-existing SNIa template spectrum (see Nugent et al. 2002) or more typically is built from a dataset with a large number of low-redshift SNIa spectra.

The K-correction, and thus the SNIa peak magnitude, is further complicated by

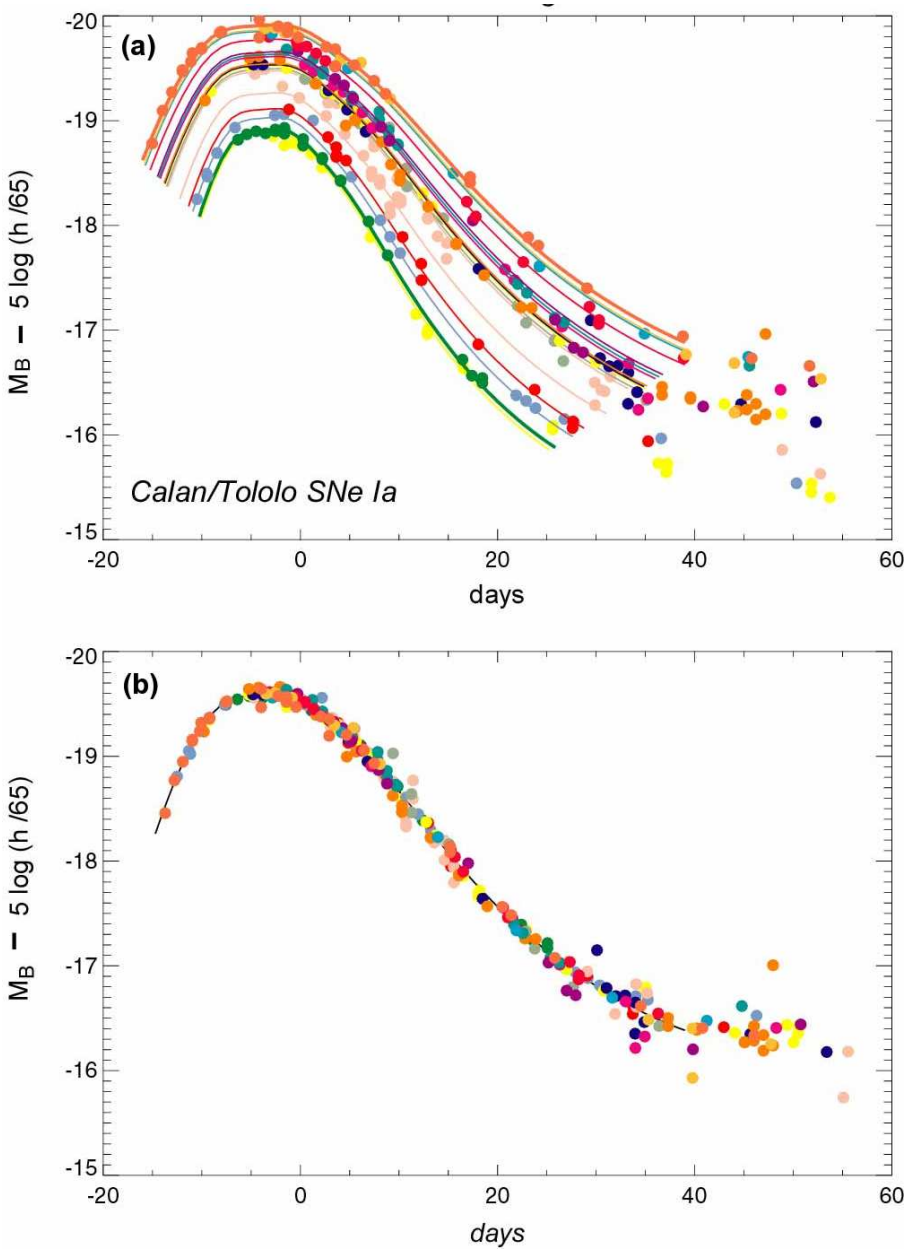

Figure 1.1. The *B*-band light curves for the 18 low-redshift type Ia supernovae of the Calán/Tololo Survey (Hamuy et al., 1996). The figure shows (a) the raw light curves and (b) the stretch corrected light curves of each of the SNIa. This plot was presented in Perlmutter et al. (1997).

the reddening of SNIa colors due to host galaxy dust extinction. Since a distant SNIa will likely have unknown host galaxy dust content, the extinction correction A_V can be measured with broadband $(B-V)$ colors of SNIa at late light curve epochs (30 - 90 days after peak) when the SNIa colors are found to be uncorrelated with the peak magnitude (Phillips et al., 1999). Another method is to use template SNIa spectra (either empirical or simulated) and calculate the expected SNIa colors after stretch and K-corrections (Riess et al., 1996; Nugent et al., 2002). The excess reddening in the corrected $(B-V)$ colors gives a measure of the host galaxy extinction and thus an unreddened peak magnitude can be calculated.

Using the values of stretch, cross-filter K-correction, and extinction correction, the final corrected SNIa B-band magnitude for a peak magnitude measured in filter band x is given by

$$m_b^{corr} = m_x^{obs} + \Delta\ m_b(s) - K_{bx} - A_x, \tag{1.19}$$

where A_x is the extinction to the peak magnitude in filter band x, K_{bx} is the K-correction between the B and x filters, and $\Delta m_b(s)$ is the stretch correction. Two popular techniques, MLCS (Riess et al., 1996) and CMAGIC (Wang et al., 2003), have been developed to determine these magnitude corrections simultaneously and reduce the scatter in peak magnitudes to $\sigma_m = 0.1$ - 0.15 mag. The corrected peak magnitudes of SNIa from Equation 1.19 and their associated redshifts z can be used to calculate the distance modulus from Equation 1.16. From the empirical data for $\mu(z)$ and combining Equation 1.13, 1.14, and 1.15, a maximum likelihood function can be calculated and the best fit cosmological parameter values of Ω_M, w_0, and w_a can be determined.

1.4 Cosmology Measurements and SNAP

The initial discovery of the accelerating expansion of the universe through SNIa measurements came from the Supernova Cosmology Project (SCP) (Perlmutter et al.

1998, hereafter SCP98) and the High-z Supernova Search Team (Riess et al., 1998). Both experiments found that the expansion history was consistent with a universe with low mass density (Ω_M) and a non-zero vacuum energy density (Ω_Λ). The SNIa data used for the SCP98 result is shown in Figure 1.2 and consisted of 42 SNIa from $0.2 < z < 1.0$ and 18 local SNIa at $z < 0.1$ from the Calán/Tololo Survey. Using this data to probe the expansion history (see Equation 1.16), SCP98 found a best fit value of $\Omega_M \sim 0.3$ and a $> 99\%$ confidence in a non-zero Ω_Λ. This result provided evidence for an universe accelerating in expansion and perhaps driven by a form of dark energy.

The concordance of the SNIa results with those of cosmic microwave background (CMB) experiments (Melchiorri et al., 2000; Balbi et al., 2000; Spergel et al., 2003) and galaxy cluster counting experiments (Bahcall and Fan, 1998) is shown in Figure 1.3 (reprinted from Yao et al. 2006 with modification from Aldering et al. 2002). The CMB measurements are the most sensitive to the geometry of the universe while the cluster counting measures only the matter energy density. The overlap of the error contours from these cosmological probes provide a "prior" constraint on fit cosmologies and increase the statistical confidence in the cosmological parameter values of Ω_M and Ω_Λ. These priors lead to energy densities of $\Omega_M = 0.25^{\pm 0.07}_{\pm 0.06}(stat) \pm 0.04(sys)$ and $\Omega_\Lambda = 0.75^{\pm 0.06}_{\pm 0.07}(stat) \pm 0.04(sys)$ for an assumed flat universe ($\Omega_M + \Omega_\Lambda = 1$) and a cosmological constant $w = -1$ (Knop et al., 2003). An important point to mention is that each of these experiments use completely independent techniques and yet determine cosmological parameters that are consistent with one another. This fact gives confidence that a non-zero value of Ω_Λ is indeed a property of the universe.

The general result of a non-zero Ω_Λ leaves open the possibility of dark energy either as a cosmological constant or a time-varying energy density[2] Determining the nature of the dark energy equation of state w through the luminosity distance of

[2]Alternative theories to explain the accelerated expansion rate exist, including modifications to gravity on cosmic distance scales (Ishak et al., 2006).

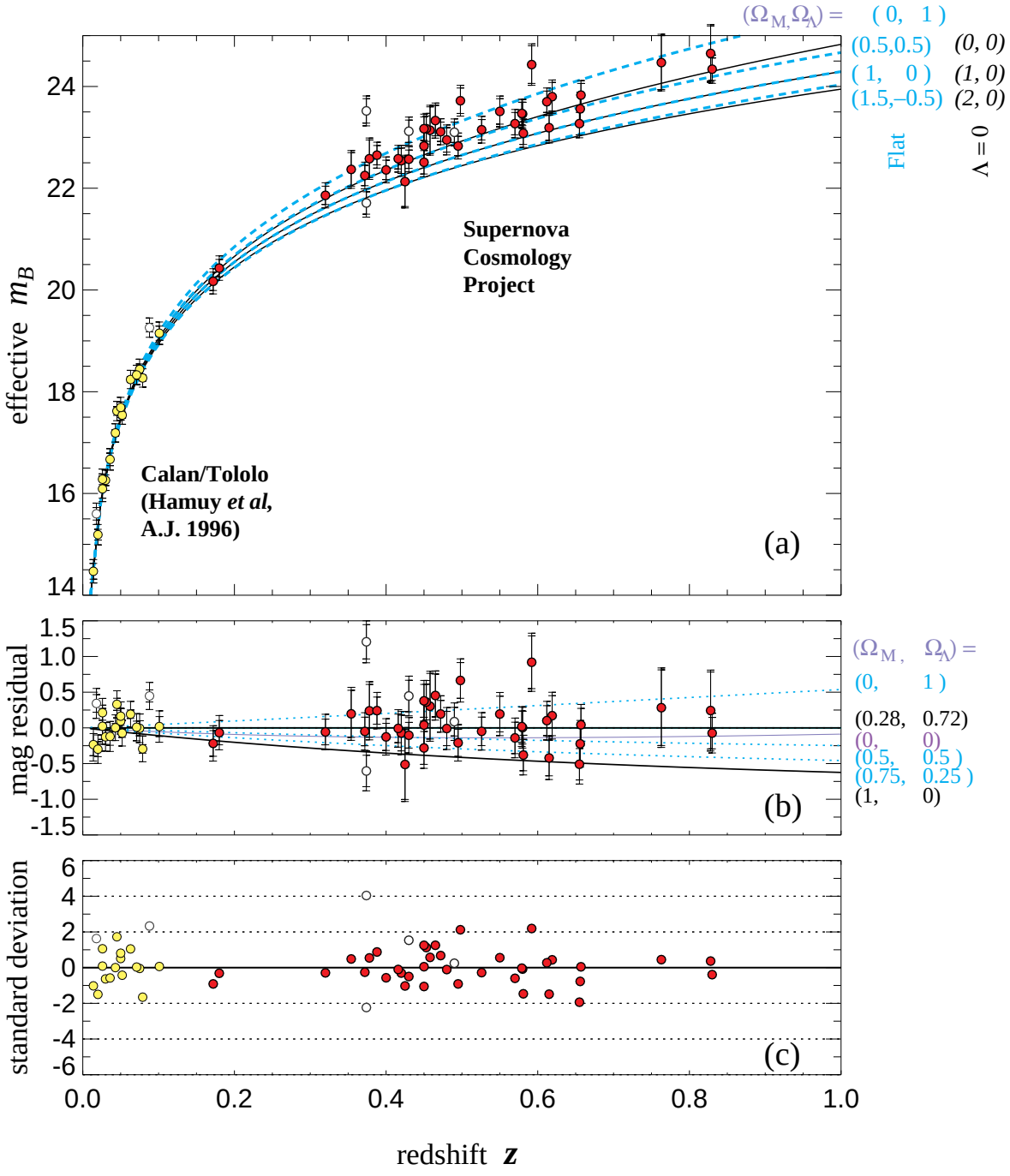

Figure 1.2. The SNIa data used to discover the accelerating expansion of the universe (Perlmutter et al., 1998). (a) The Hubble diagram shows the SNIa magnitudes as a function of redshift, thus directly probing the expansion history through Equation 1.16. (b) The measured magnitude residuals relative to the expected magnitude using the best fit flat cosmology. (c) The standard deviation of the measured magnitudes relative to the best fit flat cosmology.

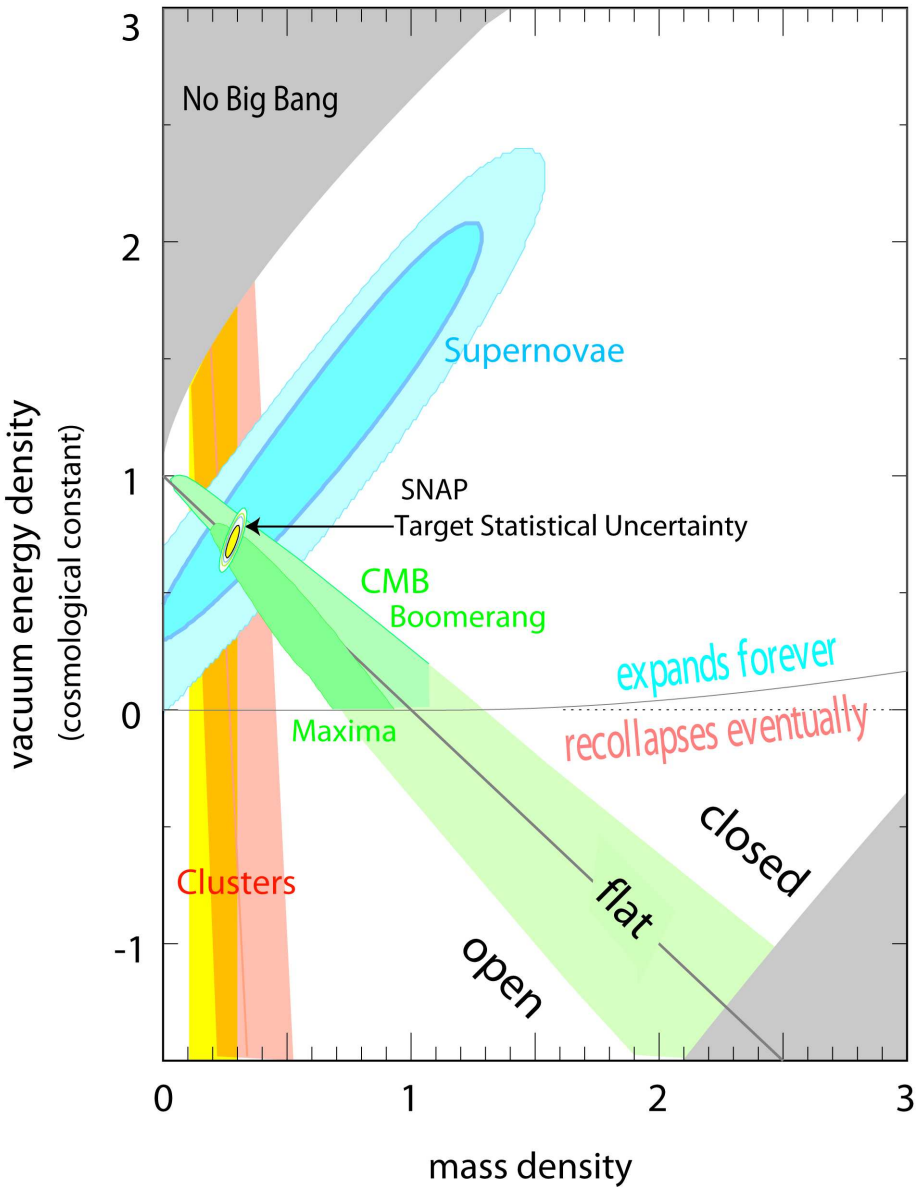

Figure 1.3. The concordance of cosmology experiments for the cosmological parameters of mass energy density, Ω_M, and the vacuum energy density, Ω_Λ. The results of the SNIa measurements (Perlmutter et al., 1998; Riess et al., 1998), CMB measurements (Melchiorri et al., 2000; Balbi et al., 2000; Spergel et al., 2003), and cluster counting (Bahcall and Fan, 1998), combine to increase the statistical confidence in the best fit cosmological parameter values of $\Omega_M = 0.28$ and $\Omega_\Lambda = 0.72$. Using the results of these previous experiments as constraints on the cosmological parameters, the target statistical uncertainty for the SNAP experiment is overlayed and shows the power of the mission. This figure is reprinted from Yao et al. (2006) with modification by Aldering et al. (2002).

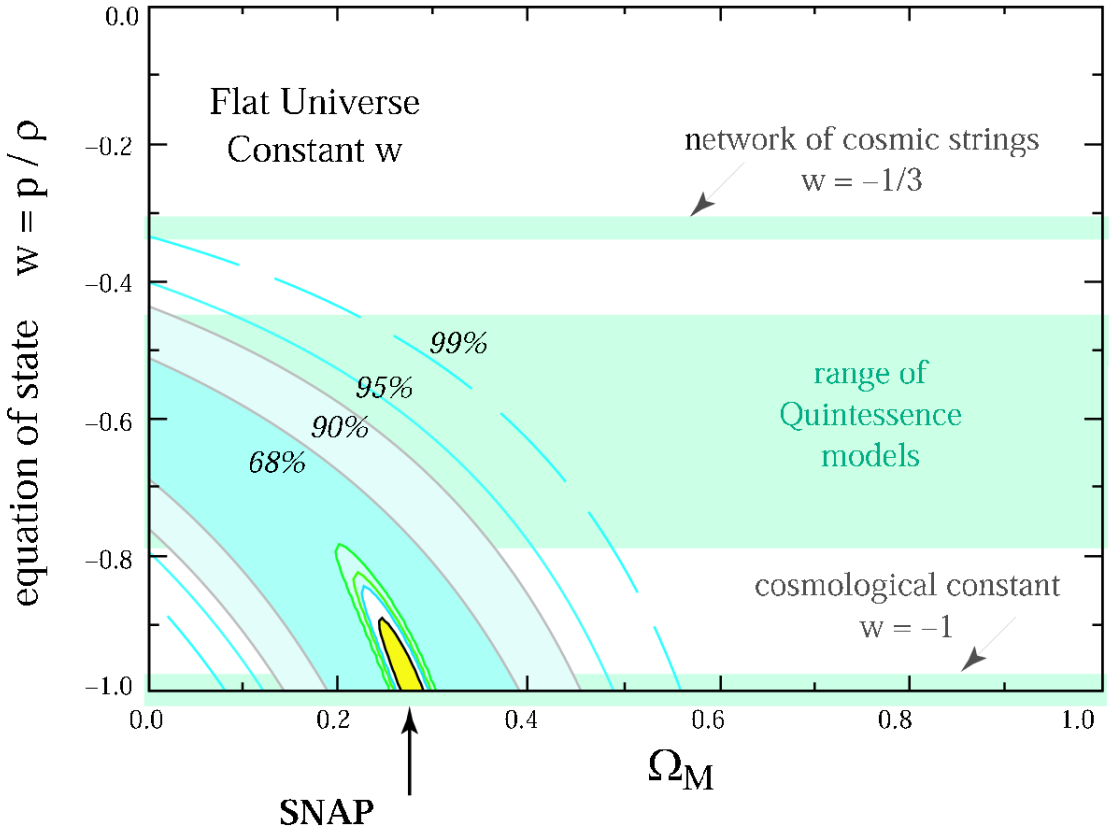

Figure 1.4. The measurement of the dark energy equation of state w and mass energy density Ω_M using SNIa data from the Supernova Cosmology Project (blue contours) (Knop et al., 2003) and the proposed SNAP mission (yellow contours) assuming a $w = 1$ model. This figure is reprinted from Schubnell (2004).

SNIa requires increased SNIa statistics out to $z > 1.5$ (Linder and Huterer, 2003). As mentioned in Section 1.3, modern techniques to measure the peak magnitude of SNIa light curves have reduced the magnitude dispersion σ_m to 0.1 - 0.15 mag. This dispersion appears to be statistical with respect to $\mu(z)$ (and thus $d_L(z)$). For a given redshift bin of $\delta z = 0.1$, the dispersion in the mean SNIa magnitude for the redshift bin will decrease as square root of the number of SNIa. Therefore, an increased sample of SNIa will increase the measurement precision of $d_L(z)$ and the cosmological parameters. With a large enough SNIa dataset, the precision of the cosmological parameters will be limited by systematic error in the SNIa measurements.

The SNAP mission is designed to measure ∼2000 SNIa light curves out to a redshift of $z = 1.7$ (refer to Chapter 2 for further discussion of the SNAP mission parameters). The SNAP SNIa dataset is designed to measure $\Delta\Omega_M$ to ± 0.01, $\Delta\ w_0$ to $\pm$ 0.05, and $\Delta\ w_a$ to $\pm$ 0.3 for a flat universe (Linder and Huterer, 2003). The expected statistical confidence on the cosmological parameters using the SNAP SNIa is overlayed on the error contours of previous cosmology experiments in Figure 1.3. Figure 1.4 shows the improved w and Ω_M parameter error using the planned SNAP SNIa dataset over the previous SCP results (Knop et al., 2003; Schubnell, 2004).

The power of the SNAP mission will be its ability to discriminate among physical models for the w EOS. Figure 1.5 shows how the SNAP SNIa data could help rule out various dark energy models and thus lead to a better understanding of the physics of dark energy (Weller and Albrecht, 2002). The plot shows the difference in the SNAP SNIa magnitudes based on a flat, $\Omega_\Lambda = 0.7$ cosmology and $N_{SN} = 50$ SNIa per data point. The binning of SNIa data reduces the intrinsic SNIa dispersion of σ_m=0.15 mag by $\sqrt{N_{SN}}$ to 0.02 mag. Further, an irreducible systematic error of 0.02 magnitudes is applied to each redshift bin, simulating the expected systematic error for SNAP. The combination of large SNIa sample statistics and low systematic error allows a statistically-significant probe of the various EOS models.

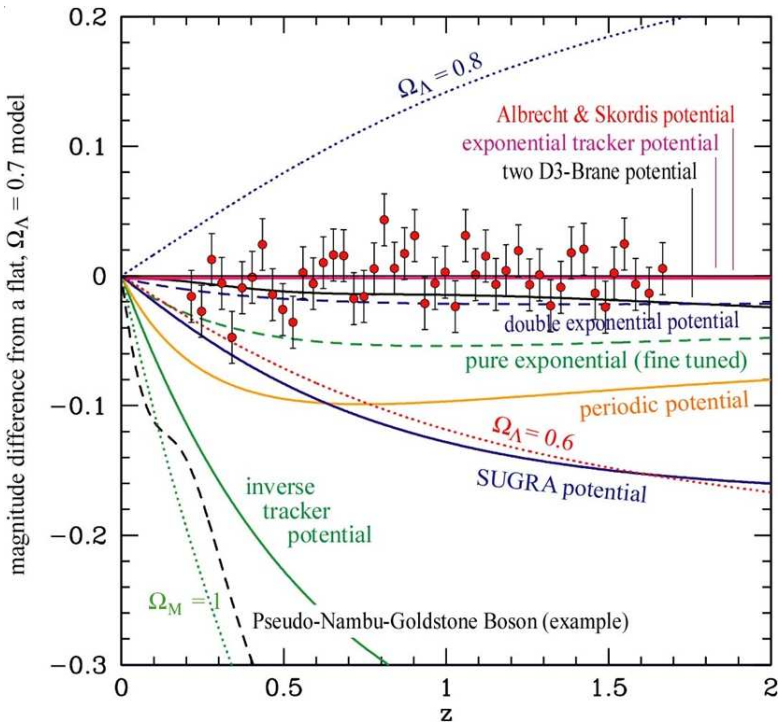

Figure 1.5. The expected SNAP SNIa magnitude error (red dots) for a flat cosmology and $\Omega_\Lambda = 0.7$. The magnitude difference for various cosmological model predictions are also plotted, demonstrating the power that the SNAP dataset will have in discriminating among energy models. This figure is based on Weller and Albrecht (2002).

1.5 Limitations due to Systematic Errors

Given the large sample number of SNIa that will be observed in the next generation cosmology experiments like SNAP, the final precision of the luminosity distance measurement technique through SNIa will be limited by the systematic errors associated with the photometric measurement process. Recognizing this fact, the Dark Energy Task Force (DETF)[3] recently stated that a high priority be given to "projects that will improve our understanding of the dominant systematic effects in dark energy measurements" (Albrecht et al., 2006). Since SNAP is designed to have enough SNIa statistics to make a systematics-limited determination of the cosmological parameters, a large portion of the R&D for the experiment is focused on identifying and reducing sources of systematic error.

An initial study of the effects of systematic errors on the determination of cosmological parameters with SNAP was performed by Kim et al. (2004)[4]. This study looked at the effects of three different toy systematic error models for the SNIa peak magnitudes. The first two error models were (1) a constant, irreducible magnitude dispersion that creates a systematic error floor, and (2) an irreducible magnitude dispersion that increases linearly with redshift. The irreducible systematic error models of (1) and (2) were implemented as:

$$\sigma_m = \sqrt{\frac{0.15^2}{N_{SN}} + dm^2}, \tag{1.20}$$

where 0.15 is the intrinsic SNIa magnitude dispersion, N_{SN} is the number of SNIa per redshift bin, and dm is either a constant (study 1) or linearly increasing error with redshift (study 2). Study (1) found a marginal increase in cosmological parameter error for $dm = 0.02$ mag and a significant increase in parameter error for $dm = 0.04$

[3]The Dark Energy Task Force was a committee formed in 2005 to study the science requirements for missions seeking to measure the effects of dark energy on the universe.

[4]I was a participant in this study.

mag. The cosmological parameter error contours for these irreducible systematic error models are shown in Figures 1.6 and 1.7. These figures use a slightly modified parameterization of the redshift-dependent dark energy component called w'. As a rule of thumb, $w' = -w_a/2$ at $z = 1$. The error model in study (1) approximates a "systematic floor" for the determination of SNIa magnitudes, and such an error could occur if there is an improper normalization of the detector response (see the discussion on Flat Fielding in Section 3.3.3 and 3.3.2).

Study (2) by Kim et al. (2004) implemented a linearly increasing dispersion of SNIa magnitudes with redshift. Sources of such a systematic error could come from a lack of precise flux calibration standards in the near-infrared (NIR) or an increase in detector noise at longer wavelengths. The study found that the redshift range of SNAP out to $z = 1.7$ provides significant leverage against systematic error in the NIR, and therefore a linearly increasing SNIa magnitude dispersion with redshift had minimal impact on the determination of cosmological parameters.

A third study performed by (Kim et al., 2004) was to offset the SNIa magnitudes linearly with redshift from the true magnitude values. It is important to point out that if such a magnitude offset is implemented as a constant for all redshifts, the "nuisance" parameter $\mathcal{M}$ (which contains the value of the Hubble constant H_0) will absorb the difference and the cosmological parameters of Ω_M and $w(z)$ remain unaffected. This fact eliminates the need to provide absolute flux values for SNIa magnitudes to probe the effects of dark energy on the universe. However, a systematic error that increasingly offsets the SNIa magnitudes with redshift may influence the cosmological parameters. This error model directly adds to the SNIa magnitudes $m(z)$ such that

$$m(z, dm) = m(z) + dm = m(z) + \epsilon \times \left[\frac{z}{1.7}\right], \tag{1.21}$$

where ϵ is the magnitude error at $z = 1.7$. A systematic error of this form could come

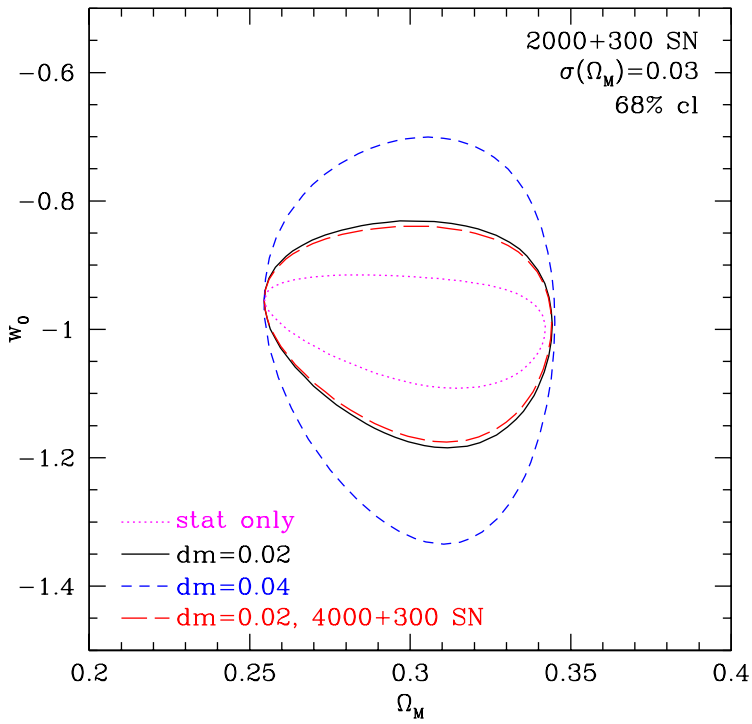

Figure 1.6. The measurement of the dark energy equation of state w_0 and mass energy density Ω_M with the SNAP survey and a constant, irreducible systematic error (dm) on the SNIa magnitudes. To help constrain the cosmology fits on Ω_M, a prior of $\sigma(\Omega_M) = 0.03$ is used from CMB measurements (see Section 1.4 for details). The parameter error increases modestly for $dm = 0.02$ and rapidly deteriorates for $dm = 0.04$. (Kim et al., 2004).

from the incorrect calibration of the magnitude system from the optical into the NIR (see Section 3.2.1 for further discussion).

Figure 1.8 shows the effect of this linearly increasing magnitude offset error with redshift on w_0 and w'. The cosmological parameters that are fit from this dataset are shifted from their true input values. (Kim et al., 2004) determined that the maximum allowable magnitude offset that increases linearly with redshift is 0.02 mag at $z = 1.7$. With the results these systematic error studies, the systematic error goal for SNAP SNIa magnitudes has been defined as 0.02 mag.

While the broad photometric error goal of 2% (0.02 mag) is useful for general planning of the SNAP mission, the calibration of SNAP SNIa photometry will require a detailed error budget to ensure that the photometric error goal is met. Therefore, it

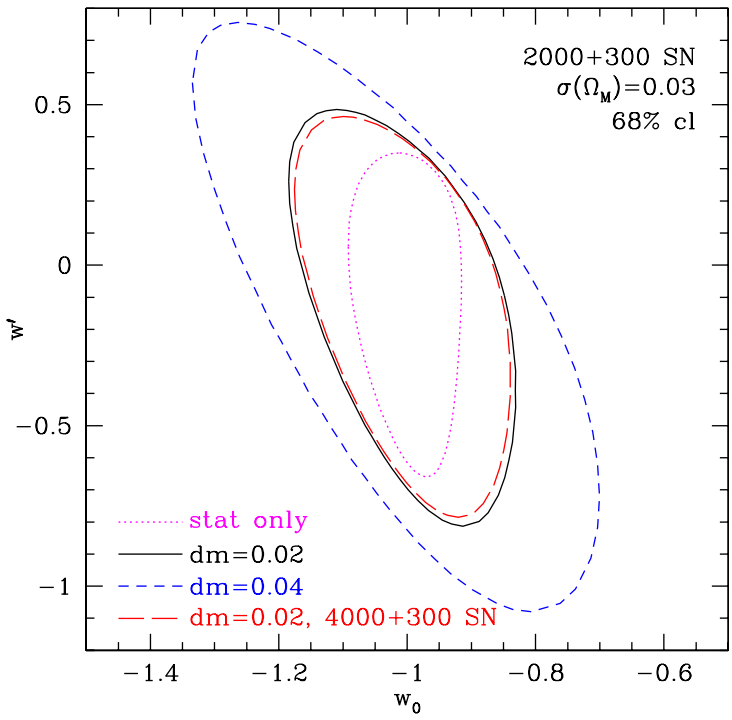

Figure 1.7. The measurement of the constant dark energy EOS component w_0 and the redshift dependent dark energy EOS component w' for a constant, irreducible systematic magnitude error (dm). There is a moderate increase in the dark energy parameter error for $dm = 0.02$ and a more severe decrease in accuracy for $dm = 0.04$. A test with 4000 SNIa shows very little increase in parameter accuracy in the presence of this systematic error. (Kim et al., 2004).

is necessary to break down the sources of systematic error in the SNAP photometric measurements. One component that directly affects the SNIa peak magnitudes is the transmission functions of the SNAP filters. A study by Kim and Miquel (2006) looked at a general calibration error in the zero-points of the SNAP filter set. The study found that a dispersion in the SNAP zero-points of 0.005 mag decreased the accuracy in determining w_0 by 10% and w_a by 4%. Further, the study found that errors in the filter zero-points contribute to errors in the SNIa colors and are amplified by the corrections for host galaxy extinction. While the behavior of the best fit cosmological parameters with respect to zero-point calibration error is interesting, it is not clear what physical effect would cause such a dispersion in the zero-points for SNAP. For ground based surveys, a dispersion in the zero-point magnitudes can easily be caused

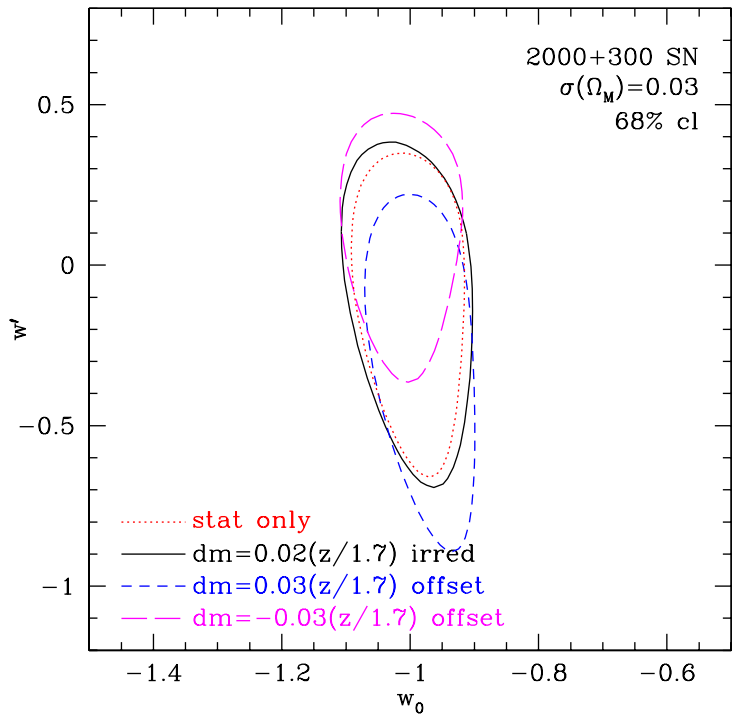

Figure 1.8. The measurement of the constant dark energy EOS component w_0 and the redshift dependent dark energy EOS component w' with SNIa magnitudes increasing offset by dm. When such an offset is present, the fit cosmological parameters are biased with respect to the true cosmology. An upper bound of $dm = 0.02$ for this type of systematic magnitude error has been recommended for the SNAP experiment. (Kim et al., 2004).

by atmospheric variations. For a space-based survey like SNAP, however, variation in the filter zero-points should only come from physical changes in the standard star source spectrum or the throughput of the telescope components such as the filter transmission functions[5].

In addition to the zero-point calibration, a critical step in the calibration of SNIa peak magnitudes from multiple filters is to apply the K-correction defined in Equation 1.18. Like the filter zero-points, the accuracy of the K-correction (and the associated extinction correction) to SNIa peak magnitudes depends on the calibration of the filter passbands (Davis et al., 2006). Since the filter transmission function $\tau_x(\lambda)$ typically defines the range of wavelengths for which these corrections are calculated,

[5]For other advantages to a space-based SNIa mission, see Section 2.1.

it is likely that errors in the SNAP filter transmission functions will result in correlated errors in the SNIa magnitudes. Therefore, two interesting questions regarding the calibration of SNAP filters are how can filter transmission functions change and what methods can be used to determine the transmission functions in orbit.

1.6 Synopsis of Filter Studies

The SNAP filter transmissions will play an important role in defining the measured SNIa peak magnitudes. Errors in the filter transmission calibration will lead to systematic error in these peak magnitudes and will affect the determination of cosmological parameters with SNAP. The goal of this dissertation is to explore the calibration requirements on the SNAP filter transmission functions. I will approach this issue with empirical measurements of filter transmission functions from commercially-available filters. I will test these filters using a calibration system built to simulate the environmental conditions that will be present on SNAP. In addition, I will look at two different techniques to measure filter transmissions onboard SNAP with the purpose of calibrating SNIa photometry. The errors from these measurements will be put into the SNAP mission simulation software to determine how they affect the determination of cosmological parameters. The results of these studies will provide science-driven guidance in defining the filter characterization process and onboard SNAP calibration hardware.

CHAPTER 2

The SNAP Mission

The Supernova Acceleration Probe (SNAP) is a proposed space-based mission whose primary goal will be to study the effects of dark energy in our universe. A major component of the SNAP mission is the survey of ∼2000 Type Ia Supernovae to determine the evolution history of the universe through accurate determination of their luminosity distance. SNAP will also perform an additional, wider survey designed to measure the matter density spectrum through weak lensing. While both surveys are considered complimentary, many of the strictest photometric calibration requirements will come from the supernova survey. For this reason, this document will focus on the calibration of the SNIa survey.

2.1 Basic Mission Plan

2.1.1 Science Drivers

As shown in Figure 1.5, many cosmological models predict the largest difference in SNIa magnitudes will be at redshifts $z > 0.8$. The new era of cosmological experiments will require a wide wavelength coverage and careful control of systematic error in order to discriminate between dark energy theories. Conducting a supernova survey that extends from the optical into the NIR provides two advantages. One important aspect is that the extensive wavelength coverage out to $z = 1.7$ provides a lever arm on w_0 and w_a in the presence of systematic photometry errors (Linder and Huterer, 2003). In addition, a survey over the SNAP wavelength range reduces the

systematic offset errors that are inherent in separate optical and NIR experiments due to different instrumental calibrations. Dark energy experiments using SNIa that focus only on the optical or the NIR actually run a greater risk of systematic error or would have difficult technical challenges in performing photometry to the required accuracy.

Driven by the powerful lever arm of the NIR to precisely determine the cosmological parameters, SNAP will be a space-based mission. By eliminating atmospheric absorption and seeing variability, measurements of supernovae at $z = 1.7$ will achieve a S/N that is equivalent to the intrinsic magnitude dispersion in a much shorter time than if the measurements were made with ground-based telescopes. Not only will SNAP be a highly efficient space-based mission in the NIR, it will also reduce systematic error in the photometry of SNIa. Systematic errors that will be minimized include the atmospheric error contribution to the zero-point calibration, diurnal thermal variations in the telescope, scattered light due to Earth-shine, and radiation effects due to near-Earth radiation belts. Much of the SNAP R&D effort has been spent developing a mission design that is both efficient and precise in the measurement of SNIa light curves.

2.1.2 SNIa Survey Parameters

The SNAP supernova survey field is rectangular 6.5° by 1.2° field located at RA=245°, Dec=+55° near the ecliptic pole. This site allows for continuous viewing year round from an L2 orbit. The field is also rotated to a position angle of 45° so that it will fit in an area of low Galactic absorption where $E(B-V)$ is less than 0.005 mag. Figure 2.1 shows the SNAP SNIa survey field overlayed on a Galactic dust map (Schlegel et al., 1998).

The SNAP supernova survey is designed to continuously monitor a 7.5 deg^2 field in a 4 day cadence for 22 months. This strategy will yield a homogenous set of ap-

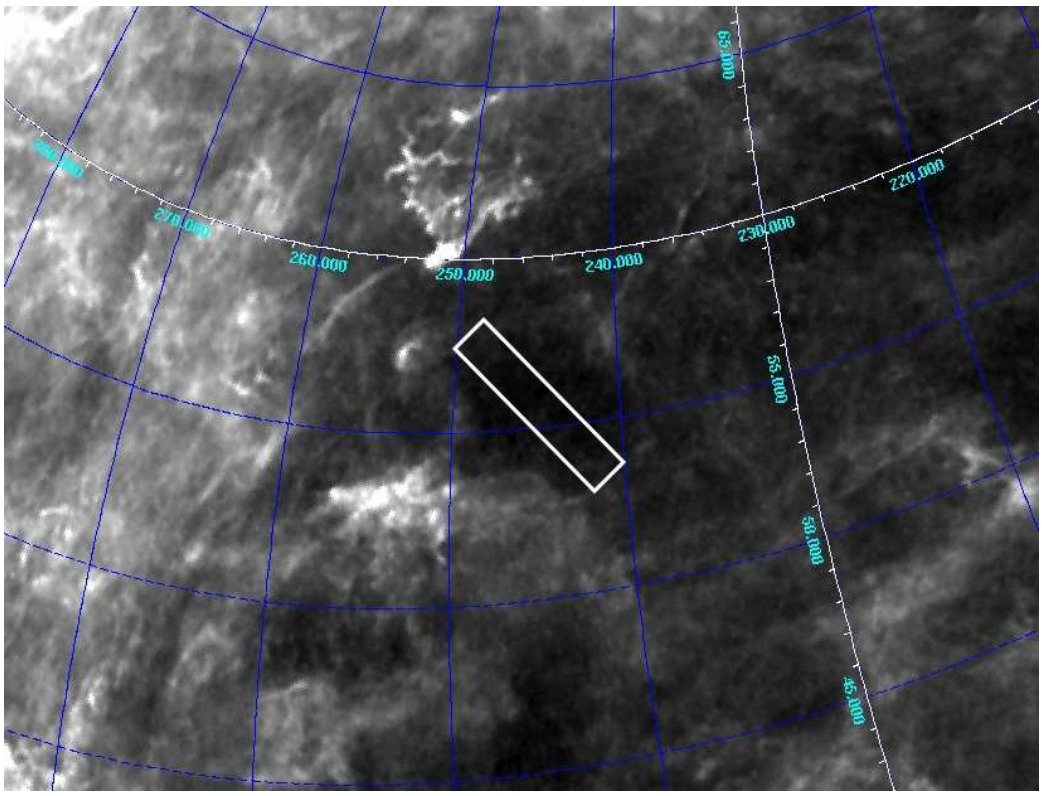

Figure 2.1. The SNAP 7.5 deg^2 field for monitoring of SNIa explosions out for $z < 1.7$ (box). The field was chosen for its position in a continuous viewing zone and low Galactic dust (background image) (Schlegel et al., 1998).

proximately 2000 Type Ia supernovae light curves based on the current understanding of the supernova rate (Pain et al., 2002), the observed redshift range of $0.3 < z < 1.7$, and photometry magnitude limit enforced by the zodiacal light background (Aldering et al., 2002; SNAP Collaboration: G. Aldering et al., 2004). While large samples of SNIa light curves can be obtained from the ground, the power of the SNAP survey will ultimately come from its wide wavelength coverage from 400 nanometers in the optical to 1700 nanometers in the near infrared and the tight control of systematics in the photometric calibration process.

2.2 Telescope Design

The SNAP telescope has been designed to optimize survey efficiency, reduce systematic errors, and limit mission risk where possible. In this section, I will describe the major telescope components for SNAP that have been developed over the last seven years.

2.2.1 Telescope

The SNAP telescope is an f/11 telescope with a 1.8 meter primary mirror. The telescope employs a three-mirror Richey-Chretien anastigmat optical design. The combination of the fast f-number and the anastigmatic design produces a large, flat focal plane in a compact telescope for space flight. The proposed SNAP telescope design is shown in Figure 2.2.

The body of the SNAP telescope is designed to be rigid for PSF stability due to temperature fluctuations. The primary mirror will be made from Zerodur, a glass ceramic with extremely low coefficient of thermal expansion. The structure of the spacecraft itself will be heated to room temperature internally to ensure thermal continuity between ground and space. To further reduce thermal variation, the SNAP telescope will always be orientated with one side facing towards the Sun. This side

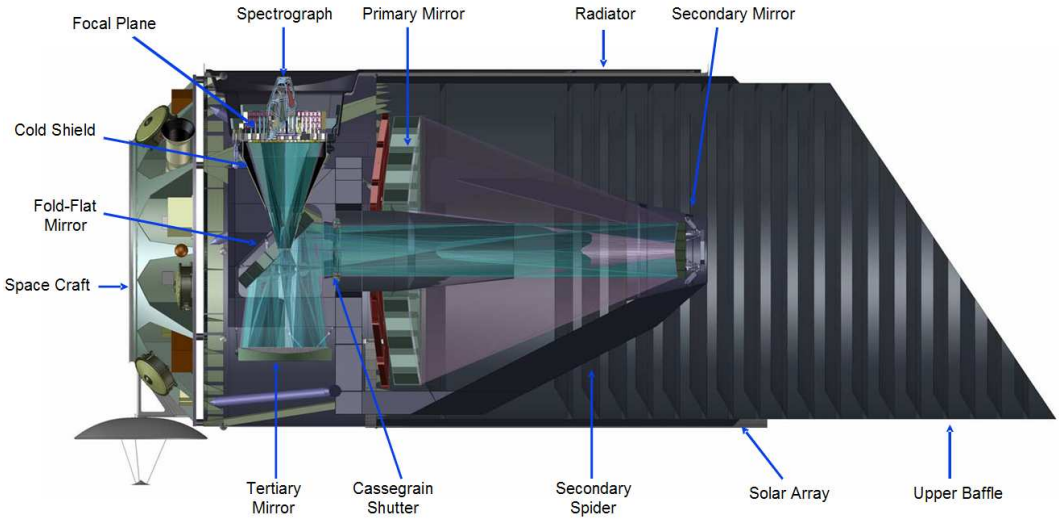

Figure 2.2. The SNAP telescope

of the telescope will have solar panels that will power the telescope and the opposing side will have a thermal radiator to cool the focal plane. This instrument design requires that the telescope perform a 90° turn every three months from its L2 orbit.

To reduce the effects of scattered light, SNAP will have extensive baffling and an angled edge to the telescope tube entrance. The baffling will ensure that the telescope will have a background dominated by zodiacal light. Extensive stray light studies have been performed to minimize scattered light in the telescope design (Sholl et al., 2004).

The SNAP design includes four shutters for the imager and a single shutter for the spectrograph, all at the Cassegrain focus. These are the only routinely moving parts onboard SNAP in the optical train. Each of the imager shutters covers a quarter of the focal plane, thus reducing the risk for single point failure if one shutter becomes inoperable. The spectrograph shutter will only be a few centimeters in size and will be operated by servo motor drives with successful space flight heritage. To reduce telescope jitter during the shutter motion, each of the imager shutters will be operated in concert with each other while the spectrograph shutter will use a counterbalance

blade.

2.2.2 Focal Plane

Figure 2.3 shows the SNAP focal plane assembly in separated sections. The SNAP focal plane field of view is 1.5 deg^2 on the sky (0.7 deg^2 degrees instrumented), which would make it the instrument with the largest field ever to be flown in space for optical and NIR photometry. The parfocal viewing area on the focal plane is from 10-20 degrees off the optical axis and is annular in shape. The unique geometry of SNAP dictates that the off-axis ray angles will vary with radial distance within the annulus. This effect is referred to as light ray apodization, and it is important to account for this range of angles when performing photometric calibrations (refer to Section 4.2 for details).

Although SNAP will be capable of making photometric measurements in the NIR, no cryogens will be used during the mission. Instead, SNAP will implement a passive cooling mechanism to reduce the temperature of the NIR detectors. While this has required significant investment to develop NIR detectors with low noise and dark current, the dividends will pay in a longer mission length with less complexity. The focal plane will be held at 140°K with a passive radiator on the sun-opposed side of the telescope body, and this temperature will be regulated to a few millikelvins.

The focal plane mounting structure will be constructed out of silicon carbide which is both thermally conductive and structurally stiff. Mounting squares will each hold the detectors, filters, and front-end electronics necessary for photometry. The focal plane will also be encased by a thin cone of aluminum extending up to the folding flat mirror. This cold shield will protect the focal plane from the thermal radiation of the room temperature telescope structure, reduce stray light, and block out some amount of the solar radiation that will be encountered at L2. The performance of this focal plane design is currently the subject of R&D study and prototyping.

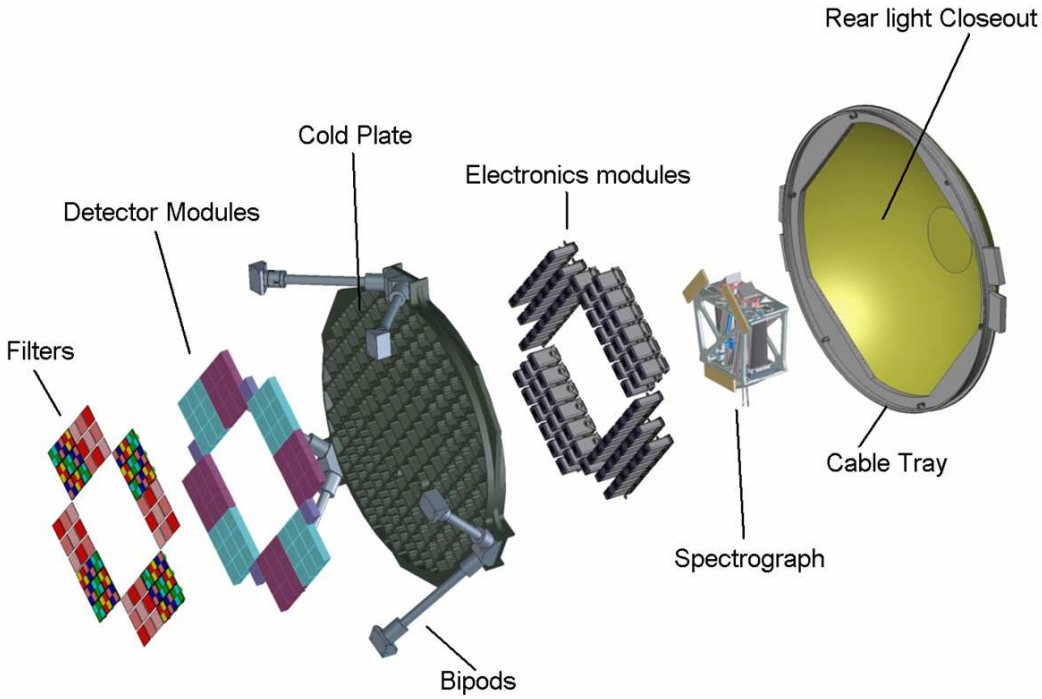

Figure 2.3. The SNAP focal plane assembly.

2.2.3 Filters

The SNAP imager is divided with nine bandpasses arranged across the best seeing portions of the focal plane. To minimize technical risk of a single point failure in changing filters, a fixed filter format has been chosen. The filters will be mounted just above the detectors in a silicon carbide frame that has a low thermal coefficient of expansion. The filters will also be connected thermally to the focal plane at a temperature of 140°K.

Particular attention has been paid to the layout of the filters across the focal plane. SNAP will observe the rectangular SNIa survey field in a step-and-stare approach which requires the filter bands be laid along the length of the survey field. However, since SNAP must perform a 90° roll every three months, the filter layout must be rotationally symmetric to reduce loss of field coverage in all nine filter bands in the four day cadence. In addition, the six optical filters must be matched with optical detectors while the remaining three NIR filters must be paired with NIR detectors.

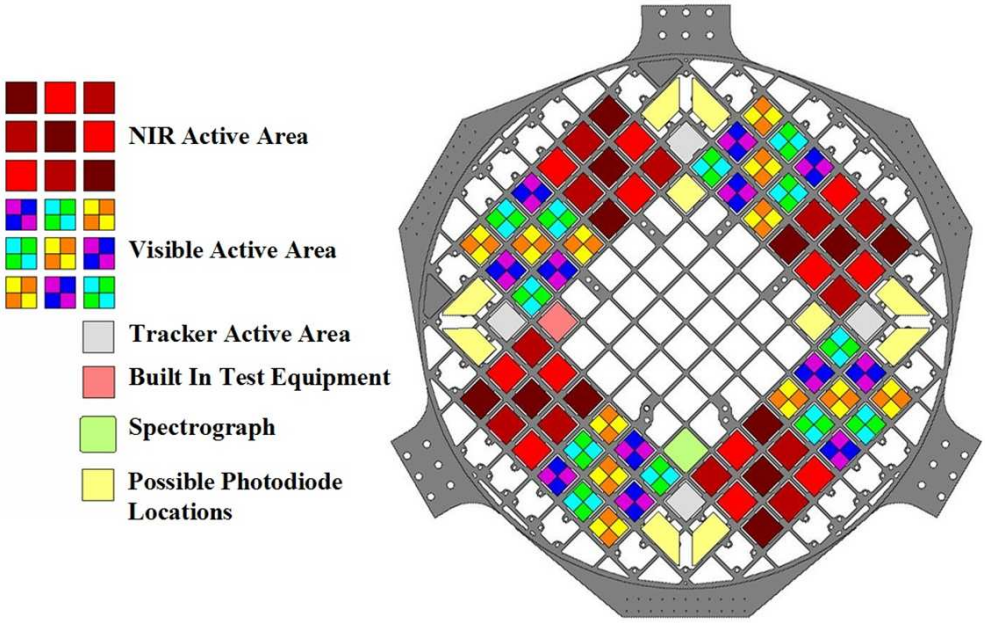

Figure 2.4. The SNAP focal plane with 90° rotationally-symmetric filter layout. Each equal sized square indicates mounting locations for an optical or NIR detector. The focal plane is just over two feet in diameter.

The optimal layout is a crosshatch pattern of the passbands in which there are 144 individual optical filters (24 of each bandpass) and 36 individual NIR filters (12 of each bandpass) (Bebek, 2004).

SNAP will fly a new filter system that is optimized for SNIa photometry. Previous experience with SNIa photometry has shown that K-corrections to standard filter systems can introduce systematic error when standardizing SNIa peak magnitudes (Nugent et al., 2002). In addition, most standard filter systems reduce overlap between passbands to increase wavelength coverage. Simulations to reduce systematics in SNIa K-corrections have determined that an optimal SNIa filter set for SNAP would be logarithmically spaced in wavelength according to

$$\tau(\lambda)_n = \tau(\lambda)_0 \times 1.16^n, n = 0 \ldots 8, \tag{2.1}$$

where $\tau(\lambda)_0$ is the filter transmission function of the rest frame bandpass and n is

the number of the filter bandpass (with a total of nine filters for SNAP). These filters should be nearly identical, redshifted copies of each other, and the minimal width of the rest frame bandpass should be 100nm to optimize S/N across the entire SNAP wavelength range (Davis et al., 2006).

Manufacturing such a logarithmic filter set from the optical to the NIR has led the SNAP Collaboration to investigate interference filter technology. Unlike the colored glass of the Johnson-Cousins system, interference filters are constructed by depositing layers of thin films on clear glass substrates to tune a bandpass to the desired design (see Section 5.3 for details). Interference filters, such as the Sloan *ugriz* filters, have been used successfully in astronomical applications for nearly two decades now. While the combination of successful experimental heritage and desirable bandpass characteristic make interference filters interesting for SNAP, my tests of commercially available filters under SNAP-like environmental conditions will help define requirements for the filter shape and transmission characterization process.

2.2.4 Detectors

The SNAP focal plane will be populated with two different types of detectors for optical and NIR wavelengths. For wavelengths from 400nm to 1000nm, 36 full-depletion CCDs from Lawrence Berkeley National Lab (LBNL) will be used. These CCDs have high efficiency, high radiation tolerance, reduced fringing at long wavelengths, and short diffusion lengths for the 10.5μm pixel size. Each chip will have 3512x3512 pixels and will be matched with an optical filter that has four independent filter bandpasses on a single glass substrate. From 900nm to 1700nm, 36 HgCdTe detectors will each be matched with a single NIR filter. The HgCdTe detectors have become popular in NIR astronomical photometry due to their low dark current and small pixel sizes. The SNAP NIR detectors will have 2048x2048 pixels with 18μm pixel size. The entire SNAP focal plane will have nearly 600 million pixels for photometry. Table 2.1 lists

Table 2.1. Survey and instrument parameters for the SNAP mission.

Primary Mirror	1.8m Aperture
Field of View	0.7 deg^2
Survey Length	22 mo.
Survey Coverage	7.5 deg^2
Operating Temperature	140K Focal Plane, 294K Mirrors
Detector Technology	LBNL CCD optical, Rockwell HgCdTe NIR
Detector Size	3.5k x 3.5k optical, 2k x 2k NIR
Number of Detectors	36 optical, 36 NIR
Read Noise	4e$^-$ optical, 12e$^-$ NIR
QE	$> 80\%$
Wavelength Coverage	400nm - 1700nm
Number of Passbands	9 log-spaced with overlap
Number of Filters	144 optical, 36 NIR, 108 substrates
Spectrograph Resolution	> 100 optical, > 70 NIR

the optical and NIR detector parameters.

SNAP will survey the supernova field with a fixed 300 second exposure time. This exposure length will ensure that the limiting noise floor be set by the background zodiacal light (12e$^-$ rms in the NIR, 8e$^-$ rms in the optical) instead of the detectors (12e$^-$ rms in the NIR, 4e$^-$ rms in the optical). The CCD arrays will operate in a typical charge-shifting readout mode, requiring the SNAP shutters to be closed for 30 seconds. During this time, the SNAP NIR detectors will also be read out, but due to new hybridized array technology, the entire NIR array can be read in 1-2 seconds. This allows the NIR array to perform Fowler sampling which reads the entire array 15 times during the 30 second shutter closed time and reduces the read noise by $\approx \sqrt{N}$. This clocking scheme eliminates kTC noise in much the same way that Correlated Double Sampling (CDS) does for the CCDs (Brown, 2007).

One unusual aspect of the SNAP detectors is that they undersample the telescope PSF. This is typically undesirable because it limits the knowledge of the PSF for photometry and increases the possibility of error through intrapixel variation. To achieve diffraction limited seeing with a critically sampled PSF, a pixel sampling

scale of $\lambda/2D$ is required. With a pixel scale of $\approx \lambda/D$, SNAP will perform small scale 2×2 dithers of each exposure to remove any instrumental signature from the PSF. This level of PSF precision is ideal for weak lensing surveys which depend on the accurate deconvolution of the PSF from galaxy shapes. It also allows for the optimization of detector noise when performing faint SNIa photometry and helps eliminate cosmic rays in the 300 second exposures.

2.2.5 Spectrograph

SNAP will carry a low-resolution spectrograph for supernova typing and host galaxy redshift measurements. This spectrograph has a resolution of R≈100 and a fixed entrance port inside the flat focal annulus that is used for imaging. Therefore, the spectrograph will be a integral field unit (IFU) spectrograph and have both spatial and wavelength information in the measurements. The IFU is comprised of imaging slicers: gratings that have an zero-order angle that varies in vertical position or "slices". Each of these slices will be collimated and redirected to two individual channels, one with an optical CCD and the other with a NIR HgCdTe device. The slices will be arranged across the chips in a single spatial direction, which is typical of any echelle or multi-object spectrograph.

The primary role of the IFU spectrograph will be to extract both the SNIa spectrum at peak brightness and also make a simultaneous measurement of surrounding host galaxy environment. This will offer an unprecedented statistical probe of supernova spectra and their evolution out to redshifts of $z = 1.7$. It will also allow for the creation of a highly homogenous set of supernovae based on supernova type and host galaxy dust extinction. In addition to the dedicated pointings for detected supernovae, the spectrograph will also make serendipitous observations during the wider weak lensing survey. These measurements will help cross calibrate the photometric redshifts of galaxies with spectroscopic redshift measurements. The size of the IFU

is currently being optimized for these ancillary observations.

CHAPTER 3

SNAP Calibration Plan

3.1 Introduction

The calibration of the SNAP imager for photometry has been the subject of rigorous study over the last five years. Since SNAP will have a large sample of SNIa per $\Delta z = 0.1$ redshift bin, the mean SNIa peak magnitude per redshift bin will have a suppressed dispersion below the systematic error of the measurements. Therefore, the final precision on the measured cosmological parameters will depend on how well the SNIa photometry can be calibrated.

As discussed in Section 1.5, the precise measurement of the cosmological parameters through the distance luminosity relation and SNIa peak magnitudes requires that the relative flux be measured accurately between bandpasses. This requirement is different from measuring the absolute flux which would present an entirely different calibration challenge. Instead, the SNAP calibration has had a top-down calibration goal of 2% color error or 1.5% in-band error.

In typical ground-based astronomy applications, the calibration of relative photometry in a particular filter set requires a measurement of the filter "zero-points". This calibration is usually done by observing a standard set of stars in the filter passbands and translating the standard magnitudes to the observed magnitudes. The zero-point process can be become complicated by several factors. First, any ground based observation must take out the effect of airmass to derive exo-atmospheric magnitudes. The atmosphere systematically dims stars by a factor of $\sec(z)$ where z is the

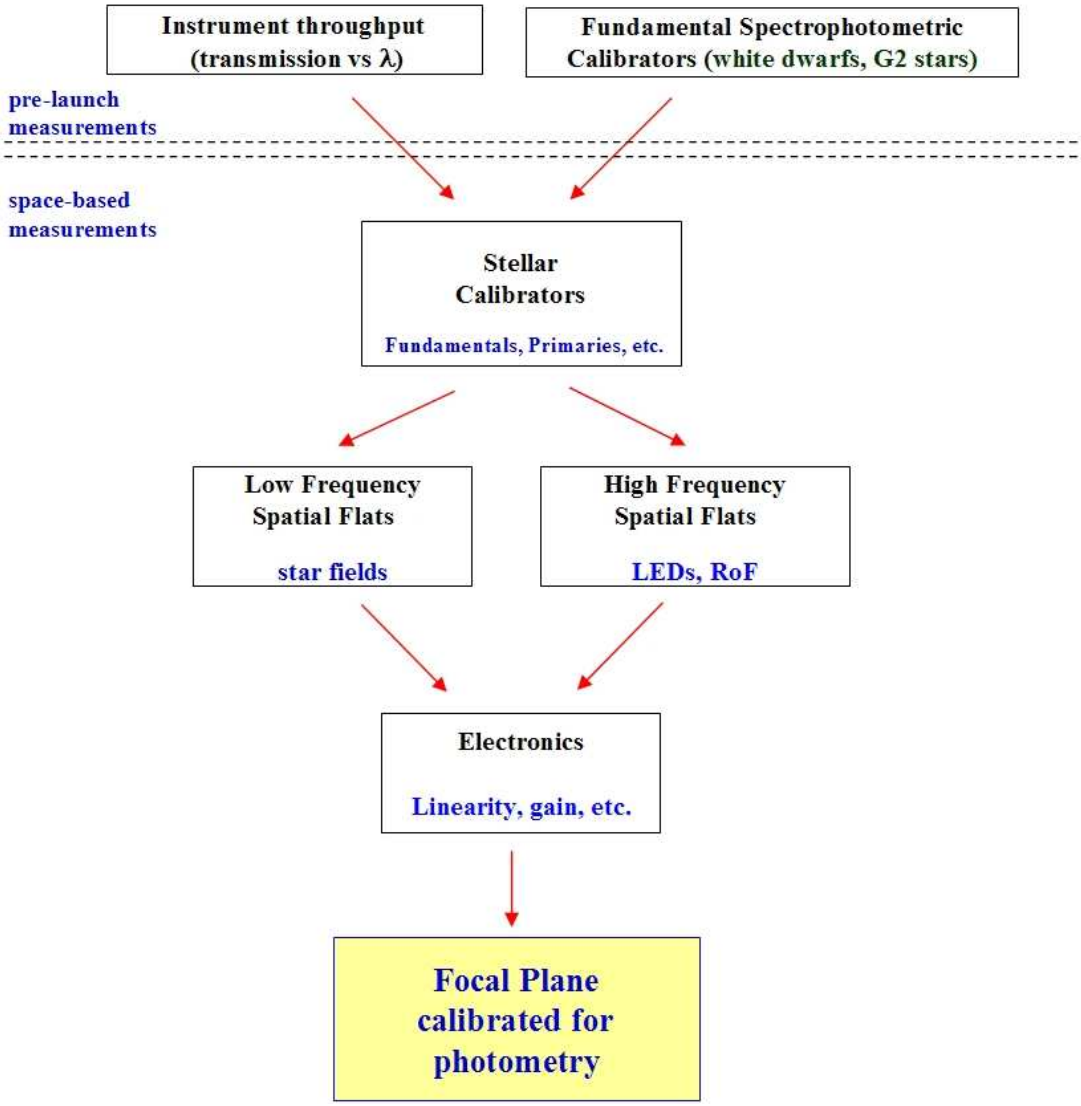

Figure 3.1. Flow diagram for the relative spectrophotometric calibration of the SNAP focal plane.

angular distance from zenith. The atmosphere can also significantly affect the stellar color through Raleigh scattering, particularly at high airmass. Second, the zero-point process uses general color transformations to measure differences in the instrumental filter bandpasses from the standard filter bandpasses. Many standard stars, such as the Landolt standards (Landolt, 1983, 1992), have been observed with common astronomical filters sets such as Johnson UBVRI. These standard magnitudes are translated to the instrumental system through color coefficients which account for differences in the system spectral throughput (Budding, 1993). However, as will be discussed Chapter 6, the determination of filter transmission functions using black-body spectra such as standard stars can be imprecise in the NIR. Furthermore, the SNAP filters will be an entirely different filter set from previously used astronomical sets and measurements of the zero-points using standards from a different photometric system would introduce large systematic error. Finally, the zero-points are subject to errors in the instrument calibration process. Typical steps in this process include bias subtraction and "flat fielding" or normalizing the interpixel variation of the camera.

To address these zero-point calibration issues in the SNAP passbands, the SNAP Calibration group has created a plan that creates a SNAP-specific photometric system. Figure 3.1 shows an overall flowdown of a feasible SNAP calibration plan, and in the rest of this chapter, I will address the major steps in calibrating out instrumental effects in the SNAP photometry.

3.2 Pre-launch Calibration

As discussed in Section 3.1, in order to achieve the best constraint on systematic error in the SNAP calibration, the Calibration group must characterize components of the new SNAP photometric system to a high precision. These characterizations will be carried out well before the launch of the spacecraft. Two critical pieces to the SNAP

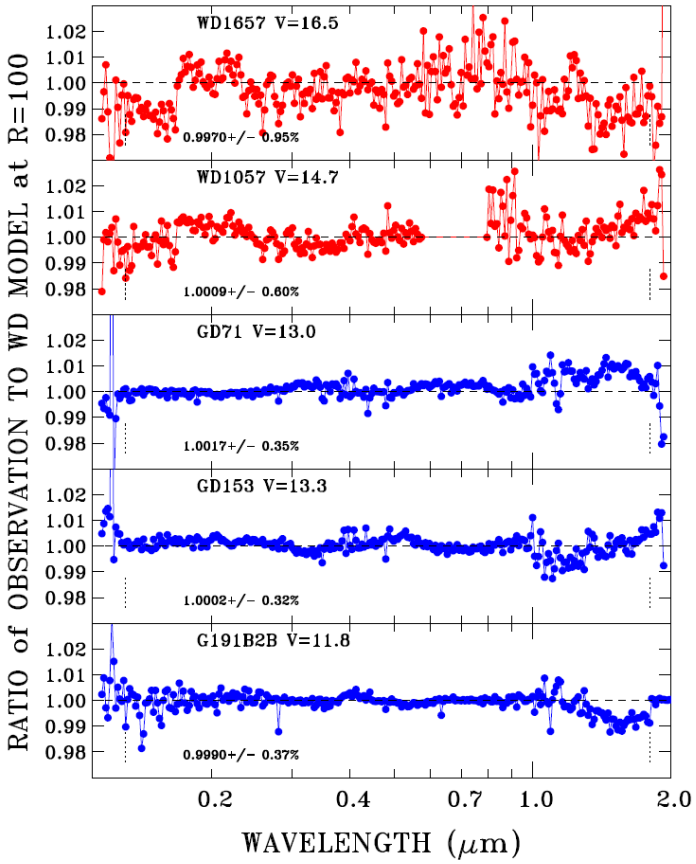

Figure 3.2. Ratio of selected white dwarf spectrophotometric fluxes measured by the HST STIS and calculated from NLTE atmospheric models. The top two plots (red) are solar analog stars which have larger error in their model fluxes when compared to the white dwarf models (blue) (Bohlin, 2007).

calibration are precise determinations of the relative fluxes from a stellar sources and the accurate spectral throughput of the telescope components.

3.2.1 Fundamental Standard Stars

The zero-points of a filter system are typically determined by observations of a known stellar flux standard. Because the SNAP passbands are unique, the flux spectrum of a known standard must be convolved with the SNAP passbands in order to understand the precise relationship between fluxes in each SNAP bandpass. In addition, standardization of the passbands will allow us to relate SNAP magnitudes to other photometric systems.

Currently, the best fundamental stellar sources that cover the wavelength range of 0.4-1.7μm are the Hubble Space Telescope (HST) pure hydrogen white dwarves (WD). These hot (35,000-60,000k) stellar remnants have generally smooth stellar spectral energy distributions (SEDs) except for strong hydrogen Balmer absorption lines. Furthermore, the relative simplicity of the stellar atmospheres in hot WDs allows for non-local thermodynamic equilibrium (NLTE) flux models to be constructed with errors at the $\sim 1\%$ level in the NIR. The flux models describe the relative flux distribution (or slope) of the WDs while the absolute flux normalization, which does not affect the cosmology measurement, is set by V-band Landolt photometry. The three best WDs with accurate atmosphere modeling are GD71, GD153, and G191B2B (Bohlin, 2002, 2007) and their measured errors relative to a NLTE WD flux models are shown in Figure 3.2. These stars have been observed regularly with HST and they are expected to remain constant over the lifetime of the SNAP mission. At V=13-14 magnitude, these stars will be observable in a regular 300 second exposure at the bright end of the SNAP dynamic range.

Since the flux of hot white dwarfs can be modeled $< 1\%$ accuracy, these WDs could work well as the fundamental calibrators for SNAP. However, there is some discrepancy between the NLTE and LTE flux models that are used for these hot white dwarfs. These differences in the model fluxes could lead to a systematic error in the flux that increases from the optical to the NIR. In Section 7.2, I will test how this systematic flux error affects the determination of cosmological parameters with SNAP. My results will show that the current level of precision in the WD fundamental calibrators should be sufficient to meet the SNAP science requirements.

3.2.2 Instrument Spectral Throughput

Another important area for the calibration of SNAP is the pre-launch spectral characterization of the SNAP optical components. While the fundamental relative flux

calibration with HST white dwarfs will set the overall relative spectral throughput from 400-1700nm, individual components such as the filters and detectors will vary over the same wavelength range. In fact, the white dwarfs will set an integrated flux reference point for each passband, which is the combination of the telescope throughput, filter transmission, and detector efficiency. Just as the zero-points depend on the accurate knowledge of the stellar source, they also depend on understanding the individual spectral components that contribute to the bandpass efficiency.

Unlike the limitations encountered when measuring an exo-atmospheric stellar source, the spectral components of SNAP can be thoroughly characterized in the lab prior to launch. It is this laboratory characterization process that Indiana University has heavily contributed to for the past five years. In particular, I have developed a technique to measure the spectral quantum efficiency of optical and NIR detectors using NIST calibrated photodiodes. I have also developed the hardware and techniques to measure interference filter transmission at the SNAP focal plane temperature and range of incident light angles. To perform these characterizations for filters and photodiodes, I have built a Monochromatic Illumination and Cryogenic Calibration System (MICCS) that I will cover in Chapter 5.

The one spectral component that the SNAP collaboration does not have the facilities to handle are the telescope mirrors. The collaboration will contract with a private industry partner who will be responsible for testing the spectral efficiency of the mirrors. SNAP will use silvered mirrors which have high efficiency and flat spectral efficiency through most of the wavelength range with an exponential drop in efficiency at wavelengths shorter than 0.4μm.

The SNAP detectors will also have relatively flat quantum efficiency, but the optical detectors will have a long wavelength cutoff near 1.0μm. The NIR detectors will overlap this optical cutoff and be sensitive to NIR wavelengths out to a cutoff wavelength of 1.7μm. The SNAP filter throughput, however, will vary significantly over

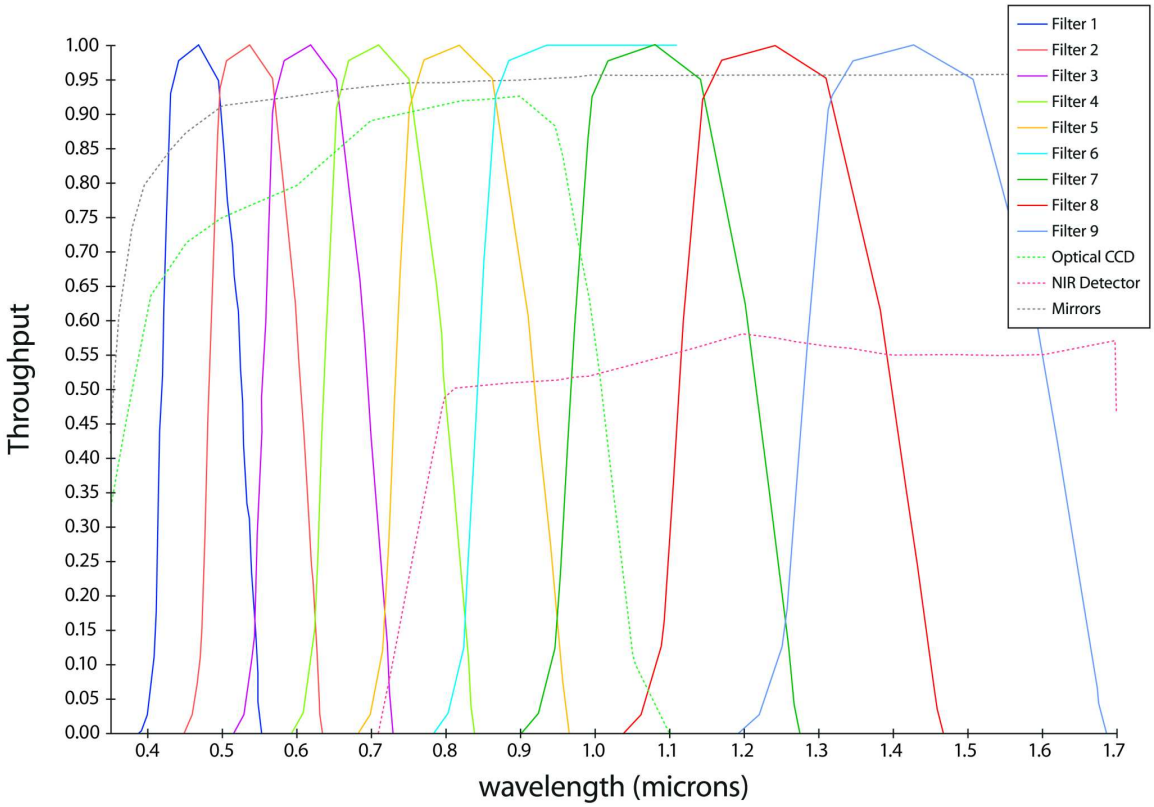

Figure 3.3. The SNAP spectral throughput will be a combination of efficiencies from the telescope mirrors, detector quantum efficiency, and filter transmission. The telescope and detector efficiencies are relatively flat and span the filter bandpasses. This design forces tight constraints on filter calibration to achieve an accurate relative spectrophotometric calibration.

the SNAP wavelength range and will set both the turn on and cutoff wavelengths for each bandpass. This makes the filter characterization essential to reducing zero-point errors and requires a precise spectral characterization of their transmission functions. Figure 3.3 shows the overlapping of spectral efficiencies for the telescope mirrors, detectors, and filters. Due to the rapid transmission change at the bandpass edges and transmission variations ("ripples") that can occur across the filter transmission function, the filter characterizations clearly pose a significant source of systematic error into the band-to-band relative calibration.

3.3 Post-launch Calibration

The launch of the SNAP mission will pose a new start in the SNAP calibration plan. Once the spacecraft is launched, we assume that all previous characterizations are subject to change. The mission calibration must trust the ground-based measurements as a beginning reference point, but verification of the calibration must also be performed routinely in orbit. The verification process will include observations of preselected standard stars and filter transmission tracking.

Some characterizations of the telescope will take advantage of the space environment and perform end-to-end measurements that are difficult to perform in a lab. One example is the flat field normalization of the imager which requires that all 600 million pixel efficiencies and geometric effects of the telescope optical train be removed from photometry. The flat field process for such a large, annular field is essential to produce meaningful photometric survey results.

The following sections will discuss the standard star system and flat field processes that will be used for SNAP. The standards are in a three-tiered system including Fundamental, Primary, and Secondary standard stars and will be discussed as such. The flat fielding process has two major components using high and low spatial frequency flats. The high frequency flats will require the use of an onboard calibration light

system and the low frequency flats will use relative photometry of stellar clusters.

3.3.1 Primary Standard Stars

Standard star observations will be carried out using a three-tiered system of standards. The first tier is referred to as the "Fundamental" standards and will be composed of the HST white dwarfs (discussed in Section 3.2.1). The second tier standards stars are grouped into "Primary" standards and span a magnitude range of V=15-18. Unlike the fundamental standards which will require specific telescope pointings, the Primary standard stars are found in the SNAP SNIa survey field. These handful of standards will constantly be in the SNAP field of view, allowing for continued monitoring of the system throughput relative to their in-band magnitudes. In addition, Primary standards with a range of stellar temperatures that will give a gross indication of changes in the color of the bandpass zero-points. A third and final tier standard stars are called "Tertiary" standards. This tier of stars will be composed of field stars that are serendipitously observed during the SNAP SNIa survey exposure sequence. The Tertiaries will span the magnitude range of V=19-22 (1% photometry limit in 300s) and will have multiple observations within a single filter bandpass. The mean magnitude of ensemble photometry performed on the Tertiaries will be compared to the Primary standard magnitudes to indicate zero-point drift in the bandpass.

Since the calibration of SNAP photometry requires a set of stable Primary standards with a wide color range in the SNAP survey field, I performed an observing campaign to find suitable Primary candidate stars to meet this SNAP requirement. Initial survey work for stable Primary standard stars in the SNAP field began in the summer of 2003. The goal of the survey was to locate stars with $< 1\%$ variability relative to the stellar ensemble mean. The survey would require a good deal of observing time to achieve sub-1% photometry in repeated observing runs. I received

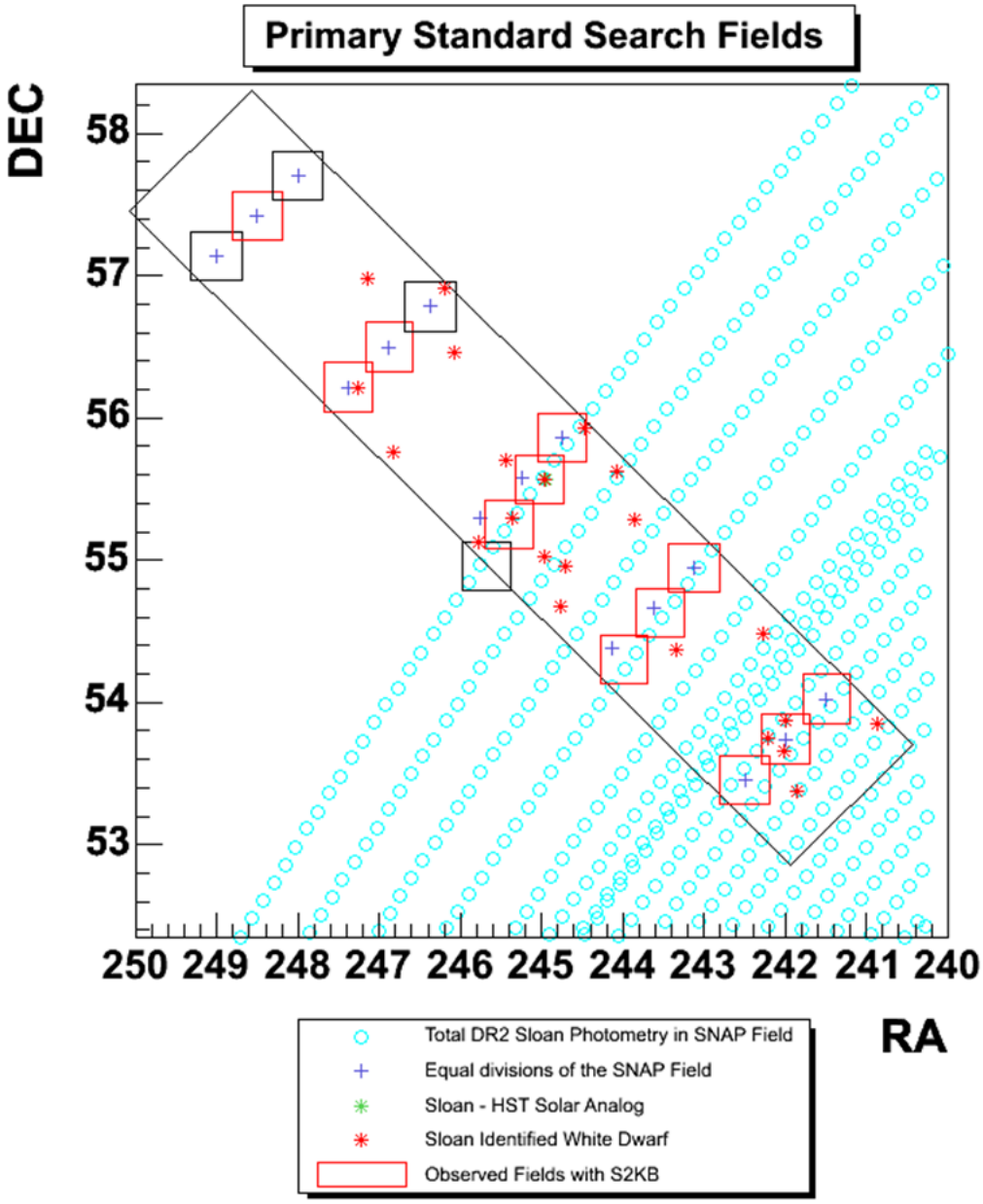

Figure 3.4. The SNAP Primary standard star field locations are arranged in vertical stripes across the SNAP SNIa survey field. They are separated approximately by 0.7 deg so that as SNAP moves across the survey field, a Primary standard will always be in its field of view. Also shown are the locations of SDSS photometrically identified white dwarfs and the position of the DR2 SDSS stripes used in the initial phase of the Primary candidate search.

an ample amount of time on the WIYN 0.9m telescope with the S2KB CCD imager through Indiana's time share in the WIYN consortium. The imager covers 0.09 deg^2 on the sky which is roughly equivalent to a block of 9 CCDs or NIR detectors on the SNAP focal plane. While this S2KB sky coverage would require over 40 individual pointings to observe the entire SNAP survey filed, I optimized my search to reflect the step-and-stare observing strategy for SNAP. I divided the SNAP survey field into five strips that span the short spatial direction of the field (see Figure 3.4). Each strip is separated by the width of the SNAP imager which is $\sim$ 0.7 degrees. With this Primary field configuration, SNAP will always have a Primary standard on the focal plane during the SNIa survey.

Each of the Primary standard survey fields had 3-4 observations in R band ranging in timescale of four weeks to two years. Achieving sub-1% photometry for each field spanning an R=16-18 dynamic range required several observations to be co-added, with integration times ranging from 300 to 1200 seconds depending on the seeing. I performed aperture photometry on the co-added frames using small apertures of 3-5 pixels in radius. I chose this aperture size to improve S/N by reducing the read noise and background signal, and I enforced that the aperture encompass over 98% of the stellar PSF for each co-added image. Since I performed a differential analysis relative to the ensemble mean, changes in the telescope focus, atmospheric seeing, or PSF variation during the course of an observation should not affect the differential magnitudes. I tested for PSF variation in my differential photometry by increasing the aperture size on the brightest stars in the co-added images and I found that the differential ensemble photometry with larger aperture sizes only increased the statistical error on stars near the 1% photometry limit.

I performed the differential ensemble photometry analysis by writing C++ code that took the apparent magnitudes of stars with 1-3% statistical photometry (above the sub-1% level of interest so as not to use stars in the mean sample) and computed a

mean magnitude and variance. I then calculated the differential magnitudes relative to the ensemble mean for unsaturated stars with sub-1% statistical error. I calculated the differential magnitudes as

$$m_0(s) = m(e,s) - em(e), \tag{3.1}$$

where $m(e,s)$ is the instrumental magnitude for a star in a given co-added exposure, and $em(e)$ is the ensemble average magnitude of the best measured reference stars in the corresponding exposure. This process is known as "strict" differential ensemble photometry and it requires that the reference stars be measured in each observation frame. Once I calculated the differential magnitudes, I then computed the differential magnitude variation from

$$\sigma^2[m_0(s)] = \sqrt{\frac{N \times \sum_{e=1}^{N} [m(e,s) - em(e) - m_0(s)]^2 / \sigma^2[m(e,s)]}{(N-1) \times \sum_{e=1}^{N} 1.0/\sigma^2[m(e,s)]}}, \tag{3.2}$$

where N is the number of exposures for the star and $\sigma^2[m(e,s)]$ is the statistical variance of the target star observation (Rengstorf, 2004).

Comparisons of these differential magnitudes among all observations of the field gives a measure of the variability of the star. I also checked the ensemble mean for robustness by comparing the differential magnitudes of the reference stars that contribute to the mean value for each co-added frame of the field. While the mean magnitude itself can vary due to airmass and seeing changes between each co-added frame, this should not be true of the differential magnitudes relative to the mean value. If the same stars are observed in each co-added frame and they are stable to 1%, then the differential magnitudes of the ensemble mean reference stars should remain constant. If I detected variation above the 1% level in the reference star differential magnitudes, I inspected the members of the sample for variation that was inconsistent with the mean value. I removed any outliers from the reference sample.

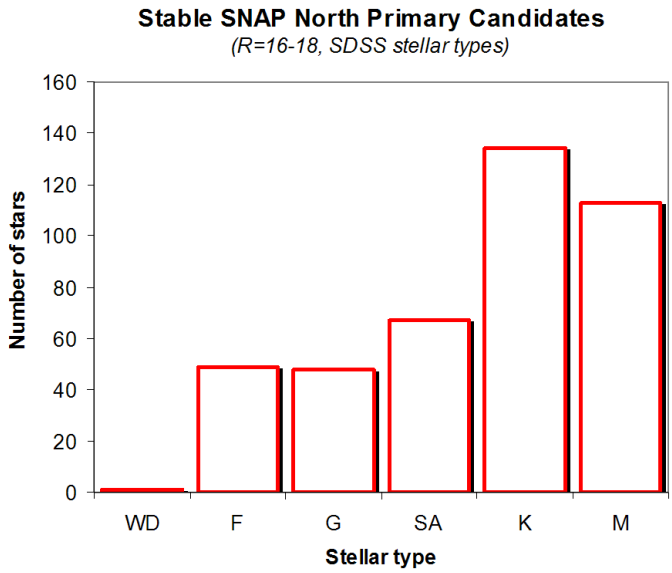

Figure 3.5. A histogram of the stellar types for my Primary candidates with $< 1\%$ photometric variability.

With this iterative method, the variance on the ensemble mean varied by $\ll 1\%$ between co-added frames.

The stable Primary standard survey has discovered over 400 candidates with less than 1% variability in the SNAP standard strips. The position, R-band magnitude and stellar type from SDSS, number of observations, and variability for Primary candidates are tabulated in Appendix A. Using data from the Sloan Digital Sky Survey (SDSS), the stellar type distribution for the candidates is shown in Figure 3.5. Several solar analog stars and a white dwarf are in this sample, which could be useful in creating simple atmospheric models as was done for the HST fundamental standards. One solar analog in particular, called SNAP II, is near the center of the SNAP field and has HST STIS measurements. As measured in my Primary search, this star had 1.2% variability which is just outside my candidate variability cut. While I expected that the small number of observations would allow stars with spurious variability to creep into my sample, such stars would be weeded out in the initial months of field monitoring performed by SNAP. As a check on my methodology, I

have compared my results with the output of AstroVar, a software package designed to detect variable stars using differential ensemble photometry (Honeycutt, 1992). The results of my analysis and AstroVar are completely consistent, bolstering my confidence in the variability calculations.

The SDSS colors provide a rough guide for stellar types, but full classification of the SED can only come through stellar spectra. While portions of the stability survey were still underway, I began a follow-up campaign to measure the spectrum of the Primary candidates with the least amount of variation. I gave preference to stars typed as solar analog or white dwarf, regardless of their variability. To obtain the spectra, I used the WIYN 3.5m telescope and the HYDRA fiber-fed spectrograph. This is an ideal instrument for typing a large sample of stars in the Primary star magnitude range. Over 200 stellar spectra have been obtained, primarily centered around the Primary candidate survey strips that overlaps with observations from SDSS.

Further effort should be put into follow up of these candidates, including a dedicated program to monitor a handful of them for a 22 month period similar to that of SNAP SNIa survey. However, I believe the current data for the Primary star candidates is sufficient for initial photometric calibration and monitoring in the SNAP supernova survey.

3.3.2 High-Frequency Spatial Flats

The flat fielding procedure determines the pixel response non-uniformity across the focal plane. The non-uniformity can occur on different spatial scales, from the small scale, pixel-to-pixel response, to the large scale, chip-to-chip response. The high spatial frequency variations, also known as inter-pixel variation, are typically caused by shadows created by particulates on the optical surfaces or are actual variation in the gain response of the detector pixels. The spatial scale for such variation is can be

on the order of 1 - 100 pixels in size, depending on the characteristics of the optical system.

The standard technique to correct for inter-pixel variation is to illuminate the focal plane with uniform illumination and then normalize all pixel values to the mean signal level. In ordinary astronomical observations, the diffuse illumination is usually provided by a lamp source reflected off the dome (dome flat) or the observations of the twilight sky (twilight flat). These sources are excellent because of their uniformity and their delivery of a high signal level in a short amount of time. In addition, precision results often require the additional use of an illumination correction to take care of global variations on the source (see Section 3.3.3). For SNAP, the Ring of Fire (RoF) functions as the diffuse source of illumination (see Sholl et al. (2004) and Section 4.2). As shown in Figure 3.6, the RoF places a series of light input ports around the entrance to the cold shield. These lamps illuminates a ring of diffuse reflecting material along the opposite wall of the radiation shield which then scatters light onto the focal plane. The resulting illumination is uniform on the scale of the high-frequency spatial variations.

There are several advantages to the SNAP RoF system. Similar high frequency flat fields can be obtained by dithering well-characterized calibration stars over the focal plane. But the large number of pixels on the SNAP focal plane, over half a billion, makes this approach impractical because it is costly in time. Therefore, the primary advantage of the RoF is its multiplexing ability in creating the high frequency flats. The flat fielding can be done routinely and quickly using an onboard light source. Another advantage is that since the input ports will be fed by optical fibers from a thermally-controlled light source enclosure (discussed in Section 4.2), a wide range of calibrations lamps can be used that otherwise would not fit at the RoF location.

However, the RoF does have a disadvantage when compared with standard flat-fielding techniques. While the RoF will deliver diffuse light to the focal plane on

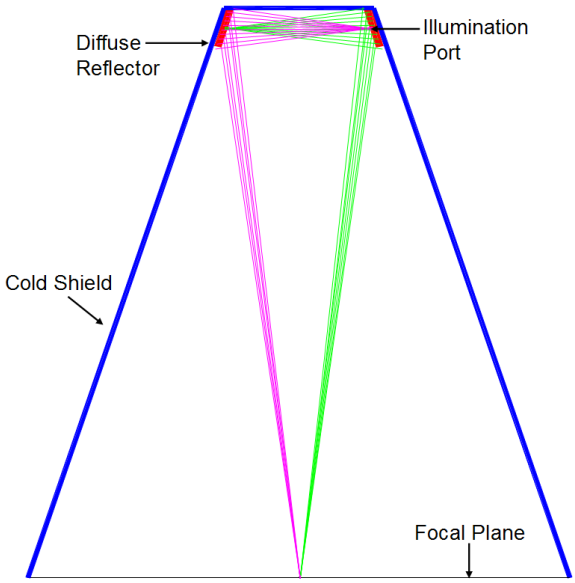

Figure 3.6. A schematic ray trace of the Ring of Fire (RoF) calibration light delivery system for the SNAP focal plane. A single point observes the illuminated RoF over a range of angles that is azimuthally uniform and has a slight fall off in intensity as one moves radially outwards from the optical axis.

small chip scales, SNAP does not currently have a scheme that puts this irradiance though the entire SNAP optical train such as a dome or twilight flat. In the RoF design, we anticipate that there will be a large scale, smooth variation in illumination from the center of the focal plane to the edge (refer to Section 4.2). This variation in the flat field will be repeatable and can therefore be corrected with "star-flats" (see Section 3.3.3) or with "super-flats" created from observations of the zodiacal light background.

In addition to the imager flat field correction, the spectrograph detectors will also require a normalization of the detector pixels. Because the spectrograph is integrated into the field, the instrument has been designed with pupil stops to keep stray light from entering the spectrograph. This design precludes the use of the RoF for flat field illumination since it is located just outside the SNAP pupil. Therefore, the SNAP calibration light system will illuminate a small amount of diffusing material on the back of the spectrograph shutter near the Cassegrain focus. The illumination

over the small shutter area (and hence the spatial direction in the spectrograph) will be highly uniform with the fiber fed illumination system. An added complication for the spectrograph is that any light incident on the detectors must be uniform spatially and cover a wide spectral range. Uniform illumination along the dispersion axis requires the use of a broadband light source with a smooth SED for the greatest simplicity in wavelength coverage. For this reason, quartz-tungsten-halogen (QTH) lamps are typically used to correct the flat field in spectrographs, and the SNAP Spectrograph group is currently investigating QTH lamps for flat field calibration of the spectrograph.

3.3.3 Low-Frequency Spatial Flats

Low-frequency spacial flats (L-Flats) are spatial variations in response that span multiple pixels and detectors. These variations are typically more difficult to correct because truly uniform sources are rare to find. Astronomers often correct a non-uniform illumination source by assuming a uniform source and applying an illumination correction to the high-frequency flat field. Flat-fielding large scale variations with uniform sources allows light rays to strike the detector and internal telescope optics and a wide range of angles, increasing the chance of scattered light to enter the measurements. Large-scale photometry variations using standard methods of dome, twilight, or background sky flats typically leave an RMS variation of $\approx$1% in the *differential* photometry (Manfroid et al., 2001; Platais et al., 2002). Since the RoF will be non-uniform on large scales, it will be critical for the SNAP calibration to reduce this large scale variation.

Over the last decade, new techniques using stellar clusters and differential photometry have been developed to achieve precise L-Flats for photometric detectors (van der Marel, 2003). By dithering large samples of stars across a telescope detector and measuring the deviation of each individual star from the ensemble mean, a

large-scale response map can be constructed that includes the effect of the instrument optics, reduces scattered light, and matches the actual photometric variation. Once the map is constructed, a χ^2 minimization using an appropriate spatial function can be performed using

$$\chi^2 = \sum_{f,s} \frac{[m_0(f,s,\mathbf{x}) - m(s) - a(f) - \phi_i(\mathbf{x})]^2}{\sigma(f,s)^2} \tag{3.3}$$

where $m_0(f,s,\mathbf{x})$ is the observed magnitude of star s on frame f at CCD position $\mathbf{x}$, $a(f)$ is the airmass correction for each frame, $m(s)$ is the mean magnitude of the star, and $\sigma(f,s)$ is the photometric error in the stellar measurement (Manfroid, 1995, 1996). The term $\phi_i(\mathbf{x})$ is a magnitude correction function that varies over the two spatial dimensions of the CCD. Once the spatial function is fit by minimizing χ^2, a correction can be applied to the measured apparent magnitudes based solely on their position on the focal plane.

To test the precision of this L-Flat method, I performed dithered observations of stellar clusters using the WIYN 0.9m telescope and S2KB CCD camera. The stellar clusters I used were selected to be of appropriate size and magnitude range from the Stetson standard star cluster catalog (Stetson, 2000). The dither pattern required a minimum of 9 pointings ranging in spatial scale of 50 to 400 pixels. I calculated the deviations in the apparent magnitudes relative to the ensemble mean as a function of position on the CCD using a variation of the differential photometry code used in Section 3.3.1. I only included stars that were unsaturated and had 0.3% Poisson error in constructing the L-Flat.

My initial calculation of the L-Flat on the S2KB camera was performed using bias-subtracted and twilight flat-fielded photometry. The twilight flat used in my analysis was not illumination corrected as the twilight sky was assumed to be uniform. My initial expectation was that the L-flat would be relatively little large scale variation, with perhaps a linear residual structure due to the actual non-uniformity in the

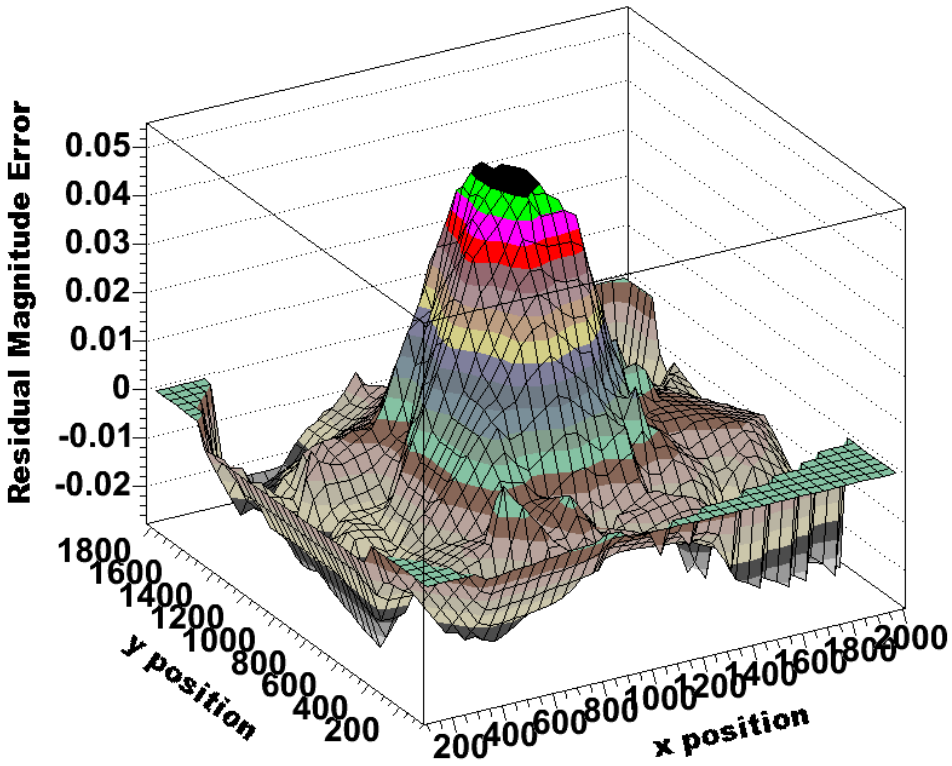

Figure 3.7. Residual magnitude error after a twilight flat correction on the S2KB camera. The map was constructed using dithered images of a stellar cluster and performing differential ensemble photometry on stars with statistical photometric error $< 0.3\%$.

twilight sky. The spatial map of the differential magnitude residuals using this data is shown in Figure 3.7. It is obvious that there is significant higher-order structure in the residual error beyond that of a simple linear variation. In fact, the map shows that photometry in the center of the camera is systematically 5% low and photometry near the edge of the camera is 2% high, resulting in a 7% peak-to-peak variation in photometry across the chip. Further, a histogram of the deviations in Figure 3.8 shows an RMS variation of 1% across the focal plane, meaning that the spatial residual errors are hidden in the tails of the distribution. The figure demonstrates that using a histogram of magnitude residuals as a measure of photometric accuracy may provide over-confidence in the quality of results, particularly if a small set of photometric measurements are being made at different positions on the focal plane.

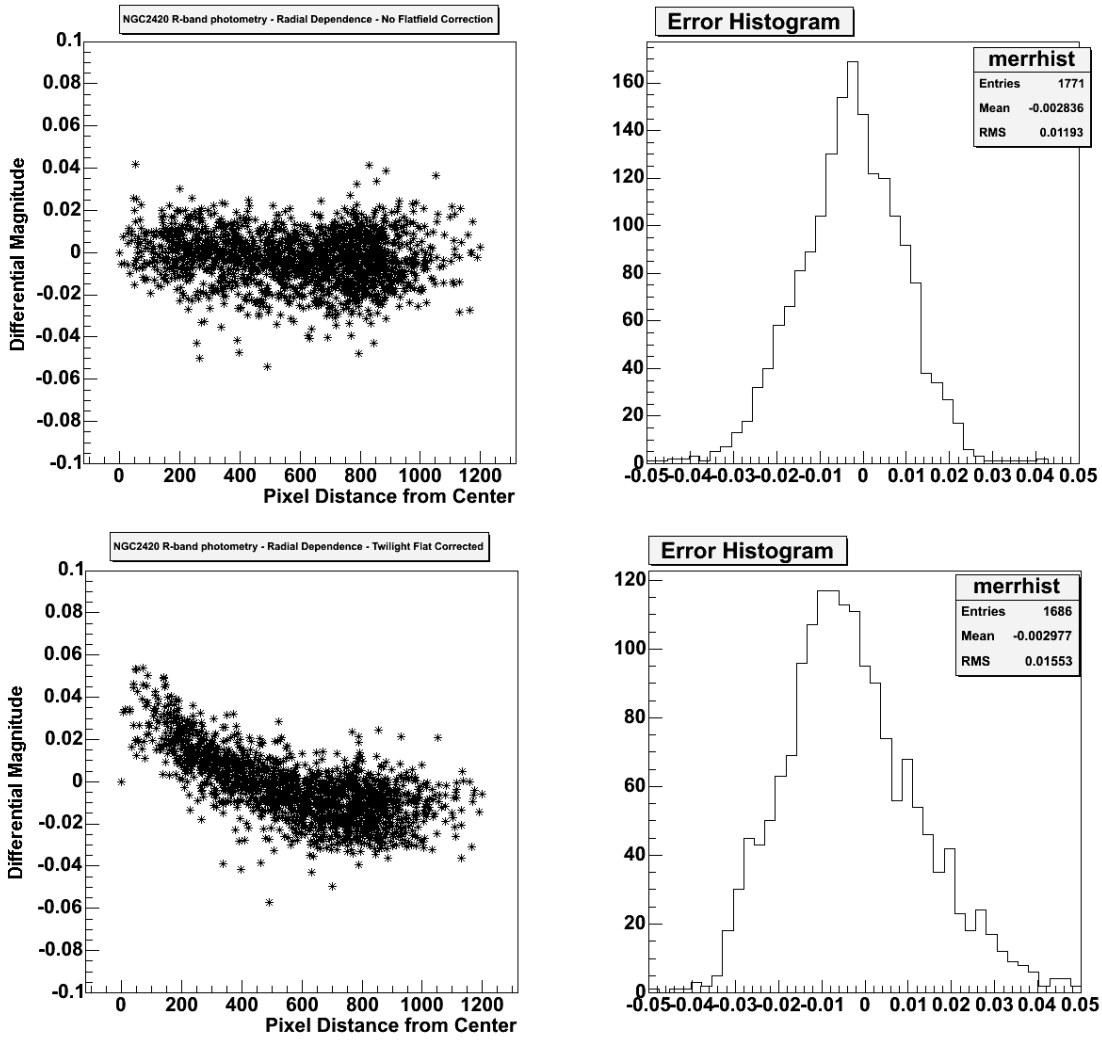

Figure 3.8. Comparison of the residual magnitude error before (top row) and after (bottom row) a twilight flat field correction is applied on the S2KB camera. The left hand column show the systematic residual error as a function of distance from the center of the chip, and the right hand column shows the RMS difference between the correction methods. In this case, both methods seem to leave 1% variation in the spatial dependence of the photometry, but the flat field corrected data clearly has a larger systematic error. No illumination correction was applied to the twilight flat.

I also performed additional tests of my photometric process to check for systematic sources of error which may produce an effect similar to the residual spatial error in Figure 3.7. In one such test, I increased the photometric aperture size from a 5 pixel radius to a 20 pixel radius. This test ensures that the measured magnitude of each star is not influenced by stellar PSF variations across the chip. The test showed that the spatial magnitude residual of Figure 3.7 remained even for larger aperture sizes. In addition, I performed PSF photometry and for the same set of dithered images and found that the magnitude residual structure was unchanged. These results indicate that my photometry process is not the source of the flat field residual error for S2KB.

An investigation into the source of the residual error ensued by testing different flat field techniques (dome flats and background dark sky flats), all of which showed similar results in the spatial residual error. A technique of combining the high S/N dome HF-flat and a smoothed twilight sky L-flat also produced similar results. Unsure if the flat field reduction was the source of the problem, I also performed the same analysis on photometry that was only bias-subtracted. The results of this test are shown in Figure 3.9. The residual deviations in the star flat were dramatically reduced by removing the typical high S/N dome or twilight HF-flat from the reduction process. In fact, careful inspection of the flat field itself (as well as unflattened observation frames) show a similar "ring" structure in the center of the field that is consistent with the residual pattern. Figure 3.9 also shows that the residual flat field error is consistent in size and shape between filter bands. These results suggest that the source of the residual photometry error is likely coming from some instrument component within the telescope when using uniform illumination to produce a flat field. The source of this "ring" is unknown, but I suspect that it is either due to scattered light in the high S/N flat field. This error would use non-uniform light in a process designed to normalize response with uniform light, thus leading to a large systematic error. In addition, a similar scattered light effect called a "ghost pupil" using the KPNO

MOSAIC imager has been found (Valdes, 2003), and this scattered light phenomenon may be related to the "ring" effect seen in the S2KB flat field images.

Regardless of the source of the flat field error, it is my recommendation that the S2KB user interested in precision photometry should be aware that the twilight and dome flats, without an illumination correction, can lead to large systematic error across the chip. There may be several different paths to remove this systematic error. However, armed with a direct test of photometric spatial variation using a star flat, the observer can calibrate out the residual error due to the HF-flat process using an appropriate fit function to the differential stellar magnituds. The star flat process is a direct test that the photometry is truly uniform across the chip. I found in my tests of S2KB that the residual structure was complicated beyond the use of simple 2-D high order polynomials. The residual "ring" structure, coupled with an overall slope in response from one corner of the chip to other diagonal corner, cannot be accurately reproduced with such simple polynomial functions. I found that simple 2-D fitting function that employ the use of Gaussian and Lorentzian shape profiles proved to be highly useful. Used typically for PSF fitting, I found empirically that the spatial structure in the residual magnitude error was best fit using the Penny2 spatial function with an overall linear slope such that

$$z = \frac{x^2}{p_1^2} + \frac{y^2}{p_2^2} + p_5 xy, \tag{3.4}$$

$$e = \frac{x^2}{p_1^2} + \frac{y^2}{p_2^2} + p_4 xy, \tag{3.5}$$

$$\phi(p_1, ..., p_9) = p_6 * (\frac{1 - p_3}{(1.0 + z)} + p_3 \exp(-0.693e)) + p_7 x + p_8 y + p_9 xy. \tag{3.6}$$

Using Equations 3.3 and 3.4, the parameters of $p_1 \ldots p_9$ can be fit to the systematic magnitude residuals created by the twilight flat field. Once the differential photometry is corrected by this spatial function, the remaining residual photometric error on the S2KB detector can be reduced to 0.6% RMS (using stars with 0.3% statistical

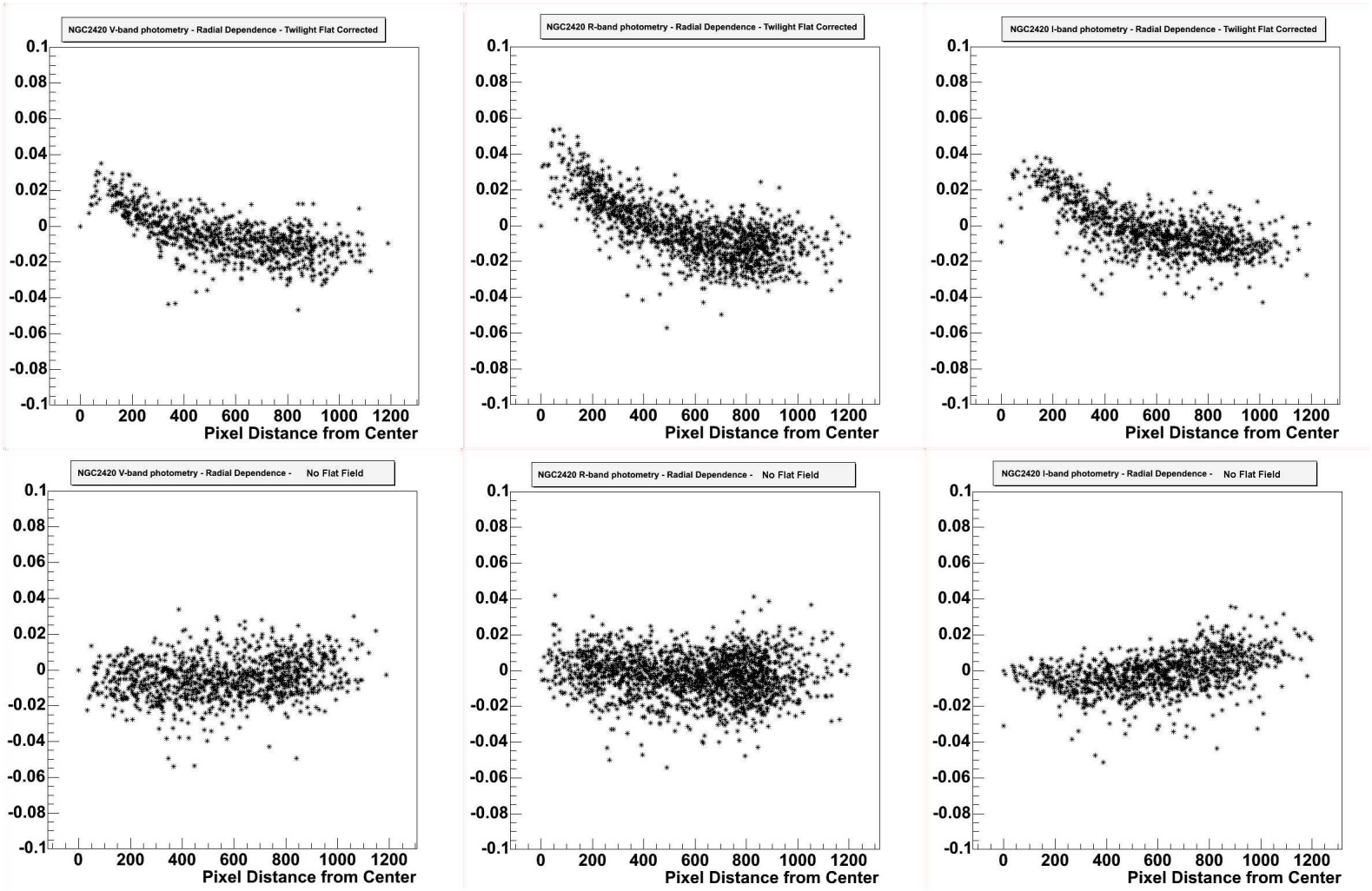

Figure 3.9. Radial cuts of the magnitude residual error in V, R, and I band across the entire S2KB CCD chip. Unflattened frames clearly have less spatially-dependent systematic error than the frames corrected via a typical twilight sky flat image. The 7% peak-to-peak systematic error appears consistent between bandpasses, suggesting the error source is geometric in nature.

photometry) as shown in Figure 3.10. While this RMS gain may seem marginal, the improvement is dramatic in the systematic peak-to-peak error across the chip, which was reduced from 7% to 1% variation across the chip. The fit parameters for $\phi(p_1, ..., p_9)$ from my tests of the S2KB flat field residuals using a twilight flat are reported in Table 3.1.

Table 3.1. The fit parameters for the star-flat R-band magnitude correction to an S2KB image that has been calibrated with a twilight flat.

Parameter	Value
p(1)	0.29742
p(2)	0.29186
p(3)	-0.20763
p(4)	23.96260
p(5)	4.90296
p(6)	-0.05450
p(7)	0.00923
p(8)	-0.00150
p(9)	-0.00437

My experience in using the star-flat technique has been important to the development of a flat-field calibration plan for SNAP. Given the success in reducing complicated large-scale variation, I am confident that similar dithered observations of stellar clusters can be performed by SNAP and produce an accurate flat-field calibration at the sub-1% level. Further, I am also confident that if SNAP uses an onboard lamp source that is not completely uniform in irradiance (such as the RoF illuminator), the large scale pattern in the differential magnitude residuals should be well characterized using the star flat technique. The SNAP in-band photometry will be well normalized regardless of position on the focal plane.

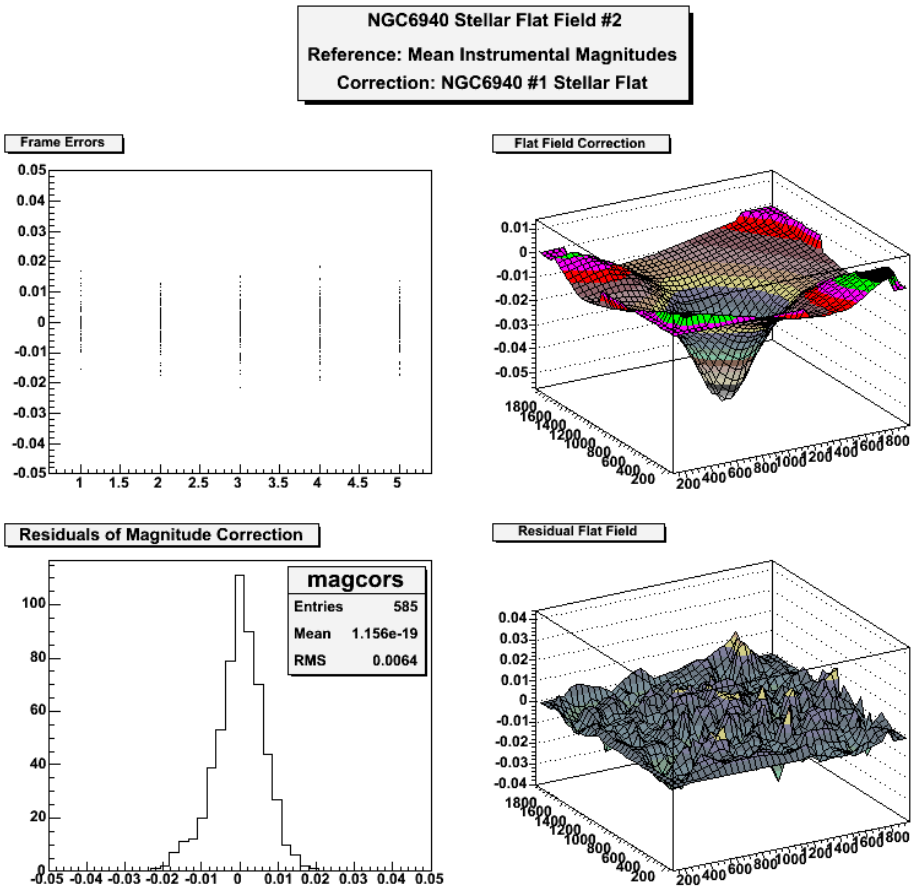

Figure 3.10. Magnitude correction analysis for the S2KB camera. Each frame for the star flat is plotted to check for variations in the ensemble mean magnitude due to clouds (*upper left*). A 2-D correction to the magnitude error residuals shown in Figure 3.7 using Equations 3.3 and 3.4 is then calculated (*upper right*). Post-correction statistics (*lower left*) and spatial mapping (*lower right*) show a residual error of 0.6% with no systematic large scale dependence.

CHAPTER 4

Flight Calibration Instrumentation

In order to calibrate the SNAP bandpasses while in orbit, components must be included to characterize the filter throughput and instrument response during the course of the survey. As discussed in Section 3.3, the calibration of SNAP photometry will require a flat field illumination source and a method to accurately monitor the throughput of the SNAP filters. These requirements can both be addressed with the addition of a onboard light source system dedicated to the calibration of the SNAP focal plane. A calibration light source system greatly improves the efficiency of calibration procedures for the focal plane. In particular, the flat field calibration procedure would consume a large amount of orbit time if it were performed with only a small set of standard stars across all 600 million pixels on the focal plane. An onboard light system that diffuses light uniformly across the focal plane will measure the response of all pixels simultaneously and therefore increase the amount of time available for science observations. Further, an onboard light system could deliver narrowband illumination to the focal plane for monitoring of complex filter transmission functions. Finally, a light source that can deliver variable flux to the focal plain could help measure detector gain and non-linear detector response. The combined advantages in calibration efficiency and accuracy argue in favor of placing a calibration light source system onboard SNAP.

I have helped develop a conceptual light system for relative photometric calibration on the SNAP focal plane. This system would be constructed with three main

components: *i*) a thermally-controlled light emitting diode (LED) illuminator, *ii*) a diffuse annular reflector, and *iii*) calibrated optical and NIR photodiodes. When combined, these components will deliver semi-monochromatic, azimuthally uniform irradiance[1] to the SNAP focal plane for relative photometric calibration.

4.1 Light Emitting Diodes

Historically, filament lamps have been commonly used in telescope calibration. Their broad, featureless emission and stable irradiance make them ideal for many calibration applications. However, as discovered by HST, the gravitational loading during launch and zero-g environment of space can cause the tungsten filament of these lamps to shift and thus change their irradiance from the ground calibration (Martel et al., 2003; Martel and Hartig, 2003). In addition, the broad spectral shape of filament lamps prevents an accurate in-flight characterization and monitoring of the spectral bandpasses of broadband filters. A mistake in characterizing the filter transmission functions could lead to systematic errors which will affect the SNAP science mission (further discussion in Chapter 6).

As precision filter calibration is gaining importance in the astronomical community, new technology and techniques using monochromatic light are being developed to accurately determine the spectral throughput of telescopic systems (Stubbs and Tonry, 2006). One important technology currently in mainstream use is that of semiconductor light emitting diodes (LEDs). I will describe the properties of these devices and propose an application of multiple LEDs into a single illuminator with the intent of tracking filter transmission functions of the SNAP filters.

4.1.1 LED Properties

Semiconductor LEDs are p-n junction devices that produce semi-monochromatic light. As an electric current is applied to the anode and cathode, photons are gener-

[1]Spectral irradiance is typically defined as flux per wavelength, such as $W/cm^2/nm$.

ated as electrons cross the bandgap between the semiconductor layers. The energy of the photons, and hence their wavelengths, are dependent on the doping material at the LED junction. Therefore, the spectral output of LEDs can be tuned to particular central wavelengths from 300nm to 2μm. These small devices have lifetimes rated in hundreds of thousands of hours, low power consumption, spectral emission with typical FWHM of 20 nm in the optical and 100nm in the NIR, and pulsing capability. Although they require thermal stabilization, the technology exists to construct an onboard light source that will deliver well-characterized narrowband illumination to the focal plane.

Since the brightness of an LED is proportional to the forward current, it is crucial to keep the forward current as stable as possible. To demonstrate the current dependency, we use the standard LED (I-V) relation,

$$I = I_s e^{q_e(V-IR_S)/(n_f kT)}, \tag{4.1}$$

where I is the forward current, I_s is the saturation current, q_e is the charge of the electron, V is the forward voltage, R_s is the series resistance, n_f is a scale factor, and T is the ambient temperature in Kelvin. Stability is achieved by a tight regulation of the forward current with a constant current power supply. LED forward currents can range from 1 - 150mA depending on the LED design.

Equation 4.1 also shows that the LED irradiance has a strong dependence on temperature. Therefore, it is necessary to tightly regulate the thermal environment of LEDs and to characterize their output at a specified temperature. To demonstrate the temperature dependence, we measured the spectral radiance of an LED over a 20°C range in our LED monochromator system (described in Chapter 6.3.1). The LED temperature was controlled by connecting the LED leads to a Lakeshore thermal controller with a heater resistor and temperature sensor. The metal LED leads are in

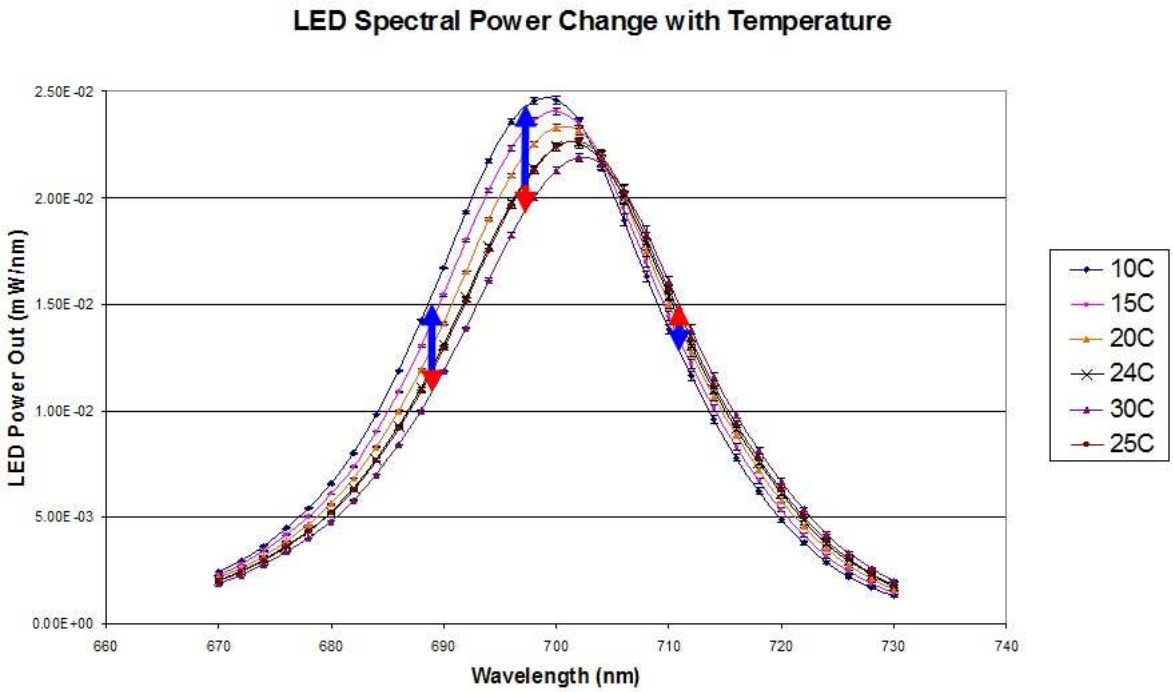

Figure 4.1. The effect of temperature on an LED spectrum (model LED-700-524 from Roithner-Lasertechnik). The spectrum for this LED becomes brighter and bluer with decreasing temperature.

direct thermal contact with the LED junction, and therefore provide a low-resistance thermal path. The emitted light from the LED was directed into our monochromator system for spectral power measurements.

Figure 4.1 illustrates the temperature sensitivity of the LED-700-524 model from Roithner-Lasertechnik. This LED becomes both brighter and bluer as its temperature decreases. Specifically, a temperature change of 5°C resulted in a 2% increase in integrated flux and 0.5nm blueshift of the LED spectrum. This results suggests that LEDs used for calibration purposes needs to be operated in an environment with precise thermal control and at a temperature for which the LED was calibrated.

An additional benefit to driving LEDs with a constant forward current is that any change in the voltage across the LED is proportional to the resistance of the LED. As for most p-n junction devices, the terminal resistance is indicative of the device temperature. As shown below, the voltage across the LED terminals tracks

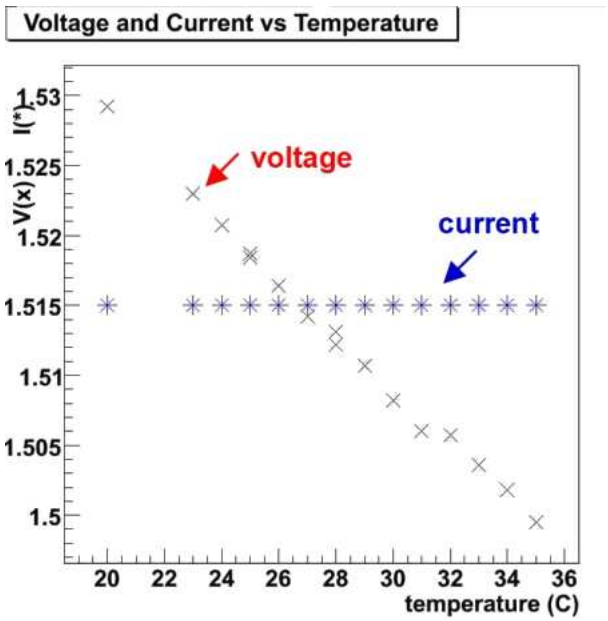

Figure 4.2. Tracking LED temperature via a voltage measurement. The current has been scaled to a value 1.515 to show that it is constant and independent of temperature.

linearly with a change in temperature of the terminals. We can exploit this behavior to monitor and regulate the LED temperature. This is a direct measurement of the LED junction temperature and it relaxes the need for an external thermal sensor. The voltage measurement can also be made across the LED terminals without a change in the output of the LED.

LEDs are also capable of being pulsed at a high repetition rate. Figure 4.3 shows a clock and forward current delivered to an LED and light pulse emitted from the LED in response. The pulse was delivered at a 1kHz repetition rate with a 5% duty cycle and 50μs pulse width. The LED emission was measured with a phototube capable of resolving fast pulse times. The pulsing capability of LEDs may be useful for SNAP calibrations that require control of flux levels on the focal plane, such as detector gain determination and detector non-linearity. The accuracy of LED pulse control is currently being investigated by Indiana University.

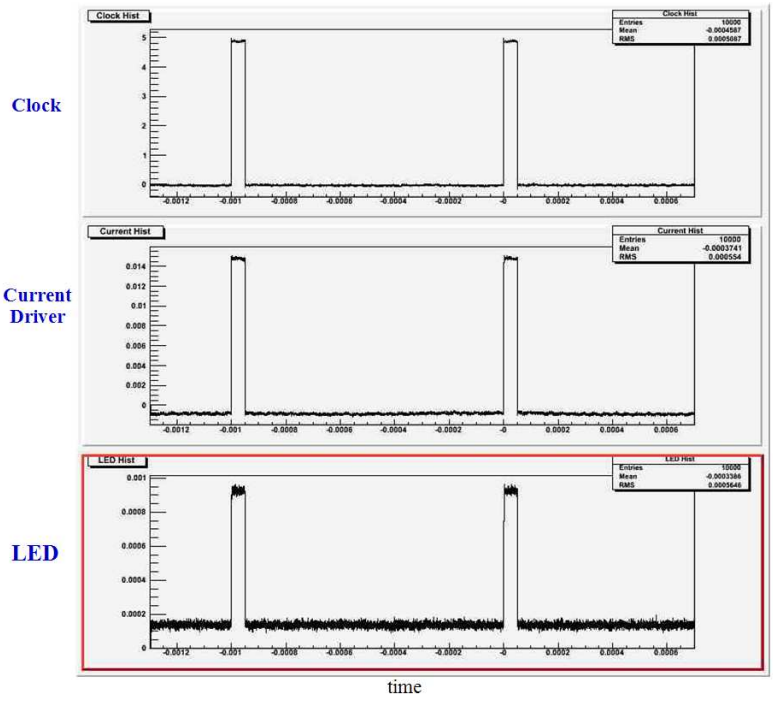

Figure 4.3. This figure shows the clock, forward current, and emission pulses for an LED. The LED was driven at a 1kHz repetition rate with a 5% duty cycle and 50μs pulse width.

4.2 Ring of Fire

The Ring of Fire is a focal plane illuminator that is fixed to the end of the SNAP cold stop. The ring shape was designed so that light from the SNAP telescope will remain unobstructed, thus minimizing system complexity. The RoF itself is annular strip of white Spectralon, a commercial diffusing material typically used in integrating spheres, that is attached to the inside of the cold stop see Figure 4.4. The Spectralon strip is illuminated via a small, annular mirror which redirects illumination from seven small input fiber ports. With a nearly 2π bi-reflectance distribution function, the Spectralon will scatter light to the focal plane in an azimuthally symmetric pattern.

Simple calculations of the RoF illumination pattern have been performed to study the uniformity of light incident on the focal plane. The results of these calculations, as shown in Figure 4.5, reveal an illumination pattern that is azimuthally uniform and radially dependent on the distance from the SNAP optical axis. Assuming seven

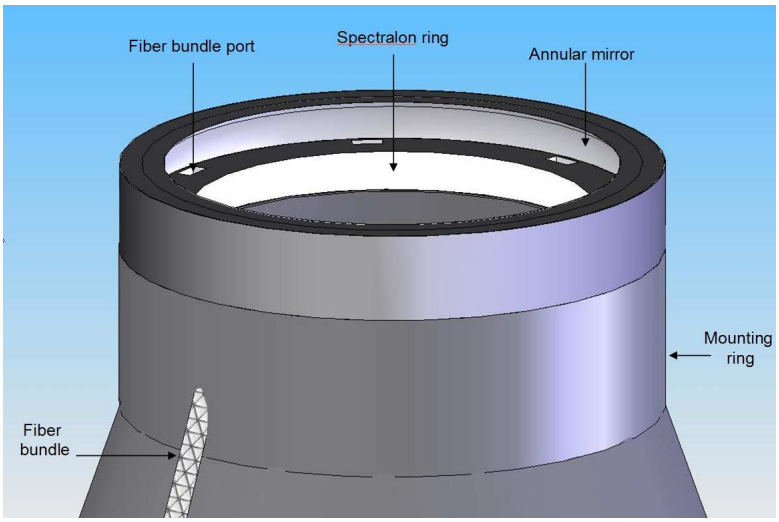

Figure 4.4. Ring of Fire placement on the SNAP cold stop.

equally spaced illumination ports on the RoF, each with an opening angle of 15°, we achieve a flat field that is uniform to 1% in azimuth on the focal plane. However, the illumination pattern does have a smooth roll-off with increasing distance from the SNAP optical axis, as shown in Figure 4.5(a). This pattern must be characterized before flight and checked with stellar flats in flight (see Section 3.3.3). Regardless, the illumination pattern is still uniform below the 1% level on small pixel scales, making it usable for pixel-to-pixel flat field response.

We also simulated a failure mode in which one of the seven illumination ports became unusable. This scenario could occur if one of the fibers bringing light to the RoF breaks. Figure 4.6 shows that in this case, an azimuthal variation becomes apparent on large pixel scale. However, the HF-Flats are still usable for small scale pixel-to-pixel variations. One way to avoid this scenario is to build in redundancy into the fiber bundles that deliver light from the calibration light source to the RoF.

Recall that even if large scale variations such as those in Figure 4.6 do occur, the procedure of using stellar clusters to perform large-scale flat fields can calibrate out the response variation to some degree. However, a complex flat field illumination will require more spatial samples in the L-Flat process and will likely have a larger residual

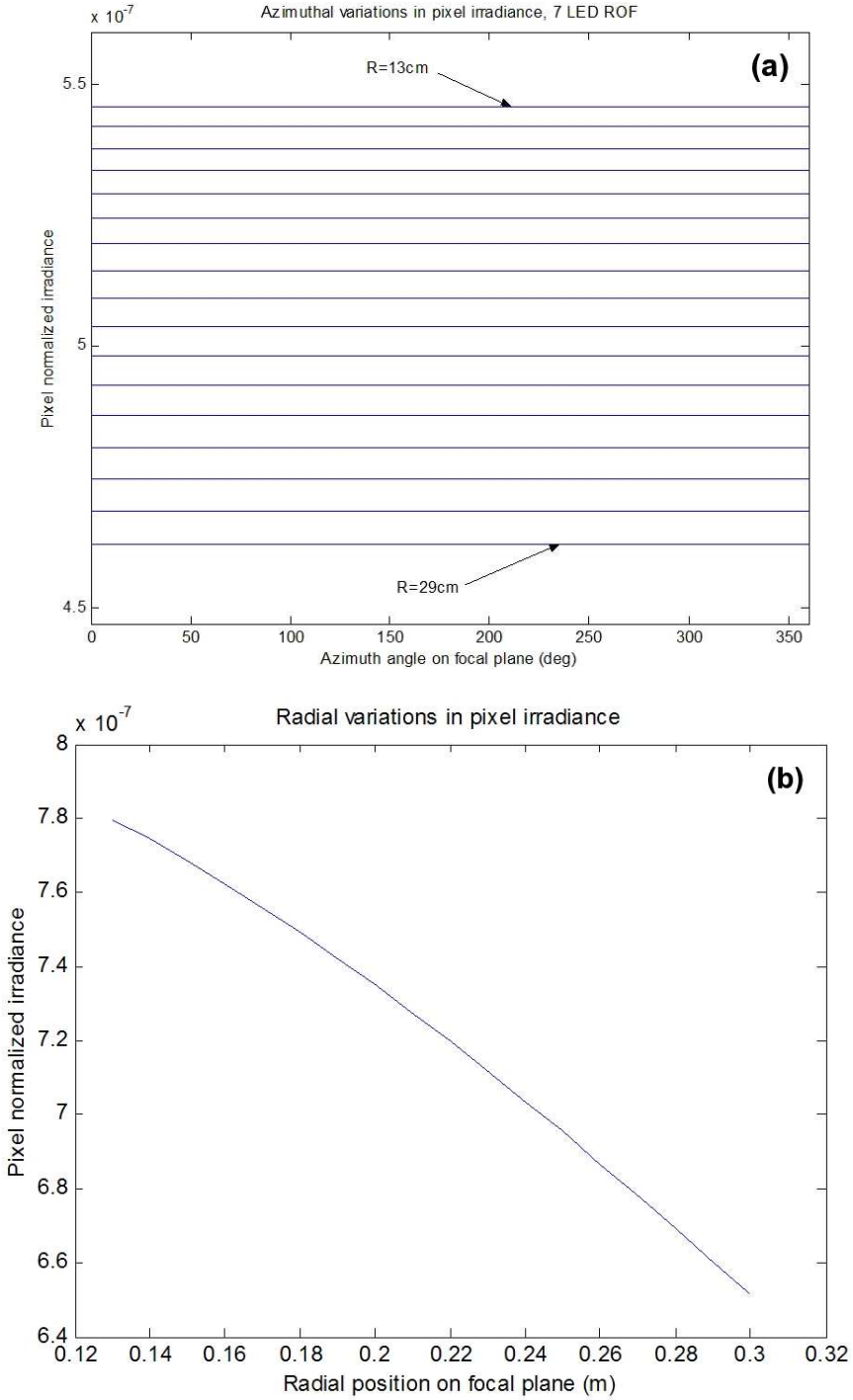

Figure 4.5. (a) The azimuthal variation in the RoF illumination with 7 LEDs and (b) the radial variation of RoF illumination.

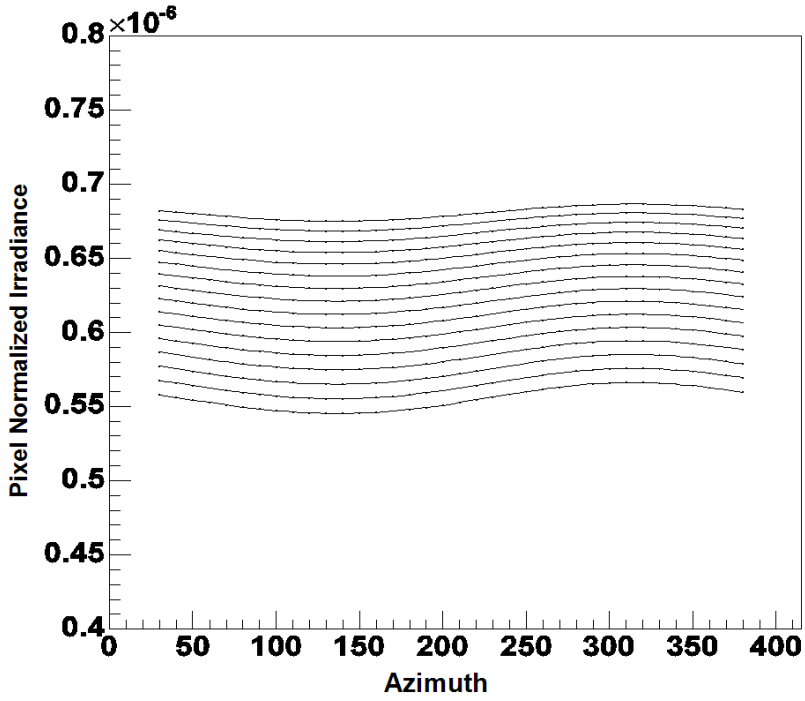

Figure 4.6. Azimuthal variation in RoF illumination with 2.7% variation on the focal plane due to a 10% illumination variation from the RoF ports.

error after the spatial response is removed. Therefore, to minimize the requirements on characterizing the L-flat, we place a 10% uniformity criterion on the azimuthal variation. This sets a 2.7% limit to the illumination variation at the RoF illumination ports as shown in Figure 4.6.

A secondary benefit to the RoF design is the ability to illuminate the focal plane with light having an angular distribution similar to stellar light from the SNAP optical train. Since SNAP will use interference filters that have angle-dependent transmission, matching the photon incidence angle distribution reduces systematic errors in color between the stellar light and the RoF light.

Figure 4.7 is the distribution of incidence angles from a single stellar source on the SNAP focal plane. The three different curves represent a single star at various radii on the focal plane. The left curve shows the range of angles that will make up a star on the inner portion of the SNAP annulus, the middle curve represents a star in the center of the annulus, and the right curve shows a star on the outer portion of the annulus.

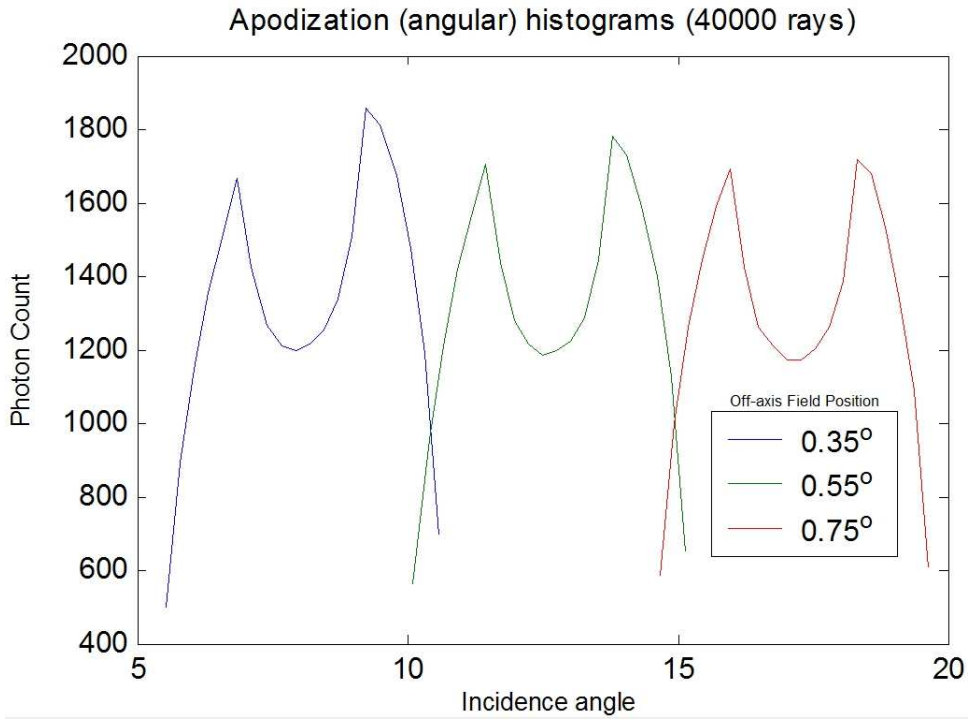

Figure 4.7. Incident angle histograms for a stellar source at three different radii on the SNAP focal plane.

Each star has a 5° range of incidence angles, while the total range of incidence angles possible on the SNAP focal plane is 15° from inner to outer edges of the annulus. This geometry is unique to the SNAP design, and because interference filters have angle dependent transmission, a proper filter calibration system must mimic the range of photon angles that will be present on the focal plane. The characterization of filter transmission function with incidence angle must be carried out on the space-based RoF system as well as the ground-based filter calibration system.

A study by Sholl (2004) calculated how well the RoF illuminator matches the incidence angle of the SNAP telescope light. The calculation used the input spectrum of a white dwarf star, the photon distributions of the SNAP pupil and RoF, and a simple model for interference filter transmission variation with respect to the photon incidence angle. The results of this calculation are shown in Figure 4.8 using an sample interference filter transmission function that is a rough approximation to the

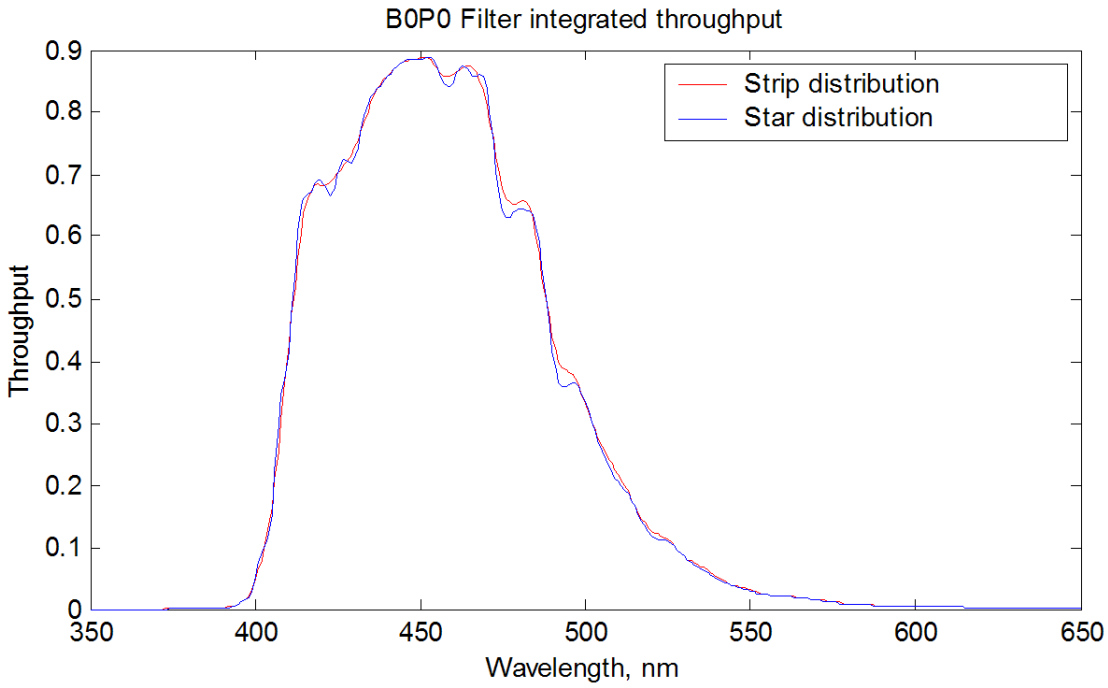

Figure 4.8. Filter throughput from the RoF and a stellar source (Sholl, 2004).

SNAP design. The calculation shows that given the annular design of the RoF and its placement at the end of the cold stop, there is minimal color difference in the photon incidence geometry between the RoF and the SNAP pupil.

4.2.1 LED Illuminator

The RoF placement at the top of the cold shield places tight space restrictions on the input light source size. A minimum set of LEDs directly on the RoF would consist of 378 LEDs (3 LEDs for each of the 9 SNAP filters, 7 LEDs of each type on the RoF and double redundancy, see Chapter **??**). The placement also requires that the input ports have the same temperature as the radiation shield, which will be approximately 140°K. Because LED spectral power is known to be strongly dependent on temperature, placing LEDs directly at the input ports would require them to be calibrated at 140°K on the ground and regulated at that temperature in space.

With the space restrictions and temperature requirements for LEDs, the light delivery to the RoF will require a sophisticated optical fiber-based system. In this

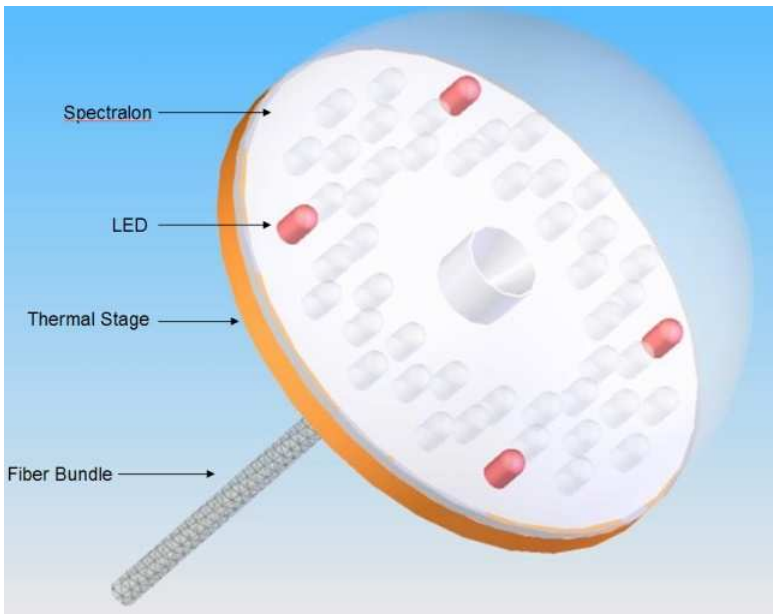

Figure 4.9. A proposed LED-based calibration light source for the SNAP focal plane.

system, the light sources can reside elsewhere in the SNAP telescope body and relax the tight space constraints of the RoF. In addition, the light sources can benefit from additional radiation shielding and the room-temperature thermal conditions of the SNAP infrastructure. Feeding off the room-temperature environment will help simplify thermal requirements on the light source ground calibration as well as help the sources maintain their ground calibration into space. The relaxation of space restrictions also allows the light source to have several optical components, including a monochromator.

While a separate RoF illuminator has many advantages, it does require a stable way to deliver light to the RoF illumination ports. The delivery system must be small enough to fit within the space around the RoF, yet sturdy enough that a violent launch will not alter the light output of the system. Figure 4.9 shows a conceptual design for a LED illuminator coupled to a fiber bundle. The 4 inch diameter hemisphere could house up to 400 LEDs. The integrating hemisphere will couple all of the necessary LEDs into one housing and uniformly illuminate a fiber bundle. The uniformity

requirement serves to prevent azimuthal illumination variation at the RoF and which will propagate to the focal plane (see Section 4.2. The hemisphere will also have a thermally stabilized base plate to be operated at 25°C. This operating temperature will ensure continuity of ground based LED calibration into space. The current fibers to be used are Polymicro 300μm core silica fiber and will be bundled in a space qualified jacket. Indiana University will test a mock up system for uniformity of the output from the fiber bundle and the overall efficiency of the design.

4.3 Photodiodes

Photodiodes are millimeter size p-n junction devices that have a current output proportional to the incident photon energy and quantity. Photodiodes are essentially the larger cousin of the imager pixels that are put into modern day astronomical cameras. As a photon strikes the semiconductor material, electrons are generated at a rate proportional to the quantum efficiency of the device. Photodiodes are made in a variety of types, but the most relevant types to the SNAP spectral range are silicon from 350-1000nm and InGaAs from 900-1700nm. These devices have large dynamic ranges, high quantum efficiencies, and are well understood in the literature.

There are a wide range of applications for photodiodes in calibration systems. One of the major advantages to photodiode calibration is that it is a detector-based calibration method. In general, detector-based calibration standards are easier to implement into instruments than source-based standards such as blackbody sources or QTH lamps. Photodiodes can be shipped to NIST for a relative power responsivity (QE) calibration that is accurate to 0.2% from the optical to the NIR Larason et al. (1998). Furthermore, with the addition of a precision aperture, photodiodes can be calibrated to make direct measurements of the total irradiance of a light source. I have developed photodiode irradiance standards in both the optical and NIR that have been calibrated by NIST and have transferred this calibration to other photodiodes

for use in SNAP detector laboratories (see Chapter 5.2 for further discussion).

Because photodiodes offer a detector-based calibration, we advocate the use several unfiltered photodiodes on the SNAP focal plane. The proposed photodiode locations are shown in Figure 2.4. The bare photodiodes will be essential in normalizing the filter transmissions by measuring (and monitoring) the unfiltered LED output through the RoF. With pointed observations, they also will help compare the LED output directly to bright, stable stars. This comparison breaks the degeneracies in any LED / filter / photodiode variation and thus closes the calibration loop.

A technical challenge in using NIST-calibrated photodiodes on SNAP is constructing electronics to aide in low signal level detection. Photodiodes are direct current devices, and electrometer measurements of direct current are typically limited to the 100fA level in the laboratory. SNAP currently plans to use white dwarf flux standards that are around 12th magnitude in brightness, which is equivalent to about 50fA in the reddest SNAP filter. The addition of a post-diode current integration circuit, coupled with reduced photodiode sizes and cold SNAP focal plane temperatures, shows promising conditions to increase the sensitivity limit of photodiodes.

CHAPTER 5

Monochromatic Illumination and Cryogenic Calibration System (MICCS)

As discussed in Section 1.5 and 3.1, the precision calibration of the spectral throughput of SNAP is essential for an accurate determination of cosmological parameters using SNe Ia. The SNAP instrumentation that could contribute systematic errors due to their varying spectral throughput over the SNAP wavelength range are the focal plane detectors and interference filters. These components require study under test environments similar to the SNAP mission to understand the tolerances demanded of their characterization.

To address the calibration of SNAP detectors and filters, I have built the Monochromatic Illumination and Cryogenic Calibration System (MICCS) shown in Figure 5.1. This system has two main functions: (1) the transfer of irradiance calibration from a NIST calibrated photodiode to transfer photodiodes and (2) measure interference filter transmission at the SNAP focal plane temperature of 140K and photon incidence angles similar to the SNAP apodization. In this chapter, I will detail the design of the MICCS by breaking it into its two major systems: the narrowband, uniform light source and the cryogenic dewar. As I describe each of these major systems, I will explain their essential components and explain why they were chosen to be in the system design. After the MICCS system description, I will present calibration data for InGaAs photodiodes and commercial interference filters.

5.1 MICCS System Design

In designing the MICCS system shown in Figure 5.1, I had two main design goals. The first goal was to build a uniform, stable, narrowband light source from 400nm to 1700nm. To reflect the overall SNAP error budget of 2% relative photometric error, I required that the illumination uniformity across two photodiode detectors must be less than 2% and the light source stability be less than 1%. These requirements minimize systematic error and ensure that a precise level of irradiance will be measured by photodiodes undergoing irradiance calibration. I also required that the width of the emitted bandpass be flexible (2 - 10nm FWHM) from the optical to the NIR.

The second design goal for the MICCS was to build a characterization system for both photodiode irradiance responsivity and filter transmission inside an 8" diameter cryogenic dewar. This design goal requires that the components necessary to perform these measurements must be discrete in size, withstand 10^{-6} torr vacuum, and be capable of holding a temperature of 140K.

The MICCS achieves both of these design goals. The system produces precision photodiode irradiance and filter transmission calibration in an environment similar to the SNAP focal plane.

5.1.1 Narrowband Light Source

The light source system that illuminates the MICCS system is shown in Figure 5.2. To fulfill the $< 1\%$ light stability requirement, the MICCS uses a 100W Quartz-Tungsten-Halogen (QTH) lamp in a Newport PhotoMax housing [1] [Figure 5.2(l)]. The PhotoMax system uses an ellipsoidal mirror to focus light from the lamp into an f/4 beam. The QTH lamp alone is relatively stable, with only slow drifts in output on the order of a few minutes. To increase stability, the MICCS has a Newport light intensity controller to regulate the QTH lamp power supply [5.2(a)]. The controller

[1]The PhotoMax is a trademark name of Newport Corporation. The light-focusing system is designed to optimize throughput in Newport monochromators

unit uses a Silicon monitoring photodiode [5.2(j)] to measure light from the lamp source and adjusts the output current to the lamp, therefore regulating the light intensity.

Implementing the monitoring photodiode required a design that allowed the light source to be viewed indirectly. The diode has no default placement on the PhotoMax housing, and the diode cannot view the f/4 beam directly without either damaging the diode or blocking the beam on its path towards the monochromator. To address this problem, the MICCS uses a ring light guide [5.2(k)] mounted at the exit of the PhotoMax which delivers illumination to the photodiode behind a 10^{-4} neutral density filter [5.2(i)]. The ring light guide is a cable composed of hundreds of optical fibers that form a 3" ring on one end and a small 0.5" diameter port on the other end. Generally, ring light guides are used with the light input at the small port end while the ring uniformly illuminates a small area. In the case of the MICCS, the ring light guide is used in reverse of its typical implementation by accepting illumination from the ring end of the cable and delivering the light to the small port end. This usage of the ring light guide allows for the PhotoMax beam to remain unobstructed as it illuminates the monochromator while delivering an attenuated illumination for light source regulation.

A motorized filter wheel [5.2(g)] at the input port to the monochromator contains three long pass filters, a blocking disk, and an open port. The transmission cut-off for the filters are at 350nm, 575nm, and 850nm. These wavelengths were chosen to block extraneous lamp emission from wavelengths shorter than the cut-off, thus reducing stray light within the monochromator and preventing overlap from the higher orders of the optical and NIR gratings.

Figure 5.3 shows the narrowband monochromator component of the MICCS system. Motorized slits are attached to both the entrance and exit ports of the monochromator [5.3(c) and (f)]. The slits, along with the grating line resolution, control the

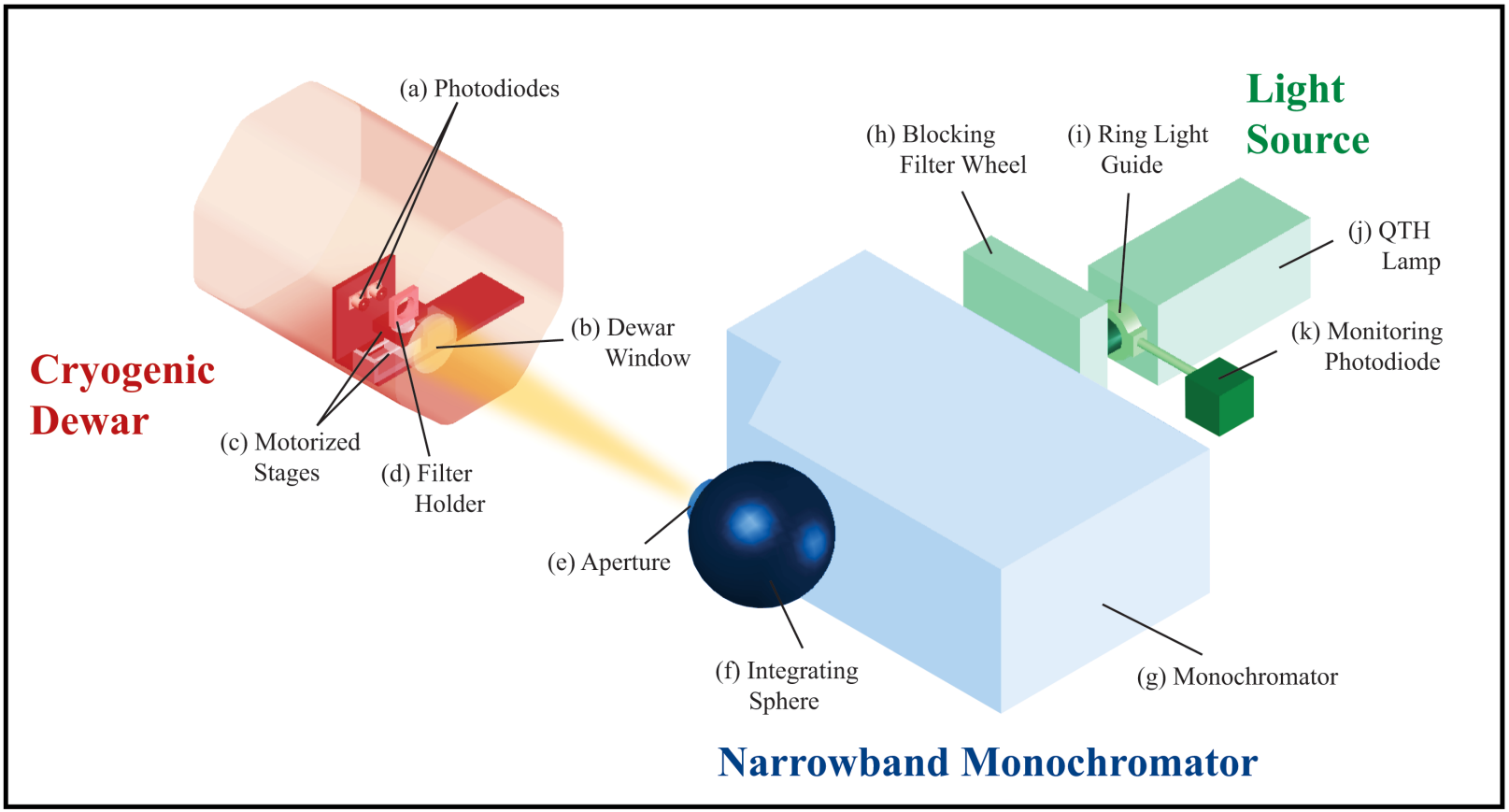

Figure 5.1. A schematic overview of the Monochromatic Illumination and Cryogenic Calibration System (MICCS).

Light Source

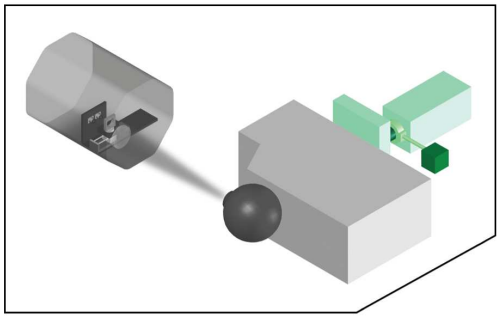

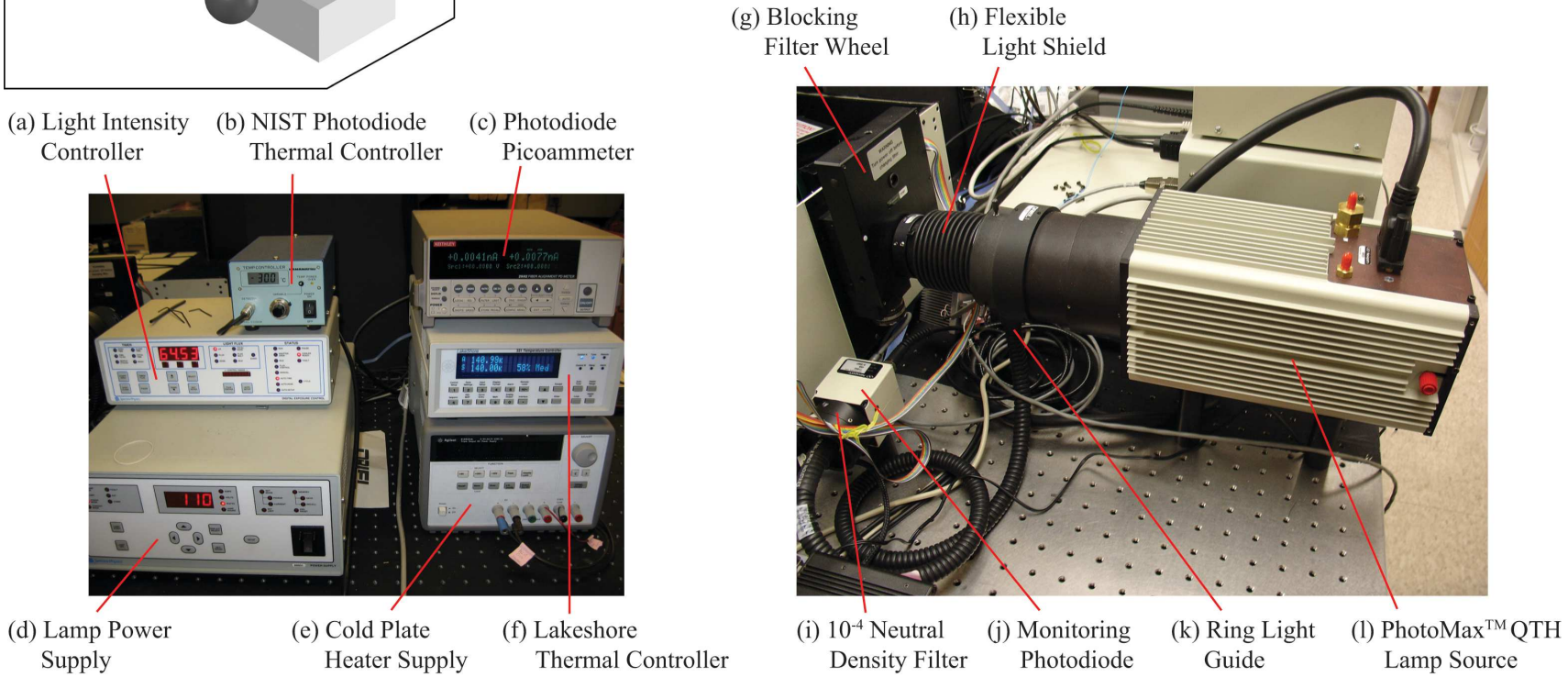

Figure 5.2. The light source system used to illuminate the MICCS.

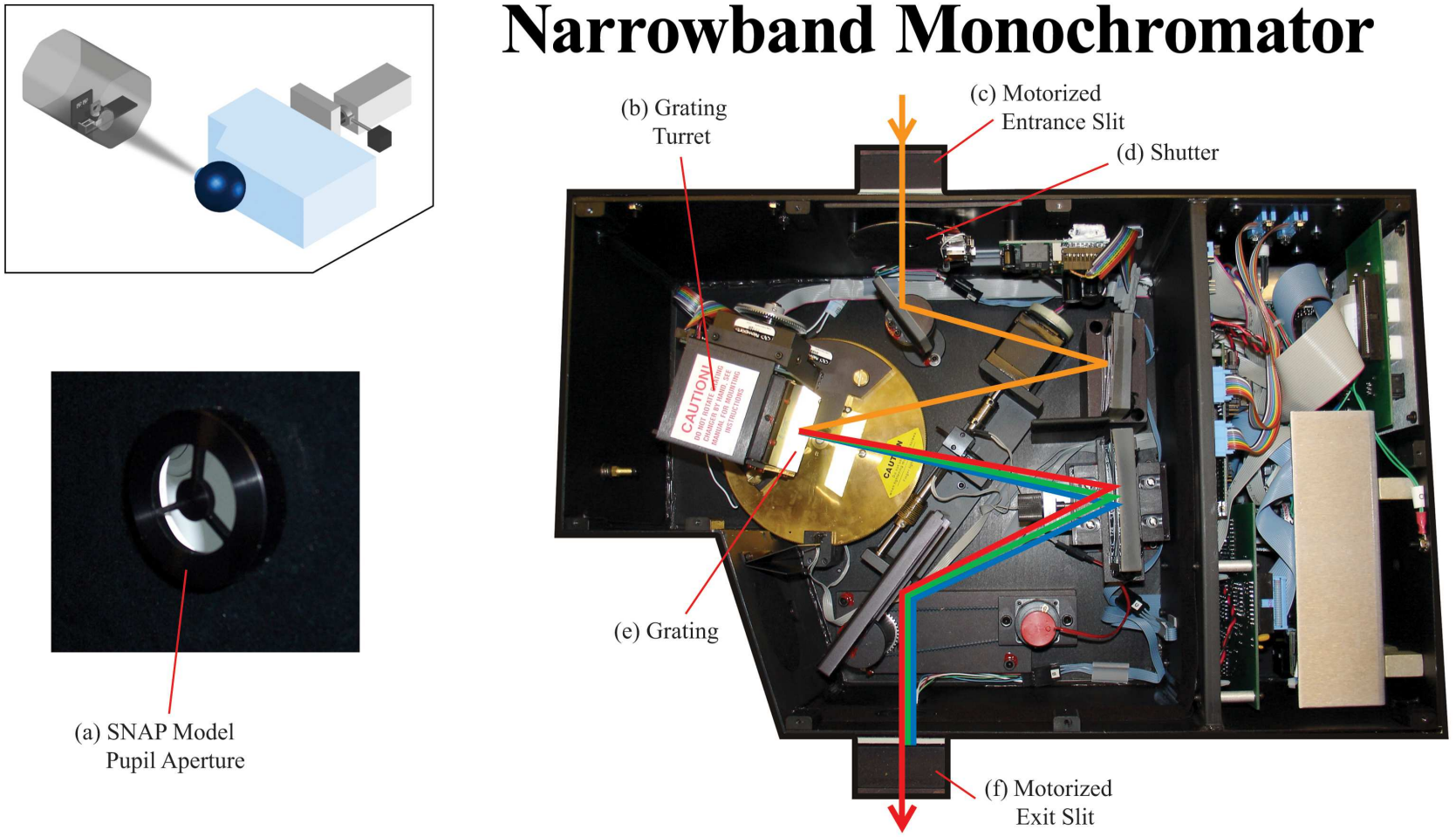

Figure 5.3. The narrowband monochromator and SNAP mock pupil aperture for the MICCS.

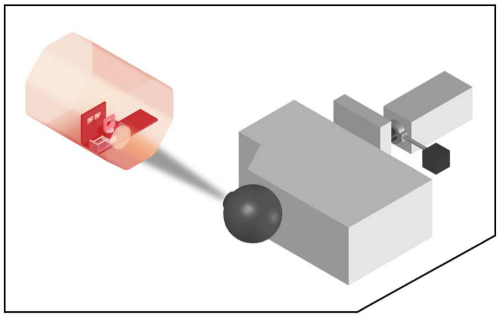

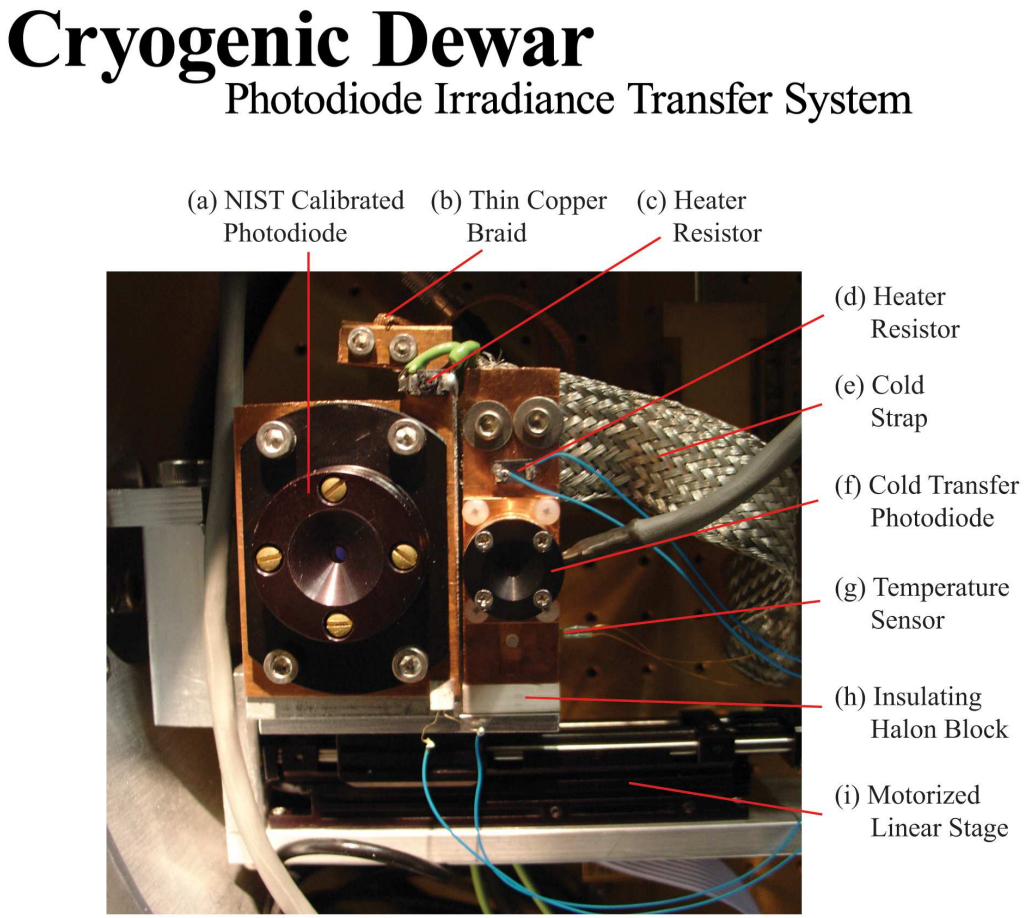

Figure 5.4. The MICCS cryogenic dewar with instrumentation for the calibration of photodiode irradiance responsivity.

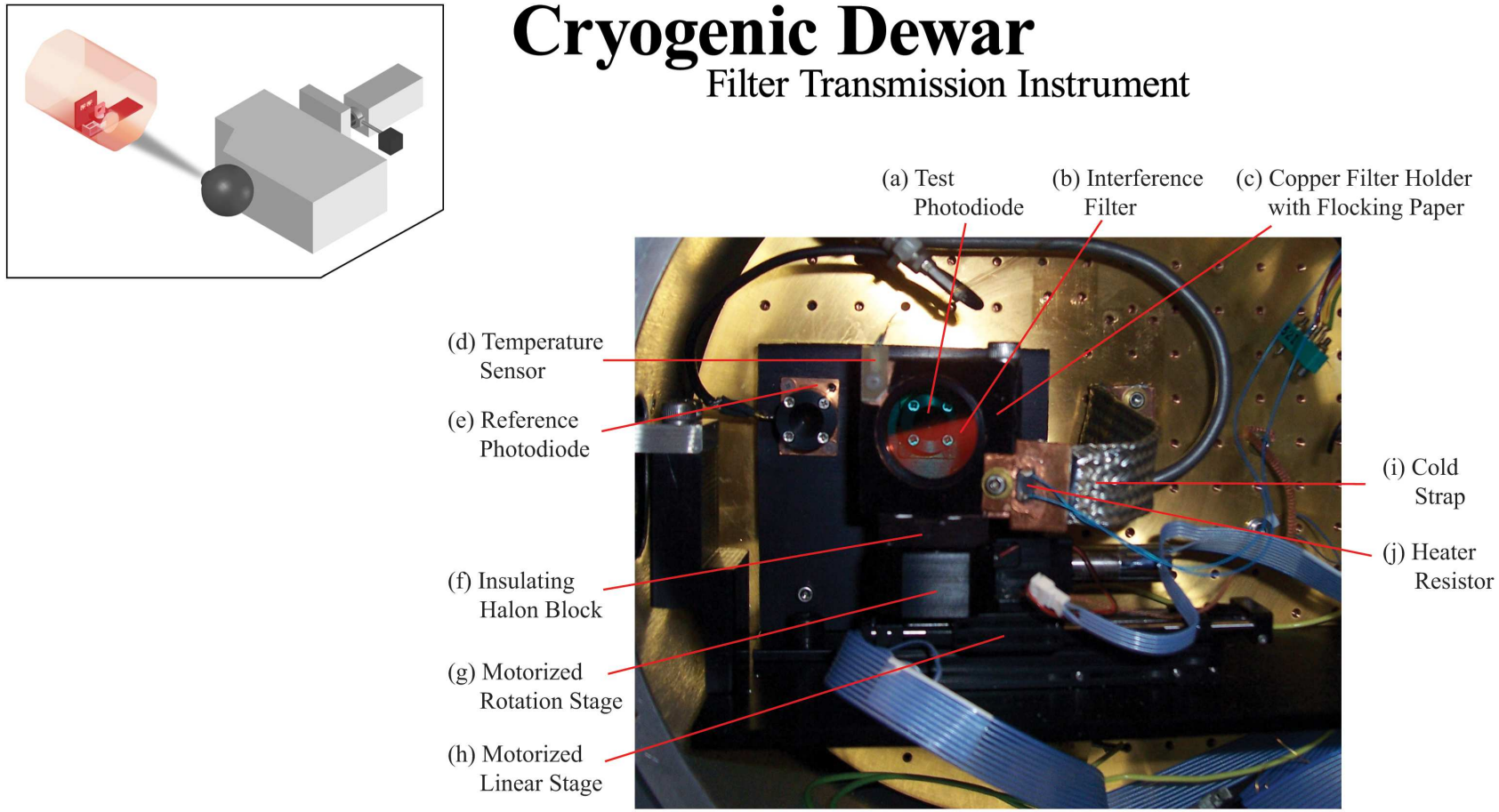

Figure 5.5. The MICCS cryogenic dewar with instrumentation for the calibration of interference filter transmission functions.

bandpass of the monochromatic light. The MICCS monochromator is capable of 1nm resolution in the optical and 2nm resolution in the NIR. The MICCS monochromator is an automated Newport MS257 monochromator with a four grating turret [5.3(b)] and a fast shutter mechanism [5.3(d)]. The monochromator has two gratings: one that is blazed at 350nm for the optical and one that is blazed at 1050nm for the NIR [5.3(e)]. Operations for the monochromator are controlled via an RS-232 connection and ASCII string commands. Any wavelength in the SNAP bandpass can be dialed in with automated switching of filters and gratings. This level of monochromator automation in addition to the regulated light source makes the MICCS a very stable, narrowband light source.

As the narrowband light exits the monochromator, it diverges in an f/4 beam and maintains the shape of the illuminated entrance slit. To remove the structure of the emergent light, a 6" diameter integrating sphere is attached to the exit port of the MS257 [5.1(f)]. An integrating sphere is an optical element that is coated internally with a diffuse reflecting material. As the light enters the sphere, it bounces around multiple times with a nearly perfect random pattern before leaving the exit port of the sphere. The light exiting the sphere fills a uniform diffuse disk at the exit port. The diffuse light from this disk is projected onto an area of uniform illumination proportional to the size of the port and distance from the port. The exit port of the integrating sphere can also be fitted with an aperture that models the SNAP pupil [5.2(a)]. When the illuminated focal plane of the MICCS dewar is placed 14" away from the exit port, the model aperture subtends an angular area similar to the telescope pupil viewed on the SNAP focal plane. Therefore, the MICCS is capable of reproducing the photon incidence angle distribution that will be present on the SNAP focal plane.

5.1.2 Cryogenic Dewar

The area illuminated by the uniform, narrowband light source must maintain 140K to replicate the focal plane temperature on SNAP. This temperature is achieved with a cryogenic dewar system purchased from IRLabs (shown in red in Figure 5.1). To reach 140K, the dewar is first pumped to 10^{-6} torr vacuum for several hours to remove all the air from the dewar volume and test items. The dewar cryogen tank is then filled with liquid nitrogen and the temperature is regulated in a closed loop by a Lakeshore Thermal Controller [5.2(f)]. The controller uses a temperature sensor and heating resistor mounted on a copper block to regulate the thermal load at 140K. The process of cooling to SNAP temperature takes about one hour and the hold time is nearly ten hours with constant dewar pumping.

The dewar has a large 3" diameter window [5.1(b)] for testing multiple photodiodes, and it will fit a SNAP filter that measures 1.5" on a side. The dewar is also mounted on linear rails along the optical axis. The linear rails allow the dewar to be placed at different working distances from the narrowband source, which allows for control of the source angular size and uniformity across the dewar window. The rails also allow for easy access to the internal dewar components. The front end of the dewar and the linear rails are mounted inside a dark box constructed from black matte foam core. To reduce scattered light from the diffuse source within the dark box, the walls of the box are matted with dark flocking paper. Further, black paper baffling is attached to the dewar cap to reduce reflections off the inner edge of the dewar window and black anodized aluminum is used within the dewar on most all mountable surfaces. The illumination uniformity has been measured and found to meet the requirement with $< 1\%$ variation across a 1" diameter area on the focal surface (see Figure 5.6). In addition, the variation is symmetric about the optical axis, so symmetric positions about the optical axis have equal illumination.

An important property of the MICCS dewar design is that it includes both a

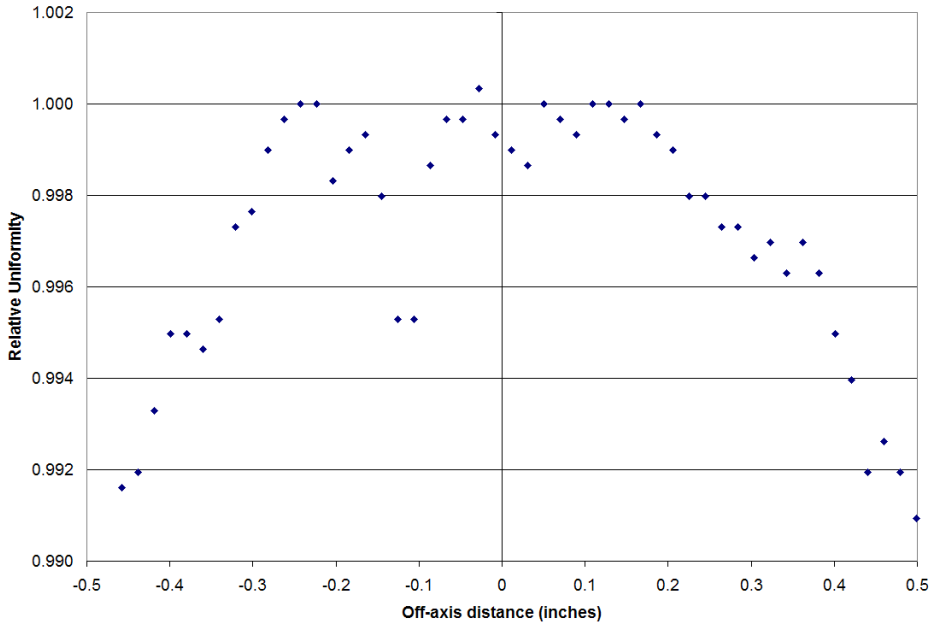

Figure 5.6. The illumination variation across the focal surface in the MICCS dewar system. The variations are less than 1% over a 1" diameter area. The variation is symmetric around the optical axis.

rotary and linear stage within the dewar [5.1(c)]. These miniature stages increase the versatility of the testing that can be done within the dewar. For example, the linear stage is capable of scanning multiple positions in the light path and measuring the uniformity of the illumination within the dewar. The ability to test different positions is ideal for a precise transfer of calibration from NIST photodiodes to other transfer photodiodes (see Section 5.2). The linear stage also can yield transmission measurements at different points on an interference filter, thus testing spatial uniformity. The rotary stage is important for testing filters at a range of photon incidence angles, measurements essential for characterization of interference filter transmissions on the SNAP focal plane.

Both stages are mounted on a surface within the dewar that is connected thermally to the warm external environment. The "warm" operation of these stages ensures proper movement of the devices. However, it also poses a challenge in mounting photodiodes and filters that must be cooled to SNAP focal plane temperature. I found

that large thermal gradients over the area of the stage mounts could be prevented by using cintered halon insulating material. By limiting the surface area contact of the warm stages with the cold mounting surface and by placing insulating halon judiciously, these stages can be successfully operated at room temperature while mounted photodiodes and filters maintain 140K.

Given the two goals of photodiode irradiance calibration and filter transmission testing, there are two different setups for the MICCS dewar. The setup for the photodiode irradiance calibration transfer is shown in Figure 5.4. A NIST calibrated InGaAs photodiode [5.4(a)] is mounted next to a transfer InGaAs photodiode [5.4(c)] that is attached to a stage held at 140K. Both photodiodes are mounted on a common linear stage [5.4(i)] so that I can measure and remove non-uniformity in the MICCS monochromatic illumination. Since the NIST photodiode heat sink package is designed to cool convectively, additional cooling must be supplied in a vacuum environment. I cooled the heat sink package by creating a small thermal conduction path to the dewar cold plate. All thermal straps to the cold plate [5.4(b) and (e)] are made from copper braid to allow for excellent thermal conduction while maintaining flexibility for stage movement.

The incoming photons from the MICCS narrowband illumination source produce a small current signal both the NIST and cold transfer photodiodes. The measurement of photodiode currents is made by a dual-channel Keithley picoammeter [5.2(c)], which has a sensitivity limit of 10 fA and can make a simultaneous ratio of current signals. The ratio measurement has significant advantage over individual measurements of each photodiode as it reduces the systematic error in the measurements by eliminating residual variation in the light source intensity. In addition, the simultaneous ratio of the current signals requires only one pass over the wavelength range of interest and therefore increases the efficiency of the calibration transfer process.

Figure 5.5 shows the dewar setup for interference filter testing. This setup uses

two silicon photodiodes to measure narrowband light with and without the filter in the beam path. The simultaneous current ratio of the test photodiode [5.5(a)] to the reference photodiode [5.5(e)] measures the filter transmission over the incident photon bandpass. The filter is mounted in copper block [5.5(c)] that is tied with a flexible copper strap [5.5(i)] to the dewar cold plate. This copper filter block is mounted to a motorized rotation stage [5.5(g)] and is insulated from the warm stage by a piece of halon [5.5(f)]. The rotation stage is also mounted on a linear stage that can move the filter to different positions on the optical axis or remove the filter from the beam path entirely [5.5(h)]. This function is useful for testing transmission at different points of the filter and for calibrating out any differences in spectral response between the two silicon photodiodes. To reduce scattered light, all aluminum surfaces have been anodized black and the halon has been dyed black. The copper filter block has also been covered with black flocking paper to prevent reflected light from entering either of the measuring photodiodes.

5.1.3 Computer Automation

The MICCS system is a complex system of motorized and electronic components that must work together to be efficient and precise in operation. To achieve the necessary level of automation and ease of use for MICCS, all necessary components capable of communication via RS-232 connections. These communications are generally strings of ASCII commands that can be handled by a Windows PC in the LabView environment.

Figure 5.7 shows the graphical user interface that I wrote within a LabView environment to operate the most useful functions of the MICCS. The upper portion of the GUI returns the current status of the entire system, including monochromator wavelength, filter bandpass, selected detector readout, and stage positions. The GUI also had dedicated sections to control each of the individual components for versatil-

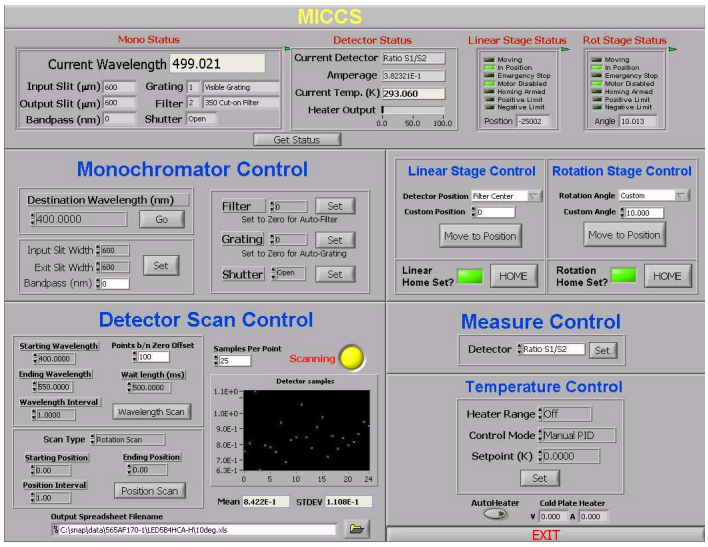

Figure 5.7. The LabView graphical user interface for the MICCS system.

ity. Most important, the GUI has an automated function to perform scan and current measurements at varying wavelengths, linear positions, and rotation positions. This functionality is extremely useful when performing repeatable measurements of spectral throughput, illumination uniformity, and the angular dependence of interference filter transmission. Each data point in the scan (wavelength or position) takes an input number of current samples from which a mean and a standard deviation is computed. In addition, an automated current pedestal subtraction is performed at regular intervals during the course of a scan. This technique removes thermal drifts (dark current) in the signal from the photodiodes and can be considered a "slow chop" of the source against the detector background.

5.2 Photodiode Irradiance Calibration Transfer

One of the primary functions of the MICCS system is the precision characterization of photodiodes. It is essential that the quantum efficiency (QE) of SNAP focal plane detectors be accurately characterized for flight. As discussed in Section 3.2.2, the calibration of the SNAP spectral throughput, including the detector quantum efficiency, makes an important contribution to SNAP error budget.

From 2002 to 2004, I made initial efforts to calibrate the QE of the NIR HgCdTe detectors acquired by the University of Michigan for SNAP R&D. My initial approach to calibrating detector QE was to generate precise irradiance ($W/cm^2/nm$) with a calibrated light source and measure the irradiance using the current signal from a photodiode (A). The system I used to make these measurements consisted of a QTH lamp with calibrated irradiance, a set of calibrated narrowband filters, a photodiode with vendor calibrated spectral responsivity, and a precisely measured aperture for the photodiode. Together, these components gave a detector-based absolute irradiance responsivity calibration ($A/W/cm^2/nm$). As a check of my detector-based irradiance calibration, I compared the expected irradiance from the calibrated light source with the measured irradiance from the calibrated detector. The comparison of the source-based and detector-based irradiance calibrations allowed for an internal check of the my methodology. I found the photodiode irradiance calibration that is accurate to 6% in absolute irradiance responsivity . This error is the quadratic sum of the vendor photodiode responsivity calibration (5%) and my internal end-to-end irradiance calibration measurement error of 3%.

Given the large error quoted by the vendor for photodiode responsivity calibration and the inherent difficulty in building a source-based irradiance standard, I decided that I could achieve the highest accuracy in photodiode irradiance calibration by obtaining a direct photodiode characterization from the National Institute of Standards and Technology (NIST). While NIST does not have the capability of calibrating photodiodes at the SNAP focal plane temperature, they can provide a precise calibration of a photodiode with an attached thermoelectric cooler (TEC) supplied by a client. This calibration procedure enabled me to transfer the NIST irradiance calibration of the TE-cooled photodiode to additional photodiodes at 140K.

The NIST irradiance responsivity calibration included a photodiode spectral responsivity measurement (A/W) using a precision double monochromator and NIST

standard photodiodes (Larason et al., 1998). The NIST source beam underfills the detector active area and delivers radiant power that is calibrated to 0.4% (1σ) in the optical to 1.4% at 1.7μm. NIST also performs a raster scan with a 1mm spot along the surface of the photodiode to determine the uniformity of photodiode response at selected wavelengths. Finally, NIST measures the area of the removable photodiode aperture in a separate apparatus designed for clear aperture metrology (Fowler and Dezsi, 1995). The combination of the aperture area, photodiode response uniformity, and photodiode spectral responsivity leads to a calibrated spectral irradiance responsivity with an error of 1.4% in the optical and 2.4% in the NIR (Shaw et al., 2000). A major contribution to the calibration error from NIST is the 1% error in the diode aperture measurement. The increase in relative uncertainty from the optical to the NIR is primarily due to the low power levels delivered by the NIST cryogenic radiometer in the NIR and signal detection limits of the NIST InGaAs photodiode detector standard.

I have obtained a Hamamatsu InGaAs photodiode that has been calibrated by NIST using the above methodology and I am now using it as my working standard. The photodiode itself is 3mm in size and has a TEC mounted on the back of the chip. The TEC is regulated with a thermal controller purchased from Hamamatsu. Combined with a heat sink, the TEC can hold the photodiode temperature at -30°C, a temperature that significantly reduces the dark current seen at room temperature. Figure 5.8(a) shows the NIST-calibrated spectral irradiance responsivity with its associated error bars, and Figure 5.8(b) shows the photodiode uniformity measured with a raster scan of the NIST narrowband light source at 1000nm.

Since the NIST calibration of photodiodes provides a precise detector-based irradiance calibration, the SNAP QE characterization should used similar detector-based calibration methods. One potential source of systematic error in detector-based irradiance calibrations is the location of the calibrated detector relative to the test

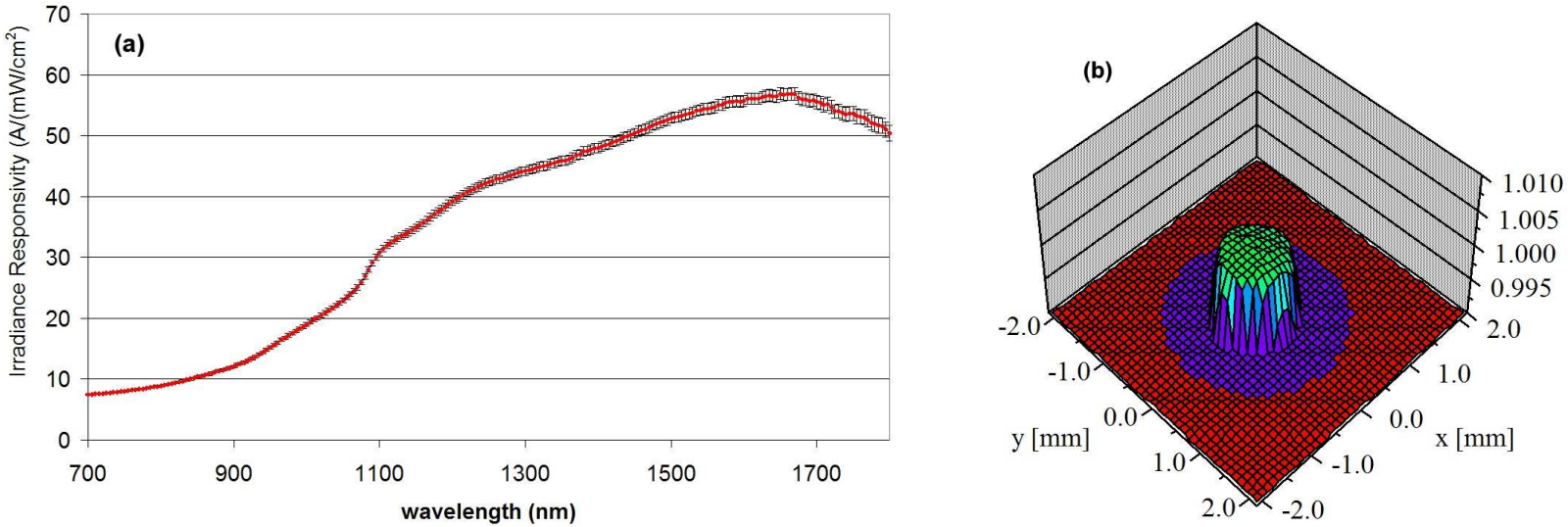

Figure 5.8. (a) The NIST irradiance responsivity calibration for an InGaAs photodiode. (b) The NIST-measured diode uniformity at a wavelength of 1000nm.

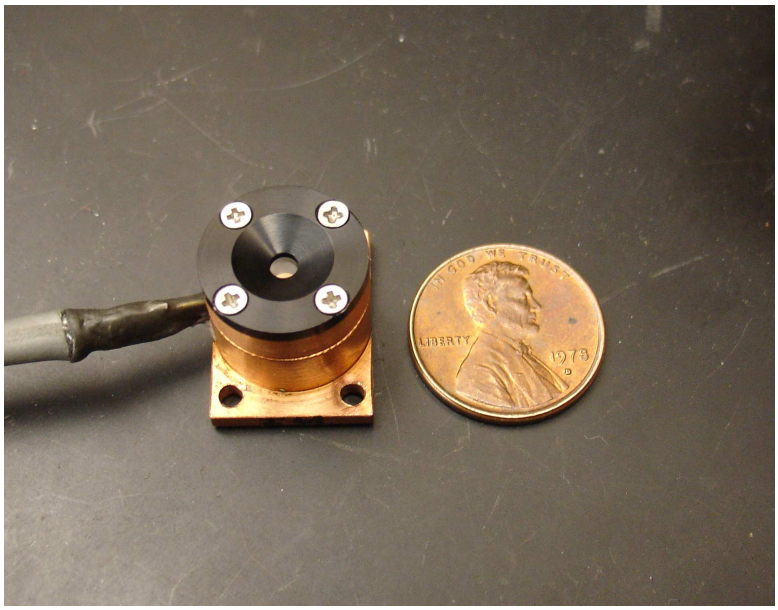

Figure 5.9. The transfer photodiode package designed to operate at 140K. The package features a copper housing, black anodized aluminum aperture, and padding that electrically isolates the package yet allows for good thermal conductivity.

detector. The SNAP detector R&D laboratories at Caltech and the University of Michigan will place the calibrated photodiode at the same location as the SNAP focal plane detector. Placing the photodiode at the same focal plane as the SNAP detector minimizes error in the photon illumination uniformity and removes the need to scale the measured flux to account for different detector distances from the narrow-band source. Given the 1.5"x1.5" size of a SNAP detector, co-locating the photodiode next to the detector in a dewar requires that the photodiode be in a small package and operated at SNAP focal plane temperature along with the detector. While the former package size requirement can be fulfilled with a compact design, the latter temperature requirement is difficult because the spectral response of InGaAs photodiodes is temperature sensitive. To address this calibration requirement, I have designed the MICCS system to perform a unique calibration transfer from the NIST calibrated photodiode to other photodiode standards operated under the same laboratory conditions as SNAP focal plane detectors.

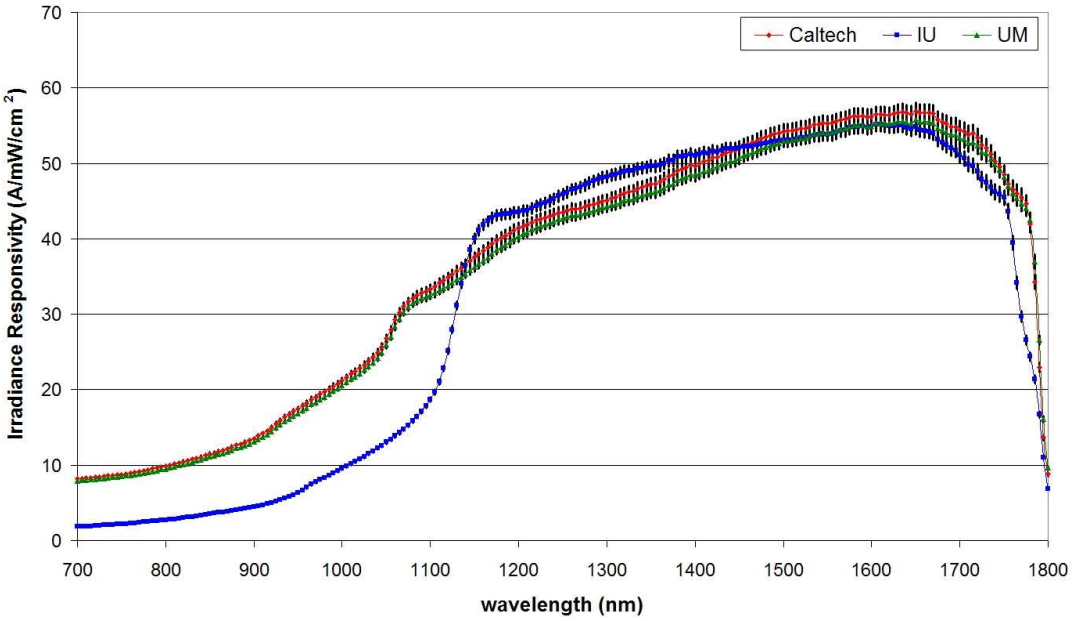

Figure 5.10. The irradiance responsivity calibration for three InGaAs photodiodes at 140K. Two diodes were found to have better response at shorter wavelengths, which was likely an improvement made in the manufacture process by the photodiode vendor. Both of these diodes have been given to the University of Michigan and Caltech for SNAP NIR detector calibration.

The transfer photodiode shown in Figure 5.9 is housed in a copper package that I designed to mount on a cold plate surface in a minimal amount of space. Each package has a black anodized aluminum aperture that can be removed to insert the photodiode. The removable aperture also allows the aperture area to be measured by an external apparatus if necessary. The copper package is electrically isolated from external RF noise with an adhesive silicon pad on its back and plastic mounting screws. Nevertheless, the package maintains good thermal conductivity with the copper stage. I applied epoxy to the photodiode leads through a hole in the copper package to provide for stability and to relieve stress on the leads. The diode packages were also designed specifically for metrology in irradiance measurements by mounting the photodiode active surface 1cm$\pm$1mm from the bottom of the package.

The calibration transfer process from the NIST calibrated photodiode to the transfer diode consists of the measurement of the simultaneous signal ratio between the

two diodes. The ratio of current signals allows for a direct transfer of the NIST irradiance calibration because both diodes receive equal power to their detector surfaces. The ratio measurement is performed with 20 samples every 5nm over the NIST calibrated wavelength range of 700nm to 1800nm. From the ratio samples, I calculated a mean and standard deviation at each data point in wavelength. Further, to account for any temporal variation in the measurement process, I measured the entire wavelength range three times and calculated a weighted mean ratio value from the sample means at each wavelength. The final weighted mean irradiance responsivity value is calculated from

$$Irr_{cal}(\lambda) = \sum_{i=1}^{n_{meas}} \frac{\mu_{s,i}(\lambda)/\sigma^2_{s,i}(\lambda)}{1/\sigma^2_{s,i}(\lambda)} * Irr_{NIST}(\lambda), \tag{5.1}$$

where n_{meas} is the number of sample means at each wavelength, $\mu_{s,i}(\lambda)$ is the mean signal ratio of the two diodes for a single wavelength, $\sigma_{s,i}$ is a standard deviation of the ratio mean, and Irr_{NIST} is the NIST irradiance calibration value. The final error is calculated from

$$\sigma_{cal}(\lambda) = \left\{ \sum_{i=1}^{n_{meas}} \frac{1}{1/\sigma^2_{s,i}(\lambda)} + \sigma^2_u(\lambda) + \sigma^2_{NIST}(\lambda) \right\}^{\frac{1}{2}}, \tag{5.2}$$

where $\sigma_u(\lambda)$ is the measured error in the irradiance uniformity and $\sigma_{NIST}(\lambda)$ is the error in the irradiance calibration from NIST.

Figure 5.10 shows the calibrated irradiance responsivity of three transfer photodiodes at 140K. Two of these photodiodes were supplied to SNAP detector R&D labs at the University of Michigan and the California Institute of Technology. These two diodes were noticeably more sensitive below 1100nm than a similar photodiode at Indiana University. Since the photodiode with poor short-wavelength sensitivity was purchased in 2001, whereas the other two were purchased in 2006, I presume that this difference is due to a refined photodiode manufacturing process by the vendor,

although I cannot rule out production variations in the photodiode responsivities. The error on these calibrated responsivity values is slightly increased from that of the NIST values due to Poisson measurement error, variance in the mean of three scans of the responsivity, and a 0.2% uniformity variation between the photodiode measurement positions.

5.3 Filter Environment Testing

The SNAP SNIa survey calls for a set of nine logarithmically-spaced interference filter transmission functions over the SNAP wavelength range. The filter transmission functions are specifically designed to minimize errors in the K-corrections necessary to correct SNIa photometry for redshift. As discussed in Sections 1.5 and 3.2.2, the calibration of the SNAP bandpasses is crucial to reducing systematic error in SNIa photometry and therefore the derived cosmological parameters. Therefore, this new astronomical filter system must be characterized for use in the SNAP imager.

Interference filters use the reflection of light from multiple thin film layers to accept or reject specific photon wavelengths (Thelen, 1989). Consider a single layer of thin interference film as shown in Figure 5.11. The refractive indices of the media create reflection boundaries for photons passing through the material. Each reflection boundary forces a phase change in the reflected photons that can be described with the function

$$\phi = \frac{2\pi}{\lambda} nd\cos\theta, \tag{5.3}$$

where n is the refractive index of the layer, d is the thickness of the layer, and θ is the photon incidence angle relative to the normal of the layer. This equation for ϕ is known as the angular phase thickness and it describes the interference behavior of photons that are incident on and reflected from a single thin film layer. To illustrate the interference behavior, a common example is the case of total destructive interference, which occurs when photons are 180° out of phase ($\phi = \pi$). Figure 5.11 shows

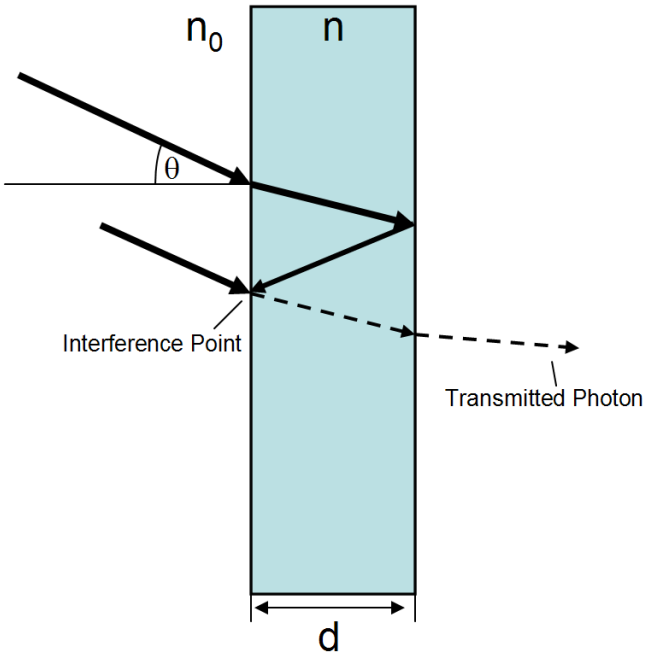

Figure 5.11. A schematic representation of a photon passing through a thin layer of interference film.

the point of interference between an incident photon and a reflected photon on the layer boundary. If $\theta = 0$, total destructive interference occurs at the layer boundary when the layer effective thickness $nd = 1/4\lambda$ (where the photon must travel the layer thickness d twice to get to the interference point). Photon wavelengths that do not interfere at the reflection boundaries are transmitted through the layer.

Equation 5.3 demonstrates that the interference behavior of a film layer is sensitive to (1) the photon wavelength λ, (2) the photon incidence angle θ, and (3) the effective thickness of the film layer nd. For these three variables, the angular phase thickness decreases for longer wavelengths, higher incidence angles, and smaller effective thicknesses. In a multiple layer environment such as an interference filter, many of these layer variables control the total reflection and transmission across the filter bandpass.

To study the effects of a SNAP-like environment on interference filter transmission functions, I chose to investigate the environmental conditions that would change the

effective thickness nd and photon incidence angle θ. I considered three environmental variables that may affect the filter bandpasses on SNAP. First, the filters will be placed in a vacuum environment that will change the refractive index of the environment surrounding the filter. Second, the filters will be held at 140K, which could cause an expansion or contraction of the layer effective thickness. Finally, the SNAP focal plane will have a range of photon incidence angles that could affect the angular phase thickness. All three of these environmental conditions can have a complex effect on an interference transmission function and must be accounted for when characterizing the filters for SNAP.

The MICCS system was designed to measure interference filter transmissions under vacuum at the SNAP focal plane temperature of 140K with photon incidence angles similar to SNAP. This function is realized by mounting a filter in a cold copper holder fixed to the top of a miniature rotation stage (see Figure 5.5). To match the 5° full cone angle from the SNAP pupil, I have constructed a model of the SNAP spider shadow and mounted it on the exit port of the integrating sphere. I then placed the filter and measuring photodiode at a working distance that matches the SNAP 5° full cone angle.

Since the SNAP filters are still being designed, I tested three commercial off-the-shelf interference filters from the Omega Optical Corporation that approximately follow the first three SNAP bandpasses given by Equation 2.1. Table 6.4 summarizes the filter properties of the sample filter set. Figure 5.12 shows the filter transmission functions in the lab environment at room temperature and 0° incidence angle. These sample filters were made from Omega's existing filter designs. Each filter substrate is composed of several elements of wavelength absorbing glass. All three filters have interference layers of dielectric material (ZnS and NaAlF) that were deposited on the substrate through a controlled evaporated process. These filters also have transmission functions that oscillate with wavelength. I refer to these transmission variations

Table 5.1. Filter specifications of effective wavelength, bandpass width, and peak transmission for three filters purchased from Omega Optical Corporation. These filter values were measured in air at room temperature with the MICCS system.

Filter	Vendor Name	λ_{eff} (nm)	FWHM (nm)	Peak Trans. (%)
SNAP BP0	493.7WB	494.8	158.	82.2
SNAP BP1	565AF170-1	568.8	180.	85.5
SNAP BP2	650.5WB	652.8	205.	86.8

as "ripples". After deposition of the layers, the substrate elements are laminated together in a 1" diameter disk encased by a black anodized aluminum ring (Grandy, 2007).

The filters were tested in the following environments: room temperature (∼295K) and atmospheric air pressure; room temperature and vacuum pressure; and 140K and vacuum pressure. During each test, the filter was rotated from 0° to 20° in 5° steps on the optical axis of one of the photodiodes in the MICCS dewar. The transmission curve is measured by taking the current ratio of the two photodiodes with and without the filter in position on the optical axis. In addition to these tests, I also made measurements at normal incidence and temperatures of 135K and 145K to obtain the temperature dependence of the filter bandpass. This data set provides a baseline characterization to study the tolerances required for the final SNAP filter set.

5.3.1 Vacuum Testing

I first measured the transmission differences between an air and vacuum environment for the sample filters. Clearly, any filter that is intended to function in space for the duration of the SNAP mission must be understood in vacuum. Transmission changes between air and vacuum while under vacuum could indicate a filter design that SNAP must avoid to minimize systematic filter errors.

Figures 5.13, 5.14, and 5.15 show the bandpasses of my three sample filters in air and in vacuum measured in the MICCS. The 493.8WB filter and the 565AF170-1

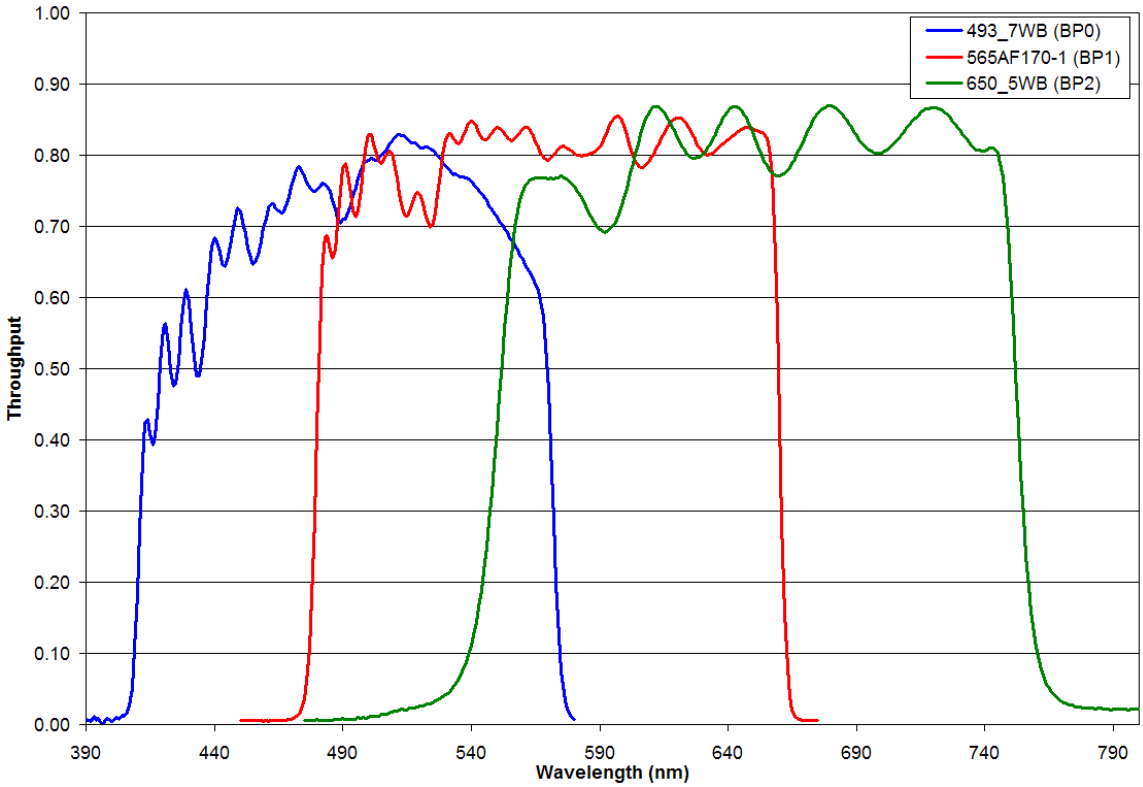

Figure 5.12. The transmission functions for three commercial interference filters. The filter transmission functions were measured by the MICCS in the lab environment at 0° incidence angle.

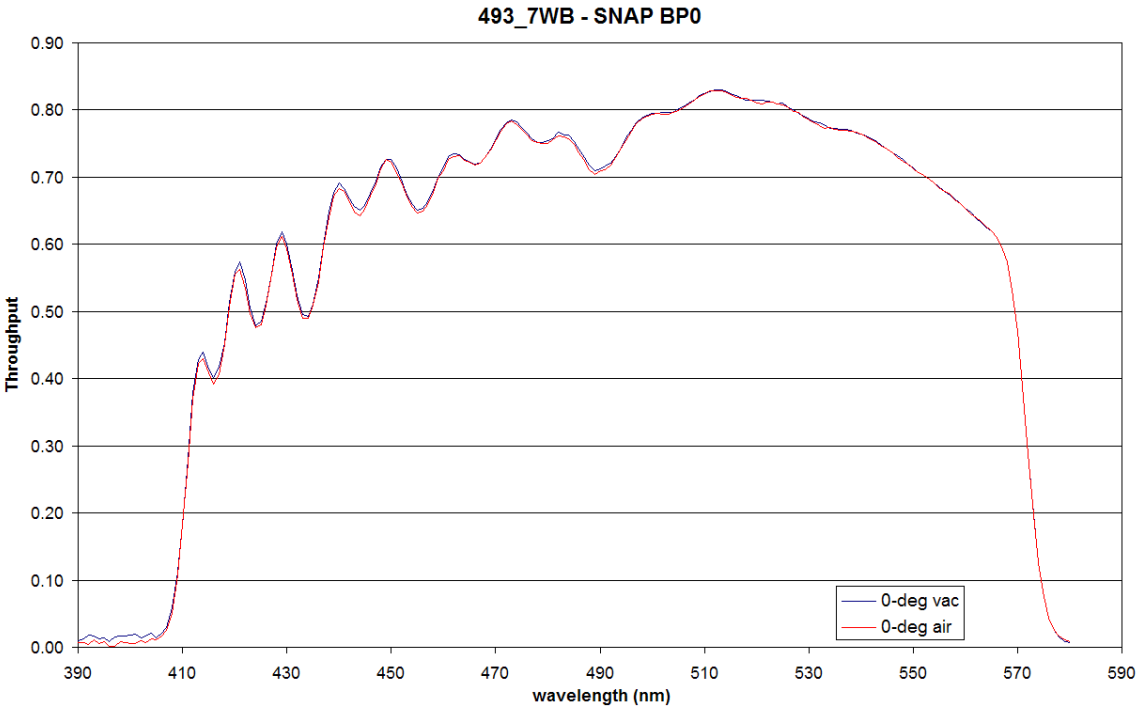

Figure 5.13. The SNAP BP0 filter in air and vacuum.

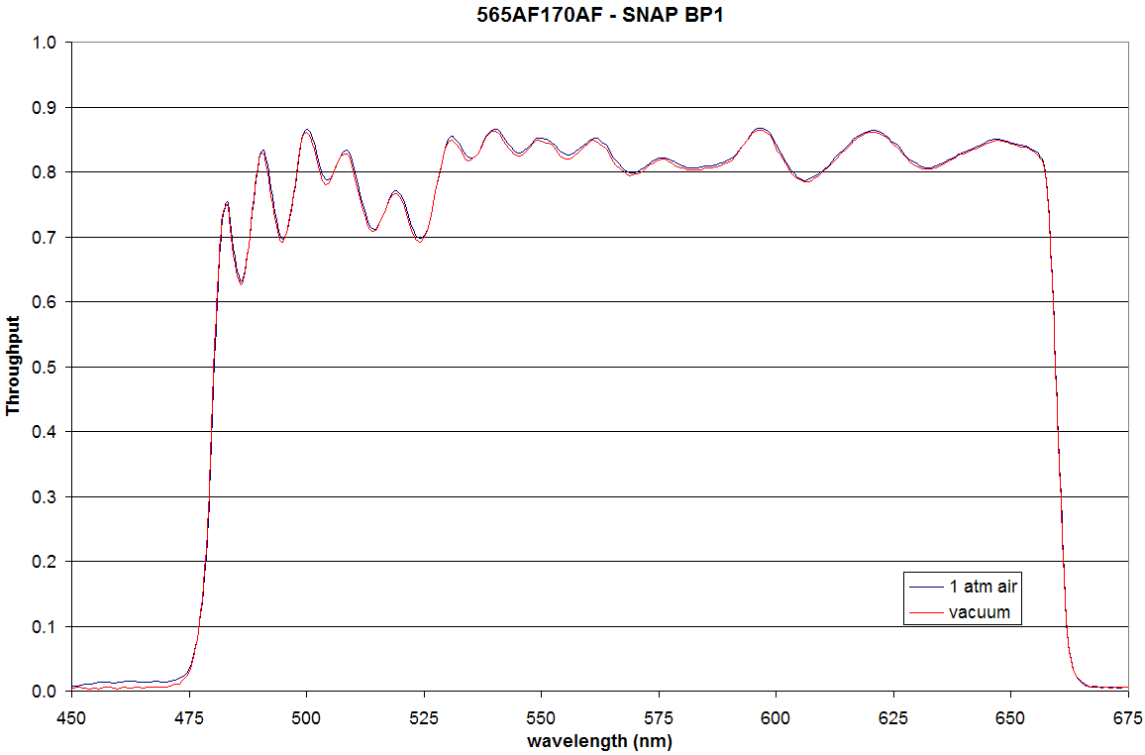

Figure 5.14. The SNAP BP1 filter in air and vacuum.

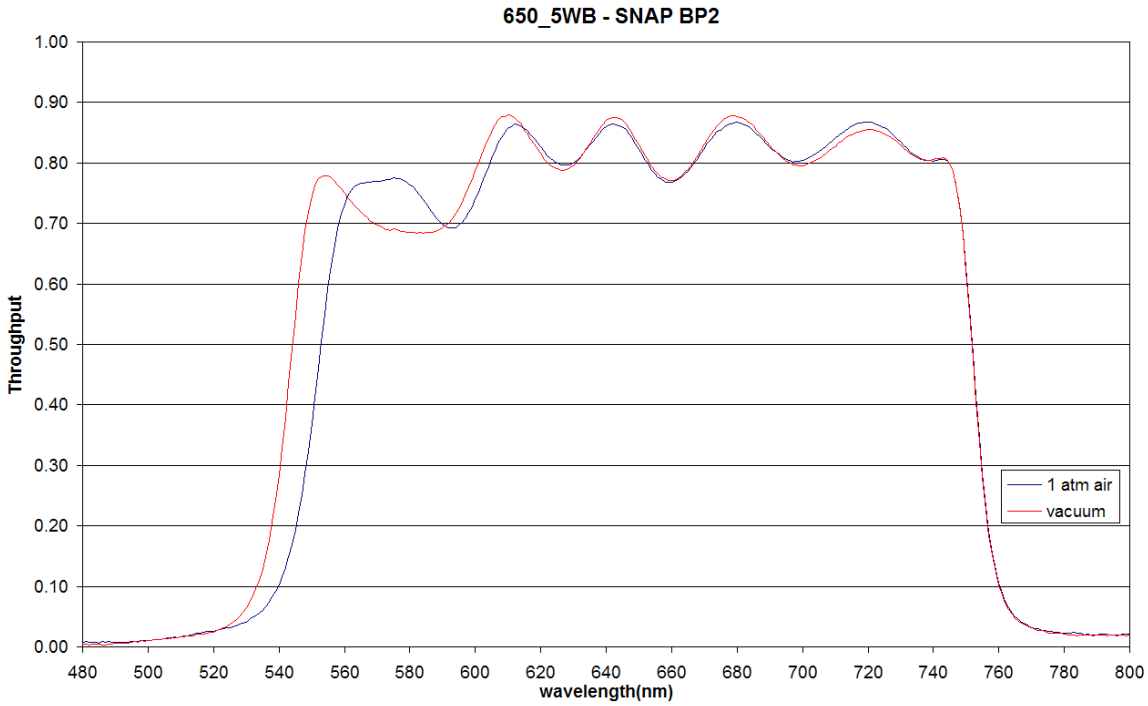

Figure 5.15. The SNAP BP2 filter in air and vacuum. This filter transmission function exhibited significant change due to the variation in atmospheric water vapor.

filter, which approximate the SNAP BP0 and BP1 bandpasses respectively, show no change between air and vacuum. However, the 650.5WB (BP2) filter shows significant transmission variation from air to vacuum. The long-wavelength edge of the 650.5WB filter remained constant, whereas the blue edge shifted to shorter wavelengths. In addition, the width of the filter transmission function "ripple" from 550nm to 575nm changed from air to vacuum.

What causes the BP2 transmission to vary from air to vacuum? Two possible environmental sources that may affect the filter transmission are atmospheric pressure and the water content in the atmosphere. To test which environmental property is responsible, I backfilled the dewar with dry nitrogen up to 1 atm of pressure. Figure 5.16 shows that there is no change in the BP2 filter transmissions from vacuum to the dry nitrogen environment at the 1% level. When I released the nitrogen and cycled the filter back to the air environment, the filter transmission function returned to the air curve shown in Figure 5.15. This result demonstrates that this particular

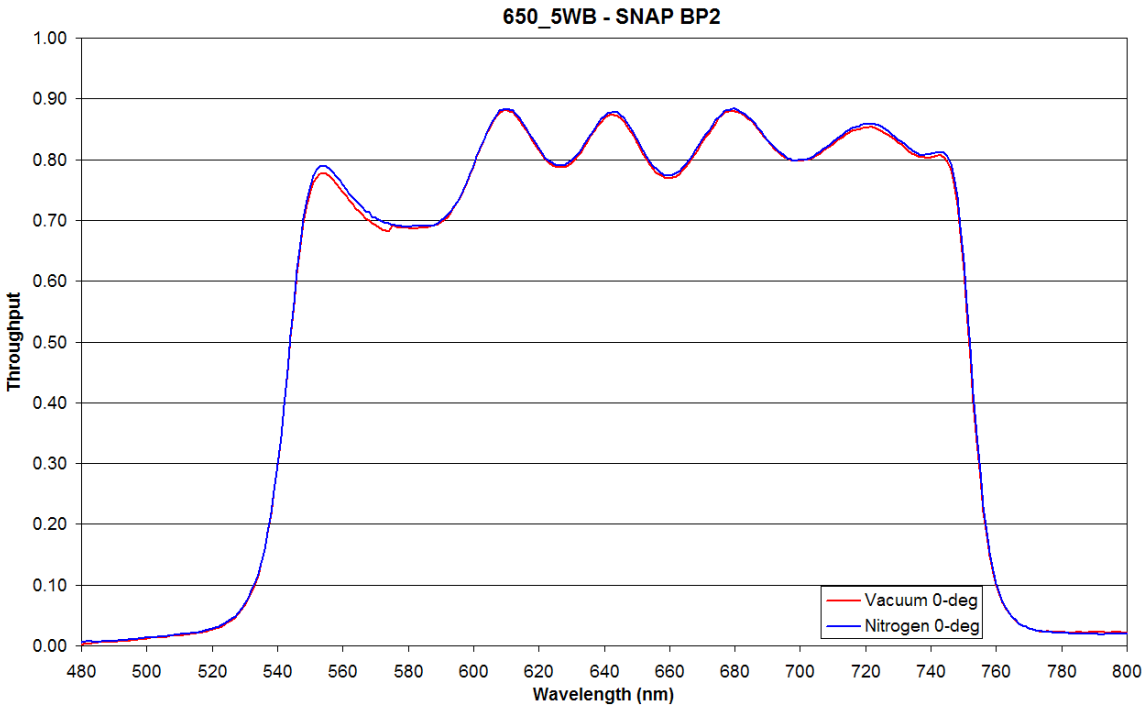

Figure 5.16. The SNAP BP2 filter under vacuum and filled with 1 atm of dry nitrogen. The bandpasses are nearly identical.

filter may be sensitive to humidity. It is possible that this filter has been damaged or the interference layers have not been properly sealed from the external environment. This result demonstrates that the MICCS filter measurements under vacuum are necessary for detecting filter variations that may occur in flight. Further, I recommend that SNAP avoid filters that are sensitive to humidity even if they are characterized in a vacuum environment. Their transmission properties could be prone to change continually during the course of the mission as water molecules slowly evaporate into the vacuum environment of space.

5.3.2 Cryogenic Testing

Once the vacuum testing was complete for each interference filter at room temperature, I then tested the filters at SNAP focal plane temperatures. The test consists of measuring the filter transmissions at 135K, 140K, and 145K. The variation of the filter bandpasses over these temperatures will bracket any possible temperature variation

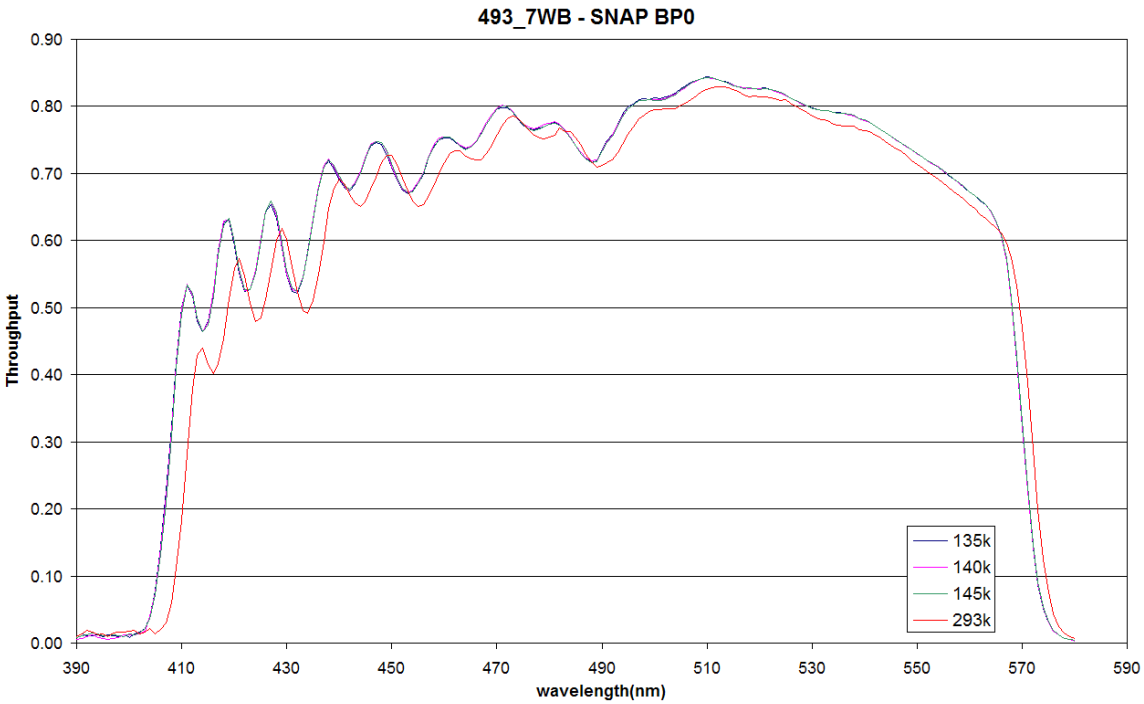

Figure 5.17. The SNAP BP0 filter at room temperature and SNAP temperatures.

on the SNAP focal plane that has been designed to hold 140K to a few millikelvins.

Figures 5.17, 5.18, and 5.19 show the results of varying the filter temperature from room temperature to the SNAP focal plane temperature of 140K. Also shown are the bandpasses as the filter temperature is varied from 135K to 145K. The largest difference in filter transmission resulted from the temperature drop from the ambient room environment to the SNAP thermal environment. This 154K difference in temperature caused the bandpass to shift nearly uniformly towards shorter wavelengths. One possible explanation for this effect is that it is a slight contraction of the substrate and spacing between interference film layers, thereby decreasing the optical thickness between layers. If this happens uniformly for all layers, the wavelengths that satisfy the transmission criteria for the filter will be slightly shorter and the overall shape of the bandpass will remain constant. I expect that when dielectric films are used to control interference filter bandpasses, the bandpass will shift according to the temperature coefficient of the interference material with typical shifts of 0.016nm per °C (Grandy,

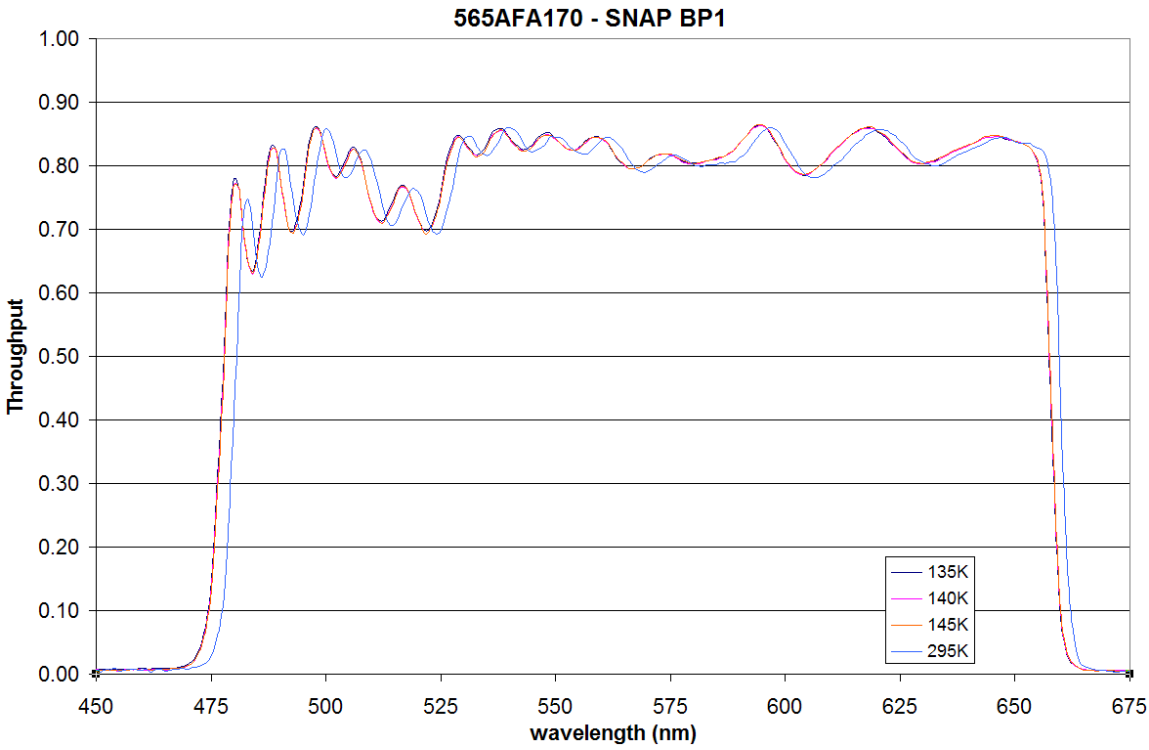

Figure 5.18. The SNAP BP1 filter at room temperature and SNAP temperatures.

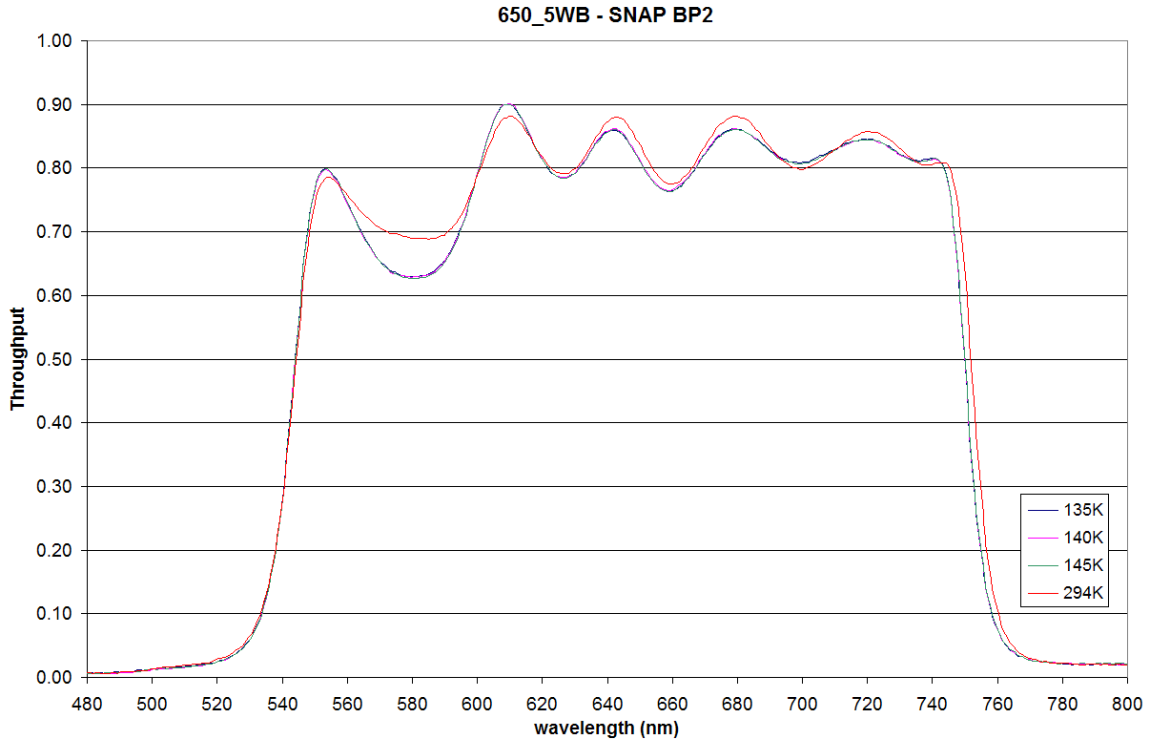

Figure 5.19. The SNAP BP2 filter at room temperature and SNAP temperatures.

2007). My filter measurements are consistent with this figure for the expected shift in bandpass due to temperature.

The change in the interference filter transmission with temperature seems to be largely negligible over a 5K temperature variation around the mean value of 140K. This result leads me to conclude that interference filters are insensitive to small temperature differences, and the millikelvin temperature tolerance in place on the SNAP focal plane will be more than sufficient to hold the bandpasses constant. However, there is an appreciable difference in the bandpass between room temperature and SNAP temperature even though the change is a generally a small shift in the bandpass. I recommend that the filter characterization for SNAP be done at the 140K temperature to account for shifts in the filter bandpass.

5.3.3 Angle of Incidence

Another important characterization that must be carried out for the SNAP interference filters is the transmission properties as a function of incidence angle. As discussed at the beginning of Section 5.3, an interference filter uses constructive and destructive photon interference imposed by thin dielectric film layers to shape the filter's transmission. A primary parameter that controls the filter transmission function is the angular phase thickness of the interference layers. One way to change the angular phase thickness is to increase the photon incidence angle away from normal incidence (see Equation 5.3). Since the SNAP focal plane will have photon incidence angles that are off-normal, the accurate characterization of the filter transmission functions with respect to incidence angle will be essential to precise SNAP photometry.

The primary effect of changing the photon incidence angle on an interference filter is a shift of the filter transmission function to shorter wavelengths. Other effects can also be present as well, including a broadening of the bandpass and a decrease in the overall transmission[2]. Further complicating the filter transmission behavior is

[2]I show a parameterization of these global bandpass effects in Chapter 6.

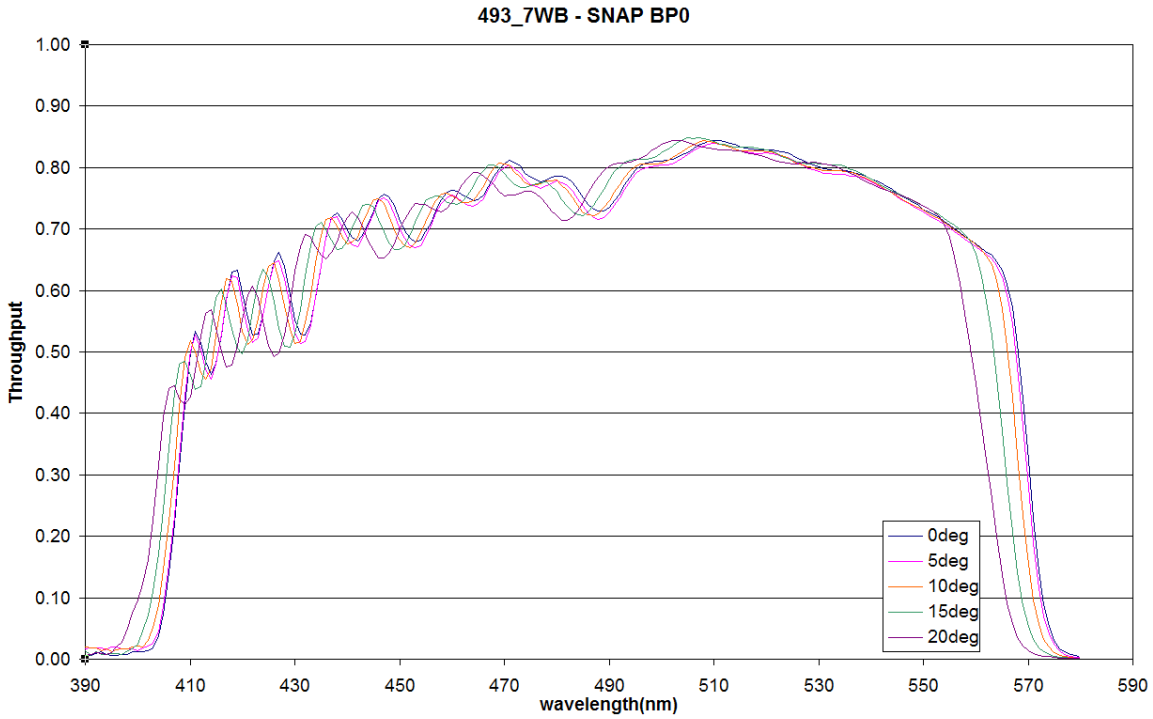

Figure 5.20. The SNAP BP0 filter at a range of incidence angles from 0° to 20° in 5° increments.

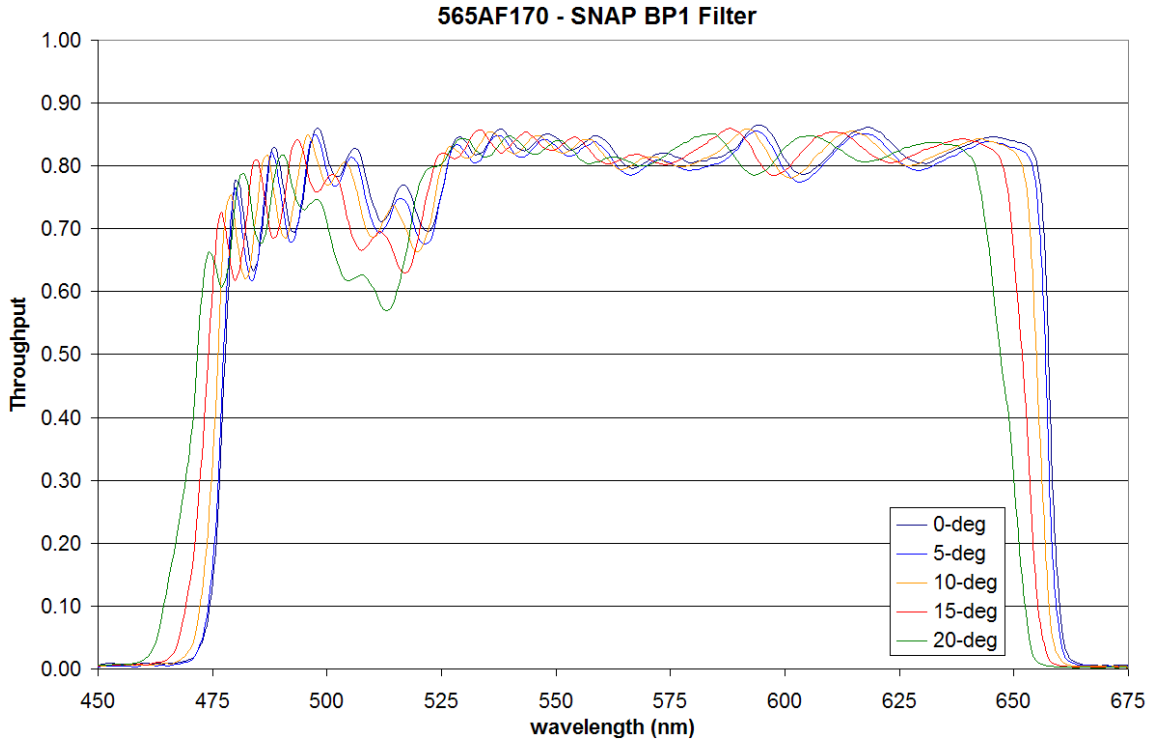

Figure 5.21. The SNAP BP1 filter at a range of incidence angles from 0° to 20° in 5° increments.

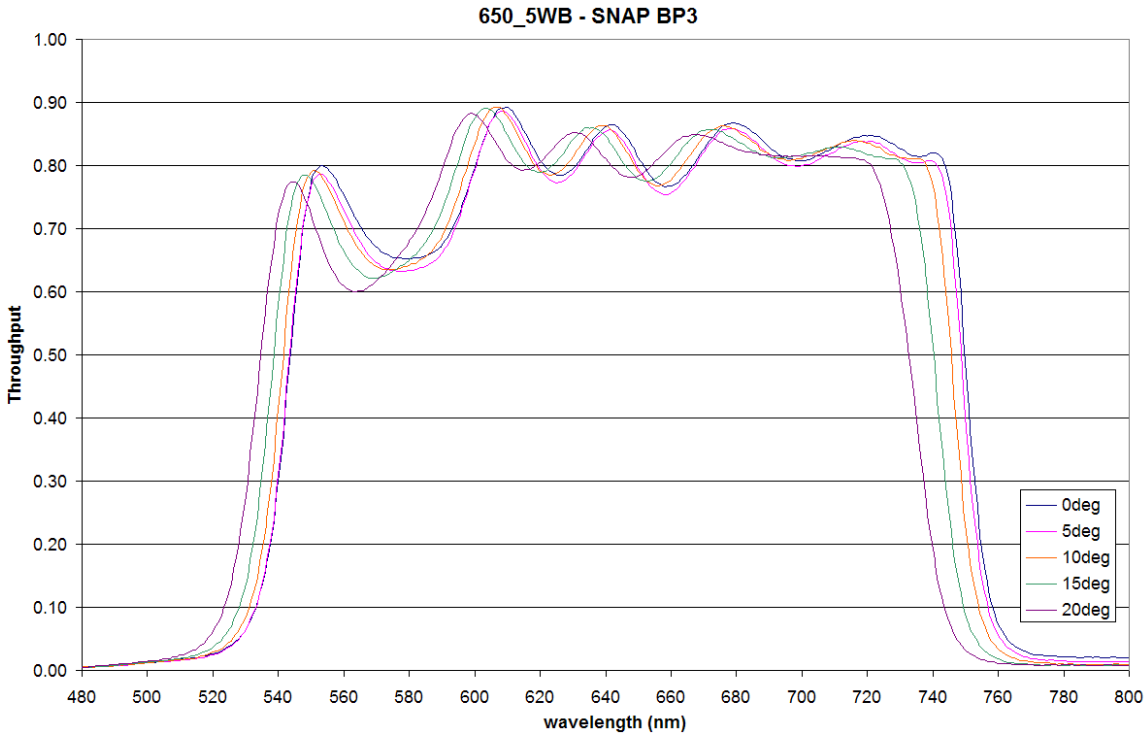

Figure 5.22. The SNAP BP2 filter at a range of incidence angles from 0° to 20° in 5° increments.

the variation in the interference film thickness, likely due to tolerance error, which contributes to the "ripples" seen in the sample filter transmissions. Figures 5.20, 5.21, and 5.22 show the behavior of the filters over a range of angles from 0° to 20° in 5° increments. The filters display a complex change in their bandpasses, including shifts of the entire filter transmission function, shifts of ripple positions and strengths, and broadening of the filter bandpass. The aggregate effect of these multiple variations have important implications for the calibration of filters on the SNAP focal plane.

5.3.4 Filter Bandpass Interpolation

Given the SNAP filter layout shown in Figure 2.4 and photon incidence angles shown in Figure 4.7, each SNAP filter will have a bandpass variation due to its position on the focal plane. The most significant photon incidence angle effect is due to the filter's radial position off the optical axis. Incoming photons from the SNAP telescope

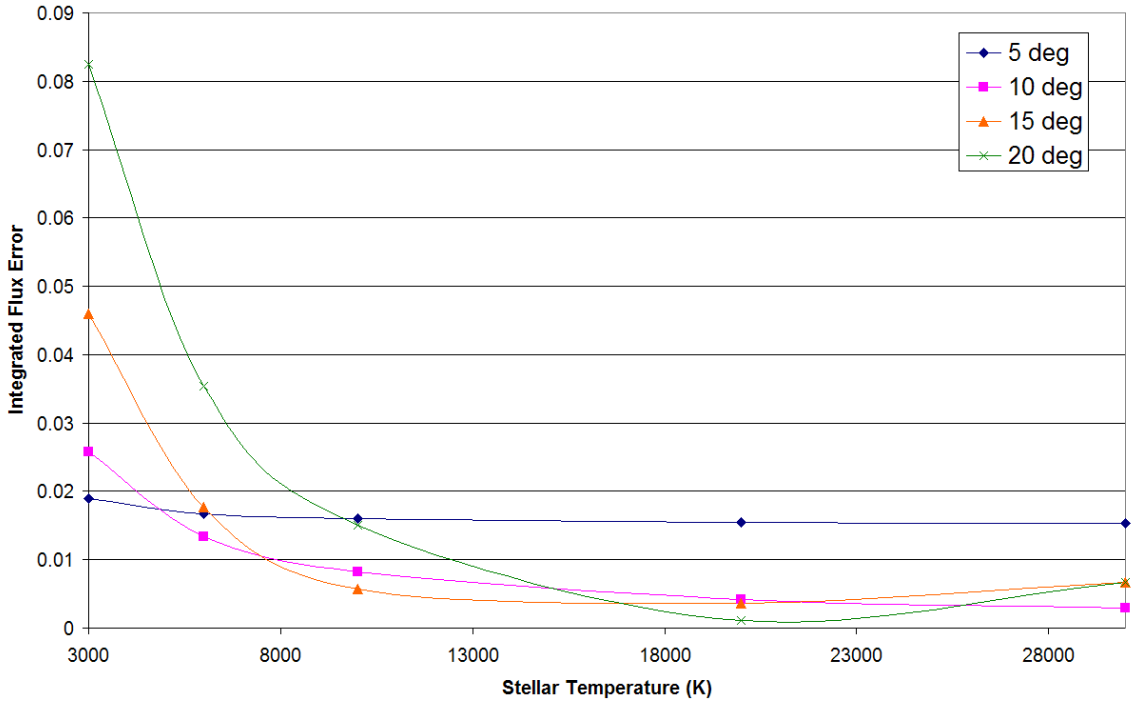

Figure 5.23. The integrated flux error in the BP1 bandpass for a range of blackbody temperatures. The flux error is calculated for each filter incidence angle relative to the bandpass at normal incidence.

will strike the filters at an incidence angle that can range from 5° to 20°, depending on the radial position on the focal plane. The measurements of the three sample SNAP filters over these angles showed that the transmission function variations are complex, particularly when ripples are present. These variations can cause significant systematic error in the SNAP photometry across the focal plane.

To quantify the photometric error due to off-axis position, I have calculated the integrated flux in the BP1 measured bandpass at 0° incidence for a range of blackbody temperatures. I then calculated the integrated flux for the same temperatures for the measured BP1 bandpasses at 5°, 10°, 15°, and 20°. An estimate of the photometric error is the deviation in the integrated flux values from off-normal incidence to normal incidence angle. Figure 5.23 shows the error in the BP1 integrated flux for blackbodies of differing temperature if the filter transmission is wrongly assumed to be at normal incidence. The largest flux error is 8% for cool blackbody temperatures

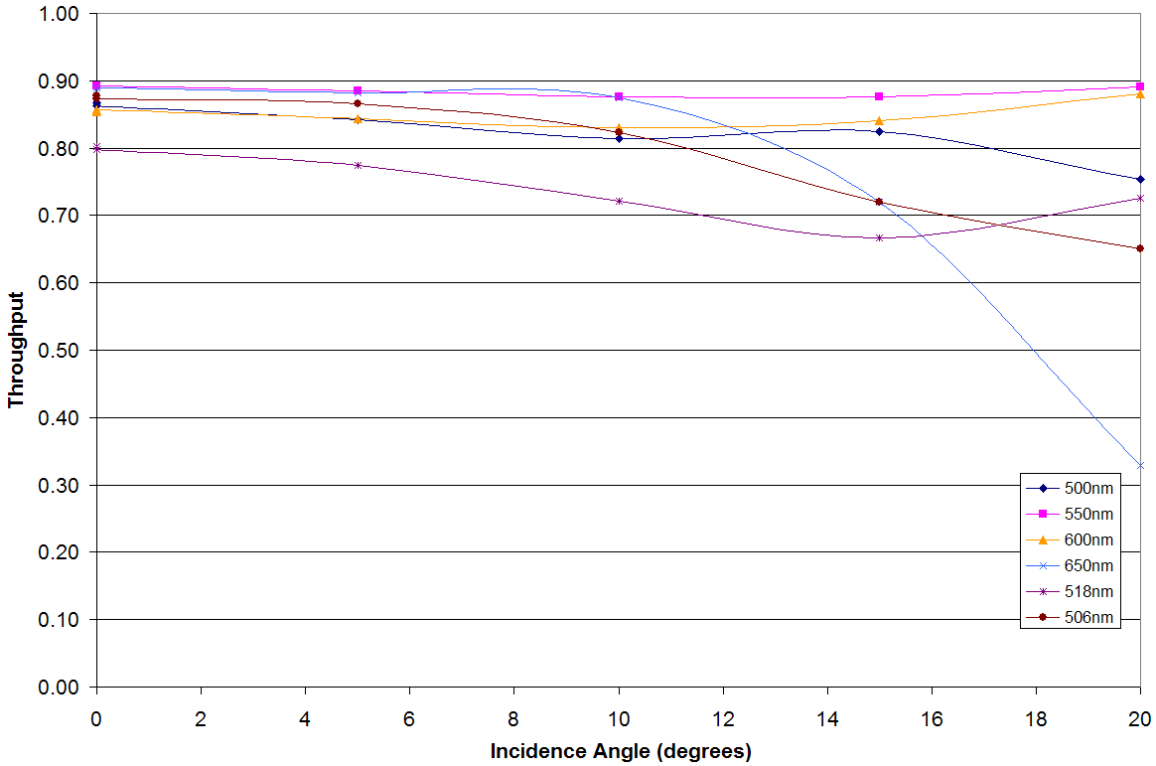

Figure 5.24. The filter transmission as a function of angle for selected wavelengths of the BP1 filter. The changes in transmission for these wavelengths are smooth and can be fit with a simple spline. Interpolated filter bandpasses at intermediate angles can then be constructed from the spline functions for each filter wavelength.

at the highest incidence angles. The large errors for cool stars are due to the rapid flux decrease on the exponential side of the blackbody curve and shifting of the filter transmission function towards shorter wavelengths. The figure demonstrates that the filters must be characterized with angle in order to achieve the 2% photometric error accuracy required by SNAP. Furthermore, since an SNIa can occur at any random radial position in the SNAP camera annulus, each SNIa light curve could have its own set of unique filter transmission functions in all nine SNAP filters. Since fitting of SNIa light curves is dependent on the accurate knowledge of the filter transmissions, these systematic variations across the focal plane must be calibrated out.

While the filter characterization process could conceivably measure each filter transmission function at very finely spaced steps in angle, the process would be incredibly tedious for the large number of SNAP focal plane filters. The MICCS system is capable of measuring a single filter at five different filter angles in 8 hours, including baseline measurements of the photodiodes and measuring the normal position angle of the filter. The hold time for the MICCS dewar is approximately 10 hours, and so exceedingly fine measurements with angle would require multiple fills of the dewar system.

To avoid finely spaced angle measurements, I have developed a simple interpolation scheme based on my filter data set. This interpolation compares the change in transmission as a function of angle for each individual wavelength of the filter and calculates an expected bandpass for a given incidence angle. Figure 5.24 shows the filter transmission as a function of angle for selected wavelengths of the BP1 filter. This figure shows that the transmission variation for the selected wavelengths is relatively smooth over the SNAP range of angles. This fact can be exploited by fitting a spline function to the transmission variation as a function of angle for each wavelength in the filter transmission function. Once these splines are fit to the data, the filter transmission function can be interpolated for any incidence angle within the

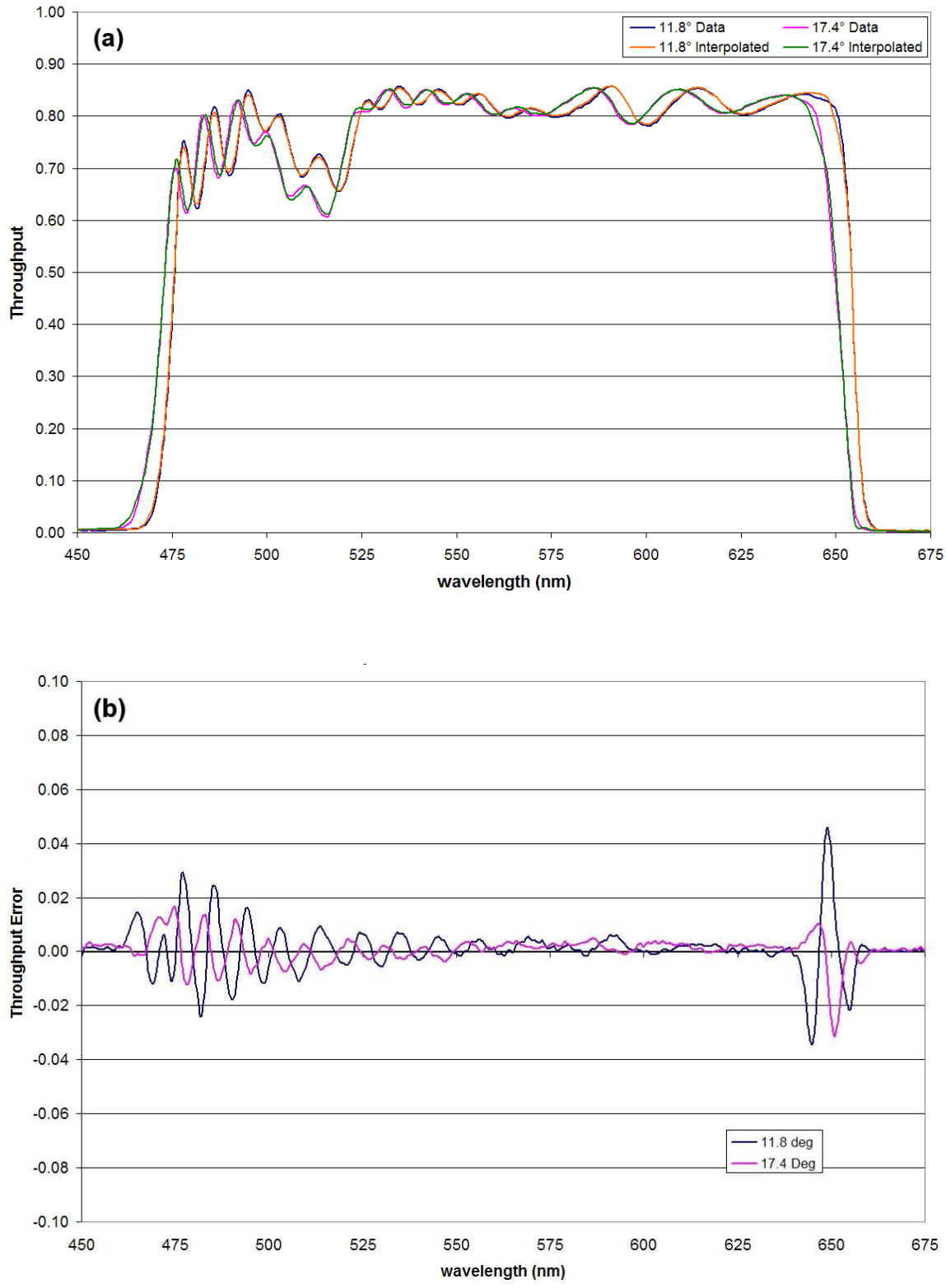

Figure 5.25. (a) The measured and interpolated SNAP BP1 filter bandpass at incidence angles of 11.8° and 18.4° and (b) the difference between the data and intepolation .

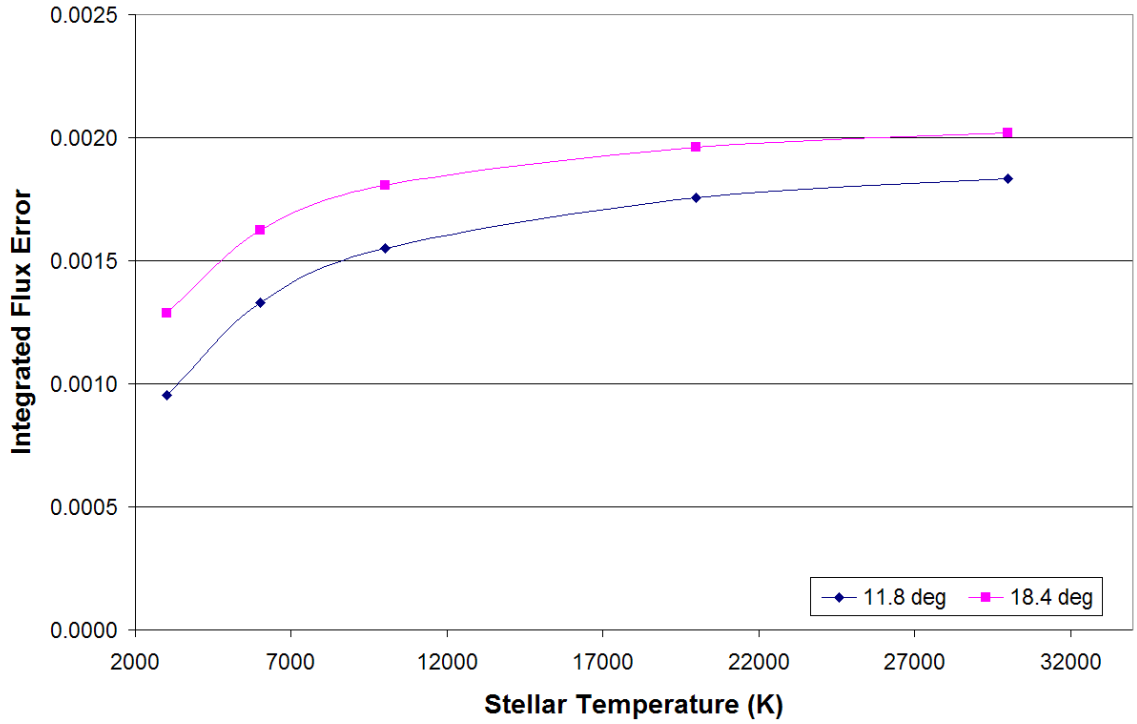

Figure 5.26. Integrated flux error over the interpolated BP1 bandpass at incident angles of 11.8 and 18.4 degrees. The largest error is 0.2% in integrated flux at the 18.4 degree angle for all stellar temperatures, which is over an order of magnitude improvement from filter bandpasses that have not been calibrated for filter angle (Figure 5.23).

measured range of angles.

I tested the accuracy of this interpolation process by measuring two intermediate filter angles and comparing the data to the interpolated bandpass. The accuracy of the interpolation is calculated as the difference in transmission between the measured bandpass and the calculated bandpass. The Figure 5.25(a) shows an overlay of the measured and interpolated bandpasses and the bottom graph illustrates the difference between the bandpasses. The error in the interpolation is largest where the filter bandpass is changing most rapidly, particularly around 530nm ($\sim$2% variation) and at the red edge of the bandpass at 650nm ($\sim$4% variation). These interpolation errors exist over a small fraction of the bandpass and generally oscillate around the true, measured transmission. Using the same calculation of integrated flux error

for a range of blackbody temperatures in Figure 5.23, the integrated flux error of the interpolated filter transmissions relative to the measured transmission is shown in Figure 5.26. The largest error for the integrated flux is 0.2% for the hottest blackbody temperatures, which is a factor of 40 improvement in flux calibration for filter transmissions without incidence angle characterization. This level of precision in the broadband transmission should be sufficiently accurate for calibrating out the angle dependence of bandpasses onboard SNAP.

CHAPTER 6

Filter Transmission Tracking

To achieve its prime scientific objective of measuring cosmological parameters Ω_M, w_0, and w_a, the SNAP mission requires a precision calibration of SNIa peak magnitudes. The baseline SNAP mission, which uses multiband photometry to compare local and distant supernovae, specifies its calibration requirement as the measurement of the ratio of the fluxes in two broadband filters with 2% error or better. This error will include the calibration error of the filter transmission. As I have discussed in Chapter 5, the filter transmission as a function of wavelength will be characterized pre-launch with a system similar to the MICCS. I have shown that the bandpasses of interference filters are sensitive to temperature, pressure, and photon incidence angle. These pre-launch characterizations, however, could change during a multi-year space mission. Further, it is possible that the filter transmission functions will change in ways that are not yet known. It is essential to accurately monitor the filter throughput during the course of the SNAP mission in order to correct the photometry for these effects.

In this chapter, I will study methods that monitor filter transmission functions onboard SNAP. I will use techniques that artificially introduce changes to a filter transmission function with the purpose of determining the changes with different calibration methods. Further, I will also study two different filter function shapes to test if these calibration methods are precise regardless of the transmission function shape. The filter transmission errors from these studies will be propagated through

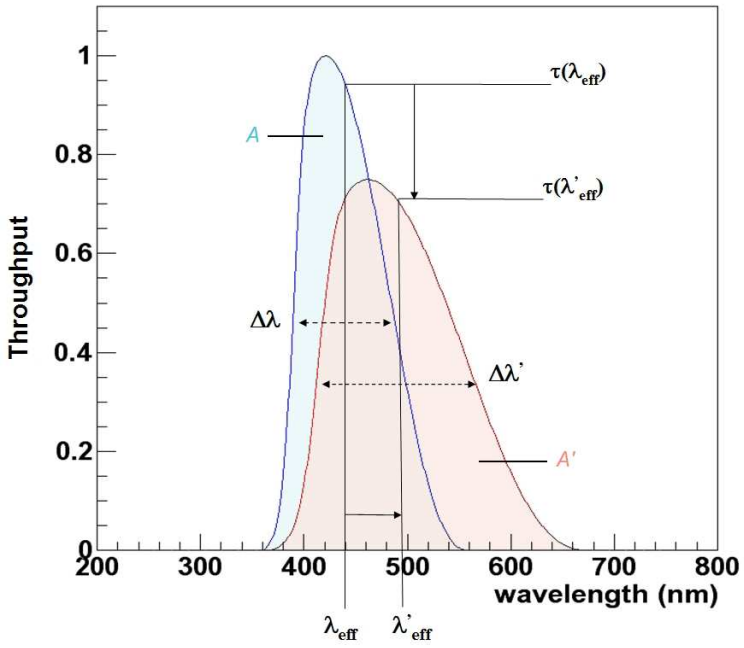

Figure 6.1. Parameterization of a filter transmission function for an analytic Bessel B filter. The effective wavelength of the filter is denoted λ_{eff}, the transmission at the effective wavelength is $\tau_(\lambda_{eff})$, the bandpass width is $\Delta\lambda$, and the total throughput of the filter is A.

to the SNAP-determined cosmological parameters in Chapter 7.

6.1 Filter Parameterization

A central point in understanding how to track filter changes is describing how the filter transmission functions can actually vary. Based on the MICCS filter data presented in Chapter 5, I have shown that transmission functions can change in several ways. The most tractable of these changes are those made to the global filter transmission properties, such as effective wavelength of the filter, width of the bandpass, and overall normalization of the transmission function. A way to study the requirements for monitoring filter transmission functions is to introduce artificial changes to these global filter properties[1].

To study how to track filter throughputs, I assume that filter transmission func-

[1]The term "global filter properties" refers to the properties that affect all wavelengths of the filter transmission function, not just a selected wavelength range of the transmission function.

tions can be parameterized with simple parameters and these parameters can accurately quantify global filter transmission properties. Figure 6.1 shows the three parameters I used to describe the filter variations on a simulated Bessel B filter. The first filter parameter is effective wavelength, which is defined as:

$$\lambda_{eff} \equiv \frac{\int \lambda \tau(\lambda) d\lambda}{\int \tau(\lambda) d\lambda}, \tag{6.1}$$

where $\tau(\lambda)$ is the transmission function of the filter. The effective wavelength is the weighted mean wavelength of the filter transmission. The second global filter parameter is the width of the bandpass. Common methods to calculate the width of a filter transmission function assume a Gaussian shape parameter of full width at half maximum (FWHM). My parameterization is slightly modified from FWHM, using the transmission at the effective wavelength instead of the maximum transmission as the central value from which to calculate the width. This generalizes the bandpass width calculation for filters that are not symmetric about the maximum transmission. I calculate the width of the bandpass using

$$\Delta\lambda = (\lambda_{\frac{1}{2},l} - \lambda_{\frac{1}{2},s}), \tag{6.2}$$

where $\lambda_{\frac{1}{2}}$ is defined as the wavelength at which $\tau(\lambda_{\frac{1}{2}}) = \tau(\lambda_{eff})/2$. The l and s subscripts denote the long and short wavelength edges of the filter bandpass. Finally, the third global filter parameter is the integrated throughput of the filter function. For simplicity, I approximated the integrated throughput using a measure of the area under the transmission curve

$$A = \Delta\lambda * \tau(\lambda_{eff}). \tag{6.3}$$

A benefit of implementing the A parameter is that it breaks the degeneracy be-

tween $\tau(\lambda_{eff})$ and $\Delta\lambda$ when calculating fits to varied transmission functions . This approximation for the integrated throughput was used in my initial simulations of tracking filter transmission curves in Section 6.2[2]. Using this parameterization, I will apply variations to the global filter parameters to create different filter transmission functions.

6.2 Simulating Sources for Filter Tracking

To study methods that track a filter function variations (or "drifts"), I looked at three different types of input light source spectra that could be used onboard SNAP. I simulated each spectrum and passed each through the original transmission function and a modified transmission function. I modeled measurements of the integrated flux through the filter using

$$F(\lambda_{eff}, \Delta\lambda, A) = \int S_\lambda * \tau_\lambda(\lambda_{eff}, \Delta\lambda, A) d\lambda, \tag{6.4}$$

where $S(\lambda)$ is the input light source function and $\tau_\lambda(\lambda_{eff}, \Delta\lambda, A)$ is the parameterized filter transmission function. I then applied a variation to the original filter function to create a modified filter function $\tau_\lambda(\lambda'_{eff}, \Delta\lambda', A')$ and then calculated the integrated flux for the modified filter. I then used the difference in the integrated fluxes from the original and modified filter transmission functions to determine how the transmission function had changed. For a single source spectrum passed through the filter transmission functions, the difference in flux is formed using

$$\Delta F^2 = [F(\lambda'_{eff}, \Delta\lambda', A') - F(\lambda_{eff}, \Delta\lambda, A)]^2. \tag{6.5}$$

[2]In Section 6.3.3.1, I will revisit the A parameter for more accurate use with filters measured from the MICCS system.

With this formulation, I performed a search of parameter space over the three global filter parameters using NAG software routines (NAG, 2002). The best fit values for the filter parameters are returned when ΔF is at its minimum value. I then compared the best fit filter parameters to the perturbed filter parameters. The fractional error in the filter parameters gives a measure of the accuracy that can be achieved with the input light source.

Using a model of the SNAP filter set, I performed this calculation on four of the nine filters covering the SNAP wavelength range. The baseline SNAP filter set is based on an analytical form for the Bessel B-band filter. The filter transmission function is calculated from 360nm to 600nm using the empirical relations

$$\tau(\lambda) = (1 + \exp(-0.17 * (\lambda - 390)))^{-1} + \left(\frac{0.006*(\lambda-390)}{30}\right), 360 < \lambda < 420,$$
$$\tau(\lambda) = \left[\cos(\frac{1.5708*(\lambda-420)}{140})\right]^{2.4}, 420 <= \lambda < 600, \quad (6.6)$$

where λ is in nanometers and $\tau(\lambda) = 0$ for all other wavelengths. Using this transmission function as a template, the SNAP filter set is calculated from Equation 2.1. I modified the filter parameters for each filter with variations using the form

$$\begin{aligned} \lambda'_{eff} &= \lambda_{eff} + \Delta\lambda_{eff}, \\ \Delta\lambda' &= \alpha \times \Delta\lambda, \\ A' &= \beta \times A. \end{aligned} \quad (6.7)$$

For my initial simulation study, I introduced modest variations of $\Delta\lambda_{eff} = 0.25$nm, $\alpha = 1.01$, and $\beta = 1.01$ to test the accuracy to which different light sources can determine variations in the global filter parameters.

The first source that I studied was a stellar source with a systematic flux error. One of the most accurate stellar source standards in use today is that of the HST

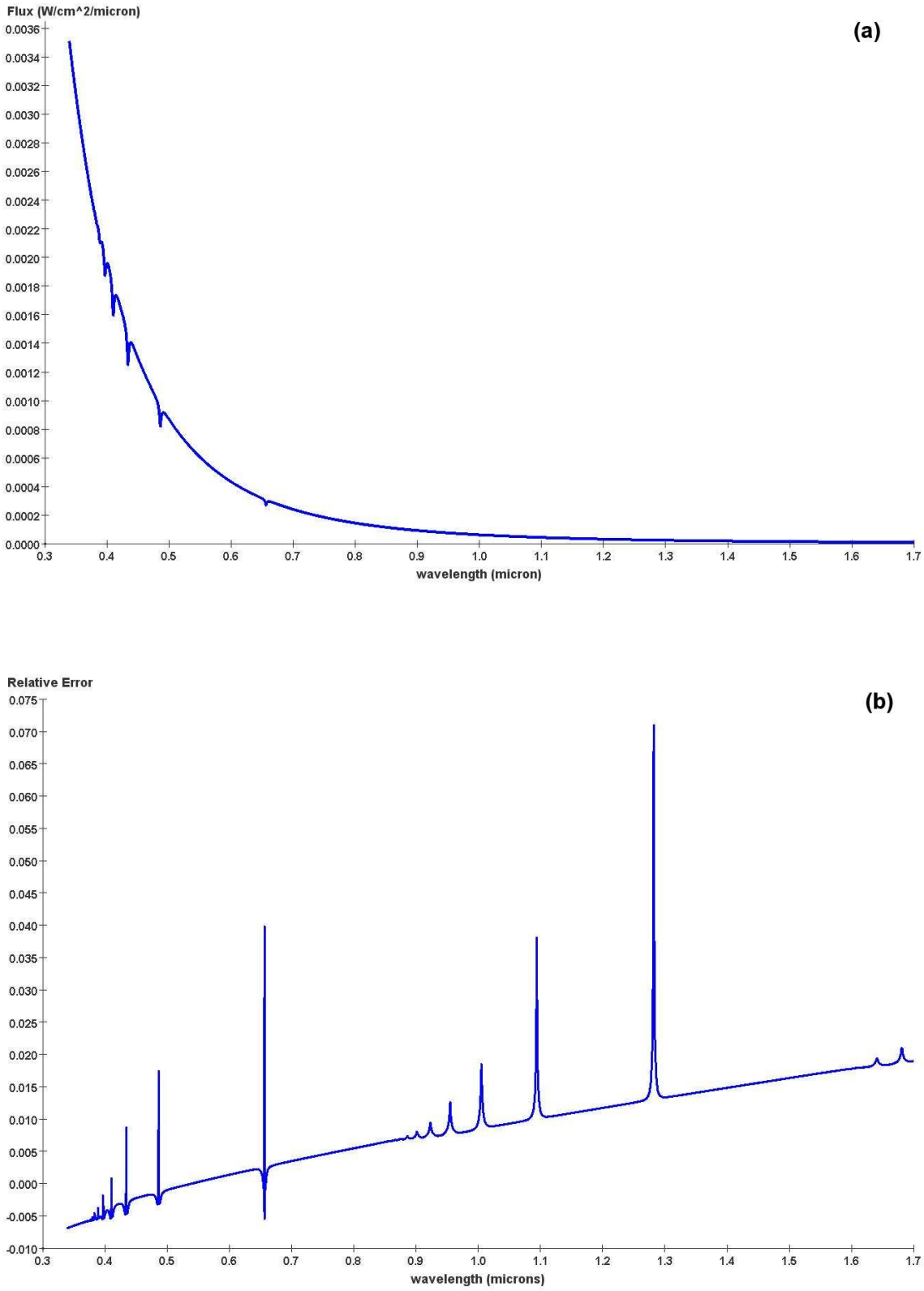

Figure 6.2. (a) The NLTE model flux spectrum of the white dwarf G191B2B and (b) the systematic error between LTE and NLTE stellar models.

white dwarf G191B2B (Bohlin, 2007). Figure 6.2 shows the Non-Local Thermodynamic Equilibrium (NLTE) atmospheric flux model of G191B2B and the systematic errors between the NLTE flux model and a Local Thermodynamic Equilibrium (LTE) flux model for the star. The systematic error between the models increases in the infrared due to a lack of high precision NIR observations to normalize the flux spectrum (Bohlin, 2002). To introduce this systematic error to the integrated fluxes in Equation 6.5, I calculated the NLTE flux with the original filter transmission function and the LTE flux with the modified filter transmission function.

Table 6.1. Filter parameters fit from the white dwarf G191B2B.

Filter	λ_{eff} (nm)	$\frac{(\lambda_{eff}-\lambda'_{eff})}{\lambda_{eff}}$ (%)	$\frac{(\Delta\lambda-\Delta\lambda')}{\Delta\lambda}$ (%)	$\frac{(A-A')}{A}$ (%)
1	420	6± 5	3± 9	34± 13
2	656	9± 2	71± 5	18± 2
3	882	13± 1	97± 2	13± 1
4	1187	17± 1	95± 10	11± 1

Table 6.1 shows the results of determining filter drifts using G191B2B. These results show the percentage difference between the input and best fit parameters of the modified filter. The single white dwarf flux source with systematic flux error does not recover the modified filter parameters, particularly in the NIR. The white dwarf spectrum is also fairly flat in the NIR, so small variations in the filter parameters are difficult to determine when there is very little change in the integrated stellar flux.

In my second calculation, I used the spectrum of a calibrated Quartz-Tungsten-Halogen (QTH) lamp. The QTH lamp has roughly a blackbody spectrum with a temperature of 3000K. These lamps were used on HST and are a common laboratory irradiance sources.

The results of the QTH lamp source simulation show that the lamp is nearly a 100 times more accurate at determining the effective wavelength and bandpass width parameters than a single white dwarf source. Both the modified wavelength effective and the modified width of the filter were recovered with less than 1% error. This im-

Table 6.2. Filter parameters fit from a QTH lamp source.

Filter	λ_{eff} (nm)	$\frac{(\lambda_{eff}-\lambda'_{eff})}{\lambda_{eff}}$ (%)	$\frac{(\Delta\lambda-\Delta\lambda')}{\Delta\lambda}$ (%)	$\frac{(A-A')}{A}$ (%)
1	420	0.15± .01	0.61± .02	7.9± .1
2	656	0.15± .00	0.33± .01	4.2± .0
3	882	0.22± .04	0.31± .02	13.7± .1
4	1187	0.34± .35	0.28± .03	24.4± .1

provement is due to the fact that the 3000K blackbody has a greater change in its flux over the entire 300-1700nm wavelength range than a white dwarf spectrum, providing leverage in determining changes in the filter function. However, the determination of the total filter transmission A using a QTH source was not improved over that of the white dwarf model determination. A possible explanation for this effect is that the smooth form of a blackbody spectrum does not provide the required leverage to determine the filter parameter drifts to $< 1\%$. Further, it is important to note that a QTH lamp has approximately the same blackbody temperature as a cool stellar atmosphere, which implies that a late type stellar source will suffer from the same decreased leverage in determining the filter parameters in the NIR. The results of the white dwarf and QTH input spectrum calculations suggest that spectral sources which vary rapidly with wavelength provide the most leverage in determining filter parameters from integrated fluxes.

Table 6.3. Filter parameters fit from three LEDs per filter bandpass.

Filter	λ_{eff} (nm)	$\frac{(\lambda_{eff}-\lambda'_{eff})}{\lambda_{eff}}$ (%)	$\frac{(\Delta\lambda-\Delta\lambda')}{\Delta\lambda}$ (%)	$\frac{(A-A')}{A}$ (%)
1	420	0.± .007	0.± .1	0.± .07
2	656	0.± .005	0.± .09	0.± .05
3	882	0.± .001	0.± .03	0.± .02
4	1187	0.± .004	0.± .1	0. ± .03

For my final input light source, I used three LEDs that cover the transmission function of each filter. Each LED has the characteristics of commercial LEDs from a vendor catalog and I placed the simulated LED spectra at both edges and the

center of the filter function. The results of using three LEDs as an flux source are shown in Table 6.3. The LEDs recover all three perturbed filter function parameters with nearly perfect precision ($\ll$ 1% error). The varying colors of the sources as well as their semi-narrow bandpasses allow modest changes in the filter transmission functions described in Equation 6.7 to be determined at a high precision.

These simple simulation studies suggest that using a broadband flux source such as a QTH lamp or a well known white dwarf will not be sufficient to determine variation in the filter bandpasses in orbit. Using narrowband light sources gives leverage in determining the filter transmission function. This result suggest that I should study LEDs as calibrating light sources for tracking variations in filter transmission functions.

6.3 Measurements of Filters Using LEDs

The results of Section 6.2 suggest that LEDs could provide an excellent calibration source for tracking filter transmission functions. However, the implementation of LEDs into a real calibration system that can measure actual filter transmission functions must be studied. In this section, I will use LEDs to make measurements of filter transmission functions that have been changed from their original shape. These changes are introduced by varying the photon incidence angle on the filter (see Section 5.3.3 for discussion on the effect of incidence angle on filter transmission functions). By treating these changes as unknown variations to a SNAP filter transmission function, I can test the accuracy of calibration methods that recover the modified transmission function using LED light sources.

The filter tracking tests using LEDs presented here are not intended to simulate a change in the filter incidence angle on the SNAP focal plane alone. More generally, this test was intended to simulate unknown variations in the filter transmission functions. By simply varying the filter incidence angle, I can investigate different

calibration techniques to measure filter transmission functions in the lab.

6.3.1 Instrumentation

As shown in Section 6.2, the narrowband emission of LEDs could in principle be used to monitor changes in the SNAP filter transmissions. To study this calibration method in a laboratory setting, I devised an experiment where I could modify the throughput of an interference filter and track the transmission changes with LED illumination. I changed the interference filter transmission function by simply turning the filter at an angle relative to a collimated light beam. The net effect of varying the incidence angle shifts the bandpass towards the blue, slightly decreases the overall transmission, and broadens the filter bandpass.

I made measurements of a filter transmission function at varying angles of incidence using an LED light source with two different measurement instruments. Each instrument used the same techniques, but the availability of each instrument required me to switch between them. The first instrument was a modification to an existing LED measurement system and is shown in the sections in Figure 6.3. This system uses a manually driven monochromator and rotation stage. Figure 6.3 illustrates that a thermally-controlled LED emits light directly into a 4 inch diameter integrating sphere to remove any spatial structure in the illumination [6.3(a)]. Once the LED light is diffused, it exits via a small port and is then imaged onto the input slit of the monochromator [6.3(b)]. A rotation stage and filter holder have been inserted between the two lenses that reimage the port. This position for the rotation stage in the collimated beam is desirable because a rotation of the filter does not affect the position of the integrating sphere port image on the monochromator input slit. After the LED light enters the monochromator [6.3(c)], the light is dispersed by a grating and redirected onto an exit slit. The LED emission then exits the monochromator and is reimaged onto a calibrated photodiode whose signal is measured by a current

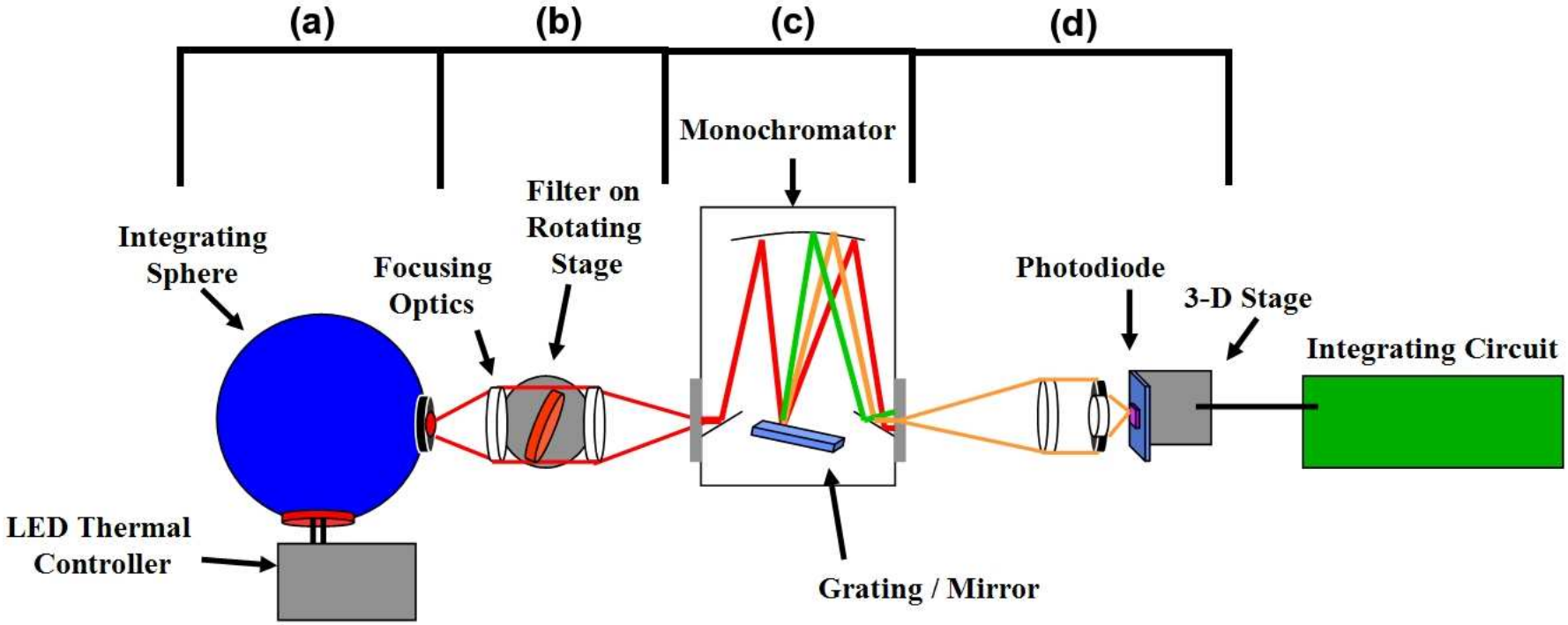

Figure 6.3. The LED measurement instrument used for spectral power measurements of LEDs and for testing of a commercial interference filter. The instrument uses (a) an integrating sphere to diffuse the illumination of a thermally-controlled LED and then (b) images the exit port onto the monochromator slit. (c) The monochromator is fitted with either a grating or a mirror for either monochromatic or total LED power measurements, respectively. (d) The output power is focused onto a calibrated photodiode where the spectral power is measured by a current integrating circuit.

integrating circuit [6.3(d)]. I made transmission measurements of the filter by measuring the LED spectrum with and without the filter in the collimated beam path. To measure the filter transmission using the total emission of the LED, I repeated the same procedure using a flat mirror instead of a grating in the monochromator.

The second instrument I used was the MICCS system described in Chapter 5. Since the MICCS system is inherently different from the LED measurement system, some adjustments had to be made for LED light input. The major problem in the MICCS system is that it has a low throughput. The MICCS uses a larger monochromator with a longer path length and is coupled with a 6 inch integrating sphere. The filter and photodiode are also placed 14 inches away from the integrating sphere port, and the current signal is not integrated as is done with the LED measurement system. These factors make the measurement of an LED spectrum in the MICCS limited by the strength of the input signal. To feed LED light into the MICCS, I use three or four LEDs of the same type and mount them in a line close to the input slit. I mounted the LEDs on an aluminum block that is thermally regulated with a Peltier cooler and a heater resistor to a constant temperature of 20°C. As with the LED measurement system, the MICCS is fitted with a mirror to replace the grating when a full LED spectral power measurement is desired. In addition, the total spectral radiance of each LED remains constant in both systems since the LED is driven by a constant current power supply and is regulated by a thermal control loop

Table 6.4. Global filter parameters of the Oriel and SNAP-BP1 Filters.

Filter	Angle	λ_{eff} (nm)	$\Delta\lambda$ (nm)	A (T*nm)
Oriel	10°	693.5	69.4	25.2
Oriel	20°	679.2	67.7	24.6
SNAP-BP1	10°	669.5	179.4	144.3
SNAP-BP1	20°	664.2	177.4	139.7

The transmission measurements using the LED instrument in Figure 6.3 were conducted on a filter purchased from Spectra-Physics / Oriel. The filter has a width

of 70nm FWHM with a very smooth transmission function shown in Figure 6.4(a). Because the filter is relatively narrow for a broadband filter, only three LEDs are required to cover the entire bandpass. The measurements using the MICCS system were performed on the SNAP BP1 filter previously measured in Section 5.3 (see Figure 5.12) and are shown in Figure 6.4(b). This filter has ripples across the bandpass and has a bandpass width of ∼180nm. The larger width of the BP1 filter, combined with the lower S/N of LEDs in the MICCS system, requires six LEDs to cover the entire bandpass. The global filter parameters for both the Oriel and SNAP-BP1 filters are summarized in Table 6.4. Since both systems use similar methods to measure the filter transmission function, the error in each measured filter function will quantify how well this LED technique can measure smooth and rippled filter transmission functions.

6.3.2 Filter Transmission Functions From Narrowband LED Emission

My first experiment to test calibration methods with LED light sources was to compare filter transmission functions measured by a QTH lamp source and an LED source fed into a monochromator. Since transmission is the ratio of signal with filter to signal without filter, my expectation was that filter transmission measured with narrowband light from a monochromator would be independent of the input source used. However, LEDs have the additional complication that they require the transmission function be "stitched" together since each LED spectral emission does not cover the entire bandpass. This experiment tests whether an LED input source is as effective as a QTH lamp at determining filter transmissions with a narrowband monochromator.

To demonstrate the LED emission spectra needed to span the measured filter transmission functions, Figure 6.4 shows an overlay of the LED emissions with their respective filter transmission functions. Figure 6.4(a) displays the transmission mea-

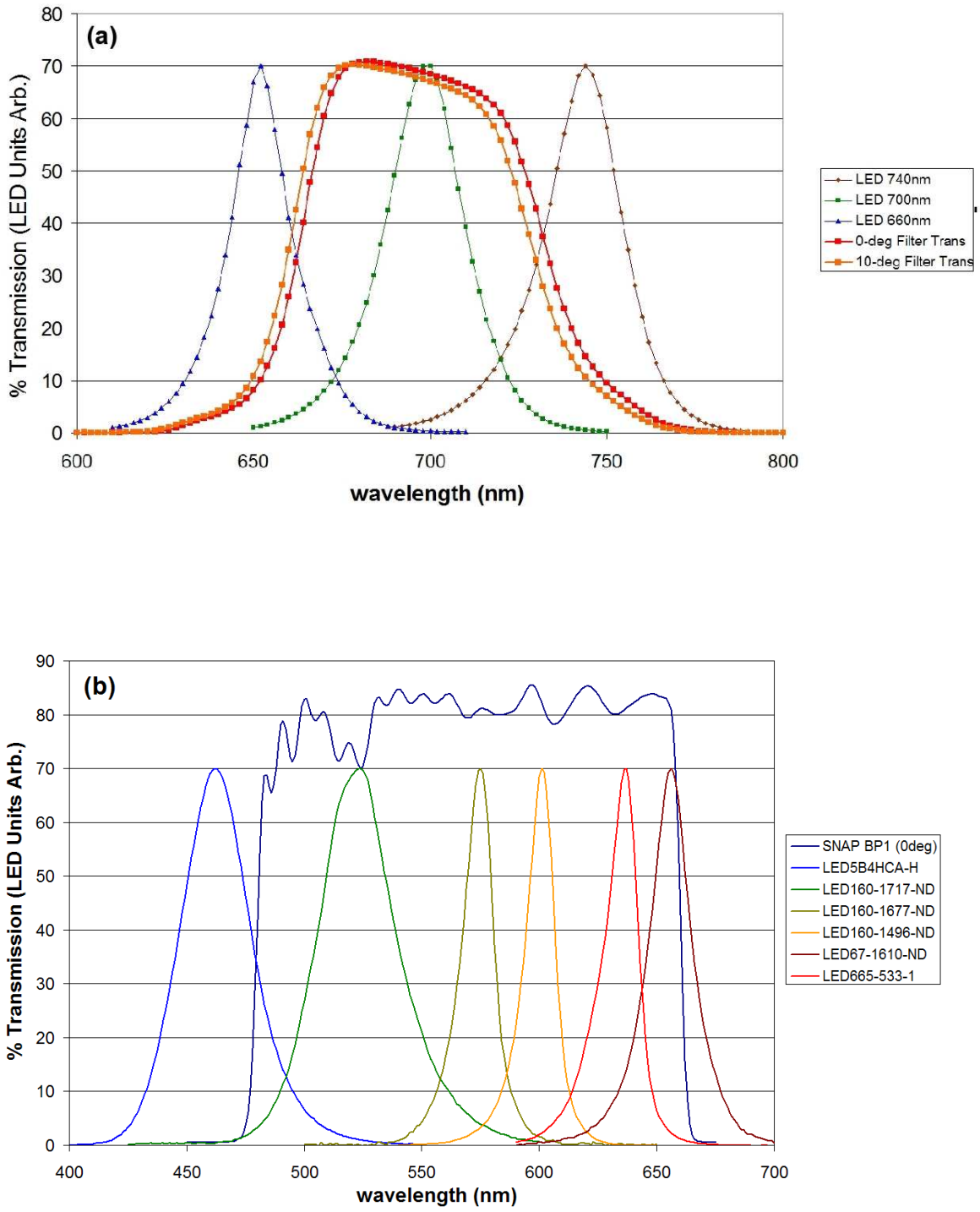

Figure 6.4. Interference filter transmissions and associated LED spectra. (a) The transmission function of an interference filter from Spectra-Physics / Oriel. Three LEDs cover the entire filter function. (b) The transmission function of the SNAP BP1 sample filter from Omega Optical. Six LEDs are required to cover the SNAP BP1 filter function. All LED spectra have been normalized to 70% of their peak emission.

surements of the smooth Oriel interference filter at two different filter angles of 0 and 10° and the three LEDs used to span the bandpass. The filter transmission shown was measured with a QTH lamp input in the LED measurement setup of Figure 6.3. Figure 6.4(b) shows the placement of the six LEDs required to span the BP1 transmission function in the MICCS measurement setup. The BP1 filter shown was also measured using a QTH lamp for comparison (originally measured in Figure 5.12). The LED spectra plotted in Figure 6.4 are normalized to 70% of their peak emission to show their filter coverage. My first test was designed to reproduce the filter transmissions measured with the QTH lamp at 0 and 10° incidence angle with an LED light source.

As shown in Figure 6.4, each LED can provide illumination for a range of wavelengths in the Oriel and SNAP-BP1 filter transmission functions. The range of measured wavelengths using each LED is limited by the width and level of output signal produced by the LED spectrum. Figure 6.5 shows the transmission measured from each of the three LEDs for the Oriel filter. By calculating the signal-weighted mean transmission from each LED at each transmission function wavelength, I have reconstructed the total filter transmission function resulting when the filter is turned by 10 degrees. I made similar transmission measurements of the BP1 filter using the narrowband emission from LEDs in the MICCS system, and the results are shown in Figure 6.6 and Table 6.5.

Table 6.5. Relative error in the global filter parameters using an LED-fed monochromator.

Filter	Angle	$\frac{(\lambda_{eff}-\lambda'_{eff})}{\lambda_{eff}}$ (%)	$\frac{(\Delta\lambda-\Delta\lambda')}{\Delta\lambda}$ (%)	$\frac{(A-A')}{A}$ (%)
Oriel	10°	0.0	0.1	0.7
Oriel	20°	0.0	0.1	0.5
SNAP-BP1	10°	0.0	-0.1	-0.4
SNAP-BP1	20°	0.0	-0.1	-0.3

Using this narrowband LED light, both instruments show excellent agreement in

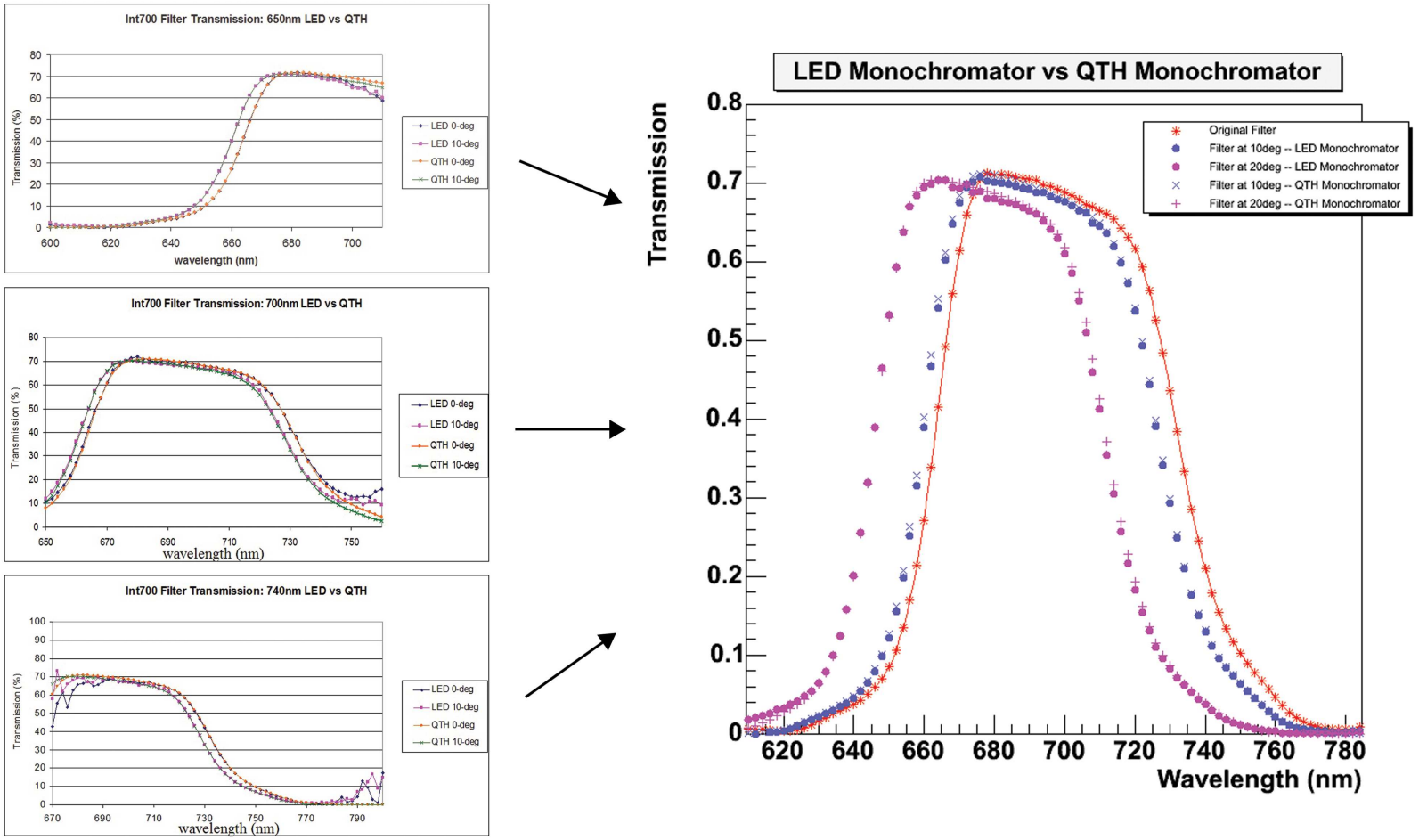

Figure 6.5. A filter bandpass is reconstructed from the transmission measurements from three LED sources. Each of the LED transmission measurements are combined via a weighted mean with the signal to noise of the measurement as the weight.

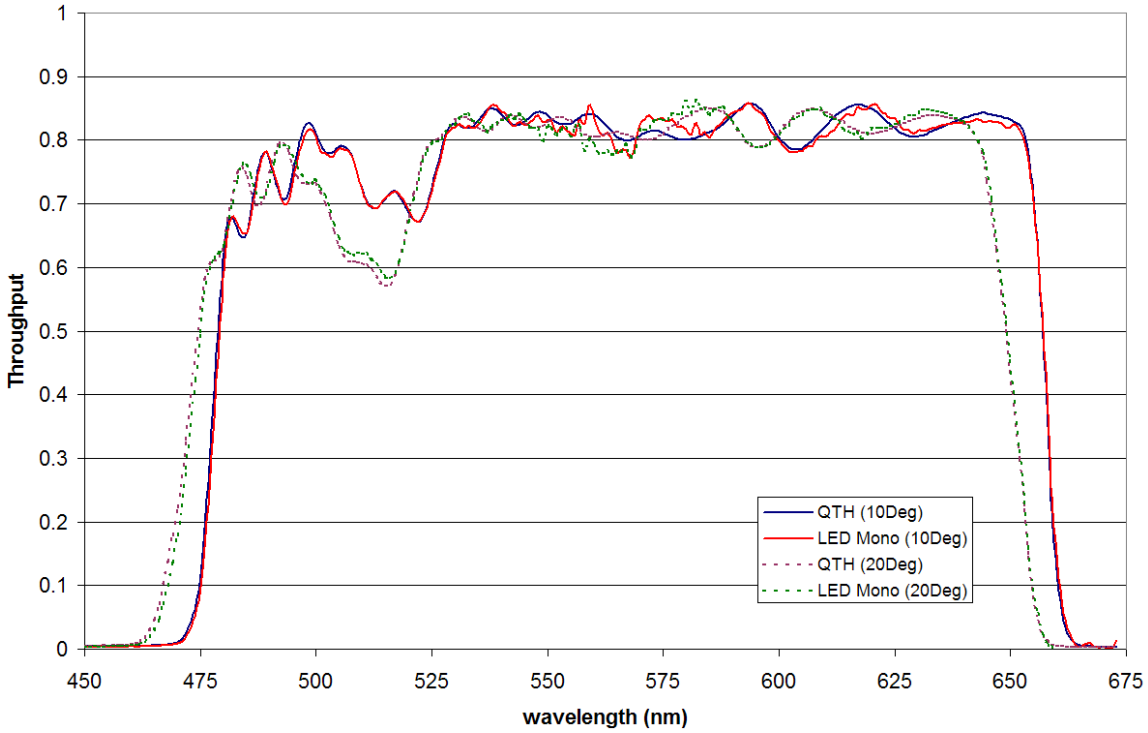

Figure 6.6. The sample SNAP BP1 bandpass is reconstructed from the transmission measurements from six LED sources in the MICCS setup.

the filter transmission functions derived from a QTH lamp input and a set of LEDs into a monochromator. Table 6.5 shows that all filter parameters were recovered with less than 1% error relative to the actual filter parameters in Table 6.4. Figure 7.6 shows the transmission error computed as the difference in transmission between the measured LED-fed monochromator transmission functions relative to the narrowband QTH transmission functions. For the smooth Oriel filter error in Figure 7.6(a), the monochromator measurements have less than 1.5% transmission error over the entire bandpass at both 10° and 20° incidence angle. The rippled SNAP BP1 filter transmission error in Figure 7.6(b) had slightly increased transmission error between the narrowband LED and QTH lamp measurements, with $< 2\%$ error over most of the bandpass and a peak of 4.2% error on the blue edge of the bandpass. Relative to the QTH transmission function measured at a 10° incidence angle, the integrated throughput error from the narrowband LED measurements is $< 0.8\%$ for the Oriel

filter transmission function and $< 0.3\%$ for the wider BP1 filter transmission function. My results show that by "stitching" together the filter transmissionss measured from individual LEDs, an LED-based light source and a QTH lamp are equally effective at measuring filter transmission functions when coupled with a monochromator.

Since there is very little loss of accuracy between LED and QTH lamp source inputs to a monochromator, the method of combining LEDs and a monochromator to monitor filter changes would work very well for SNAP. An additional benefit to using LED sources is that monochromators typically suffer from internal stray light scatter when a broadband source (such as a QTH lamp) is used at the input. Such scattered light is generally caused by spectral orders from the grating overlapping at the exit port, thereby affecting the spectral purity of light exiting the monochromator. This internal stray light can be reduced with an additional monochromator at the exit port or blocking filters at the light input port[3]. With an LED-based input source, internal stray light can be reduced significantly since LEDs have photon emission over small wavelength ranges (typically 20 - 100nm FWHM). Therefore, an LED light source could decrease the complexity of a monochromator-based calibration system flown onboard SNAP with no loss in transmission measurement precision.

6.3.3 Filter Transmission from Total LED Emission

While an LED-fed monochromator could be a viable calibration instrument to track filter transmission functions on SNAP, there are several potential drawbacks to having a monochromator in the calibration light system: 1) a monochromator typically has low throughput (10^{-7} efficiency for the instruments presented in this chapter) requiring more LED sources, 2) a monochromator requires the movement of the grating to change wavelengths, and 3) a monochromator requires wavelength calibration. Each of these issues must be addressed if SNAP is to use a monochromator in flight.

As an alternative to a monochromator, I have explored the possibility of tracking

[3]Blocking filters were used to reduce stray light in the MICCS. See Section 5.1.1.

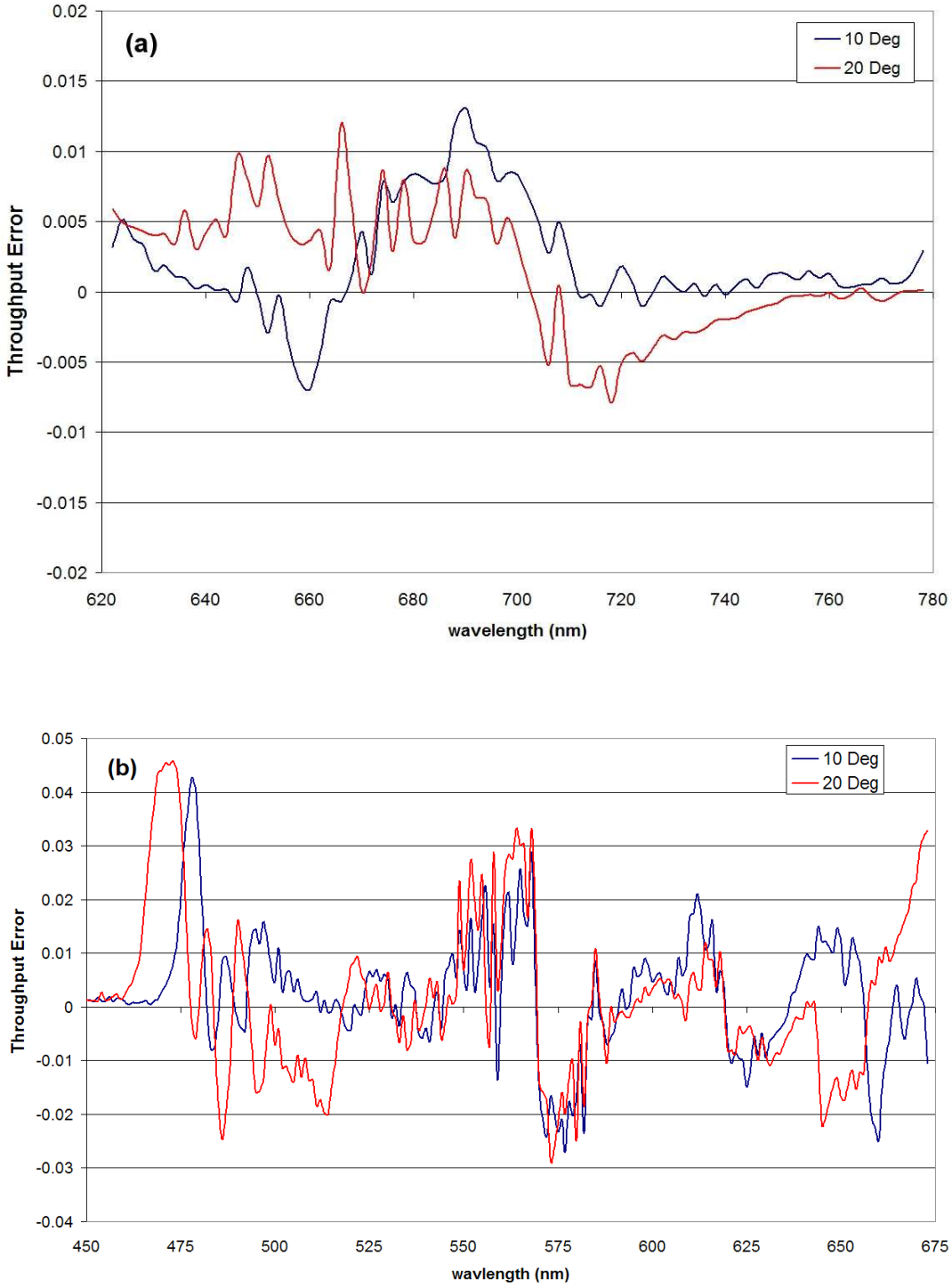

Figure 6.7. The transmission error for the (a) smooth Oriel filter and (b) the SNAP BP1 filter using narrowband light from a monochromator illuminated by LEDs. The transmission error is measured as the difference between the transmission measured with an LED-fed monochromator and the transmission measured with a QTH lamp coupled with a monochromator.

filter transmission functions with LEDs without a monochromator to investigate if a monochromator is required for the SNAP calibration light system. Using LEDs without a monochromator greatly simplifies the hardware design for an calibration system onboard SNAP. In addition, this technique greatly improves the efficiency of light that can be transmitted to the SNAP focal plane. The cost for this simplicity, however, is a decrease in the measurement resolution across the filter transmission function. Instead of an emission bandpass of 1-10 nanometers FWHM that is typical of a monochromator, the LEDs will emit in 20-100nm FWHM bandpass. I have tested the Oriel and SNAP BP1 filters using LEDs without a monochromator and investigated the accuracy to which they can track smooth and rippled filter bandpasses.

6.3.3.1 Measurement Technique

Figure 6.8 shows the spectral output of the three LEDs that cover the smooth Oriel interference filter. The LED parameters are shown in Table 6.6. The gray areas show the spectral output of the bare LED, the green areas display the LED with the filter at normal incidence angle, and the orange areas show the LED output combined with the filter at a 10° incidence angle. As shown in the figure, changing the filter transmission function by turning the filter alters the measured spectrum of the filtered LED. Since I know the 0° transmission function of the filter, the LED output spectrum, and the 0° LED spectrum with the filter, I can test whether it is possible to monitor changes in the filter transmission function through measurements in the integrated flux measurements of LEDs using the techniques in Section 6.1.

Table 6.6. Parameters of the three LEDs used to measure the Oriel Filter. (Constant Current = 25mA)

LED model	Figure	λ_{eff} (nm)	$\Delta\lambda$ (nm)	Total Power (mW)
67-1610-ND	6.8(a)	653.8	20.0	1.7
ELD-700-524	6.8(b)	699.1	26.2	1.5
ELD-740-544	6.8(c)	741.9	26.5	2.7

In both of my test instruments, the simple ratio of the LED irradiances with and without the filter will show any changes in the filter transmission. For example, if the filter transmission shifts towards the blue, a signal from the bluest LED will increase as the bandpass allows more light through and the signal from the reddest LED will decrease as the filter cuts off the LED emission. Using the knowledge of the unfiltered LED spectral shape allows me to fit changes to the original transmission function and reconstruct the perturbed transmission function. While this method was tested theoretically in Section 6.2, I will measure how accurately the technique can be performed with real filters and LEDs in practice.

To use the spectral information from measurements of the filtered LED emission, I begin by constructing spline functions of the measured LED spectral power, $P(\lambda)$, and 0° filter transmission $\tau^0(\lambda)$. In terms of the SNAP mission, these measurements represent the pre-launch characterizations for SNAP LEDs and filters, and I will refer to them as the "original" measurements. I then computed the expected transmission for each LED spectrum by integrating the functions for each LED i:

$$\tau_i^0 = \frac{\int \tau_i^0(\lambda) * P_i(\lambda) d\lambda}{\int P_i(\lambda) d\lambda}. \tag{6.8}$$

In addition to the expected transmission for each LED, I calculated filter parameter values for λ_{eff}^0, $\Delta\lambda^0$, and A^0 from this original filter transmission function (see Section 6.1). Once I computed the expected LED throughput at 0°, I then measured it for the test filter at 10° and 20° incident angles. These off-normal incidence angles represent a "modified" filter transmission function that has been altered from the "original" measurements assumed at 0°. To test if LEDs without a monochromator can measure the modified filter transmissions, I passed the total emission spectrum of the LED through the a monochromator with the dispersion grating replaced by a mirror. I found that this method eliminated many of the systematic errors involved

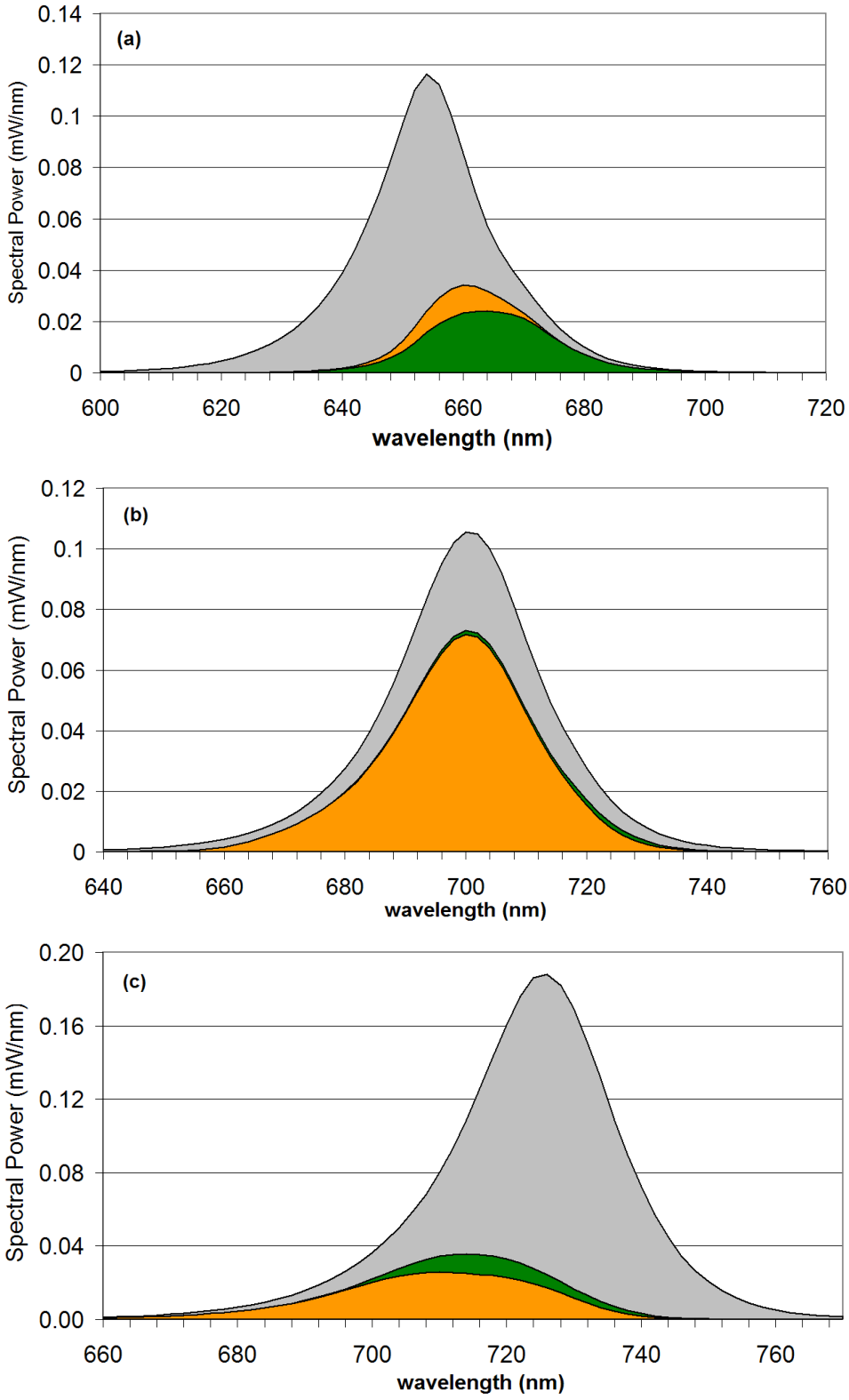

Figure 6.8. The spectral power of the three LEDs used to measure the smooth Oriel filter transmission function. The spectra of the three LEDs are centered at (a) 650nm, (b) 700nm, and (c) 740nm. Each LED spectrum is shown without a filter (gray), with a filter at normal incidence (green), and with a filter at a 10° tilt (orange). The parameters for these LEDs can be reference in Table 6.6.

in modifying the setup with a second detector or creating an entirely different LED emission measurement system.

With the expected throughput of the original filter transmission function from Equation 6.8 and the measured LED throughputs from the original and modified filter transmission functions, I formulated a fit function that tracks the parameters describing the filter transmission function. The fit function is based on the ratio of a modified filter transmission function to the original filter function. This ratio is first calculated for each LED i with

$$\mathcal{R}_i^{calc} = \frac{\tau_i'(\lambda_{eff}^0 + \Delta\lambda_{eff}, \alpha\Delta\lambda^0, \beta A^0)}{\tau_i^0}, \tag{6.9}$$

where $\Delta\lambda_{eff}$, α, and β are free parameters that are allowed to vary. The calculation of τ_i' follows the same parameterization of a filter bandpass developed in Section 6.1 and shown in Figure 6.1. However, the calculation of the filter throughput A was modified to integrate the measured filter transmission function instead of using the approximation $A = \Delta\lambda \times \tau(\lambda_{eff})$. Similar to Equation 6.9, a ratio can be formed from the measured LED transmission through the modified filter transmission function and the original filter function using

$$\mathcal{R}_i^{meas} = \frac{T_i'}{T_i^0}, \tag{6.10}$$

where T_i' is the measured LED transmission with the modified filter transmission function and T_i^0 is the LED transmission with the filter at 0°. I fit the LED measurements by altering the filter transmission function parameters through $\Delta\lambda_{eff}$, α, and β, recalculating $\mathcal{R}_i^{calc}$ with the modified filter, and then comparing the calculated $\mathcal{R}_i^{calc}$ with measured $\mathcal{R}_i^{meas}$. I fit the filter perturbation by minimizing the fit function

$$\Delta\mathcal{R}^2 = \sum_{i=1}^{3} \frac{[\mathcal{R}_i^{calc} - \mathcal{R}_i^{meas}]^2}{\sigma_i^2}, \tag{6.11}$$

where σ_i^2 is the variance in the LED transmission measurements[4]. The minimum value of the fit function corresponds to the best fit values for $\Delta\lambda_{eff}$, α, and β, from which I calculated the best fit transmission function for the modified filter function.

6.3.3.2 Results

I have summarized the relative filter parameter error for both the Oriel and SNAP-BP1 filters in Table 6.7. The determination of $\Delta\lambda$, λ_{eff}, and A using the total LED emission technique has $\leq$1% error relative to the filter parameters in Table 6.4. These results show that the filter parameter fit is accurate using the total LED emission technique.

Table 6.7. Relative error in the global filter parameters using the total LED emission technique.

Filter	Angle	$\frac{(\lambda_{eff}-\lambda'_{eff})}{\lambda_{eff}}$ (%)	$\frac{(\Delta\lambda-\Delta\lambda')}{\Delta\lambda}$ (%)	$\frac{(A-A')}{A}$ (%)
Oriel	10°	-0.1	-0.9	-0.7
Oriel	20°	0.1	1.0	0.0
SNAP-BP1	10°	0.0	0.9	-0.1
SNAP-BP1	20°	-0.2	0.9	0.9

Since the relative error in the filter parameters is small, the filter transmission functions that are fit from the total LED emissions should match the transmission functions measured with a QTH lamp and a monochromator. To make this comparison, I plot the results of the LED fitting technique for the smooth Oriel filter transmission function in Figures 6.9 and 6.10. Figure 6.9 shows the modified filter function as measured with an monochromator with a QTH lamp source and the fit from my total LED emission technique. From this figure, it appears that the filter tracking technique using total LED emission matches the narrowband monochromator measurements very well, with the only noticeable differences coming the 20° filter angle. Figure 6.10 shows the difference between the LED fit results and the narrowband measurements made with a monochromator. The figure shows that the largest

[4]I used the NAG C++ minimizing software routines to perform this calculation (NAG, 2002).

Table 6.8. The peak transmission error (PTE) in the fit Oriel and SNAP-BP1 filter transmission functions.

Technique	Oriel PTE (%)		SNAP-BP1 PTE (%)	
	10° angle	20° angle	10° angle	20° angle
Narrowband LED	1.3	1.2	4.2	4.5
LED emission fit	-2.5	1.8	-14.0	-21.0

transmission difference is 2.5% (excluding the error beyond 760nm where the filter transmission is small), but that the overall fit error across the bandpass is centered about zero for both filter angles of 10° and 20°.

However, what happens if a filter has ripples in its transmission function? As discussed in Sections 5.3.3, the commercial SNAP BP1 filter has ripples in its transmission function that seemingly vary independently from one another when the filter is tilted to off-normal incidence angles. To test how well the ripples in transmission can be tracked using the same three parameter model of the filter, I performed the same LED tracking technique on the rippled SNAP BP1 filter.

Figure 6.11 shows the filter transmission of the SNAP-BP1 bandpass at 10° and 20° filter angle using the total LED emission technique. As with the narrowband filter measurements made in Section 6.3.2, six different LED spectra were required to span the filter bandpass. Table 6.8 summarizes the largest transmission error for both the Oriel and SNAP-BP1 filters. My results show that the fit filter transmission function from the total LED emission technique is not nearly as precise for the rippled SNAP-BP1 transmission function as it is for the smooth Oriel transmission function.

Figure 6.12 shows that for the 10° filter angle, the fit transmission function deviates by less than 3% in transmission from the narrowband measurements made with monochromator and a QTH lamp for over 75% of the bandpass. This result suggests that the recovered transmission function is roughly in agreement with the transmission function measured with a monochromator. However, the largest error for the 10° filter angle is found at the red edge of the filter function where the transmission

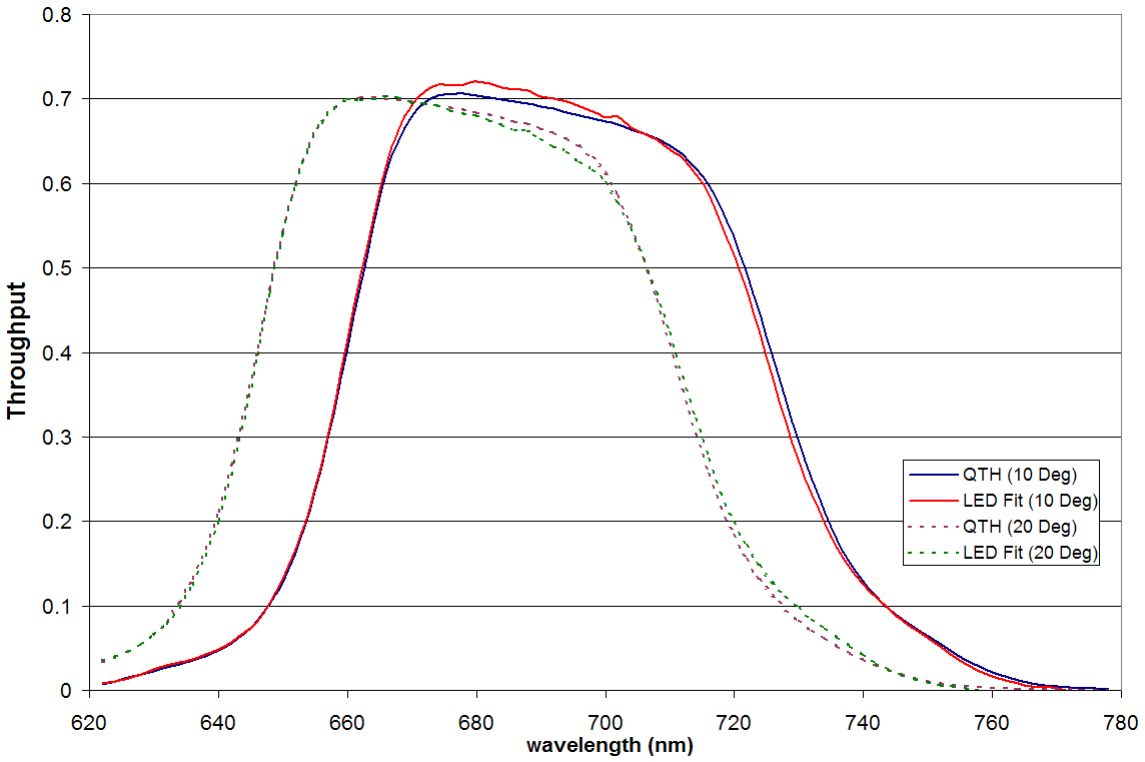

Figure 6.9. This figure shows an overlay of the transmission measurements for the smooth Oriel filter from an QTH lamp fed into a monochromator (blue and purple lines) to the transmission measurements from the total LED emission fit technique (red and green lines) at 10° and 20° incidence angle.

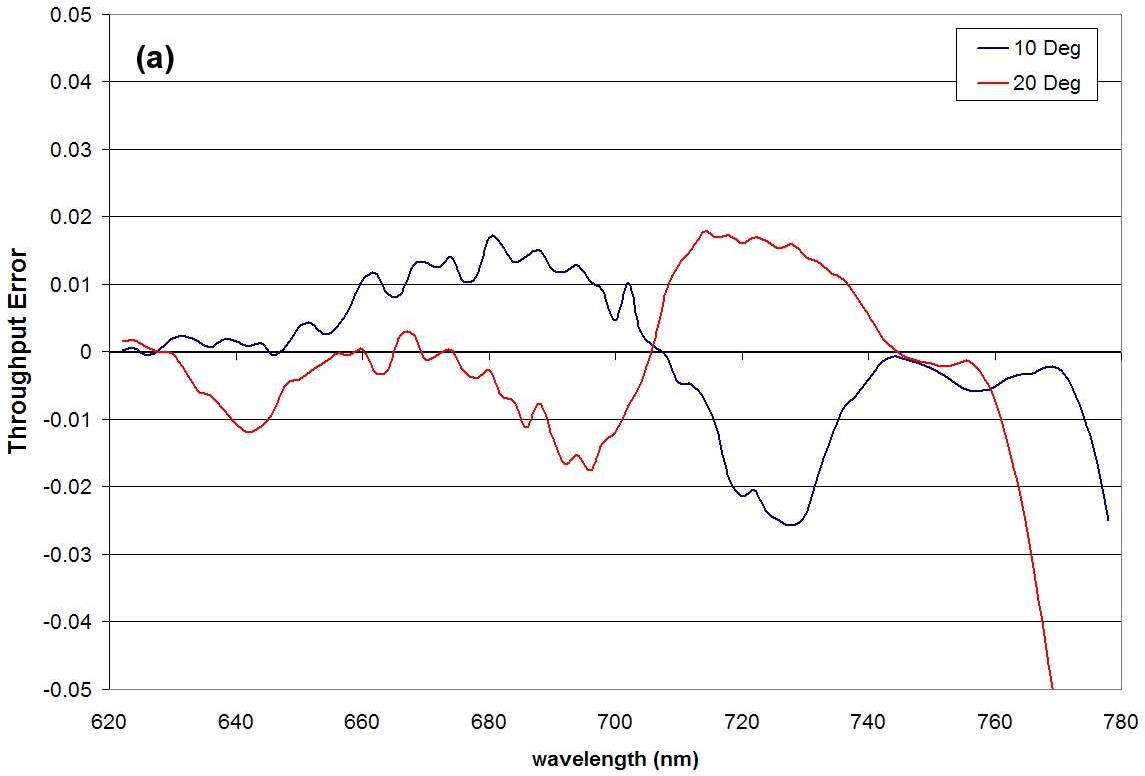

Figure 6.10. This figure shows the difference in transmission between the LED-fed monochromator technique and the total LED emission fit technique for te Oriel filter at 10° and 20° incidence angles.

error peaks at nearly 14%. For the 20° filter angle, the fit transmission from the total LED emission deviates even further from the narrowband measurements, peaking at over 20% in transmission error at the red edge of the filter. In addition, there is a large range of wavelengths from 495nm to 525nm where the measured narrowband filter transmission function is systematically 5-10% lower than the fit transmission function. This range of systematic error in the fit transmission may be due to the inability of the total LED emission to track the filter changes in a rippled filter with only a three parameter model. The transmission over this range of wavelengths behaves independently from the global filter parameters of $\Delta\lambda$, λ_{eff}, and A of the filter, and therefore is not fit well using the fit function in Equation 6.11.

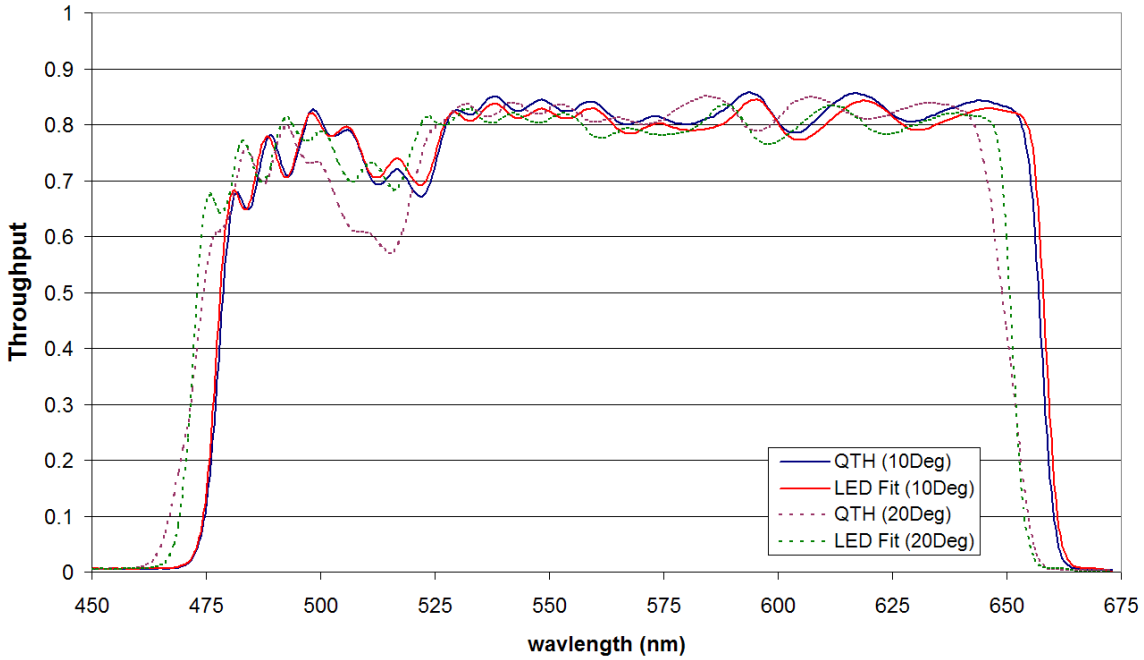

Figure 6.11. The transmission measurements for the rippled SNAP BP1 filter. The measurements from an LED-fed monochromator (blue and purple lines) are plotted with the transmission measurements from the total LED emission fit technique (red and green lines). The solid lines refer to the filter transmission at 10° incidence angle and the dotted lines refer to filter transmission at 20° incidence angle.

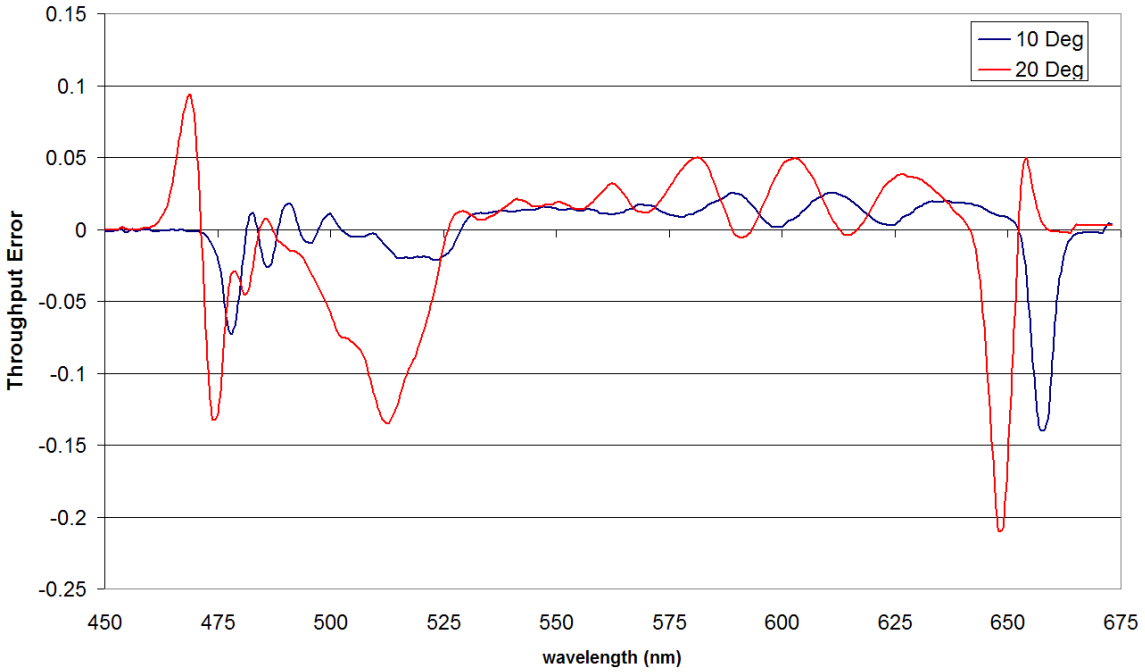

Figure 6.12. This figure shows the difference in transmission between the LED-fed monochromator technique and the total LED emission fit technique for the SNAP BP1 filter at 10° and 20° incidence angles.

6.4 Conclusions

I have developed a parameterization of the global filter transmission function properties and made theoretical calculations of the accuracy to which the filter parameters can be tracked using different observed sources. The calculations showed that blackbody-like sources such as a model white dwarf flux or a calibrated QTH lamp irradiance cannot accurately track the filter parameters. However, my calculations using the total emission of LED sources showed that they have a promising ability to precisely determine variations in the filter parameters.

To test LEDs in practice, I have made laboratory transmission measurements of two commercial interference filters using monochromatic light with both a QTH lamp and multiple LEDs as input sources. The measurements were made with the filters at 10° and 20° incidence angles to represent an unknown change in the filter transmission function during the SNAP mission. The results of these tests are summarized in

Tables 6.5 and 6.7. These results showed that the filter parameters were recovered with $< 1\%$ error when using either a QTH or a LED light source coupled with a monochromator. The LED-fed monochromator also returned similar transmission curves to those measured with a QTH lamp and were in agreement over the entire bandpass.

I have also used total LED emission to track changes to filter transmission functions. The relative error in the Oriel and SNAP-BP1 filter parameters using the total LED emission technique was $\leq 1\%$, which demonstrates that the total LED emission technique does track the filter parameters accurately in practice. In the case of the smooth Oriel filter, I have recovered the modified transmission functions through a three parameter fit to better than 3% across the filter bandpass. For the rippled SNAP BP1, however, the filter transmission does not appear to change only with respect global filter parameters. As mentioned in Section 5.3, ripples in the filter transmission function appear to change independently as the filter angle is changed. Since the LED-fit transmission technique uses a three parameter model for the global filter parameters, the independent changes in the ripples are not fit well by the model, and therefore I find larger peak transmission errors of up to 20% in the fit process using the total LED emission.

From the results presented in this chapter, it appears that either an LED-fed monochromator or the LED emission fitting technique could be used to monitor filters for SNAP. Both methods track the filter parameters with $\leq 1\%$ error. However, the narrowband measurements from an LED-fed monochromator accurately reproduce the shape of the filter transmission function as shown in Figures 7.6(a) and 7.6(b) better than the LED emission fit method shown in Figures 6.10 and 6.12. The LED emission fit technique produces the largest peak transmission error for both filters, with significant transmission error for the rippled SNAP BP1 filter transmission function. The SNAP BP1 filter transmission has transmission changes which can not

be reproduced with my simple three parameter model alone.

The level of tolerable transmission error must be driven by their impact on the top-level science, namely the measurement of SNIa and calculation of the cosmology parameters. In the next chapter, I will input the transmission error from both the smooth Oriel filter and the rippled SNAP BP1 filter into the SNAP simulation and I will calculate the errors on the final cosmological parameters. I will use the results of these investigations to determine science-driven requirements on the filter design and the onboard calibration light system.

CHAPTER 7

Cosmology Fitting

The science-driven requirements of the SNAP mission flow down into technical requirements on the mission parameters such as the survey size, telescope size, integration times, and so on. These science-driven requirements will also flow down to the calibration of the SNAP experiment, including the calibration of the SNAP filters (see Sections 1.5 and 3.2.2). In this chapter, I will study how errors in the calibration of filter transmission will affect the determination of cosmological parameters with SNAP. The results of this study will help define technical requirements of the onboard calibration light source and filter design for SNAP.

7.1 The SNAP Simulation

To determine the science requirements for the SNAP mission, the collaboration has developed a mission simulation software package called SNAPsim. This Java-based software package is built upon a framework that is both thorough and flexible. A few of its capabilities include photon generation, host galaxy extinction, SN Ia light curve time series, instrumental throughput, and the analysis of mock SNIa peak magnitudes to determine cosmological parameters.

Figure 7.1 shows a flow chart for the SNAPSim software package. The simulation starts by setting up a universe with a set of fiducial cosmology parameters. The default cosmological parameters in SNAPSim are a flat universe with $\Omega_M = 0.3$, $w_0 = -1.0$, and $w_a = 0$ (refer to Section 1.2 for the definition of these cosmological

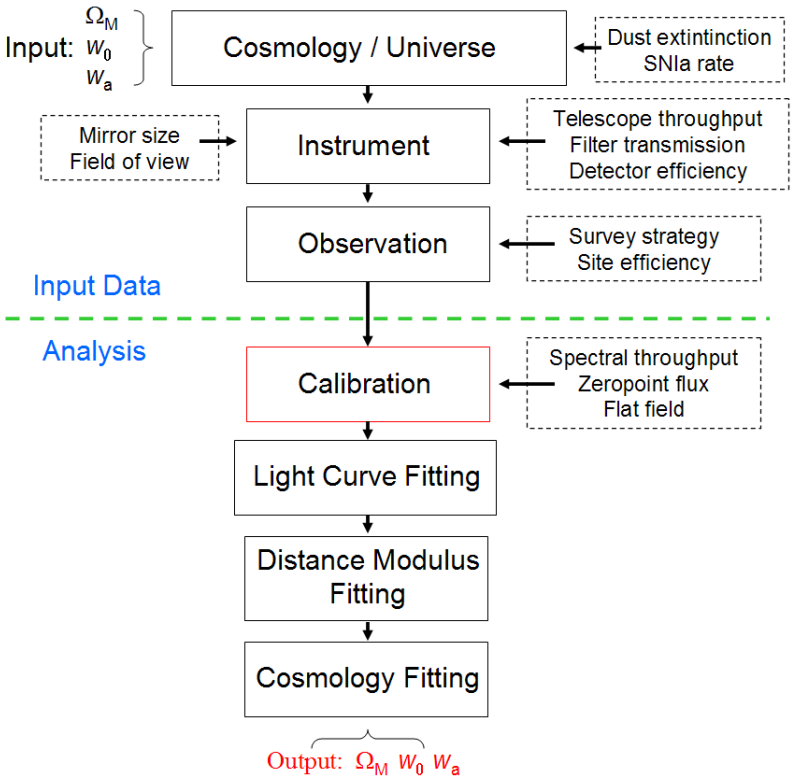

Figure 7.1. Flow chart for the SNAP simulation software.

parameters). The values for these parameters can be adjusted to simulate other possible cosmologies. Several additional input parameters can be adjusted by the user in the "Universe" domain shown in Figure 7.1, including host galaxy extinction, intergalactic dust extinction, and the SNIa explosion rate in an observable volume. Adjusting these input parameters allows the SNAP simulation team to study various physical effects in the universe that may affect the determination of the cosmological parameters with SNIa measurements.

After the parameters for a model universe have been chosen, the next step in the simulation generates a telescope configuration. The baseline configuration follows that of the SNAP mission with a two meter primary mirror, nine filter bands, two detectors types for the optical and NIR, and a 0.7 square degree field of view (see Table 2.1 in Section 2.2.4 for the baseline SNAP mission parameters). The simulation is also flexible enough to allow for other telescope configurations, including the

telescopes of other proposed cosmology experiments. The ability to change telescope configuration is essential to deriving science-driven requirements for the mission hardware. A proposed change to any of the major mission parameters can be simulated and studied for its impact on the cosmological parameters. Since my particular interest is in the requirements on the filter transmission functions, I have developed simulation software that takes a user supplied filter transmission function and generates a nine band filter set to use in the SNAP simulation chain. I used this custom software to input filter transmissions that have been measured by the MICCS system into the simulation. This software will allow me to study the impact of empirical filter transmission functions on the determination of cosmological parameters.

Once the user-specified mission configuration has been generated, the program simulates observations of SNIa events using the standard SNAP survey strategy. In this step, the survey coverage, integration times, and SNIa light curve cadence can all be adjusted to optimize the mission. The user can also choose to perform a Monte-Carlo simulation to generate photons for the SNAP focal plane or use the expected signal-to-noise output from an internal exposure time calculator. The result from this step is a data set of SNIa light curves that represent a single realization of the SNAP experiment. Redshifts for each of the SNIa events are also generated during this step. In addition to the simulated SNAP SNIa, 300 SNIa are added to the data set with redshifts between 0 to 0.1. These additional SNIa represent the dataset from the ground-based Supernova Factory observing program (Copin et al., 2006) which is currently measuring a large sample of nearby SNIa.

The next step in the SNAP simulation chain begins the analysis portion of the code as seen in Figure 7.1. The analysis of the SNAP simulated data begins with the calibration of the SNAP telescope. In the current SNAP simulation, the calibration consists only of the SNAP spectral throughput. The spectral throughput is defined as the transmission through the four telescope mirrors, the transmission of the filter,

and the quantum efficiency of the detectors, all as a function of wavelength. The throughput of these three components, collectively known as a "channel", are then multiplied together to form a channel efficiency. Since there are nine filters that divide up the SNAP spectral range, there are nine channels in SNAPSim. While there are many other calibrations that are necessary for the SNAP data (flat fields, detector gain, bias subtraction, etc.), the calibrations that will most affect the cosmological parameters are those that vary with wavelength. To study a calibration error, the user inputs a spectral throughput for each channel that is offset from the actual spectral throughput used to generate the data. The SNAP channel calibration flows down into the remaining SNAP analysis steps.

Building the SNIa light curve templates is a critical step in the SNAP analysis chain. These templates convolve the calibrated channel efficiencies with a template SNIa spectrum (Nugent et al., 2002). The templates simulate the observation of SNIa spectra at finely spaced redshift intervals ($\Delta\ z$=0.005) over the SNAP wavelength range. The templates also take into account changes in the SNIa spectrum at various epochs in the light curve. The calibration of the channel efficiencies, however, play an important role in the *expected* SNIa magnitudes from each bandpass at each epoch. This fact will make the determination of luminosity distances using SNIa peak magnitudes sensitive to error in the filter transmission (refer to Section 1.3, Equations 1.15 for the definition of luminosity distance).

After the light curve templates have been built, a light curve fitter utilizes them to calculate the peak magnitudes of the SNIa measurements, which are then fed to another fitter that applies light curve stretch corrections, K-corrections, and extinction corrections to transform the magnitudes into the rest-frame bandpass (refer to Equation 1.19 for how these corrections are applied to SNIa magnitudes). Given the standard absolute magnitude of SNIa and the observed rest-frame peak magnitude, the distance modulus μ (from Equation 1.16) is calculated for each SNIa event.

In the final step, the SNAP simulation software fits the cosmological parameters. Using the redshifts and SNIa distance moduli calculated in the previous step, luminosity distances are calculated using Equation 1.16. The relation of SNIa distance moduli and redshifts is often shown in a Hubble diagram such as Figure 1.2. To get the cosmological parameters from the SNIa data, a Gaussian likelihood function is calculated from the fitted distance moduli weighted by the Poisson error in the SNIa measurement. To reflect the expected results of CMB cosmological missions (Melchiorri et al., 2000; Balbi et al., 2000; Spergel et al., 2003; Heinämäki, 2006), the SNAP analysis imposes a prior likelihood value of $\sigma(\Omega_M) = 0.03$ to constrain the determination of the mass energy density. Additional priors may be added to the SNAP likelihood function as new cosmology experiments come online. Using the luminosity distance formula from Equation 1.15, the program finds the cosmological values of Ω_M, w_0, and w_a by maximizing the likelihood fit to the data. Since the distance modulus is a dimensionless quantity, the units of the luminosity distance are removed by introducing an additional "nuisance" parameter defined as $\mathcal{M} \equiv M - 5log_{10}[H_0/100kmsec^{-1}Mpc^2]$ where M is the absolute luminosity of a SNIa[1] (see Equation 1.16). $\mathcal{M}$ is fit concurrently with the cosmological parameters, but the actual value does not impact the dark energy parameters of w_0 and w_a.

While the values and associated errors of the cosmological parameters are of primary interest, many other diagnostics are available from the SNAPsim software. Some of the more interesting quantities that can be returned from the simulation are the errors between the input values and the calculated values. In particular, useful error values can be found for the SNIa distance moduli and host galaxy extinction parameters. Because the actual values for these quantities are not known prior to the experiment, the error diagnostics are only available in a simulation environment and will not be available in the real SNAP data. Therefore, SNAPSim provides a

[1]The $\mathcal{M}$ parameter is dubbed a "nuisance" parameter since the absolute magnitude of the object only affects H_0 and not the expansion history $H(z)$.

unique toolset to explore how the SNAP mission could introduce systematic error into the measurements of SNIa. I will use these diagnostics to examine the effect of calibration error in the determination of cosmological parameters.

7.2 Fundamental Flux Calibration Error

In Section 3.2.1, I detailed a calibration plan to use a calibration star to provide the absolute flux scale for the SNAP mission. To date, the most accurate stellar flux sources to use for this task are white dwarf stars that have modeled fluxes that are tied to spectrophotometric measurements made by HST. In Section 6.2, I discussed one of these white dwarf standard stars, G191B2B. The model flux is based on a Non-Local Thermodynamic Equilibrium model of the white dwarf atmosphere and is pinned to HST spectrophotometric measurements of the stellar temperature and surface gravity (Bohlin, 2002). However, using the same measured values and a Local-Thermodynamic Equilibrium model, the G191B2B flux values gives systematically different fluxes with 1% error in the optical to 2% error in the NIR. The G191B2B NLTE model flux and NLTE - LTE systematic flux error are both shown in Figure 6.2.

An important question for the SNAP calibration to answer is how this systematic fundamental flux error affects the determination of the cosmological parameters. Using the SNAPSim framework, I have addressed this question by incorporating this flux error into the calibration portion of the simulation chain. Since the calibration within SNAPSim is modeled as the spectral throughput of the nine SNAP channels (where a channel is composed of the telescope throughput, detector efficiency, and filter transmission), a photometric measurement of the fundamental standard star will be the convolution of the stellar flux with each channel throughput. If the error is specified as the fractional error $\epsilon(\lambda)$ of the model stellar flux $S(\lambda)$, the perturbed

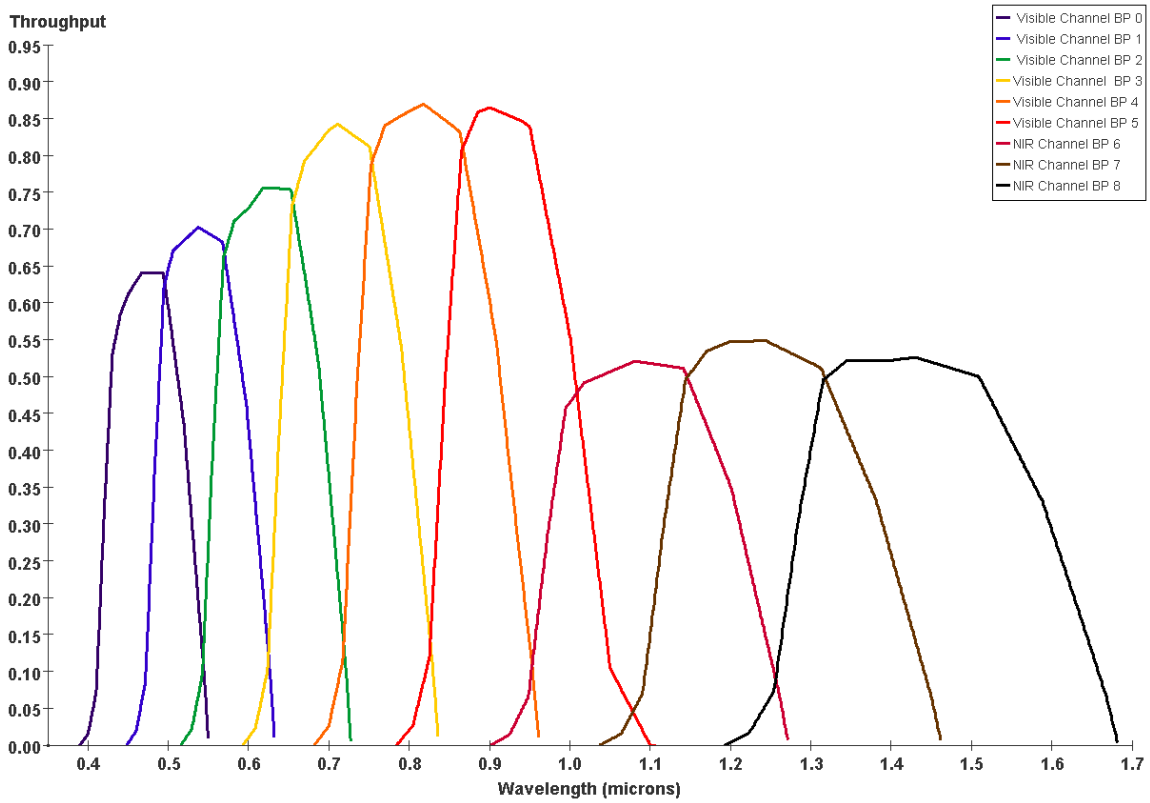

Figure 7.2. The nine default channel throughputs in the SNAPSim environment.

photometric flux can be written as

$$F(\lambda) = \int S(\lambda)(1 + \epsilon(\lambda))T(\lambda)d\lambda, \tag{7.1}$$

where $T(\lambda)$ is the throughput of the channel. In this formulation, an error in the stellar flux in a perfectly known channel is equal to an error in the channel with a perfectly known stellar flux. Using this property, I propagate the fractional error from the fundamental flux to the channel throughput in SNAPSim. The nine default channel throughputs are shown in Figure 7.2.

The effect of this calibration error on the determination of the cosmological parameters can be measured by the difference between parameter values with and without the calibration error. Therefore, the simulation without a calibration error is referred to as the "truth" and the simulation with calibration error is referred to as the "test".

The cosmological parameters errors calculated from the flux calibration error test simulation relative to the truth simulation are shown in Table 7.1. The parameters show that the effect of the calibration error incurred by NLTE and LTE model differences for G191B2B is generally a small offset in fit parameter values, with $< 1\%$ relative error between the truth and best fit cosmological parameters. The small error suggests that the systematic error between NLTE and LTE flux models error will have minimal impact on the determination of cosmological parameters with SNAP.

Table 7.1. The cosmological parameter error induced by the G191B2B systematic model flux error

Parameter	Truth	Parameter Error
Ω_M	0.3	-0.002
w_0	-1.0	-0.008
w_a	0.0	-0.001

The cosmological parameter error induced by the systematic model flux error G191B2B is only one such calibration error model. In order to test different flux calibration errors that may come from other standard stars, I modeled a wavelength-dependent error as a linear error function with an adjustable slope and intercept across the SNAP wavelength range. This model roughly follows the trend of the model flux error for G191B2B shown in Figure 6.2(b). Using this model, I can test a range of systematic model flux errors that will bracket the actual standard star error imposed on SNAP. I implemented the linear error model with

$$\epsilon(\lambda) = b(\lambda - \lambda_0), \tag{7.2}$$

where b is the slope, λ_0 is the wavelength where $\epsilon = 0$, and the wavelength values used in this study range from 0.35 to 1.7 microns. For this particular study, I chose to model the G191B2B error by pinning λ_0 to 0.4 microns and only vary the slope of the error from -0.1 to 0.1. This range of linear error slopes should bracket the

HST standard star flux errors which may be used to calibrate SNAP (Bohlin, 2007). The steps in the error slope b were 0.005, 0.01, 0.02, 0.03, and 0.1, each of which correspond to the error imposed 1.4 microns according to Equation 7.2.

The results of this linear calibration error study on the cosmological parameters of Ω_M, w_0, and w_a are shown in Figure 7.3. As seen in the G191B2B calibration error result, the effect of the linear calibration error pushes the cosmological parameter values away from the input cosmological parameters. The error for each parameter is slightly non-linear and non-symmetric about the true cosmological parameter values. However, the cosmological parameter errors imposed by the linear calibration error appears to be well behaved and continuous for both positive and negative error slopes. Therefore, each of the parameter errors in Figure 7.3 can be fit using a simple least squares fit to a third order polynomial. The polynomial coefficients of A(0)...A(3) are summarized in Table 7.2. This simple fit for the effect of linear calibration error on the cosmological parameters may be used when determining requirements for the SNAP fundamental standard star flux error.

Table 7.2. The coefficients of a third order polynomial fit to the cosmological parameters that have been biased by a linear calibration error.

Coefficient	Ω_M	w_0	w_a
A(0)	0.30	-1.00	0.01
A(1)	0.23	0.23	-4.50
A(2)	0.58	-0.69	4.70
A(3)	-1.47	0.64	2.40

This study suggests that a systematic calibration error that linearly increases from the optical into the NIR will likely contribute to an offset in the fit parameter values. Given the expected level of uncertainty in the parameters, however, these errors do not appear to be significant for SNAP. If other priors are imposed on the cosmology fit to help reduce the dark energy parameter uncertainty, then this study should be revisited to ensure that the calibration error does not exceed the new uncertainties.

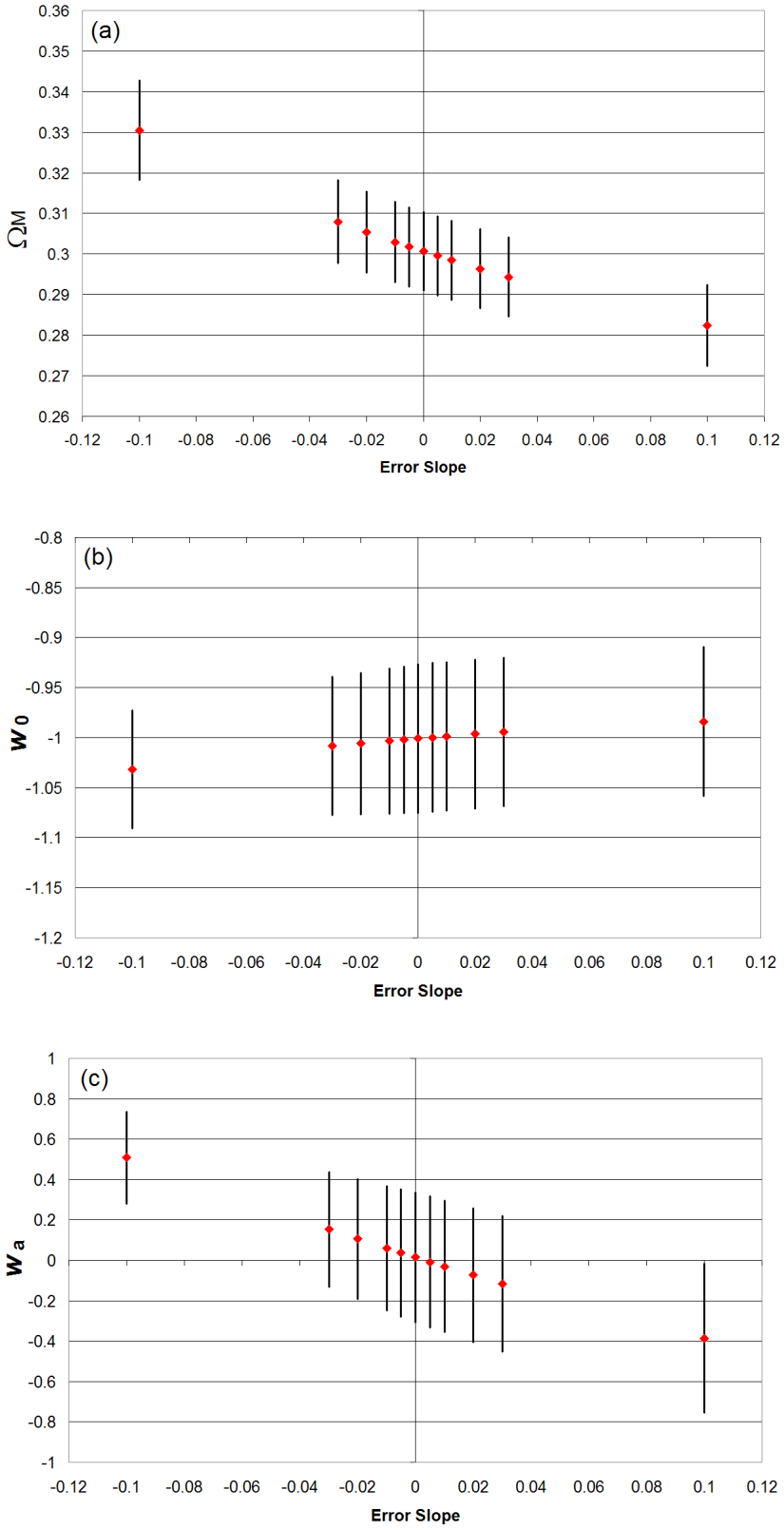

Figure 7.3. The effect of linear calibration error on the cosmological parameters of (a) Ω_M, (b) w_0, and (c) w_a.

For the NLTE and LTE flux models of the HST white dwarf standards, I conclude that the current level of precision is sufficient for calibrating the SNAP SNIa survey within the dark energy parameter uncertainties.

7.3 Filter Calibration Error

As discussed in Section 6.3, I have developed two techniques to measure filter transmission functions using LEDs. The first technique uses LED input to a monochromator to produce narrowband light that is characterized by the ratio of an unfiltered photodiode to a filtered photodiode. The use of LED sources into a monochromator requires that the resulting transmission function be calculated as the weighted mean of the individual LED measurements. The second technique was to use the total LED emission without a monochromator to track filter transmission changes. This technique uses a three parameter filter function model and initial measurements of the LED spectrum and filter transmission to calculate changes in the function.

For both of these approaches, I introduced variations to the transmission functions of two different filters by rotating them with respect to normal photon incidence. The two filters tested by these techniques had very different transmission functions. One filter was purchased from Oriel, was narrow in width, and had a smooth shape. The second filter was purchased from Omega Optical, had twice the width of the Oriel filter, and had "ripples" in the transmission shape (see Table 6.4 for the filter specifications). Section 6.3.3.2 showed that LED-fed monochromator method works nearly as well as a QTH-fed monochromator to measure changes in the transmission function of both filter types. The main problem with this method is that a monochromator is inefficient, and therefore coupling LEDs with a monochromator to measure filter transmission functions can be limited by signal to noise. When using the total LED emission to track filter transmission changes, the smooth Oriel filter shape was more accurately tracked than the SNAP-BP1 filter which contains ripples in the transmis-

sion. Overall, the LED-fed monochromator technique is more precise than the total LED emission technique at measuring changes in a filter transmission function.

The central question to answer is how the precision of these two transmission measurement techniques affect the determination of the cosmological parameters with SNAP. Using my measurements of filter transmission functions and the routines available in SNAPSim, I can answer the following questions: Is the filter tracking method using total LED emission sufficient to monitor filter transmission on SNAP? If not, is an LED-fed monochromator is required to deliver the precision filter calibration necessary to meet SNAP's science goals? Further, since I have measured a filter with a smooth transmission function and a filter with a rippled transmission function, I can determine if my characterization of the ripples using LED total emission affects the cosmology fit.

7.3.1 Implementation of Filters in SNAPSim

Using the SNAPSim routines, my measured filter transmission functions and errors from the LED-fed monochromator technique and total LED emission technique can be incorporated into the SNAP mission simulation environment. Since I have only measured two different filter transmission functions, however, I have generated a SNAP filter set from each of my measured filter functions. I placed the following requirement on these simulated filter sets: (1) each set contains nine filter bands, (2) each set has filters that are logarithmically spaced in wavelength according to Equation 2.1, and (3) the filters must cover the wavelength range from 0.4 to 1.7 microns. With these requirements, I have written code in SNAPSim that takes input from a user supplied transmission function and generates a filter set that is appropriate to the SNAP mission. Figures 7.3.1 and 7.3.1 show each of the filter sets constructed from the measured transmission curves of the smooth Oriel filter and the SNAP-BP1 filter. Further, I have also written code to implement the measured filter transmission error

to these calibration of these filter sets. If the calibration of a filter set was perfect, the SNAPSim calibration routine returns the transmission function for the filter set used as input into the simulation. To calculate the effect of the filter calibration error on the cosmological parameters, I compared the best fit cosmology parameters between a simulation with perfect filter calibration and a simulation with the measured filter calibration error.

There are two ways I implemented the calibration errors in the SNAPSim filter set. For the first method, I simply applied the measured filter error from one transmission function equally on all transmission functions in the filter set. This method is considered the worst-case scenario and it represents a filter calibration method that has a systematic, wavelength dependent error for each SNAP filter. Such a systematic error would be completely correlated for all filters, and I will refer to it as the "correlated systematic error" implementation. For the second implementation method, I created a histogram with the filter error measured at every nanometer across the filter transmission curve. I then propagated this error to the other filters in the set by randomly choosing an error at every nanometer from the error distribution. This error implementation method gives the same flux error as the correlated systematic error implementation and makes the errors uncorrelated in wavelength.I will refer to it as the "random error" implementation. The "real" SNAP error case should be bracketed by these implementations with the correlated systematic error as the worst case scenario and the random error the best case scenario.

I have chosen to perform all tests using the filter transmission curves measured at a 10° incidence angle. The measurements made at 10° represent a transmission function that has been varied from its original 0° incidence angle. In terms of the SNAP mission, this variation introduced to the original transmission function represents and unknown change to the filter transmission function while SNAP is in flight. As discussed in Section 6.3, two transmission measurement techniques using an LED-fed

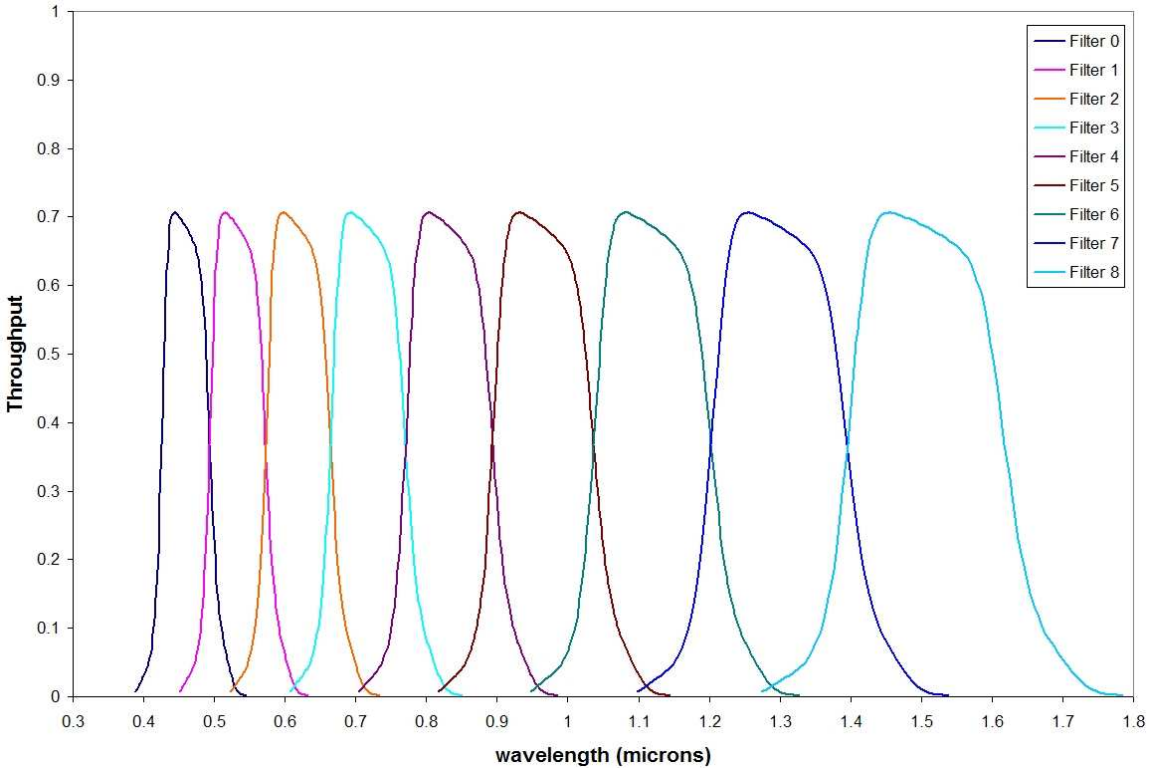

Figure 7.4. The simulated SNAP filter set using the transmission measurements of the smooth Oriel filter. This filter set was based on Oriel filter transmission function at 10° incidence angle and measured with a monochromator fed by a QTH lamp (see Figure 6.9).

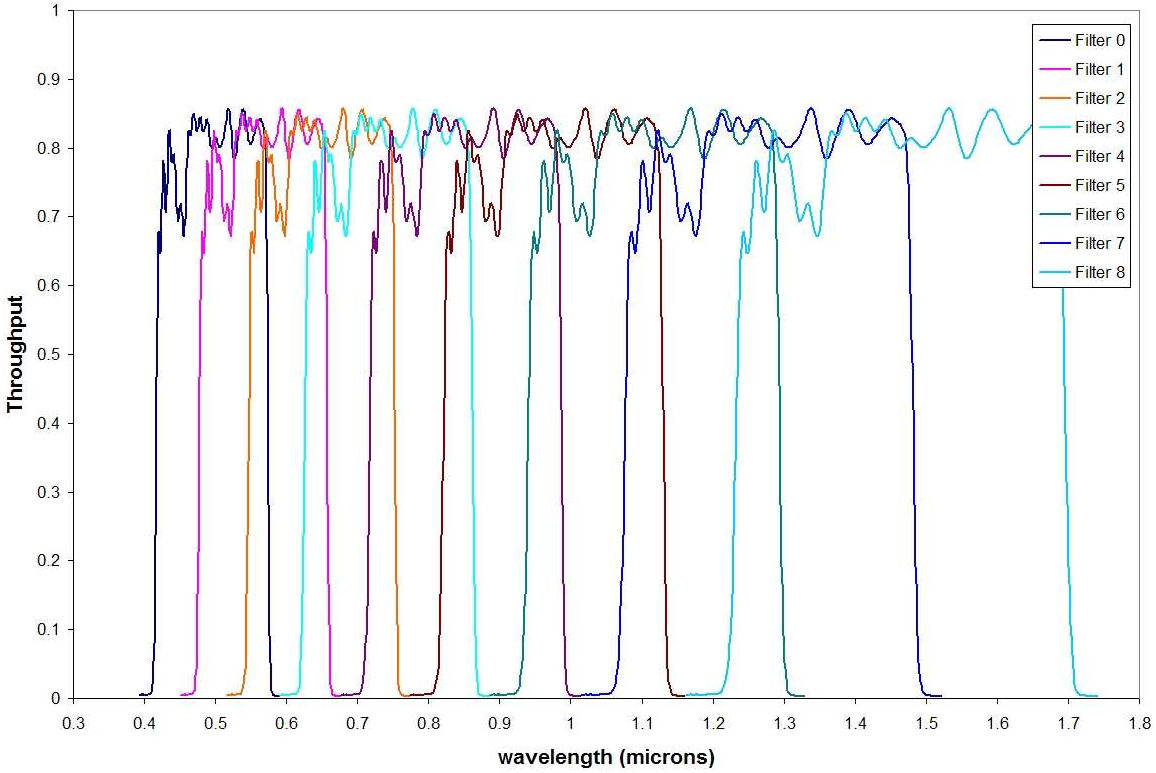

Figure 7.5. The simulated SNAP filter set using the transmission measurements of the rippled SNAP BP1 filter. This filter set was based on SNAP BP1 filter transmission function at 10° incidence angle and measured with a monochromator fed by a QTH lamp (see Figure 6.11).

monochromator or total LED emission measure the modified transmission function at 10°. The transmission error from these measurement techniques represents the precision to which each method can recover the altered filter transmission function. In the next two sections, I will study the effects of the transmission errors on the determination of cosmological parameters.

7.3.2 Filter Transmission from an LED-fed Monochromator

In Section 6.3.2, I measured the shape of a smooth filter function and a rippled filter function using the emission from multiple LEDs to illuminate a monochromator and to produce narrowband light. The resulting transmission functions for both filters at 10° incidence angle are shown in Figures 6.5 and 6.6. The difference between these LED-determined filter transmission curves and those measured using a QTH input light source are shown in Figure 7.6. For the purposes of testing the modified transmission functions at 10° incidence angle, the curves determined by the QTH lamp source are designated as the "true" transmission and the curves measured with the LED source are the "test" transmission functions. The figure shows that difference between the test and true transmission functions at 10° using an LED-fed monochromator is $< 1.5\%$ for the smooth filter function and $< 4.5\%$ for the rippled filter function. Figure 7.6 also demonstrates that the error in the rippled filter function varies more over the filter bandpass than the smooth filter. This variation can be attributed to the lower signal-to-noise that was present I measured the rippled filter in the MICCS system.

I then applied the measured error from the LED-fed monochromator technique as a calibration error to the simulated SNAP filter set based on either the Oriel or SNAP-BP1 filter. A simple way to implement the measured error from one filter transmission function to the entire simulated filter set is to apply the error equally to each filter function. I applied the measured error with the same functional form as it

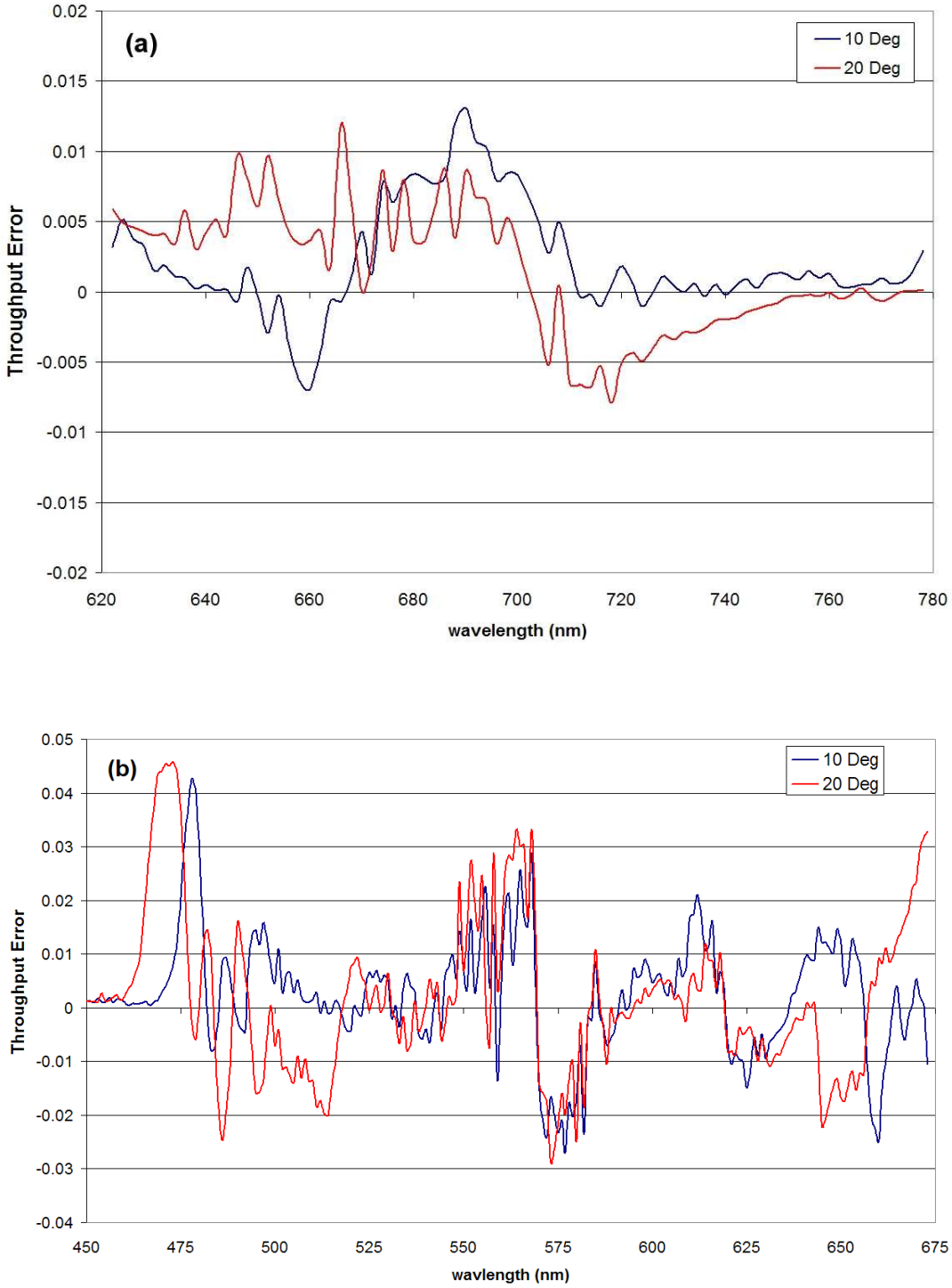

Figure 7.6. The measurement error using narrowband light from a monochromator illuminated by LEDs for the (a) smooth Oriel filter and (b) the SNAP BP1 filter.

was measured to every filter in the SNAP filter set, and therefore, this implementation of the error is systematic and correlated for all filters.

As discussed in Section 7.2, when a calibration error is applied within SNAPSim, the analysis chain produces cosmological parameter fit values that can be compared to the input cosmological values. The deviation of each parameter from its input value due to calibration error provides a measure of the accuracy of the calibration method for SNAP. In the case of the LED-monochromator filter calibration method, the deviations in the cosmological parameters are summarized in Table 7.3.

Table 7.3. The error in cosmological parameter values due to filter transmission error using an LED-fed monochromator as the transmission measurement method.

Parameter	Input	σ_{fit}	Parameter Error	
			Oriel	SNAP-BP1
Ω_M	0.3	0.01	0.001	0.001
w_0	-1.0	0.07	-0.002	-0.004
w_a	0.0	0.32	0.014	-0.009

The table shows that errors in the cosmological parameter values are small relative to the fit error, which demonstrates that the determination of cosmological parameters is accurate when an LED-fed monochromator with narrowband emission is used for filter transmission calibration. Further, the results show that the difference in parameter determination between smooth and rippled filter function is minor, even though the measurements of the SNAP-BP1 filter had a lower signal to noise than the Oriel filter measurements. Relative to the fit uncertainty, the fit parameter error from both filter transmission functions is $< 6\%$ in w_0 and w_a and 10% for Ω_M due to the smaller fit uncertainty.

I can conclude from these results that a monochromator illuminated by an LED source can determine filter transmissions, regardless of shape, with a minimal amount of contribution to cosmological parameter error.

7.3.3 Filter Transmission from Total LED Emission

Section 6.3.3.1 demonstrated a technique using total LED emission to measure changes in a filter transmission function. I calculated the measured error for this technique as the difference between the transmission determined by the LEDs and the transmission determined with narrowband light from a QTH lamp and monochromator. The error for the smooth Oriel filter transmission at 10° and 20° filter incidence is shown in Figure 7.7(a) and the error for the rippled SNAP-BP1 bandpass is shown in Figure 7.7(b).

Following the two error implementations discussed in Section 7.3.1, I incorporated these filter transmission errors into the SNAPSim environment and determine their effect on the cosmological parameters. As was done for the transmission error from the LED-fed monochromator technique, the transmission error from the total LED emission was applied equally to each filter in the SNAP filter set, thus making the error systematic and correlated between filters. In addition, I also implemented the transmission errors by creating an error distribution from the measured errors and then randomly drawing an error value from the distribution at every nanometer. The error distributions created from the Oriel and SNAP-BP1 filter transmission function errors are shown in Figure 7.8.

Once the filter transmission error has been implemented to the filter calibration in SNAPSim, I ran the analysis software on the generated SNIa data and fitted the cosmological parameters (see Section 7.1 for details). Since calibration errors tend to alter the fit values from their input values, the effect of the filter calibration error on the cosmological parameters has been characterized as the deviation of the parameter values between the simulation case with and without filter error. The results of the filter error implementations for the total LED emission technique are summarized in Table 7.4.

The table values show a significant increase in parameter error for the total LED

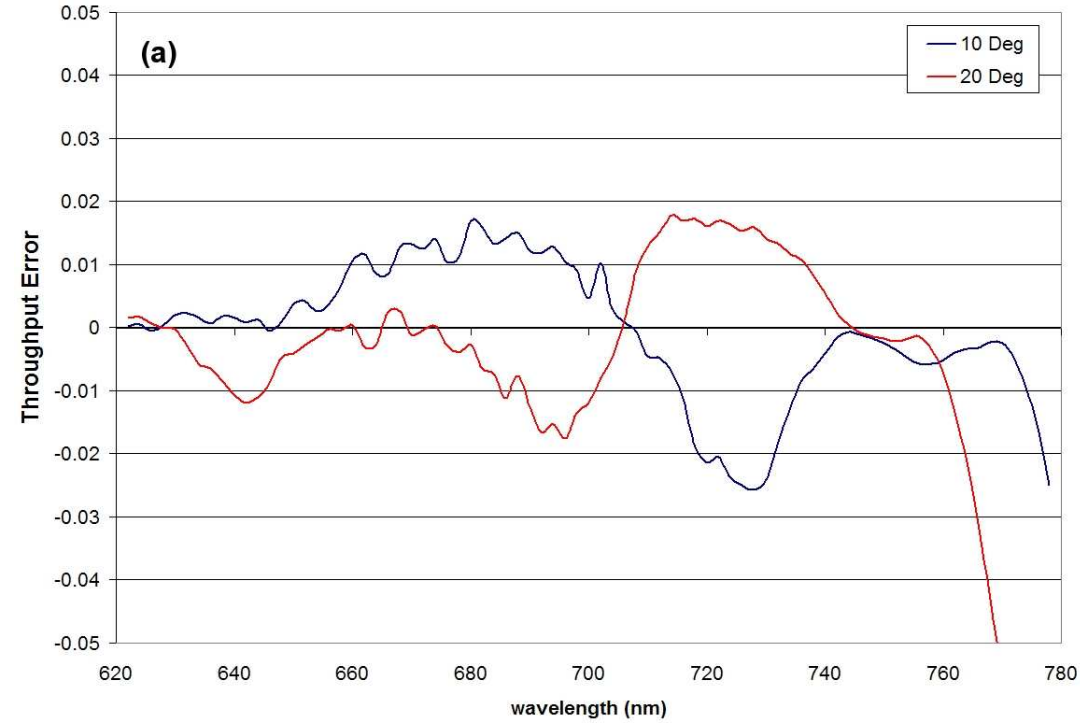

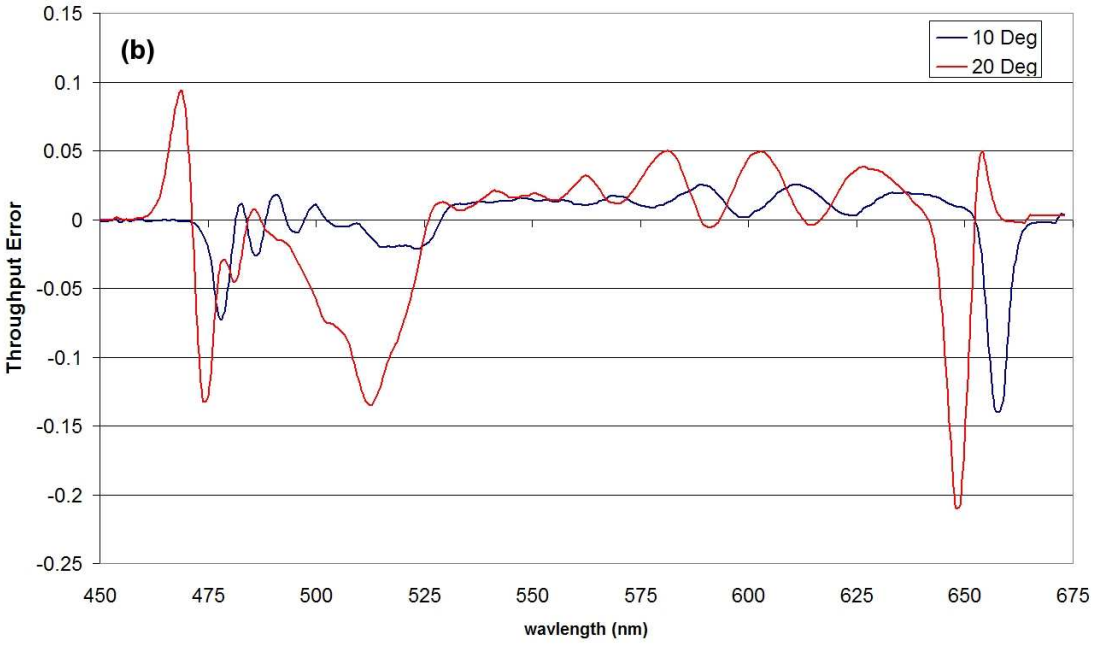

Figure 7.7. The measurement error for the smooth Oriel filter (a) and the SNAP BP1 filter (b) using narrowband light from a monochromator illuminated by LEDs.

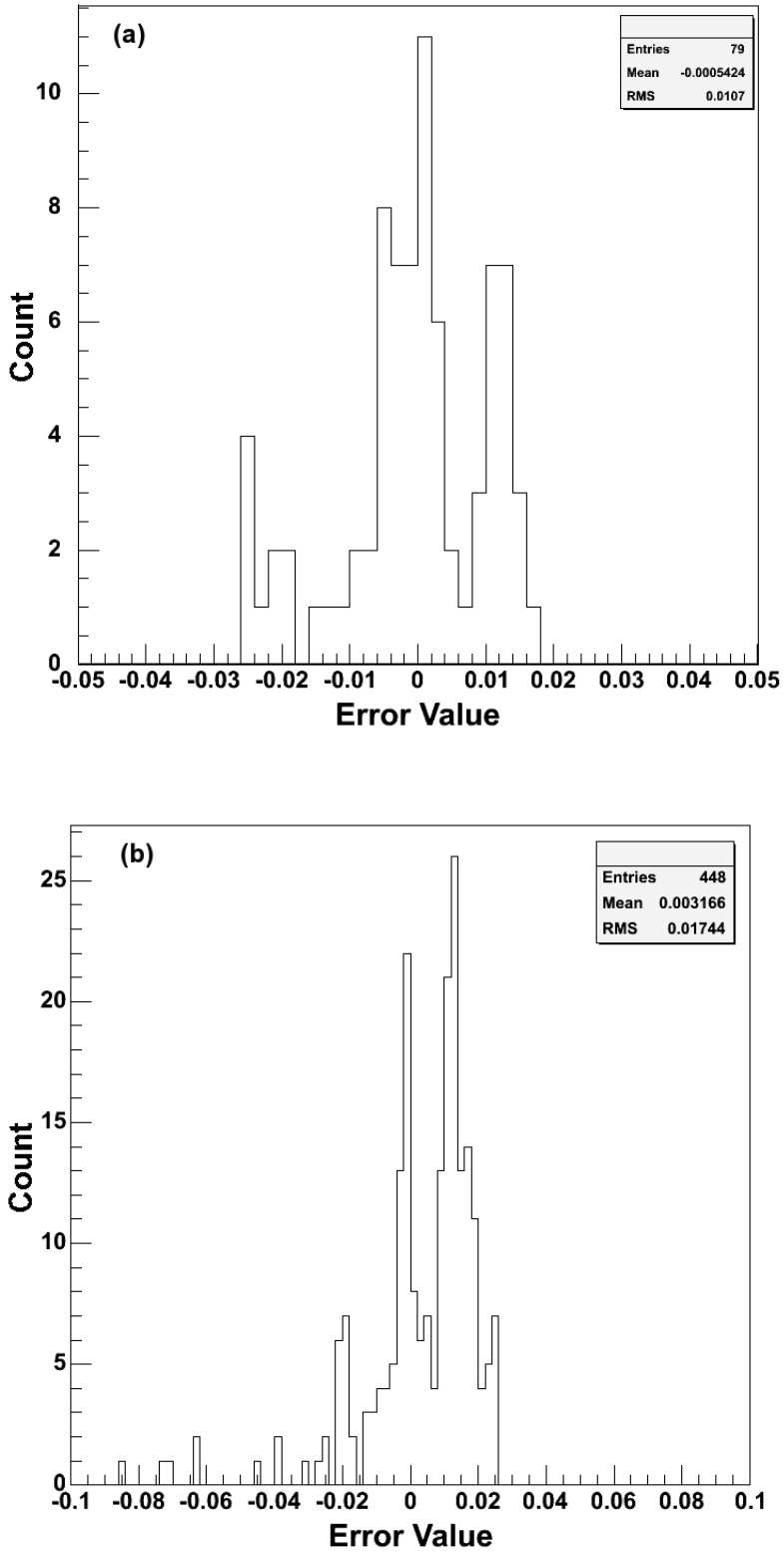

Figure 7.8. The error distributions created from the filter transmission function error using the total LED emission technique for (a) the Oriel filter and (b) the SNAP-BP1 filter. In the random error implementation, error values are randomly drawn from these distributions and applied to the filter transmission functions of the SNAP filter set.

Table 7.4. The offset in cosmological parameter values due to filter transmission error using the total emission from LEDs. The random and correlated headings denote how the transmission error was implemented in the simulated filter set.

Parameter	Oriel Filter		SNAP-BP1 Filter	
	Random	Correlated	Random	Correlated
$\Delta\Omega_M$	0.003	0.016	0.009	-0.001
Δw_0	-0.018	-0.103	-0.052	0.035
Δw_a	0.124	0.573	0.303	-0.148

emission technique over the parameter error values using the LED-fed monochromator technique shown in Table 7.3. In fact, the parameter error produced from the LED-fed monochromator technique is an order of magnitude smaller for all cosmological parameters. For the w_0 parameter and the smooth Oriel filter, the LED-fed monochromator is over 100 times more accurate than the total LED emission technique when the correlated systematic error implementation was used. These results indicate that the LED-fed monochromator technique is the more accurate method to track filter transmission changes between the two techniques.

However, it is not clear *why* the cosmological parameter error is so different between the two techniques, regardless of filter type or error implementation method. By comparing Tables 6.5 and 6.7, I have noticed there is a small difference in the filter parameter error between both measurement methods. The largest difference in filter parameter error is in the filter width $\Delta\lambda$, which increased from 0.1% to 1%. Table 6.8 shows that the LED-fed monochromator method also has a smaller peak transmission error than the total LED emission method, but this difference is only $\sim 1\%$ in transmission for the smooth Oriel filter. This small difference between the peak transmission errors likely cannot produce a factor of ten difference in cosmological parameter accuracy because it introduces very little error ($\ll 1\%$) in the integrated SNIa flux.

However, if I compare the filter transmission error functions in Figures 7.6 and 7.7, I notice that the transmission error from the LED-fed monochromator technique is $<$

1% across the majority of the transmission function in both the Oriel filter and SNAP-BP1 filter and that the error tends to vary around zero. This is not the case for total LED emission technique, which produces transmission errors that are over 1% across a large portion of the transmission functions in both filters, and the transmission errors tend to be systematically positive or negative. For example, the error in the Oriel filter transmission function from 700-750nm is nearly zero in Figure 7.6(a) in the case of the LED-fed monochromator, whereas the transmission is systematically low by 1-2% in the case of the total LED emission shown in Figure 7.7(a). This correlation suggests that both the shape and size of the filter transmission error may play a factor in the cosmology fit, but the precise behavior is not apparent from my limited set of cosmology fits.

Other implications from the cosmological parameter errors in Table 7.4 are difficult to decipher. The random error implementations seems to behave as expected, with the larger parameter error coming the larger error distribution from Figure 7.8(b) for the SNAP-BP1 filter. Also, the parameter error is larger for the correlated systematic error implementation than the random error implementation for the Oriel filter, which I would expect if there are correlated errors in the SNIa peak magnitudes that bias the cosmology fit. However, in the case of the SNAP-BP1 filter, the correlated systematic error produces a parameter error that is smaller than the random error.

To investigate how the filter calibration error affects the cosmology fits, I plotted the SNIa data that is fit by the cosmology fitter: SNIa effective peak B-band magnitudes against SNIa redshift. This plot is called a Hubble diagram, and an example can be seen in Figure 1.2. In a similar way, I plotted the Hubble diagram for the SNIa data using smooth Oriel filter with the correlated systematic error implementation from the LED-fed monochromator technique and the total LED emission technique in Figure 7.9. I also plotted the expected magnitudes for the SNIa data given the input cosmology of $\Omega_M = 0.3$, $w_0 = -1$, and $w_a = 0$. Figure 7.9 shows that the peak

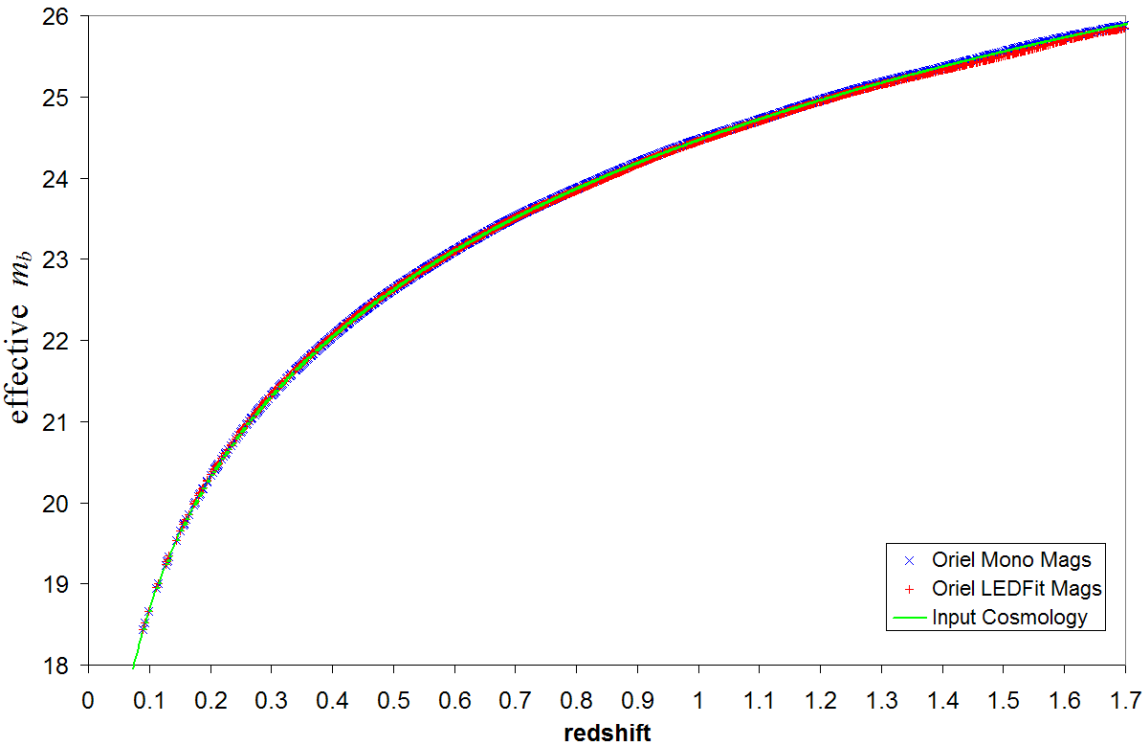

Figure 7.9. The Hubble diagram for the SNAPSim data using the LED-fed monochromator filter calibration technique (blue) and the total LED emission technique (red). The expected SNIa magnitudes for the input cosmology is also shown (green).

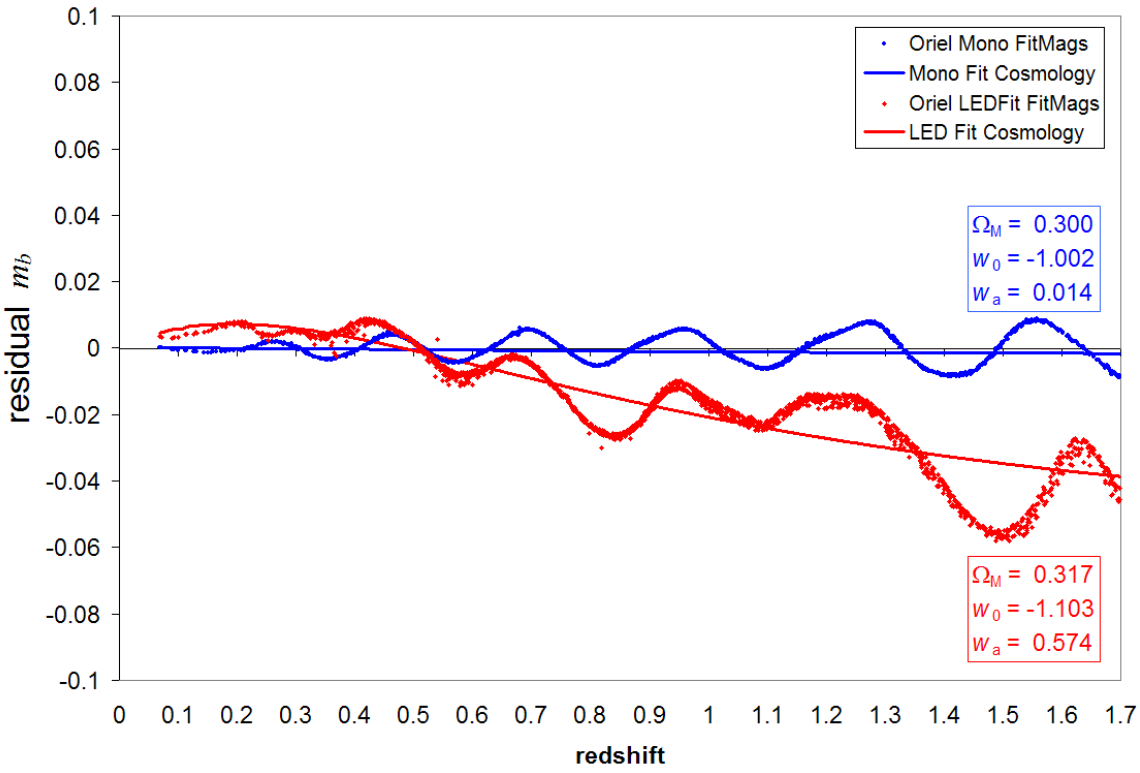

Figure 7.10. The difference between the fit SNIa peak magnitudes and the expected magnitudes from the SNAPSim input cosmology of $\Omega_M = 0.3$, $w_0 = -1$, and $w_a = 0$. Using the Oriel filter and the systematic correlated error implementation, the fit magnitude residuals from the LED-fed monochromator filter calibration technique (blue) and the total LED emission technique (red) are shown. The cosmological parameter fits for each technique are also plotted with the data.

magnitudes are all closely overlapped, and yet the best fit cosmological parameters are widely different between the two calibration methods for the Oriel filter. This qualitatively demonstrates that a high level of photometric accuracy is required to precisely determine the cosmological parameters.

To better see the differences between the best fit cosmologies for both techniques, I plotted the differences between the fit peak magnitudes for each calibration technique and the expected peak magnitudes given the input cosmology (see Figure 7.10). This figure shows the effect of the transmission errors from both calibration techniques on the cosmological parameter fits. Clearly, the LED-fed monochromator method results in smaller residuals in the fit magnitudes than the total LED emission method,

thus producing a more accurate determination of the input cosmological parameters. The correlated systematic error implementation of the filter transmission errors have also introduced oscillations in the fitted SNIa magnitudes versus redshift. The ripple behavior could be problematic for the cosmology fitter, which is essentially attempting to fit a curved line to the SNIa distance moduli against the SNIa redshift values. The largest concern is in the optical data at the lowest redshifts. For the SNIa at low z, their signal to noise is much greater than the high redshift SNIa, giving them larger statistical significance to the cosmology fit.

The importance of filter calibration in the optical can be better seen by plotting the peak magnitude residuals using the SNAP-BP1 filter for both calibration techniques. Figure 7.11(a) shows the correlated systematic error implementation of the transmission error using the LED-fed monochromator and total LED emission methods for the SNAP-BP1 filter. The plot shows similar variations in the magnitude residuals between calibration methods, and yet the cosmological fit parameters using the monochromator calibration method are nearly 10 times more accurate at reproducing the input cosmological values of w_0 and w_a than the total LED emission method. One noticeable difference between the cosmology fits for both methods can been seen at low redshifts where the optical photometry determines the SNIa magnitudes. In Figure 7.11(b), I plotted the low redshift end of the SNAP-BP1 results to better show the differences in the fit cosmologies. The cosmological fit to the total LED emission calibration method clearly shows a turn-over in the fit at low redshifts, whereas the cosmology fit with the monochromator method does not have a turn-over at low redshifts. This result suggests that filter calibration errors in the optical filters cause oscillations in the SNIa magnitudes that may hamper the ability of the cosmology fitter to accurately determine the expansion behavior at low redshifts. The imprecise fit of the optical data leads to an incorrect fit of the cosmological parameters.

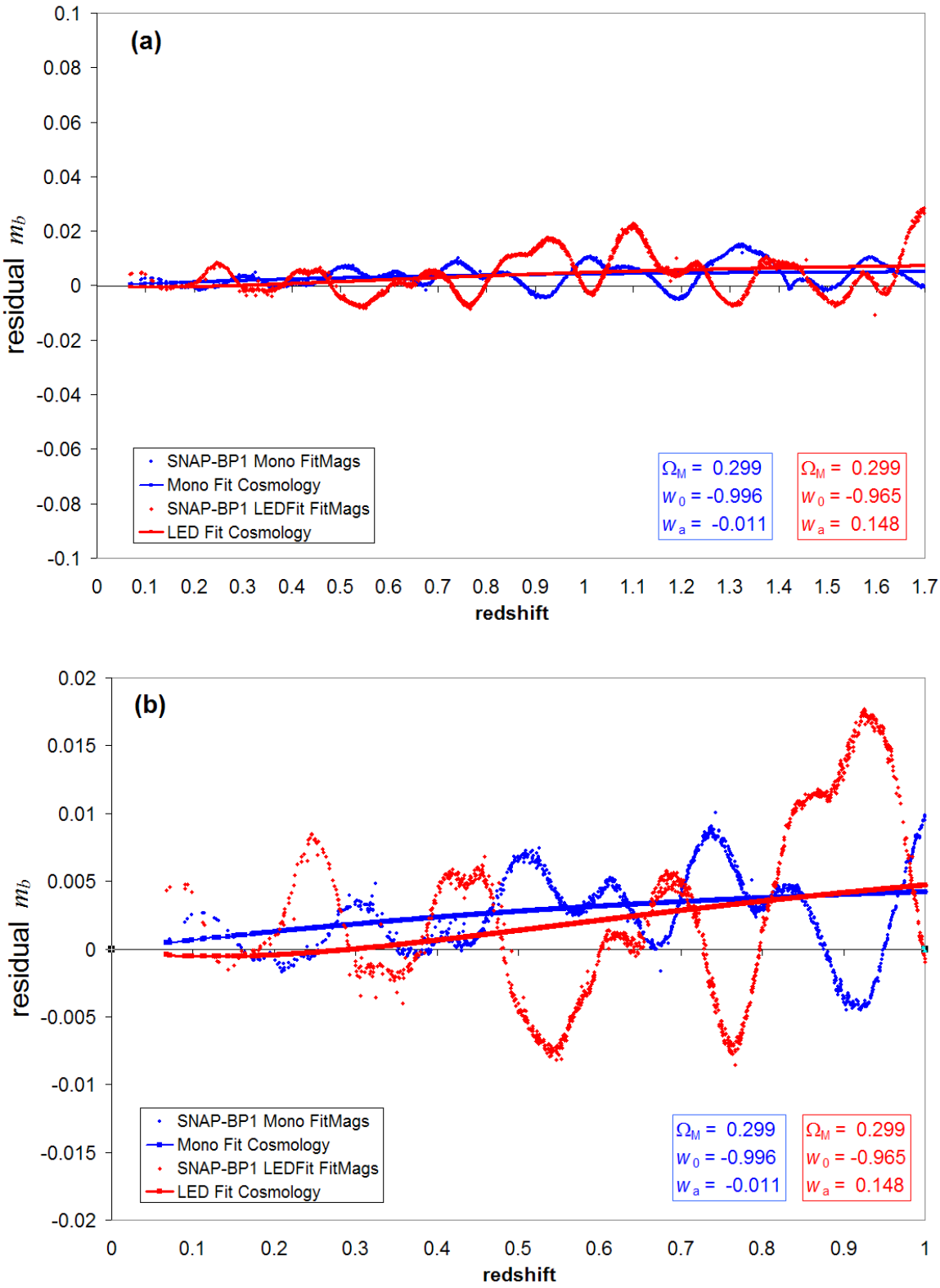

Figure 7.11. The fit magnitude residuals for the SNAP-BP1 filter using the systematic error implementation with the transmission error of the LED-fed monochromator method (blue) and the total LED fit emission method (red). Figure (a) shows the entire SNAP redshift range and Figure (b) emphasizes the low redshift range.

The source of the oscillation behavior in the fit magnitude residuals is a complex mix of the filter transmission error, multi-epoch SNIa spectra, instrument channel efficiency, K-corrections, and host galaxy extinction. Filter calibration errors not only affect the SNIa peak magnitude measurement, but they also affect our understanding of the SNIa colors (the ratio of fluxes from two different filters) and the effect of extinction on SNIa. To fully understand the systematic effect of filter transmission errors on the cosmological parameter determination, the full simulation and analysis chain provided by SNAPSim is required.

Another important result from the values in Table 7.4 is the difference in cosmological parameter errors between the smooth Oriel filter transmission function and the rippled transmission function of the SNAP-BP1 filter. The results from using the LED-fed monochromator technique to determine filter transmissions indicates that both smooth and rippled transmission shapes can be measured with high enough accuracy to cause only a small error in the determination of cosmological parameters (see Section 7.3.2 for discussion). However, as shown in Figure 7.7, the filter transmission errors measured using the total LED emission technique are larger for the rippled SNAP-BP1 filter function than the smooth Oriel filter function. To study the effect of filter shape on the determination of cosmological parameters using the total LED emission technique, I compared the transmission errors from the Oriel and SNAP-BP1 filter using the random error implementation. Figure 7.12 plots the fit magnitude residuals and the best fit cosmologies for both filters. It is clear from the figure that the fit cosmology is more accurate relative to the input cosmology if a smooth filter function is used with the total LED emission technique. By comparing the cosmological parameter errors from the random error implementation in Table 7.4, I have calculated that parameter error increases by a factor of 2.9 for w_0 and 2.4 for w_a when calibrating a rippled filter function rather than a smooth filter function (see Table A.1).

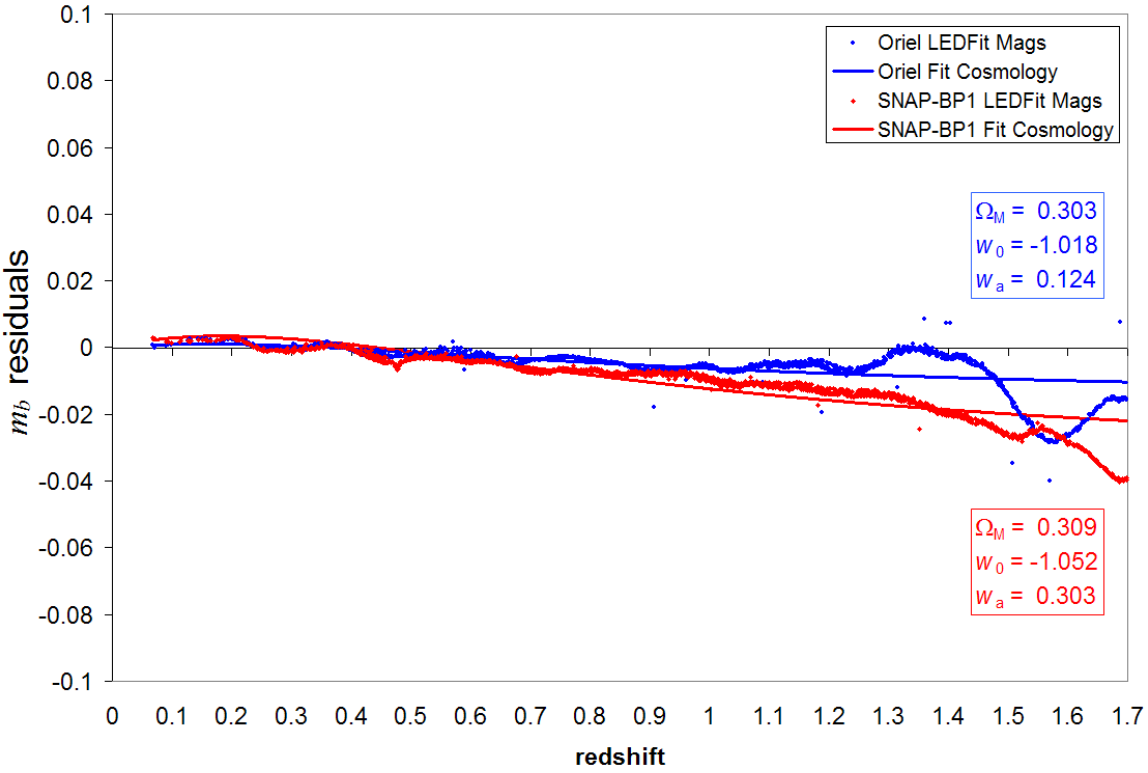

Figure 7.12. The error in the fit SNIa magnitudes for the smooth Oriel filter (blue) and the rippled SNAP-BP1 filter (red). The total LED emission technique was used to determine the filter transmission functions, and the filter errors were applied with the random error implementation.

I expect the parameter error to increase since the filter transmission error is larger for the rippled SNAP-BP1 filter function than the smooth Oriel filter function. One reason for the increased error is that the total emission of each LED used to measure the transmission is wider than the transmission ripples, and therefore any changes to the ripple shape is more difficult to track accurately. Further, some transmission ripples appear to behave independently from the global filter parameters that I have used to perform the transmission tracking.

The increase in parameter error from the LED tracking technique suggests that if the technique is used, the best results will come from filters that have smooth transmission functions. The results also suggest that if rippled filter transmission functions are used, a more detailed parameterization of the filter transmission may be required to deliver an accurate filter calibration and measurement of the cosmological parameters.

7.3.4 Conclusions

Table A.1 summarizes the increase in parameter error for the filter calibration errors discussed in Sections 7.3.2 and 7.3.3. The error increase is calculated as a factor γ multiplied by the parameter error. Case 1 of Table A.1 shows the increase in parameter error using the total LED emission technique instead of the LED-fed monochromator technique to measure filter transmissions. For this case, only the correlated systematic error implementation of the transmission function errors are considered. The transmission measurement technique using total LED emission clearly degrades the accuracy of the cosmological parameters in comparison to the an LED-fed monochromator technique. This observation is true for both the Oriel and SNAP-BP1 filters. I have suggested that the reason for the increase in parameter error with the total LED emission method appears to be correlated with the shape and size of the transmission error.

Table 7.5. Summary of the parameter error increase factor γ using (Case 1) the total LED emission method instead of the LED-fed monochromator and (Case 2) a rippled filter instead of a smooth filter for the total LED emission method.

Parameter Error	γ(Case 1)		γ(Case 2)
	Oriel	SNAP-BP1	
$\Delta\Omega_M$	16.0	0.0	3.0
Δw_0	51.5	8.9	2.9
Δw_a	40.9	16.4	2.4

I have also shown that the increase in parameter error between calibration techniques may be influenced by the transmission error in the optical filters. The SNIa magnitudes measured in the optical filters have high signal-to-noise which gives them more weight in the cosmology fit. In addition, errors in the filter transmission functions cause oscillations in the fit magnitudes versus redshift. These two factors combine to produce systematic error in the SNIa magnitudes at low redshifts. These systematic errors may influence the cosmology fit and produce incorrect cosmological parameter fits.

Case 2 of Table A.1 shows the parameter error increase when the total LED emission technique is used to measure a rippled filter transmission function instead of a smooth filter function. The cosmological parameter error increase suggest that a smooth filter is better suited for use with the total LED emission technique. Rippled filter transmission functions are more difficult to measure with the total LED emission technique since the transmission ripples do not behave the same as the global filter properties I have used to parameterize the filter transmission changes. This fact leads to larger error in the fit transmission function and larger error in the fit cosmological parameters.

CHAPTER 8

Conclusions

SNAP is a next generation space mission designed to precisely measure the cosmological parameters by reducing the systematic errors in SNIa distance measurements. In this thesis, I have addressed several key calibration issues for photometry and filters on SNAP. Each of these issues contribute to the calibration error budget and the final science-driven requirements for the calibration hardware. I will summarize the findings of my research to address these calibration problems. Finally, I offer recommendations for the SNAP calibration plan and hardware design.

8.1 SNAP Focal Plane Flux Calibration

The calibration plan requires white dwarf standard stars with spectrophotometry from HST to set the fundamental flux scale. Both NLTE and LTE flux models have been previously calculated for these fundamental calibration stars, and I have calculated the systematic error between the two models. The model flux error increases linearly from the optical to the NIR to nearly 2%. I have put this systematic model error into the SNAP simulation software and I have shown that this fundamental calibration error will not have a large impact on the determination of cosmological parameters. Further, I have generalized this systematic error into a linearly increasing error model with adjustable slope and intercept. Again, the error in the cosmological parameters were shown to be relatively insensitive to a linearly increasing error, with an upper limit of 2-3% error in the slope of the calibration from the optical to the

NIR.

Since the white dwarf standards will not be in the SNAP field, the photometric calibration plan calls for a second set of fainter standard stars in the survey field for monitoring of the SNAP throughput. These "Primary" standards must be observed to be stable at the <1% level in order to be used as stable standard stars for use with SNAP. To address this stability requirement, I have conducted a observing campaign using the WIYN 0.9m telescope to find stable standards with a range of stellar temperatures within the SNAP field. A candidate list of Primary standards can be found in Appendix A.

I have also demonstrated a flat field method using dithered images of stars to normalize photometry on large spatial scales. This stellar flat field process will be useful to calibrate the SNAP focal plane with multiple detectors and filters. Combined with an onboard illuminator called the "Ring of Fire" (RoF), the SNAP photometry will be normalized across small (pixel-sized) and large (detector-sized) scales with <1% error.

8.2 Filter Characterization

One essential component that influences the relative photometry of SNAP are the filter transmission functions. Because the SNAP filter transmissions will be nine logarithmically spaced copies of each other, interference filters have been proposed as the baseline technology for filter development. While interference filter technology has been used successfully in astronomical systems, there is little data on how their filter functions change in space environments. Further, interference filters are known to have transmissions that are dependent on the incident angle of the incoming photons. The SNAP focal plane filters will have a range of photon incidence angles from 5° to 20°, and these angles will alter the filter transmission functions across the focal plane. It will therefore be necessary to characterize the filter transmissions in the laboratory

and track them while SNAP is in orbit.

To address the question of what measurements are required to characterize the SNAP filters before launch and in orbit, I have designed and built the MICCS laboratory calibration system. The system was designed to place interference filters in a space environment similar to what SNAP will encounter and match the range of photon incidence angle that will be present on the SNAP focal plane. I have measured the transmission function of three different interference filters that were purchased from a commercial vendor. While two of the filters showed no change in transmission when measured under vacuum, the SNAP-BP2 filter showed a significant deviation from the original function measured in air. I concluded that this difference may be due to the humidity in the air and that this particular filter may not have properly sealed interference film layers. The MICCS system provides an excellent way to test for such filter effects that could alter the filter transmission in a vacuum environment. I also tested the filters for variation with respect to temperature and found that all three filters have a shift in their filter function when held at 140K relative to room temperature. However, variations in the filter transmission functions were negligible between 135K and 145K. The temperature and vacuum effects on filter transmission functions are potentially significant sources of error, and I recommend that all testing of SNAP interference filters be performed under vacuum at 140K.

Because interference filters are sensitive to photon incidence angles, I have tested the three commercial interference filters at a range of angles that are similar to that seen on the SNAP focal plane. Significant variations in the filter transmission functions were found as I varied the photon incidence angle from 5° to 20°. The transmission functions varied in effective wavelength, bandpass width, and integrated throughput. Further, "ripples" in the transmission functions appeared to change independently from the global filter properties. Some ripples increase in strength while other ripples are suppressed or disappear altogether. This sort of unpredictable be-

havior can be difficult to measure and track without the use of narrowband light that can resolve the ripples. Since individual SNIa measurements on SNAP will occur at random positions anywhere within the field of view, it will be essential to precisely characterize the filter transmission functions with respect to off-axis field angle. Given a narrowband characterization of the filter functions every 5° from 0° to 20°, I have developed an interpolation method that will deliver the precise filter transmission function for any photon incidence angle that will be present on SNAP focal plane.

8.3 Filter Transmission Measurement Techniques

Initial simulations of the SNAP filter calibration showed that if the spectral emission of LEDs are precisely known, a filter transmission function could be measured more accurately with LEDs than a QTH lamp or a single white dwarf standard star with model flux error. This initial finding led me to measure filter transmissions using a monochromator with an LED illumination source. When LEDs are used, their narrowband emission requires several LEDs to span the entire bandpass. By weighting the mean transmission measurements of each of the LEDs by the signal to noise of the measurement, the filter transmission function can be measured nearly as well as a monochromator fed by a QTH lamp source.

However, a monochromator-based calibration system on SNAP poses technical challenges that might be avoided if the filters can be calibrated with the total LED emission alone. Using a three parameter model for filter transmission function variations, I developed a technique to track filter transmissions using the known spectral shape of the LED emissions, initial filter transmission function, and measurements of the filtered LED emission before and after the change to the filter function. The LED filter tracking technique can in fact measure altered filter transmission functions quite well, particularly if the filter function does not contain large ripples in transmission. For a smooth filter, the filter transmission function was measured to within 3% of

the transmission function measured using narrowband light. The technique did not perform as well for a rippled filter transmission function with errors that varied by up to 20% at the edges of the filter bandpass. All filter parameters for both the smooth filter and rippled filter were determined to 1% or better.

Using the SNAPSim software, I implemented the measured filter transmission function errors from the LED-fed monochromator technique and total LED emission technique into a simulated SNAP SNIa survey. I calculated the cosmological parameter error using the difference between the input and best fit cosmological parameters. From these studies, I found that there is minimal error imposed on the determination of cosmological parameters by using an LED-fed monochromator to measure the filter transmissions. This result holds for both smooth and rippled transmission functions. For the total LED emission calibration technique, the errors in the cosmological parameters were over an order of magnitude larger than the errors from narrowband monochromator technique. I found that when the total LED emission technique is used for filter calibration, smooth filter transmission functions are more precisely determined than rippled transmission functions, and therefore introduce less systematic error to the cosmological parameters.

One area that has yet to be explored is how the filter transmission errors affect the correlated errors in the SNIa distance moduli. There is some evidence to suggest that filter transmission errors in the optical regime are more significant in determining the cosmological parameters than in the NIR. Filter calibration errors in the optical may heavily influence the cosmology fit given the larger weight of their SN values. Therefore, future studies of filter transmission calibration should include an investigation of the calibration requirements on the optical filter transmission functions for low-redshift SNIa. Such statements about the nature of the required filter calibration for SNAP are just beginning to be understood. Given the filter transmission measurement and simulation techniques developed in this thesis, tolerances on the filter

design and calibration error can now be explored in detail.

8.4 SNAP Calibration Hardware

LEDs are a very attractive light source technology for space flight applications. Their low power usage, solid state mechanics, and semi-narrowband emission make them an excellent alternative to broadband QTH lamps. If LEDs are used on SNAP, they should have their temperatures regulated at room temperature to maintain consistency with laboratory calibrations. LEDs could be tested for operation at 140K, but the availability of a room temperature environment onboard SNAP relaxes the need to calibrate LEDs at 140K. Given their narrowband output, multiple LEDs will be required to cover then entire SNAP wavelength range with no gaps in coverage and have redundancy for each LED device. Therefore, a thermally-regulated enclosure will be required to house all the LEDs into one illumination source.

The results of the filter calibration studies suggest that the complexity of the onboard calibration light source system used for SNAP must match the complexity by which the filter bandpasses will vary. If the SNAP filter set has many ripples, all of which act independently, then the onboard light system should be capable of producing very narrowband light ($\sim$2nm FWHM) to monitor these ripples. If the filter ripples are suppressed through higher tolerances in the manufacturing process *and* the filter tracking technique can be improved with a better parameterization, then a light system based on LEDs alone might be flown to track the global changes in the filter transmission. However, the latter scenario requires additional R&D to produce smooth filter transmissions from a vendor and improve the precision of the LED tracking technique. Without such R&D, the use of an LED-fed monochromator onboard SNAP should not be overlooked in the design of a calibration light source.

To satisfy the space and thermal constraints onboard SNAP, light from the LED illumination system should be routed to the RoF. One method that has been proposed

is to route the light through silica fibers up to seven ports on the RoF. Although silica fibers do have space flight heritage, testing should be done on the desired SNAP fiber type to characterize their properties in the thermal and radiation environment of SNAP.

Finally, following the design of the MICCS system, unfiltered photodiodes are essential to measure the output of the calibration light source. Photodiodes can be used for simple monitoring of the light source stability, or with a NIST-traceable calibration, can measure the precise irradiance incident on the focal plane. Photodiodes can also be used to periodically measure a bright, stable stellar source to measure the stability of the throughput of the telescope. The measurement of a stellar source can break correlations between a change in LED output, a change in the filter throughput, or a change in the photodiode itself. Because SNAP may use photodiodes in low light level situations, future efforts should be devoted to developing a circuit capable of integrating the current output to increase signal to noise.

8.5 Final Thoughts

The current environment for cosmological discovery is filled with a deluge of theoretical ideas as to the nature of dark energy, but there is a sparse amount of data available to discern between proposed physical models. Through increased statistics and reduction of systematic errors, the measurement of SNIa with SNAP could make a decisive measurement of the dark energy parameters. In this sense, the calibration of SNAP plays an important role in the scientific return of the experiment. The calibration techniques and hardware developed in this thesis are aimed at reducing systematic photometric errors and enhancing the measurement of the cosmological parameters using SNIa. With the MICCS measurement system and SNAPSim analysis software, the science-driven requirements on manufactured filter transmissions can be defined for the SNAP mission. Further, an LED-based illumination system

designed to deliver narrowband illumination onboard SNAP can begin to be designed and prototyped. The calibration research discussed herein represents a significant step forward in understanding the requirements for calibration of SNIa photometry for dark energy measurements.

BIBLIOGRAPHY

Albrecht, A., G. Bernstein, R. Cahn, W. L. Freedman, J. Hewitt, W. Hu, J. Huth, M. Kamionkowski, E. W. Kolb, L. Knox, J. C. Mather, S. Staggs, and N. B. Suntzeff (2006, September). Report of the Dark Energy Task Force. *ArXiv Astrophysics e-prints*.

Aldering, G., C. W. Akerlof, R. Amanullah, and the SNAP Collaboration (2002, November). Overview of the SuperNova/Acceleration Probe (SNAP). In A. M. Dressler (Ed.), *Future Research Direction and Visions for Astronomy*, Volume 4835 of Proc. SPIE, pp. 146–157.

Bahcall, N. A. and X. Fan (1998, September). The Most Massive Distant Clusters: Determining Ω and δ_8. ApJ *504*, 1.

Balbi, A., P. Ade, J. Bock, and the Maxima Collaboration (2000, December). Constraints on Cosmological Parameters from MAXIMA-1. ApJ *545*, L1–L4.

Bebek, C. J. (2004, December). SNAP Focal Plane Development. In BAAS, Volume 36 of BAAS, pp. 1559.

Benford, D. J. and T. R. Lauer (2006, July). Destiny: a candidate architecture for the Joint Dark Energy Mission. In *Space Telescopes and Instrumentation I: Optical, Infrared, and Millimeter.*, Volume 6265 of Proc. SPIE.

Bohlin, R. C. (2002). STIS Flux Calibration. In S. Arribas, A. Koekemoer, and B. Whitmore (Eds.), *The 2002 HST Calibration Workshop : Hubble after the Installation of the ACS and the NICMOS Cooling System, Proceedings of a Workshop*

held at the Space Telescope Science Institute, Baltimore, Maryland, October 17 and 18, 2002., pp. 115.

Bohlin, R. C. (2007, April). HST Stellar Standards with 1 Percent Accuracy in Absolute Flux. In C. Sterken (Ed.), *The Future of Photometric, Spectrophotometric and Polarimetric Standardization*, Volume 364 of *Astronomical Society of the Pacific Conference Series*, pp. 315.

Brown, M. G. (2007). *Development of NIR Detectors and Science Requirements for SNAP*. Ph. D. thesis, University of Michigan.

Budding, E. (1993, September). *Introduction to Astronomical Photometry*. Introduction to Astronomical Photometry, by Edwin Budding, pp. 286. ISBN 0521418674. Cambridge, UK: Cambridge University Press, September 1993.

Copin, Y., N. Blanc, S. Bongard, and the Supernova Factory Collaboration (2006, June). The Nearby Supernova Factory. *New Astro. Rev. 50*, 436–438.

Davis, T. M., B. P. Schmidt, and A. G. Kim (2006, February). Ideal Bandpasses for Type Ia Supernova Cosmology. PASP *118*, 205–217.

Dodelson, S. (2003). *Modern cosmology*. Academic Press.

Fowler, J. B. and G. Dezsi (1995). High Accuracy Measurement of Aperture Area Relative to a Standard Known Aperture. *J. Res. Natl. Inst. Stand. Technol. 100*(3), 277–283.

Grandy, C. (2007, May). Priv. Comm., Omega Optical Corp.

Hamuy, M., M. M. Phillips, J. Maza, N. B. Suntzeff, R. A. Schommer, and R. Aviles (1995, January). A Hubble diagram of distant type IA supernovae. AJ *109*, 1–13.

Hamuy, M., M. M. Phillips, N. B. Suntzeff, R. A. Schommer, J. Maza, and R. Aviles (1996, December). The Hubble Diagram of the Calan/Tololo Type IA Supernovae and the Value of H_0. AJ *112*, 2398.

Heinämäki, P. (2006, December). The Planck Mission and beyond. In H. J. G. L. M. Lamers, N. Langer, T. Nugis, and K. Annuk (Eds.), *Stellar Evolution at Low Metallicity: Mass Loss, Explosions, Cosmology*, Volume 353 of *Astronomical Society of the Pacific Conference Series*, pp. 403.

Höflich, P., C. Gerardy, E. Linder, and et al. (2003). Models for Type Ia Supernovae and Cosmology. In D. Alloin and W. Gieren (Eds.), *Stellar Candles for the Extragalactic Distance Scale*, Volume 635 of *Lecture Notes in Physics, Berlin Springer Verlag*, pp. 203–227.

Honeycutt, R. K. (1992, June). CCD ensemble photometry on an inhomogeneous set of exposures. PASP *104*, 435–440.

Ishak, M., A. Upadhye, and D. N. Spergel (2006, August). Probing cosmic acceleration beyond the equation of state: Distinguishing between dark energy and modified gravity models. Phys. Rev. D *74*(4), 043513.

Kim, A., S. Deustua, S. Gabi, and the Supernova Cosmology Project (1996, February). K Corrections For Type Ia Supernovae and a Test for Spatial Variation of the Hubble Constant. *ArXiv Astrophysics e-prints*.

Kim, A. G., E. V. Linder, R. Miquel, and N. Mostek (2004, January). Effects of systematic uncertainties on the supernova determination of cosmological parameters. MNRAS *347*, 909–920.

Kim, A. G. and R. Miquel (2006, January). Optimal extraction of cosmological information from supernova data in the presence of calibration uncertainties. *Astro. Part. Phys. 24*, 451–458.

Knop, R. A., G. Aldering, R. Amanullah, and the Supernova Cosmology Project (2003, November). New Constraints on Ω_M, Ω_Λ, and w from an Independent Set of 11 High-Redshift Supernovae Observed with the Hubble Space Telescope. ApJ *598*, 102–137.

Landolt, A. U. (1983, March). UBVRI photometric standard stars around the celestial equator. AJ *88*, 439–460.

Landolt, A. U. (1992, July). UBVRI photometric standard stars in the magnitude range 11.5-16.0 around the celestial equator. AJ *104*, 340–371.

Larason, T. C., S. S. Bruce, and A. C. Parr (1998). NIST Measurement Services: Spectroradiometric Detector Measurements: Part I Ultraviolet Detectors and Part II Visible to Near Infrared Detectors. Spec. Publ. 25041, Natl. Inst. Stand. Technol., Gaithersburg, MD.

Linder, E. V. (2003, March). Exploring the Expansion History of the Universe. Phys. Rev. Lett. *90*(9), 091301.

Linder, E. V. and D. Huterer (2003, April). Importance of supernovae at z>1.5 to probe dark energy. Phys. Rev. D *67*(8), 081303.

Manfroid, J. (1995, November). Stellar calibration of CCD flat fielding. A&AS *113*, 587.

Manfroid, J. (1996, August). On CCD standard stars and flat-field calibration. A&AS *118*, 391–395.

Manfroid, J., P. Royer, G. Rauw, and E. Gosset (2001). Correction of Systematic Errors in Differential Photometry. In F. R. Harnden, Jr., F. A. Primini, and H. E. Payne (Eds.), *Astronomical Data Analysis Software and Systems X*, Volume 238 of *Astronomical Society of the Pacific Conference Series*, pp. 373.

Martel, A. R. and G. Hartig (2003). HRC and WFC Internal Tungsten and Deuterium Lamp Count Rates. Technical report, STSCI, Baltimore, MD.

Martel, A. R., G. Hartig, and M. Sirianni (2003). On-orbit HRC and WFC Internal Tungsten Lamp Count Rates. Technical report, STSCI, Baltimore, MD.

Melchiorri, A., P. A. R. Ade, P. de Bernardis, and the BOOMERANG Collaboration (2000, June). A Measurement of Ω from the North American Test Flight of Boomerang. ApJ *536*, L63–L66.

NAG (2002). http://wwwasd.web.cern.ch/wwwasd/lhc++/Gemini/.

Nugent, P., A. Kim, and S. Perlmutter (2002, August). K-Corrections and Extinction Corrections for Type Ia Supernovae. PASP *114*, 803–819.

Oke, J. B. and A. Sandage (1968, October). Energy Distributions, K Corrections, and the Stebbins-Whitford Effect for Giant Elliptical Galaxies. ApJ *154*, 21.

Pain, R., S. Fabbro, M. Sullivan, and the Supernova Cosmology Project (2002, September). The Distant Type Ia Supernova Rate. ApJ *577*, 120–132.

Perlmutter, S., G. Aldering, M. Della Valle, S. Deustua, R. S. Ellis, S. Fabbro, A. Fruchter, G. Goldhaber, A. Goobar, D. E. Groom, I. M. Hook, A. G. Kim, M. Y. Kim, R. A. Knop, C. Lidman, R. G. McMahon, P. Nugent, R. Pain, N. Panagia, C. R. Pennypacker, P. Ruiz-Lapuente, B. Schaefer, and N. Walton (1998). Discovery of a Supernova Explosion at Half the Age of the Universe and its Cosmological Implications. Nature *391*, 51.

Perlmutter, S., G. Aldering, S. Deustua, and the Supernova Cosmology Project (1997, December). Cosmology From Type IA Supernovae: Measurements, Calibration Techniques, and Implications. In BAAS, Volume 29 of BAAS, pp. 1351.

Phillips, M. M., P. Garnavich, Y. Wang, D. Branch, E. Baron, A. Crotts, J. C. Wheeler, E. Cheng, and M. Hamuy (2006, July). The Joint Efficient Dark-energy Investigation (JEDI): measuring the cosmic expansion history from type Ia supernovae. In *Space Telescopes and Instrumentation I: Optical, Infrared, and Millimeter.*, Volume 6265 of Proc. SPIE.

Phillips, M. M., P. Lira, N. B. Suntzeff, R. A. Schommer, M. Hamuy, and J. Maza (1999, October). The Reddening-Free Decline Rate Versus Luminosity Relationship for Type IA Supernovae. AJ *118*, 1766–1776.

Platais, I., V. Kozhurina-Platais, T. M. Girard, W. F. van Altena, A. R. Klemola, J. R. Stauffer, T. E. Armandroff, K. J. Mighell, I. P. Dell'Antonio, E. E. Falco, and A. Sarajedini (2002, July). WIYN Open Cluster Study. VIII. The Geometry and Stability of the NOAO CCD Mosaic Imager. AJ *124*, 601–611.

Rengstorf, A. W. (2004). *Quasar Detection via Variability in a High Galactic Latitude Drift-Scan Survey.* Ph. D. thesis, Indiana University.

Riess, A., W. Press, and R. Kirshner (1996). A Precise Distance Indicator: Type Ia Supernova Multicolor Light Curve Shapes. ApJ *473*, 88.

Riess, A. G., A. V. Filippenko, P. Challis, and the High-Z SN Search Team (1998). Observational Evidence from Supernovae for an Accelerating Universe and a Cosmological Constant. AJ *116*, 1009.

Schlegel, D. J., D. P. Finkbeiner, and M. Davis (1998, June). Maps of Dust IR Emission for Use in Estimation of Reddening and CMBR Foregrounds. ApJ *500*, 525.

Schubnell, M. (2004, February). Probing Dark Energy in the Accelerating Universe with SNAP. In Z. Parsa (Ed.), *Intersections of Particle and Nuclear Physics*, Volume 698 of *American Institute of Physics Conference Series*, pp. 323–327.

Shaw, P. S., T. C. Larason, G. R., S. W. Brown, and K. R. Lykke (2000). Improved NearInfrared Spectral Responsivity Scale. *J. Res. Natl. Inst. Stand. Technol. 105*(5), 689.

Sholl, M. J. (2004, May). SNAP Stray Light Monitoring Status. SNAP Internal Note.

Sholl, M. J., M. L. Lampton, G. Aldering, and the SNAP Collaboration (2004, October). SNAP Telescope. In J. C. Mather (Ed.), *Optical, Infrared, and Millimeter Space Telescopes.*, Volume 5487 of Proc. SPIE, pp. 1473–1483.

SNAP Collaboration: G. Aldering, W. Althouse, R. Amanullah, J. Annis, P. Astier, C. Baltay, E. Barrelet, S. Basa, C. Bebek, L. Bergstrom, G. Bernstein, M. Bester, B. Bigelow, R. Blandford, R. Bohlin, A. Bonissent, C. Bower, M. Brown, M. Campbell, W. Carithers, E. Commins, W. Craig, C. Day, F. DeJongh, S. Deustua, T. Diehl, S. Dodelson, A. Ealet, R. Ellis, W. Emmet, D. Fouchez, J. Frieman, A. Fruchter, D. Gerdes, L. Gladney, G. Goldhaber, A. Goobar, D. Groom, H. Heetderks, M. Hoff, S. Holland, M. Huffer, L. Hui, D. Huterer, B. Jain, P. Jelinsky, A. Karcher, S. Kent, S. Kahn, A. Kim, W. Kolbe, B. Krieger, G. Kushner, N. Kuznetsova, R. Lafever, J. Lamoureux, M. Lampton, O. Le Fevre, M. Levi, P. Limon, H. Lin, E. Linder, S. Loken, W. Lorenzon, R. Malina, J. Marriner, P. Marshall, R. Massey, A. Mazure, T. McKay, S. McKee, R. Miquel, N. Morgan, E. Mortsell, N. Mostek, S. Mufson, J. Musser, P. Nugent, H. Oluseyi, R. Pain, N. Palaio, D. Pankow, J. Peoples, S. Perlmutter, E. Prieto, D. Rabinowitz, A. Refregier, J. Rhodes, N. Roe, D. Rusin, V. Scarpine, M. Schubnell, M. Sholl, G. Smadja, R. M. Smith, G. Smoot, J. Snyder, A. Spadafora, A. Stebbins, C. Stoughton, A. Szymkowiak, G. Tarle, K. Taylor, A. Tilquin, A. Tomasch, D. Tucker, D. Vincent, H. von der Lippe, J. Walder, G. Wang, and W. Wester (2004, May). Supernova / Acceleration Probe: A Satellite Experiment to Study the Nature of the Dark Energy. *ArXiv Astrophysics e-prints*.

Spergel, D. N., L. Verde, H. V. Peiris, and the WMAP Collaboration (2003, September). First-Year Wilkinson Microwave Anisotropy Probe (WMAP) Observations: Determination of Cosmological Parameters. ApJS *148*, 175–194.

Stetson, P. B. (2000, July). Homogeneous Photometry for Star Clusters and Resolved Galaxies. II. Photometric Standard Stars. PASP *112*, 925–931.

Stubbs, C. W. and J. L. Tonry (2006, August). Toward 1 Percent Photometry: End-to-End Calibration of Astronomical Telescopes and Detectors. ApJ *646*, 1436–1444.

Thelen, A. (1989). *Design of Optical Interference Coatings*. McGraw-Hill Book Company.

Valdes, F. (2003). http://www.noao.edu/noao/noaodeep/ReductionOpt/Skyflat.html.

van der Marel, R. P. (2003). Determination of Low-Frequency Flat-Field Structure from Photometry of Stellar Fields. *ACS ISR 10*, 1–21.

Wang, L., G. Goldhaber, G. Aldering, and S. Perlmutter (2003). Multi-Color Light Curves of Type Ia Supernovae on the Color-Magnitude Diagram: A Novel Step Toward More Precise Distance and Extinction Estimates. ApJ *590*, 944.

Weller, J. and A. Albrecht (2002, May). Future supernovae observations as a probe of dark energy. Phys. Rev. D *65*(10), 103512.

Yao, W.-M., C. Amsler, D. Asner, and the Particle Data Group (2006). Review of Particle Physics. *Journal of Physics G 33*, 1+.

APPENDICES

APPENDIX A

SNAP Stable Primary Standard Star Candidates

Table A.1. The stable Primary standard star candidates. The stellar types and R-band magnitudes are taken from the SDSS survey.

Obj	**RA (J2000)**	**DEC (J2000)**	R **Mag**	$\sigma[m_0(s)]$	$\mathbf{N}_{obs}$	**Type**
1	243.747399	54.140055	16.060	0.007	3	M
2	244.038185	54.161104	16.600	0.009	3	K
3	244.023621	54.175454	17.130	0.005	3	M
4	244.206224	54.172874	17.080	0.002	3	K
5	244.146628	54.176081	18.340	0.007	3	M
6	243.900716	54.182424	16.840	0.009	3	G
7	243.738612	54.189178	18.610	0.007	3	M
8	243.816066	54.191965	18.140	0.009	3	M
9	244.154097	54.188418	17.700	0.007	3	M
10	244.219005	54.187548	15.490	0.007	3	S
11	243.790402	54.199759	16.630	0.009	3	S
12	244.218632	54.192752	16.750	0.005	3	M
13	243.996786	54.203034	15.360	0.006	3	G
14	243.839450	54.206043	18.480	0.002	3	K
15	243.893994	54.210856	17.310	0.002	3	K
16	244.191248	54.207432	15.630	0.001	3	K
17	244.209992	54.207430	17.220	0.004	3	M
18	243.991604	54.214140	16.930	0.004	3	M
19	244.208782	54.222031	16.300	0.006	3	S
20	243.761368	54.241231	18.220	0.002	3	K
21	244.237669	54.243998	16.210	0.002	3	K
22	244.150182	54.252165	15.710	0.007	3	F
23	243.784039	54.269067	17.700	0.007	3	S
24	244.231799	54.271461	17.880	0.006	4	M
25	244.240469	54.289171	16.560	0.006	4	S
26	243.889983	54.335551	17.400	0.006	4	S
27	243.903121	54.357757	18.730	0.005	4	M
28	244.103974	54.373804	17.030	0.009	4	F
29	244.068257	54.382387	16.910	0.009	4	M
30	244.099189	54.433913	16.800	0.009	4	K

Obj	**RA (J2000)**	**DEC (J2000)**	R **Mag**	$\sigma[m_0(s)]$	$\mathbf{N}_{obs}$	**Type**
31	244.263682	54.432124	16.190	0.008	3	S
32	243.540141	54.484766	19.000	0.003	3	M
33	243.578558	54.487781	17.310	0.008	3	M
34	243.449393	54.493899	16.690	0.007	3	F
35	243.265736	54.502037	16.540	0.006	3	G
36	243.734279	54.494277	16.070	0.003	3	S
37	243.354442	54.502419	18.320	0.006	3	F
38	243.471216	54.502097	17.870	0.004	3	S
39	243.346662	54.506735	18.270	0.002	3	S
40	243.613177	54.502751	15.700	0.006	3	S
41	243.475670	54.513028	16.580	0.004	3	M
42	243.704725	54.512653	16.860	0.004	3	K
43	243.501609	54.517451	16.220	0.003	3	K
44	243.723626	54.514296	17.530	0.006	3	M
45	243.445062	54.519582	17.790	0.008	3	M
46	243.252739	54.524800	15.260	0.009	3	S
47	243.526322	54.522122	17.750	0.001	3	F
48	243.680331	54.520961	15.220	0.002	3	K
49	243.755554	54.523626	18.080	0.005	3	K
50	243.759874	54.534976	18.240	0.007	3	M
51	243.428456	54.543088	18.970	0.006	3	K
52	243.586214	54.541493	18.080	0.003	3	K
53	243.453929	54.544633	17.160	0.007	3	G
54	243.371437	54.546057	17.900	0.004	3	M
55	243.331946	54.549674	18.470	0.001	3	K
56	243.429793	54.550548	18.520	0.006	3	M
57	243.716859	54.546319	16.570	0.001	3	K
58	243.338255	54.553896	18.600	0.004	3	K
59	243.471671	54.556822	17.400	0.006	3	K
60	243.461742	54.559225	15.740	0.006	3	S
61	243.709027	54.555719	17.630	0.007	3	M
62	243.291194	54.569676	18.510	0.008	3	M
63	243.756413	54.562776	15.690	0.007	3	S
64	243.387759	54.574959	15.090	0.006	3	S
65	243.401675	54.578138	17.150	0.005	3	M
66	243.294869	54.585421	16.040	0.004	3	K
67	243.564879	54.586224	17.280	0.003	3	S
68	243.594864	54.586177	15.530	0.003	3	S
69	243.541083	54.590029	16.610	0.003	3	F
70	243.703722	54.590461	17.310	0.009	3	M

Obj	**RA (J2000)**	**DEC (J2000)**	R **Mag**	$\sigma[m_0(s)]$	$\mathbf{N}_{obs}$	**Type**
71	243.710592	54.599409	18.590	0.007	3	K
72	243.728899	54.600889	18.260	0.005	3	M
73	243.595891	54.604039	17.210	0.004	3	S
74	243.430757	54.607522	18.320	0.006	3	K
75	243.672751	54.608616	15.310	0.006	3	S
76	243.339113	54.614459	16.530	0.005	3	F
77	243.776009	54.609269	15.400	0.004	3	G
78	243.624238	54.615440	17.040	0.006	3	S
79	243.654596	54.615880	17.760	0.003	3	G
80	243.350285	54.628033	17.350	0.004	3	K
81	243.584675	54.629405	17.160	0.001	3	S
82	243.726401	54.629278	17.760	0.007	3	M
83	243.597433	54.633473	15.940	0.004	3	K
84	243.273634	54.639002	18.500	0.007	3	M
85	243.368418	54.641190	16.340	0.007	3	F
86	243.334106	54.642390	17.490	0.009	3	K
87	243.313110	54.645276	17.690	0.008	3	M
88	243.362958	54.646824	15.620	0.007	3	G
89	243.489773	54.653195	19.000	0.005	3	S
90	243.623315	54.651894	15.900	0.001	3	G
91	243.587644	54.652652	16.070	0.005	3	M
92	243.305041	54.658732	16.370	0.008	3	S
93	243.561803	54.657528	17.280	0.005	3	M
94	243.410739	54.664443	17.760	0.008	3	M
95	243.536316	54.662422	17.890	0.009	3	M
96	243.552549	54.664560	15.380	0.001	3	G
97	243.762777	54.662854	16.300	0.001	3	S
98	243.311917	54.673218	17.100	0.006	3	S
99	243.648595	54.668356	15.230	0.005	3	K
100	243.457443	54.676310	15.080	0.009	3	S
101	243.735714	54.673872	18.110	0.006	3	F
102	243.473533	54.678629	17.980	0.005	3	F
103	243.602011	54.685869	18.410	0.006	3	K
104	243.417561	54.692796	17.520	0.003	3	F
105	243.310074	54.698939	15.800	0.005	3	M
106	243.311820	54.704572	16.820	0.007	3	S
107	243.245970	54.709156	15.420	0.008	3	F
108	243.498782	54.711717	16.370	0.005	3	G
109	243.343528	54.721555	18.050	0.007	3	K
110	243.757374	54.715439	17.970	0.003	3	K

Obj	**RA (J2000)**	**DEC (J2000)**	R **Mag**	$\sigma[m_0(s)]$	$\mathbf{N}_{obs}$	**Type**
111	243.681297	54.719075	16.140	0.003	3	K
112	243.742793	54.718918	15.810	0.001	3	S
113	243.715034	54.725816	17.740	0.004	3	M
114	243.705132	54.735471	16.240	0.002	3	M
115	243.519315	54.742307	18.480	0.008	3	G
116	243.752201	54.738723	16.350	0.003	3	K
117	243.769096	54.739038	18.180	0.006	3	M
118	243.470110	54.745847	16.480	0.001	3	M
119	243.578005	54.747825	15.270	0.003	3	K
120	243.266582	54.754177	16.900	0.006	3	K
121	243.768664	54.746519	15.530	0.004	3	K
122	243.432653	54.753735	18.630	0.006	3	K
123	243.481099	54.764497	15.790	0.008	3	M
124	242.982962	54.778259	15.110	0.009	3	G
125	243.026655	54.784947	17.420	0.004	3	F
126	243.017896	54.786073	17.250	0.002	3	M
127	243.235721	54.788723	16.840	0.003	3	M
128	243.027493	54.795961	16.250	0.006	3	K
129	243.339088	54.798273	16.100	0.006	3	M
130	243.155325	54.806380	16.020	0.008	3	K
131	242.932162	54.809303	15.870	0.007	3	S
132	243.291736	54.808298	15.440	0.006	3	K
133	243.059137	54.812643	16.440	0.007	3	K
134	243.147348	54.812684	15.780	0.007	3	G
135	243.020620	54.815540	17.420	0.009	3	K
136	243.337401	54.828939	16.760	0.006	3	K
137	243.023524	54.837903	18.790	0.008	3	M
138	243.332191	54.837113	16.540	0.005	3	K
139	243.284904	54.841001	18.230	0.002	3	K
140	243.015458	54.853601	18.080	0.009	3	F
141	242.933842	54.857298	16.470	0.003	3	K
142	243.217297	54.864473	17.240	0.005	3	F
143	243.223052	54.886858	18.530	0.009	3	M
144	243.288067	54.887175	16.120	0.005	3	K
145	243.331652	54.892808	15.270	0.006	3	F
146	243.083002	54.925527	15.870	0.009	3	M
147	243.076497	54.937788	15.860	0.009	3	M
148	243.337584	54.938260	16.320	0.006	3	F
149	242.942039	54.955589	17.200	0.003	3	K
150	243.349899	54.955967	16.580	0.005	3	F

Obj	**RA (J2000)**	**DEC (J2000)**	R **Mag**	$\sigma[m_0(s)]$	$\mathbf{N}_{obs}$	**Type**
151	242.994567	54.972642	15.240	0.002	3	K
152	242.990601	54.978105	17.600	0.005	3	K
153	243.358245	54.977700	15.090	0.009	3	K
154	243.332615	54.978417	18.060	0.001	3	M
155	243.286302	54.982217	17.030	0.004	3	G
156	242.959776	54.985147	16.470	0.002	3	F
157	242.961674	54.990743	15.280	0.005	3	S
158	242.977423	55.001692	18.270	0.008	3	K
159	242.960926	55.005079	15.260	0.003	3	G
160	243.230573	55.004031	15.160	0.006	3	S
161	243.316577	55.006042	18.010	0.003	3	M
162	243.297351	55.009535	15.720	0.005	3	F
163	243.347686	55.013381	17.850	0.003	3	K
164	242.952494	55.018678	17.170	0.003	3	G
165	243.103160	55.019362	16.780	0.006	3	K
166	243.289708	55.020557	18.100	0.007	3	G
167	243.139396	55.025217	16.000	0.006	3	M
168	243.168529	55.025462	15.030	0.006	3	K
169	242.962487	55.028753	17.980	0.009	3	K
170	243.352905	55.027965	18.170	0.007	3	M
171	243.318600	55.028704	15.980	0.004	3	G
172	243.177383	55.030598	16.830	0.005	3	K
173	243.115113	55.040531	17.650	0.007	3	K
174	242.937472	55.051901	15.750	0.006	3	G
175	243.076432	55.051092	18.220	0.007	3	M
176	243.346565	55.058555	16.570	0.003	3	F
177	242.534426	53.301329	16.910	0.009	3	K
178	242.448237	53.306064	16.210	0.008	3	G
179	242.312441	53.309717	18.240	0.009	3	F
180	242.676752	53.307557	15.950	0.008	3	S
181	242.433948	53.310580	15.190	0.006	3	G
182	242.550576	53.313207	17.610	0.009	3	F
183	242.482411	53.315083	15.980	0.004	3	M
184	242.663935	53.315183	15.960	0.007	3	S
185	242.568011	53.319177	18.850	0.009	3	M
186	242.298485	53.321263	18.190	0.007	3	K
187	242.439581	53.320866	17.040	0.004	3	M
188	242.304157	53.325321	18.960	0.008	3	M
189	242.617893	53.326171	16.910	0.005	3	S
190	242.454254	53.329703	18.340	0.009	3	M

Obj	**RA (J2000)**	**DEC (J2000)**	R **Mag**	$\sigma[m_0(s)]$	$\mathbf{N}_{obs}$	**Type**
191	242.322615	53.334585	17.870	0.009	3	K
192	242.517962	53.334300	18.070	0.007	3	F
193	242.395081	53.348885	18.520	0.008	3	K
194	242.511178	53.352237	16.090	0.004	3	M
195	242.513361	53.365349	18.810	0.008	3	K
196	242.472703	53.366865	16.530	0.004	3	F
197	242.713964	53.365949	17.460	0.003	3	K
198	242.624718	53.370110	15.240	0.009	3	K
199	242.320199	53.379275	15.020	0.007	3	K
200	242.485816	53.378525	17.010	0.005	3	G
201	242.374026	53.379673	16.260	0.004	3	G
202	242.365051	53.387850	15.470	0.002	3	S
203	242.396799	53.390879	18.160	0.008	3	F
204	242.489541	53.391727	18.270	0.006	3	M
205	242.492699	53.396716	17.250	0.008	3	M
206	242.398749	53.400003	18.330	0.004	3	F
207	242.491769	53.403097	17.870	0.006	3	M
208	242.662741	53.404936	15.810	0.005	3	M
209	242.478767	53.417551	16.960	0.001	3	M
210	242.687021	53.416269	15.180	0.006	3	F
211	242.328412	53.421756	18.450	0.008	3	M
212	242.321652	53.431389	16.170	0.004	3	K
213	242.326048	53.437438	16.810	0.004	3	K
214	242.508057	53.442557	17.660	0.009	3	K
215	242.453983	53.447090	15.770	0.009	3	K
216	242.478568	53.449076	16.660	0.002	3	K
217	242.579094	53.449601	17.640	0.009	3	G
218	242.397190	53.455630	15.260	0.005	3	K
219	242.335308	53.458268	17.100	0.003	3	K
220	242.518434	53.458115	16.320	0.002	3	S
221	242.422575	53.460068	18.560	0.008	3	M
222	242.635477	53.459743	17.340	0.002	3	M
223	242.714055	53.459819	17.100	0.006	3	F
224	242.365770	53.463930	16.450	0.005	3	M
225	242.415440	53.473996	16.570	0.004	3	S
226	242.510074	53.483163	16.610	0.006	3	K
227	242.693620	53.485868	16.910	0.004	3	S
228	242.387732	53.491413	17.610	0.009	3	S
229	242.680750	53.496345	16.540	0.006	3	K
230	242.349381	53.502722	16.390	0.001	3	S

Obj	**RA (J2000)**	**DEC (J2000)**	R **Mag**	$\sigma[m_0(s)]$	$\mathbf{N}_{obs}$	**Type**
231	242.643580	53.510785	18.700	0.009	3	M
232	242.455297	53.514282	17.450	0.009	3	K
233	242.673271	53.515847	17.440	0.008	3	M
234	242.670432	53.524779	15.270	0.007	3	F
235	242.507801	53.531793	15.420	0.002	3	M
236	242.635544	53.531605	17.640	0.005	3	G
237	242.411017	53.534231	16.000	0.005	3	S
238	242.685578	53.533229	18.210	0.009	3	S
239	242.733518	53.537189	16.240	0.009	3	M
240	242.357997	53.545512	17.330	0.004	3	M
241	242.306383	53.555168	15.470	0.005	3	G
242	242.629741	53.555818	17.080	0.003	3	M
243	242.542020	53.564398	17.690	0.008	3	M
244	242.747760	53.567232	17.320	0.004	3	S
245	242.684992	53.571173	16.410	0.005	3	M
246	242.598673	53.574431	17.900	0.008	3	M
247	242.400657	53.578984	15.730	0.005	3	K
248	242.470887	53.578822	17.830	0.009	3	F
249	242.508443	53.579335	15.520	0.006	3	S
250	242.652825	53.578246	16.040	0.004	3	K
251	242.336093	53.581235	18.160	0.008	3	M
252	242.751745	53.578304	16.460	0.007	3	K
253	242.488470	53.580999	15.050	0.004	3	M
254	242.467802	53.590815	17.820	0.008	3	F
255	242.299326	53.600966	15.290	0.004	3	K
256	242.479891	53.610519	18.240	0.004	3	M
257	242.583969	53.611217	18.820	0.005	3	M
258	242.729196	53.615635	15.750	0.006	3	M
259	242.330415	53.619772	16.680	0.008	3	K
260	241.816572	53.589150	17.530	0.003	4	F
261	241.764140	53.597696	18.020	0.003	4	M
262	242.150980	53.595120	17.860	0.006	4	F
263	241.941704	53.604013	18.660	0.005	4	K
264	241.726836	53.607865	17.920	0.004	4	F
265	241.712714	53.610653	17.900	0.008	3	M
266	242.035594	53.612813	17.770	0.007	4	M
267	241.975075	53.614644	17.230	0.001	4	K
268	242.049458	53.620671	15.270	0.002	4	F
269	242.027323	53.622390	18.640	0.006	4	M
270	241.769032	53.627857	16.660	0.004	4	S

Obj	**RA (J2000)**	**DEC (J2000)**	R **Mag**	$\sigma[m_0(s)]$	$\mathbf{N}_{obs}$	**Type**
271	241.853876	53.626564	16.900	0.007	4	K
272	241.792711	53.628692	17.250	0.002	4	K
273	241.832943	53.630906	16.880	0.005	4	G
274	241.938186	53.633041	17.150	0.005	4	K
275	241.871016	53.638678	15.250	0.003	4	S
276	242.170008	53.637484	17.710	0.008	4	S
277	241.782905	53.652806	17.230	0.003	4	S
278	241.765954	53.654260	18.300	0.001	4	K
279	241.899139	53.653878	18.140	0.004	4	M
280	241.915958	53.660059	17.070	0.001	4	G
281	242.041859	53.660823	16.930	0.006	4	K
282	242.146387	53.660377	16.080	0.003	4	K
283	242.021946	53.665074	15.010	0.001	4	S
284	242.091978	53.669688	17.630	0.007	4	S
285	242.180331	53.668514	17.880	0.008	4	M
286	241.911541	53.673543	16.350	0.002	4	M
287	241.772972	53.677406	18.460	0.007	4	S
288	241.869895	53.677150	16.280	0.003	4	F
289	241.955930	53.678775	16.440	0.008	4	M
290	241.909352	53.681846	18.130	0.006	4	G
291	242.028547	53.681942	16.890	0.004	4	K
292	241.775155	53.688661	15.930	0.003	4	K
293	241.864252	53.690469	17.560	0.003	4	G
294	242.042287	53.692442	17.660	0.003	4	K
295	242.145103	53.694409	17.690	0.006	4	F
296	242.056222	53.699127	16.840	0.006	4	K
297	242.256458	53.695986	16.160	0.007	3	G
298	242.128045	53.698696	16.520	0.003	4	F
299	241.852724	53.712078	17.280	0.005	4	K
300	241.768737	53.719235	17.520	0.006	4	M
301	241.850515	53.718641	18.530	0.002	4	G
302	242.247571	53.713017	17.890	0.006	3	K
303	242.130700	53.721903	17.730	0.006	4	K
304	241.849859	53.740251	18.390	0.008	4	K
305	241.868882	53.743937	16.800	0.006	4	K
306	242.009314	53.743825	17.820	0.008	4	G
307	242.090212	53.744755	15.750	0.003	4	K
308	242.209441	53.743552	17.990	0.005	4	WD
309	241.883831	53.751437	18.630	0.006	4	M
310	241.874632	53.753039	16.670	0.006	4	K

Obj	**RA (J2000)**	**DEC (J2000)**	R **Mag**	$\sigma[m_0(s)]$	$\mathbf{N}_{obs}$	**Type**
311	241.815350	53.758025	16.940	0.005	4	K
312	242.065867	53.754459	17.320	0.004	4	G
313	242.205479	53.754185	15.610	0.005	4	K
314	242.269031	53.754160	16.840	0.008	3	K
315	242.219609	53.761673	17.320	0.003	4	F
316	241.756856	53.772065	16.850	0.004	4	K
317	242.089579	53.769418	18.690	0.006	4	S
318	242.037706	53.778379	17.820	0.007	4	K
319	242.167756	53.781360	15.660	0.003	4	G
320	241.727491	53.791427	17.250	0.001	4	S
321	242.094961	53.786223	16.450	0.004	4	K
322	242.078948	53.788383	18.030	0.007	4	M
323	242.041396	53.791958	15.530	0.004	4	F
324	242.214064	53.793135	15.760	0.003	4	K
325	242.259595	53.794201	16.700	0.005	3	K
326	241.779995	53.806572	16.200	0.003	4	M
327	242.134988	53.806355	17.210	0.003	4	M
328	242.086593	53.807130	17.090	0.002	4	G
329	241.876019	53.813042	18.680	0.004	4	K
330	242.019315	53.817920	17.100	0.007	4	K
331	241.912909	53.820560	15.940	0.009	4	S
332	242.146978	53.817911	16.180	0.005	4	K
333	241.758746	53.826389	16.230	0.002	4	K
334	241.741156	53.827124	17.150	0.003	4	G
335	242.018780	53.824673	16.010	0.005	4	F
336	242.064261	53.824240	16.200	0.003	4	K
337	241.732387	53.830819	15.690	0.001	4	S
338	241.808888	53.830466	18.280	0.004	4	K
339	241.914579	53.829383	16.890	0.007	4	S
340	241.726538	53.839009	18.350	0.007	4	M
341	242.143165	53.843652	16.730	0.002	4	K
342	241.786549	53.851230	17.940	0.007	4	M
343	242.018072	53.847768	17.570	0.002	4	M
344	242.172795	53.849837	18.010	0.002	4	F
345	242.152924	53.853044	18.000	0.009	4	K
346	242.068559	53.854661	17.430	0.002	4	M
347	241.830982	53.859848	16.680	0.006	4	G
348	241.751045	53.862667	18.860	0.006	4	M
349	241.765549	53.862863	17.420	0.005	4	F
350	242.048516	53.862843	17.540	0.004	4	F

Obj	**RA (J2000)**	**DEC (J2000)**	R **Mag**	$\sigma[m_0(s)]$	$\mathbf{N}_{obs}$	**Type**
351	241.975877	53.867050	17.110	0.004	4	S
352	241.832927	53.869594	15.620	0.002	4	G
353	242.025513	53.873397	16.290	0.003	4	S
354	241.952605	53.883294	15.930	0.002	4	K
355	241.844333	53.889798	17.000	0.001	4	K
356	241.887514	53.896778	18.710	0.005	4	M
357	242.059551	53.734497	17.760	0.008	3	G
358	241.611140	53.894950	18.920	0.009	3	M
359	241.705460	53.895637	16.740	0.006	3	K
360	241.617620	53.899980	17.090	0.005	3	F
361	241.688020	53.914604	16.030	0.005	3	K
362	241.655520	53.926304	17.580	0.006	3	K
363	241.485530	53.930793	17.950	0.006	3	M
364	241.475120	53.941335	18.360	0.006	3	K
365	241.274060	53.959781	18.230	0.007	3	M
366	241.639910	53.964217	18.560	0.008	3	M
367	241.351160	53.968825	17.610	0.005	3	F
368	241.383420	53.972766	15.810	0.006	3	M
369	241.655260	53.986793	17.800	0.002	3	G
370	241.387940	53.993038	15.660	0.009	3	K
371	241.210440	54.002183	18.420	0.004	3	M
372	241.325390	54.003901	17.590	0.008	3	S
373	241.284190	54.014016	15.110	0.006	3	K
374	241.719970	54.016187	17.790	0.008	3	S
375	241.349550	54.018163	17.390	0.008	3	M
376	241.210110	54.018890	18.930	0.009	3	M
377	241.617410	54.024178	17.040	0.009	3	K
378	241.723210	54.033405	17.790	0.006	3	K
379	241.723770	54.041857	16.040	0.002	3	S
380	241.333870	54.057099	16.460	0.005	3	M
381	241.251790	54.068111	18.710	0.005	3	G
382	241.704090	54.068088	15.990	0.003	3	G
383	241.576150	54.071014	16.660	0.004	3	K
384	241.319550	54.075606	18.160	0.004	3	K
385	241.713330	54.075900	18.320	0.008	3	M
386	241.627440	54.081003	17.640	0.008	3	S
387	241.528900	54.085698	17.940	0.004	3	S
388	241.239070	54.092568	15.200	0.002	3	M
389	241.278400	54.094619	18.830	0.007	3	M
390	241.250950	54.097388	16.210	0.003	3	G

Obj	**RA (J2000)**	**DEC (J2000)**	R **Mag**	$\sigma[m_0(s)]$	$\mathbf{N}_{obs}$	**Type**
391	241.369380	54.101649	18.520	0.009	3	F
392	241.466270	54.101658	16.090	0.004	3	M
393	241.574440	54.102362	17.500	0.003	3	G
394	241.248700	54.102739	15.330	0.005	3	G
395	241.359240	54.107775	16.760	0.006	3	G
396	241.245980	54.108527	17.930	0.005	3	K
397	241.526490	54.111717	16.460	0.002	3	G
398	241.258350	54.113185	17.830	0.006	3	K
399	241.564280	54.113412	16.960	0.002	3	K
400	241.382830	54.117613	15.220	0.003	3	K
401	241.318470	54.122431	18.700	0.004	3	K
402	241.636350	54.128407	15.150	0.004	3	K
403	241.331990	54.131876	16.200	0.004	3	S
404	241.722420	54.135026	17.590	0.004	3	K
405	241.339370	54.136850	18.060	0.007	3	S
406	241.315650	54.141670	18.280	0.008	3	K
407	241.438150	54.150908	17.410	0.005	3	S
408	241.309260	54.152285	17.540	0.006	3	S
409	241.344720	54.151795	17.210	0.006	3	M
410	241.532450	54.162663	16.260	0.002	3	K
411	241.283120	54.165001	18.380	0.005	3	M
412	241.340000	54.171723	18.610	0.007	3	F

Curriculum Vita — Nick Mostek

Address: Department of Astronomy
Indiana University
Swain Hall West 319
727 E. Third St.
Bloomington, IN 47405
e-mail: nmostek@astro.indiana.edu

Education

- Indiana University — Astronomy — Ph.D, 2007 (*expected*)
  - Thesis: *Calibration System Design and Determination of Filter Calibration Requirements for SNAP*
- Indiana University — Astronomy — M.A., 2004
- Iowa State University — Physics — B.S., 2000

Research Interests

- Hardware development for photometric calibration of space-based telescopes
- Active collaboration with the SuperNova/Acceleration Probe (SNAP)
- Effect of calibration errors on type Ia supernovae and cosmological parameters
- Techniques for precision radiometry with optical and NIR photodetectors

Academic Positions

- Research Associate, Indiana University Department of Astronomy, 2001-2007
- Instructor, A105 Stars and Galaxies, Indiana University, SCS, 2003-2007
- Associate Instructor, Indiana University Department of Astronomy, 2000-2001
  - *E105 Stars and Galaxies* — Fall 2000
  - *A100 Introduction to Astronomy* — Spring 2001
- REU Participant, National Optical Astronomy Observatory, Summer 1999
- Research Assistant, Iowa State University, 1998-2000

Other Educational Experience

- Laboratory Supervisor of Undergraduate Research, 2005-2007
- Course Text Revision, A105 Stars and Galaxies, Indiana University, SCS, 2005
- Tour Guide and Outreach Volunteer, Kirkwood Observatory, 2000-2007

Selected Publications

- Schubnell, M. et al., including **Mostek, N.**, 2006, *"Near Infrared Detectors for SNAP"*, SPIE, 6276
- Kim, Alex G.; Linder, Eric V.; Miquel, R.; **Mostek, N.**, 2004, *"Effects of systematic uncertainties on the supernova determination of cosmological parameters"*, MNRAS, 347, 909
- Deustua, S. et al., including **Mostek, N.**, 2003, *"Calibrating SNAP"*, SPIE, 5164, 84

Conference Presentations

- **Mostek, N.**; *"SNAP Calibration Report"*, plenary oral presentation at the SNAP Collaboration Meeting, Lawrence Berkeley National Labs, Berkeley, CA, June 1-3, 2006
- **Mostek, N.**; Bower, C. R.; Mufson, S. L.; Sholl, M.; *"SNAP Calibration Hardware"*, oral presentation for SNAP Calibration Program Review, Lawrence Berkeley National Labs, Berkeley, CA, July 14, 2006
- **Mostek, N.** and the SNAP Collaboration *"A Search for Stable Calibration Stars in the SNAP North Field"*, presented at the 205th Meeting of the American Astronomical Society, San Diego, CA, Jan. 9-13, 2005, Abstract in BAAS, 36, 1456

Awards

- Joseph Swain Research Award, Indiana University Astronomy Department, 2007

Professional Affiliations

- American Astronomical Society, 1999 - present